

Experimental Studies and Multi-Scale Modelling of Advanced Ceramics: Fracture, Fragmentation, and Failure

by
Jie Zheng

A thesis submitted in partial fulfillment of the requirements for the degree of

Doctor of Philosophy

Department of Mechanical Engineering
UNIVERSITY OF ALBERTA

©Jie Zheng, 2024

Abstract

The objectives of this thesis is to explores the mechanical behaviour of alumina ceramics, focusing on fracture and fragmentation response through a blend of experimental investigations and advanced computational modelling. To bridge the gap between micro-mechanisms and macroscopic material behaviors, the microstructure and mechanical properties of the CeramTec ALOTEC 98 SB (CeramTec 98%) alumina ceramic are examined using microscopic characterization and mechanical testing under various strain-rate and stress-state loading conditions. The mechanical tests employs a modified split-Hopkinson pressure bar complemented by high-speed imaging and digital image correlation (DIC), to capture the fracture processes and stress fields. The testing results indicate that this ceramic exhibits superior mechanical properties to other commercial alumina ceramics, with strengths becoming stronger with higher strain rates. Further, a three-dimensional hybrid finite-discrete element model considering the flaw system of advanced ceramics is developed and validated against experimental data. These models successfully simulated crack initiation, propagation, and fragmentation processes, offering new perspectives on the failure process of alumina ceramics. Sensitivity analyses explore the influence of material properties, such as elastic modulus, fracture properties and flaws, on mechanical strength, including the tensile and compressive strength of advanced ceramics. By integrating experimental and computational approaches, this research advances the fundamental understanding of failure mechanisms of alumina ceramics. The findings provide valuable insights into the design and optimization of advanced ceramics, contributing to the development of next-generation advanced ceramic materials for defence and aerospace applications.

Preface

I, Jie Zheng, declare that this thesis titled, ‘Experimental Studies and Multi-Scale Modelling of Advanced Ceramics: Fracture, Fragmentation, and Failure’ and the work presented in it are my own. Furthermore, permission is hereby granted to the University of Alberta Libraries to reproduce single copies of this thesis and to lend or sell such copies for private, scholarly or scientific research purposes only. Where the thesis is converted to, or otherwise made available in digital form, the University of Alberta will advise potential users of the thesis of these terms.

The author reserves all other publication and other rights in association with the copyright in the thesis and, except as herein before provided, neither the thesis nor any substantial portion thereof may be printed or otherwise reproduced in any material form whatsoever without the author’s prior written permission.

Chapter 2 of this thesis has been published as **Jie Zheng**; Ji, M; Zaiemyekeh, Z; Li, HY and Hogan, JD. *Strain-rate-dependent Compressive and Compression-shear Response of an Alumina Ceramic*, Journal of the European Ceramic Society (2022). I was responsible for conceptualization, theoretical methodology, experimentation, software, investigation, validation, resources, data curation, writing – original draft, writing – review editing, visualization; Ji, M was responsible for experimentation, investigation, validation, writing – review; Zaiemyekeh, Z was responsible for experimentation, investigation, validation, writing – review editing; and Li, HY provided experimentation, software, investigation, validation, resources, writing – review editing, guidance; and Hogan, JD was the principal investigator and provided revisions to the scientific content, and stylistic/grammatical suggestions of the manuscript.

Chapter 3 of this thesis has been published as **Jie Zheng**; Li, HY and Hogan, JD. *Strain-rate-dependent Tensile Response of an Alumina Ceramic: Experiments and Modelling*, International Journal of Impact Engineering (2023). I was responsible for conceptualization, theoretical methodology, conceiving the ideas and experimental design of the study, Performed experiments/data collection, Data analysis and interpretation, and Primary author (drafted the manuscript); Li, HY provided revisions to the scientific content of the manuscript; and Hogan, JD was the principal investigator and provided revisions to the scientific content, and stylistic/grammatical suggestions of the manuscript.

Chapter 4 of this thesis has been published as **Jie Zheng**; Li, HY and Hogan, JD. *Hybrid Finite-discrete Element Modeling of the Mode I Tensile Response of an Alumina Ceramic*, Modelling (2023). I was responsible for conceptualization, theoretical methodology, experimentation, software, investigation, validation, resources, data curation, Writing – original draft, writing – review editing, visualization; Li, HY provided revisions to the scientific content of the manuscript; and Hogan, JD was the principal investigator and

provided revisions to the scientific content, and stylistic/grammatical suggestions of the manuscript.

Chapter 5 of this thesis has been published as **Jie Zheng**; Li, HY and Hogan, JD. *Advanced Tensile Fracture Analysis of Alumina Ceramics: Integrating Hybrid Finite-discrete Element Modeling with Experimental Insights*, Engineering Fracture Mechanics (2024). I was responsible for conceptualization, theoretical methodology, experimentation, software, investigation, validation, resources, data curation, Writing – original draft, writing – review editing, visualization; Li, HY provided revisions to the scientific content of the manuscript; and Hogan, JD was the principal investigator and provided revisions to the scientific content, and stylistic/grammatical suggestions of the manuscript.

Chapter 6 of this thesis is under review as **Jie Zheng**; Li, HY; Zaiemyekheh, Z; Sun, N.; Sayahlatifi, S.; Chen, ZT and Hogan, JD. *Modified Hybrid Finite-discrete Element Modeling of Compressive Failure in Alumina Ceramics*, International Journal of Mechanical Sciences (2024). I was responsible for conceptualization, theoretical methodology, experimentation, software, investigation, validation, resources, data curation, Writing – original draft, writing – review editing, visualization; Li, HY provided revisions to the scientific content of the manuscript; Zaiemyekheh, Z provided revisions to the scientific content of the manuscript; Sun, N. provided revisions to the scientific content of the manuscript; Sayahlatifi, S. provided revisions to the scientific content of the manuscript; Chen, ZT provided revisions to the scientific content of the manuscript; and Hogan, JD was the principal investigator and provided revisions to the scientific content, and stylistic/grammatical suggestions of the manuscript.

Signed: *Jie Zheng*

Date: 2024 July 11

"The important thing is to never stop questioning."

- Albert Einstein

Acknowledgements

I am profoundly grateful to my supervisor, Dr. James D. Hogan, for his exceptional guidance and unwavering support throughout my PhD journey. His mentorship granted me the freedom and flexibility essential for my research, and his constant encouragement during challenging times has been a significant source of inspiration for my career. The invaluable experiences gained under his supervision have deeply influenced me and will forever be a part of who I am.

I sincerely thank Dr. Chong-qing Ru and Dr. Zengtao Chen from the University of Alberta for their insightful discussions on theoretical methods and support in my experimental and simulation work. Further, a portion of the experimental research presented in this thesis was conducted at the Engineering Workshop within the Department of Mechanical Engineering at the University of Alberta, where I deeply appreciate the help and support of the laboratory staffs. Special thanks go to Mitul Patel for his invaluable guidance.

I am deeply grateful to Dr. Geneviève Toussaint from Defence Research and Development Canada for the enriching technical conversations during our collaborations on multiple projects.

I seize this opportunity to express my gratitude to my colleagues at the Mechanical Engineering Department: Haoyang Li, Junhao Chang, Kasra Rezasefat, Luyue Mao, Saman Sayahlatifi, Sara Sheikhi, Yogesh Kumar, Zahra Zaiemyekeh, Benhour Amirian, Brendan Koch, Calvin Lo, Chenwei Shao, Hannaneh Manafi Farid, Harshil Pisavadia, Kapil Bharadwaj Bhagavathula, Min Ji, Mohammad Parsazadeh, and Shuo (Alex) Yang. Their willingness to share their expertise and assist me throughout my time at the Center for Design of Advanced Materials (CDAM) has been invaluable. Additionally, I thank all the unnamed colleagues and friends in Canada who have offered their support. To each of you, I wish you nothing but success in your future endeavours.

Lastly, I express profound gratitude to my parents for their unwavering love and steadfast moral support throughout my journey. I am incredibly fortunate to have a family that stands by me with love and encouragement, making me feel truly blessed.

Contents

Abstract	ii
Preface	iii
Acknowledgements	vi
List of Tables	x
List of Figures	xi
Abbreviations	xix
Symbols	xxi
1 Introduction	1
1.1 Motivation	1
1.2 Background and Literature Review	2
1.2.1 Failure processes in advanced ceramics	2
1.2.2 Experimental methods in advanced ceramics	4
1.2.3 Computational methods for describing failure in brittle materials	6
1.3 Thesis Objectives	7
1.4 Thesis Goals	7
1.5 Key Contributions	9
1.6 Thesis Structure	9
2 Strain-rate-dependent Compressive and Compression-shear Response of an Alumina Ceramic	14
2.1 Abstract	14
2.2 Introduction	15
2.3 Experimental methods	17
2.3.1 Material characterization	18
2.3.2 Quasi-static uniaxial compression and compression-shear tests	18
2.3.3 Dynamic uniaxial compression and compression-shear tests	19
2.3.4 Digital image correlation	20
2.4 Data processing method for combined compression and shear loading	23

2.5	Experimental results	26
2.5.1	Material characterization	26
2.5.2	Strain-rate dependent uniaxial compression tests	27
2.5.3	Strain-rate dependent compression-shear tests	30
2.6	Discussion	33
2.6.1	Microstructure and mechanical properties of comparable alumina ceramics	33
2.6.2	Shear-induced failure on mechanical response	37
2.7	Conclusion	40
3	Strain-rate-dependent Tensile Response of an Alumina Ceramic: Experiments and Modelling	41
3.1	Abstract	41
3.2	Introduction	42
3.3	Experimental and modelling methods	44
3.3.1	Material and specimens	44
3.3.2	The flattened Brazilian disk tests	44
3.3.3	Post-mortem fractographic analysis	48
3.3.4	Theoretical considerations	48
3.3.5	The strain-rate-dependent tensile strength model	54
3.4	Results and discussion	56
3.4.1	The temporally- and spatially-evolving strain components	56
3.4.2	The fracture process of the FBD sample in a dynamic test	61
3.4.3	Unraveling structure vs. material failure	63
3.4.4	Strain-rate-dependent tensile strength and post-mortem fractographic analysis	65
3.5	Conclusion	72
4	Hybrid Finite-discrete Element Modeling of the Mode I Tensile Response of an Alumina Ceramic	74
4.1	Abstract	74
4.2	Introduction	75
4.3	Computational approach	77
4.3.1	The cohesive law	78
4.3.2	The microscopic stochastic fracture model	80
4.4	The hybrid finite-discrete element method	81
4.4.1	Modeling mode I failure considering distributed flaws	82
4.4.2	The effect of flaw distribution	86
4.5	Conclusion	89
5	Advanced Tensile Fracture Analysis of Alumina Ceramics: Integrating Hybrid Finite-discrete Element Modeling with Experimental Insights	91
5.1	Abstract	91
5.2	Introduction	92
5.3	Computational approach	95
5.3.1	The coupled damage and friction cohesive model	95
5.3.2	The microscopic stochastic fracture model	97
5.4	The hybrid finite-discrete element model (HFDEM)	98

5.4.1	Material properties and HFDEM	98
5.4.2	The direct tension HFDEM model	101
5.5	Experiments and numerical simulation of indirect tensile testing	104
5.5.1	Experimental method and results of FBD testing	104
5.5.2	The numerical simulation of FBD testing	106
5.5.3	The fracture patterns and fragmentation	108
5.6	Conclusion	113
6	Modified Hybrid Finite-discrete Element Modeling of Compressive Failure in Alumina Ceramics	115
6.1	Abstract	115
6.2	Introduction	116
6.3	Experimental methods and results	119
6.3.1	Experimental method	120
6.3.2	Experimental results	120
6.4	Computational approach	121
6.4.1	The coupled damage and friction law of the cohesive zone method	122
6.4.2	Damage evolution with linear- and power-law characteristic	123
6.4.3	The microscopic stochastic fracture model	125
6.4.4	The modified hybrid finite-discrete element method	125
6.5	The comparison between linear- and power-law simulation results	128
6.5.1	The stress-strain response	130
6.5.2	The fracture and fragmentation processes	131
6.6	Results and discussion	134
6.6.1	The effect of basic mechanical properties	135
6.6.2	The effect of fracture properties	137
6.7	Conclusion	139
7	Concluding Remarks	141
7.1	Summary	141
7.2	Future works and recommendations	144
	Bibliography	145

List of Tables

2.1	Pulse shaping configurations used in dynamic experiments	20
2.2	Elemental composition of the CeramTec 98% alumina as determined by EDS	29
2.3	The mechanical properties and responses of the CeramTec 98% alumina . .	33
3.1	The experimental results of the FBD tests under different loading rates . .	66
4.1	The properties of CeramTec 98% alumina for the HFDEM model	82
4.2	Statistics of four FEM meshes	83
5.1	The properties of CeramTec 98% alumina for the HFDEM model	99
5.2	Input parameters for the four different mesh sizes	102
5.3	The experimental results of the FBD tests	106
6.1	Mechanical and fracture properties of the alumina ceramic	126

List of Figures

- 2.1 The split-Hopkinson pressure bar configuration for dynamic testing with an ultra-high-speed camera, a high-speed data acquisition system (DAQ) and an ultra-bright LED ring light. The insert below shows the geometries of the specimen: (a) uniaxial compression specimen with a tilting angle of 0° , and (b) compression-shear specimen with a tilting angle of 5° 19
- 2.2 For specimen under dynamic uniaxial compression, the stress profile obtained from the transmitted gauge and the local strain profiles computed from six different areas of interest (AOI) by DIC are matched in time. The locations of the six AOIs are shown in the inset. The linear portions of the strain-time curves is taken as the strain rate, and the average strain rate in this experiment is approximately 383 s^{-1} 21
- 2.3 For specimen under combined dynamic compression and shearing loading, the axial stress profile obtained from the transmitted gauge and the local axial strain profiles computed from six different areas of interest (AOI) by DIC are matched in time. The locations of the six AOIs are shown in the inset. The linear portions of the strain-time curves is taken as the axial strain rate, and the average strain rate in this experiment is approximately 392 s^{-1} . The axial direction is the horizontal direction. 22
- 2.4 The analysis of force and deformation of the specimen during compression-shear testing: (a) the force analysis of the specimen, where the specimen is sprayed with a speckle pattern for digital image correlation which allows for measurements of compression and shear strains. F_n and F_t are the normal force and the tangential force applied on the specimen, respectively, where the tangential force is induced by friction. (b) the deformation analysis of the specimen with the assumption that no surface sliding happens, as indicated by the red dashed lines. The black dashed lines demonstrate the initial location of the specimen, and the solid line is the specimen under compression and shear loads. α is the tilting angle of 5° , θ is the shear strain, d is the loading displacement, and h is the length of the specimen. 24
- 2.5 (a) SEM image of a polished alumina surface which shows the micro-structural features of the alumina. The grey regions correspond to the alumina, and the surface pores can be observed. (b) EBSD maps for the CeramTec 98% alumina, and this map shows the grain size and the crystal orientation of the grains at the surface of the sample. 28

2.6	The histogram distribution of the equivalent circle diameter of the grain in the CeramTec 98% alumina, which is obtained from several regions of the sample. Approximately 88% of the grain size (the equivalent circle diameters) distribution is between 0.4 and 2.8 μm , and they are nearly circular small grains. There are also a relatively small number of large horizontal high-aspect-ratio grains with the equivalent circle diameters ranging from 5 to 8 μm	29
2.7	(a) and (b): The central volume of the sample, a cylinder with a height of 0.61 mm and a diameter of 0.53 mm, was considered for the XRM analysis. The colored volumes in (b) are the defects (pores and impurities) in the sample. (c) The histogram of defects with different size volumes. The volume value of the defects is dominated by small ones (less than 160 μm^3), and large defects are infrequent (the largest volume of the defect is around 10200 μm^3). The histogram of the volumes less than 1200 μm^3 is enlarged in the inset.	30
2.8	SEM coupled with EDS investigating the chemical composition of the alumina. (a) SEM micrograph showing a magnified view of a mechanically polished surface of the CeramTec 98% alumina. (b) EDS map of the distribution of oxygen. (c) EDS map of the distribution of aluminum. (d) EDS maps of magnesium element. (e) EDS maps of silicon element. and (f) EDS maps of the calcium element. The magnesium, silicon and calcium elements are present in low quantities.	31
2.9	Representative stress-strain curves in the axial direction at quasi-static and dynamic strain rates (with three different pulse shaping configurations shown in Table 2.1) for the CeramTec 98% alumina. The solid lines correspond to the uniaxial compression tests, and the dashed lines correspond to the compression-shear tests. Additional summarized data is provided in Table 2.3.	32
2.10	Representative lateral-axial strain curves at quasi-static and dynamic strain rates (with three different pulse shaping configurations shown in Table 2.1) for the CeramTec 98% alumina. The solid lines correspond to the uniaxial compression tests and the dashed lines correspond to the compression-shear tests, noting little differences between the two types of tests.	34
2.11	Semi-log plot of the equivalent peak stress and the equivalent strain rate for the CeramTec 98% alumina. The black rectangle points represent the uniaxial compression tests, and the red circle points represent the compression-shear tests. A black rectangle point in the figure is circled, because there are two points almost overlapped. A red circle point in the figure is circled, because there are three points almost overlapped.	35
2.12	The shear strain-time curves from compression-shear tests at various strain rates. The black curves are the shear strain obtained from DIC analysis, and the red curves are the predicted shear strain by Equation (2.15): (a) shear strain-time curve at a quasi-static strain rate ($1.6 \times 10^{-5} s^{-1}$), (b) shear strain-time curve at a quasi-static strain rate ($1.6 \times 10^{-3} s^{-1}$), (c) shear strain-time curve at a strain rate of $83 s^{-1}$ (tin pulse shaper), (d) shear strain-time curve at a strain rate of $347 s^{-1}$ (thin HDPE pulse shaper), (e) shear strain-time curve at a strain rate of $392 s^{-1}$ (thin HDPE pulse shaper), and (f) shear strain-time curve at a strain rate of $706 s^{-1}$ (thick HDPE pulse shaper).	36

2.13	Time-resolved failure visualization for uniaxial compression test. The strain rate is around 638 s^{-1} . Ultra-high-speed photographs are shown in the inset, and their corresponding points are shown as the black points on the red stress-time curve. The cracks are pointed out by yellow arrows.	37
2.14	Time-resolved failure visualization for compression-shear test. The strain rate in the axial direction is around 706 s^{-1} . Ultra-high-speed photographs are shown in the inset, and their corresponding points are shown as the black points on the red stress-time curve. The cracks are pointed out by yellow arrows.	38
2.15	Summary of uniaxial compression strengths of various alumina ceramics with cylindrical or cuboidal shaped specimen. The black points are the uniaxial compression strength of the CeramTec 98% alumina from this study, and the other colored points are the uniaxial compression strength of other alumina obtained from literature [5, 104–110]. A black rectangle point in the figure is circled because there are two points almost overlapped.	39
3.1	The schematic diagram of the FBD sample. The diameter D is 8 mm, thickness t is 4 mm, the loading angle $2\omega_0$ is 20° , and F is the applied loading in the test.	45
3.2	The split-Hopkinson pressure bar configuration for dynamic testing. This figure shows the schematics of the experimental setup and the typical camera view of an FBD sample.	45
3.3	The check for force equilibrium in the dynamic FBD test. The F_{in} is the incident bar force obtained from the incident and reflected signals. The F_{out} is the transmitted bar force obtained from the transmitted signal. R_f is a factor related to the force equilibrium. R_{fmean} is the mean value of R_f during the loading process in the dynamic FBD test when the force equilibrium is achieved. Finally, the \dot{F} is the loading rate obtained from the slope of the loading curve.	47
3.4	Schematic representation of two kinds of loading types exerted on the disk, and these equivalent methods can provide an approximate analytical solution for the FBD tests [138]. The blue load is the equivalent uniformly distributed load and the red load is the equivalent sinusoidal distributed load. The $2\omega_0$ is the loading angle, and its value is the same as that in an FBD with $2\omega_0 = 20^\circ$. R and t are the radius and thickness of the sample, respectively, and their values are the same as the FBD. (r, θ) is an arbitrary point on the sample in polar coordinates.	49
3.5	The stress distribution along the vertical diameter under a total compressive force of $F = 5.25 \text{ kN}$ obtained by different models. The σ_{yy} and σ_{xx} curves under uniform load are obtained by Equations (3.3) and (3.4) [156], and the σ_{yy} and σ_{xx} curves assuming a sinusoidal load are obtained by Equations (3.6) and (3.7) [163]. The point of σ_{xx} is obtained by Equation (3.2) [136–138].	53
3.6	An example of the tensile stress (σ_{xx}) and strain (ε_{xx}) history of the disk's center ($x = 0$ and $y = 0 \text{ mm}$) in a dynamic test. Here, the stress and strain curves are in different system times, the SHPB or MTS system time and the DIC system time, respectively.	57

- 3.7 The DIC strain vs. predicted strain for the disk's center ($x = 0$ and $y = 0$) of the FBD sample in a dynamic test with a loading rate of $\dot{F} = 8.69 \times 10^8$ N/s. The predicted strain is obtained by Equations (3.4) and (3.7) and Hooke's law. The DIC strain history $\varepsilon_{xx}(t_2)$ in (a) is the same as that in Figure 3.6, and here we only show some part of it for the value of $\varepsilon_{xx}(t_2)$ within 0.005. The $\dot{\varepsilon}$ is the tensile strain rate calculated from the slope of $\varepsilon_{xx}(t_1 - t_0)$ obtained by the theoretical model. The stress history curves are also shown in the figures, and the stress history $\sigma(t_1 - t_0)$ is matched with the DIC strain history $\varepsilon_{xx}(t_2)$ in time. 58
- 3.8 This figure shows ε_{xx} and ε_{yy} distributions under a total compressive force of $F = 5.25$ kN. a) The blue and red curves are the ε_{xx} distribution along the vertical diameter ($x = 0$ and $y = 0$ to 4 mm) obtained from the uniform (Equation (3.4)) and sinusoidal (Equation (3.7)) loading models. The points in the figure are obtained from experimental results with different loading rates. b) The ε_{xx} field of the sample surface obtained from the "Qs 7.55×10^2 N/s" test. c) This figure includes the ε_{yy} distribution along the vertical diameter ($x = 0$ and $y = 0$ to 4 mm) obtained from the uniform Equation (3.3) and sinusoidal Equation (3.6) loading models, and the points are obtained from experiments with different loading rates. d) The ε_{yy} field of the sample surface in the "Qs 7.55×10^2 N/s" test. 60
- 3.9 This figure shows the fracture process of the FBD sample in a dynamic test with a loading rate of $\dot{F} = 8.69 \times 10^8$ N/s. a) and b) are the tensile strain (ε_{xx}) field of the sample at 69 and 70 μ s, respectively; c) is the ε_{xx} history curves of the disk's center obtained by DIC and the predictive model, which are from Figure 3.7a; d), e) and f) are the fracture process of the FBD sample obtained by the ultra-high-speed camera. The yellow arrows in e) are main cracks, and the red arrows in f) are secondary cracks. The fragmentation process is found in the red rectangle zone. 62
- 3.10 The DIC tensile strain history vs. predictive tensile strain history for the disk's center in the FBD test with various loading rates. The predictive tensile strain history is obtained theoretically using Equations (3.4) and (3.7) and Hooke's law. The tensile strain rates $\dot{\varepsilon}$ and loading rates \dot{F} are listed in the legend. In this figure, a) and b) are quasi-static experimental results, and c) and d) are dynamic experimental results. 65
- 3.11 SEM images of the fracture surface of the CeramTec 98% alumina by the indirect tension tests. a) and b) are quasi-static experimental results, where the fracture surface is rough and full of sharp edges, indicating intergranular cracking is the dominant failure mechanism. c) and d) are dynamic experimental results, and the failure process is governed by a mixed-mode of intergranular and transgranular fracture. Pores and cleavages are observed in both quasi-static and dynamic tests. 67

- 3.12 Strain-rate-dependent tensile strength of various alumina ceramics. The red points are the material tensile strength of the CeramTec 98% alumina studied here. The other colored points are the tensile strength of different alumina obtained from literature [78–82]. The legend includes the testing types, the material names, and the corresponding literature citation. The black dash curve in the figure is the strain-rate-dependent tensile strength model for the CeramTec 98% alumina with $\sigma_{cr} = 314$ MPa and $a = 31$ in Equation (3.18). The black full curve in the figure is the model for the A94, A98 and A99 with $\sigma_{cr} = 181$ MPa and $a = 15$ in Equation (3.18). A red dash rectangle is used to denote some data because their strengths are lower than those of the same material at a lower strain rate. These data lie outside the model prediction but are still included in the figure for completeness. 70
- 3.13 The relationship between the normalized tensile strength and normalized strain rates of various alumina ceramics. The black curve is the normalized strain-rate-dependent tensile strength model obtained by Equation (3.19). The red points are the normalized tensile strength of the CeramTec 98% alumina. The other colored points are the normalized tensile strength of different alumina obtained from literature [78–82]. The experimental data is normalized by Equation (3.20). A red dash rectangle is used to denote some data because their strengths are lower than those of the same material at a lower strain rate. These data lie outside the model prediction but are still included in the figure for completeness. 72
- 4.1 The mode I constitutive behaviour of the cohesive element with $K_1 = 4.6 \times 10^7$ N/mm³, $\sigma_0 = 440$ MPa, and $G_1^c = 0.04$ N/mm. In the inset figure, a cohesive (crack) element is interspersed throughout two tetrahedral elements. 79
- 4.2 The green line is Weibull's statistical strength distribution of cohesive elements obtained from Equation (4.8) with $m_0 = 11.0$, $m_a = -11.0$, $\sigma_0 = 440.0$, $A = 0.01268$ and $A_0 = 0.013$. The orange bar is the statistics of the facet strength of the cohesive element with random flaws generated by Monte Carlo simulations. The percentage of low-strength cohesive elements (below 350 MPa) is around 7.9%, which is associated with the big flaws in the material. The rest of the cohesive elements (around 92.1 %) have strong strength (between 350 and 530 MPa), which corresponds to the material with smaller flaws. 81
- 4.3 a) Variation of engineering stress-strain response of the CeramTec 98% alumina during the direct tension simulations with four kinds of mesh sizes. b) The shaded region is the tensile strength of the CeramTec 98% obtained by Brazilian disk experiments [208], and the dots are the simulation results with four kinds of mesh sizes. 84
- 4.4 The failure pattern of the samples with different mesh sizes. The legends in the figure correspond to the displacement of the samples in the z-direction (U_3). It is observed that a horizontal crack perpendicular to the loading direction is generated during the loading process. The single main crack causes catastrophic failure. In some cases, the main crack may split into multiple branches. Some fragments appear near the crack surfaces due to the branching behaviour of the cracks. 86

- 4.5 Microscopic strength distributions with different Weibull modulus ($m_0 = 9, 10, 11, 12, \text{ and } 13$). 87
- 4.6 a) The engineering stress-strain response of the CeramTec 98% alumina during the direct tension simulations with different Weibull modulus ($m_0 = 9, 10, 11, 12, \text{ and } 13$). b) The full dots are the tensile strength and the hollow dots are the elastic modulus obtained by simulation with five different Weibull modulus. 88
- 4.7 The failure pattern of the simulation results with different Weibull modulus ($m_0 = 9, 10, 11, 12, \text{ and } 13$). The U_3 legend in the figure indicates the displacement of the samples in the z-direction. The failure pattern is consistent with Figure 4.4, a horizontal crack forms perpendicularly to the loading direction during the loading process, ultimately leading to a catastrophic failure caused by the single main crack. In certain instances, the main crack can divide into multiple branches, resulting in fragments near the crack surfaces due to the crack's branching behaviour. 89
- 5.1 a) The blue line is the mode I constitutive behaviour of the cohesive element under tensile loading derived from Equation (5.1) and Table 5.1, and the inset figure shows the loading state of the cohesive element. b) The curves are the mode II constitutive behaviour of the cohesive element under compression-shear loading derived from Equation (5.1) and Table 5.1, and the inset figure shows the loading state of the cohesive element. c) The purple line depicts a Weibull's statistical strength distribution by Equation (5.9). The blue bar is the statistical data related to the facet strength of the cohesive elements generated by the Monte Carlo simulations. d) The cumulative probability distribution obtained from the Monte Carlo simulations shown in (c). 101
- 5.2 a) The purple-shaded area represents the indirect tensile strength of the CeramTec 98% alumina obtained by the FBD experiments in Section 5.5.1. The plotted points correspond to simulation results obtained using four distinct mesh sizes. b) The bar graph represents the tensile strength simulated by three distinct samples under four different tensile loading rates in quasi-static loading conditions. c)-f) The results show the vertical displacement field and the crack patterns across four distinct mesh sizes. Notably, a horizontal crack perpendicular to the loading direction is generated. In certain instances, this primary crack might bifurcate into several branches. The black arrows in c) show the tensile loading direction. 103
- 5.3 a) The flattened Brazilian disk (FBD) tests are performed using a MTS 810 material testing machine coupled with a high-intensity light and a high-speed (HS) camera. b) The schematic diagram of the FBD sample. The diameter D is 8 mm, thickness t is 4 mm, the loading angle $2\omega_0$ is 20° , and F is the applied loading during the test. c) The specimen is sprayed with speckle patterns to facilitate digital image correlation measurements. 105
- 5.4 The area shaded in pink signifies the indirect tensile strength of CeramTec 98% alumina, as documented in Table 5.3. The area shaded in red corresponds to the simulated direct tensile strength derived using a 0.15 mm mesh size, as detailed in Figure 5.2. The points plotted on the graph represent the tensile strength from the HFDEM simulations of FBD testing (also known as indirect tension simulation) using a 0.15 mm mesh size, which are carried out with six different shear strengths. 107

5.5	Fracture patterns observed in the BD tests of a) a coarse-grained, hot-pressed magnesium aluminate spinel by Swab et al. [185] and b) a rock material by Gui et al. [262]. The black arrows in (a) show some cracks initiated from the load application points.	109
5.6	Fracture patterns and fragmentation observed in the indirect simulation of case 1 with $\tau = 2.5 \sigma$. a) two cracks are generated at the loading points. b) the sample breaks into three primary fragments in the simulation.	109
5.7	Fracture pattern and fragments observed in the indirect simulation of case 2 with $\tau = 3 \sigma$. a) Two kinds of cracks emerge simultaneously: the central crack along the central diametral plane and the loading point cracks. b) Fragments generated in the indirect simulation of case 2 with $\tau = 3 \sigma$. c) Fragments generated in the FBD testing.	110
5.8	Fracture pattern and fragments observed in the indirect simulations of case 3 with $\tau = 3.5 \sigma$ and case 4 with $\tau = 4.0 \sigma$. a) Two kinds of cracks emerge simultaneously: the central crack along the central diametral plane and the straight loading point cracks. b) Fragments generated in the indirect simulation.	111
5.9	Fracture pattern and fragments observed in the indirect simulation of case 5 with $\tau = 5.0 \sigma$ and case 6 with $\tau = 8.0 \sigma$. a) and d) are the central crack running along the central diametral plane that appears in the indirect simulation and FBD experiment respectively, and the yellow arrows in d) highlight the central cracks observed in the experiment. b) and e) are three kinds of cracks, including the central crack, the secondary crack and the loading point crack, observed in the indirect simulation and FBD experiment respectively. c) and f) are fragments generated in the indirect simulation and FBD experiment respectively.	112
6.1	The alumina ceramic sample under a quasi-static uniaxial compression experiment, sprayed with a speckle pattern necessary for DIC measurements of axial and lateral strains.	119
6.2	(a) The engineering axial stress-strain curves of alumina ceramic specimens under quasi-static uniaxial compressive loading at strain rates of 1.6×10^{-5} to $1.6 \times 10^{-3} \text{ s}^{-1}$. (b) Lateral and axial strain curves obtained from the DIC analysis are used to determine Poisson's ratio of the material.	121
6.3	The mode I constitutive behaviour of the cohesive element is obtained from a validation model (shown as the inset in the figure). In this validation model, a cohesive (crack) element is interspersed throughout two tetrahedral elastic elements. The black line represents the linear cohesive law, and the red curves represent the cohesive law developed in the present study with power-law characteristics.	127
6.4	The mode II constitutive behaviour of the cohesive element is illustrated in terms of the tangential bonding stresses (or shear stress) versus the relative shear displacement. The dash curves show the pure shear behaviour, and the solid curves represent the shear behaviour of the cohesive element subjected to a compressive stress of 1000 MPa.	128
6.5	The red curve represents the Weibull statistical strength distribution of cohesive elements, derived from Equation (6.13), featuring parameters $m_0 = 11.0$, $m_a = -11.0$, $\sigma_0 = 440.0$, $A = 0.01268$, and $A_0 = 0.013$. The grey bar illustrates the strength statistics of cohesive elements with randomly generated flaws, as determined by Monte Carlo simulations.	129

6.6	Variation in the engineering stress-strain response of alumina ceramic obtained by the HFDEM model with linear and power damage evolution laws. Results using the linear damage evolution law are presented as solid curves, and those using the power damage evolution law are depicted with dashed curves. a) The power damage evolution law results are shown as transparent. b) The linear damage evolution law results are displayed transparently.	131
6.7	The fracture and fragmentation process of alumina ceramic of the linear damage evolution law at three different representative strain points, which are shown in the red solid curve of Figure 6.6. These three strain points (ε_1 , ε_2 and ε_3) correspond to the average strain of 0.75%, 0.80% and 0.84%. To better observe the cracks on the specimen surface, we use the displacement legend for the three images, and the unit here is mm.	132
6.8	The fracture and fragmentation process of an alumina ceramic in the current experiments. The strain points (ε_1 and ε_2) correspond to the average strain of 0.84% and 0.86%. At the strain of ε_3 and ε_4 , the DIC loses correlation due to the appearance of cracks.	133
6.9	The fracture and fragmentation process of alumina ceramic of the power damage evolution law at three different representative strain points, which are shown in the red dash curve of Figure 6.6. These three strain points (ε_1 , ε_2 and ε_3) correspond to the average strain of 0.72%, 0.76% and 0.81%. To better observe the cracks on the specimen surface, we use the displacement legend for the three images, and the unit here is mm.	133
6.10	The fracture and fragmentation process of an alumina ceramic [267]. The strain point (ε_1) correspond to the average strain of 0.75%. At the strain of ε_2 , ε_3 and ε_4 , the DIC loses correlation due to the appearance of cracks.	134
6.11	The predicted engineering stress-strain behavior of alumina ceramic for various Poisson's ratio ν while the other properties remain the same as the ones used to generate the red reference curve shown in Figure 6.6. The changes in the stress-strain curves are negligible over these values of ν	136
6.12	The predicted engineering stress-strain behavior of alumina ceramic for various elastic modulus E , while the other properties are set to the reference values. According to these curves, the failure strain is affected by the change in stiffness, but the change in the peak compressive stress is minor over these values of E	136
6.13	The predicted compressive strength of alumina ceramic for various shear strengths while the other properties are set to the reference values. The compressive strength increases with higher shear strength.	137
6.14	The predicted compressive strength of alumina ceramic for various Weibull characteristic tensile strengths, while the other properties are set to the reference values. The impact of increasing the Weibull characteristic tensile strength on the compressive strength is weakened.	138

Abbreviations

DIC	Digital image correlation
FPS	Frames per second
SEM	Scanning electron microscopy
SHPB	Split-Hopkinson pressure bar
XCT	X-Ray computed tomography
EDS	Energy-dispersive X-ray spectroscopy
EBSD	Electron backscatter diffraction
DAQ	Data acquisition system
HDPE	High density polyethylene
ZNSSD	Zero-normalized sum of squared differences
AOI	Areas of interest
XRM	X-Ray microscopy
FBD	Flattened Brazilian disk
BD	Brazilian disk
Qs	Quasi-static
Dyn	Dynamic
PMMA	Polymethylmethacrylate
FEM	Finite element method
CDM	Continuum damage mechanic
XFEM	Extended finite element method
VCCT	Virtual crack closure technique
CZM	Cohesive zone method
HFDEM	Hybrid finite-discrete element method
FS	Flash sintering
HPS	Hot-pressing sintering

SPS	Spark plasma sintering
VUMAT	FORTRAN vectorized user-material
3D	Three-dimensional
REA	Representative elementary area
HS	High-speed

Symbols

D	Scalar damage parameter
K	Penalty stiffness of cohesive elements
δ	Relative displacements of cohesive elements
σ	Stress tensor of cohesive elements
σ^d	Stress in the damaged part of cohesive elements
μ	Coefficient of friction
λ	Internal variable
δ_e	The effective relative displacement
δ_c	The critical relative displacement
δ_m^0	The relative displacement when the damage initiates
G	Energy release rate
G_c	The critical energy release rate
P	The cumulative failure probability
V	The volume of the investigated component
V_0	The characteristic volume of the investigated component
m	Weibull modulus
σ_0	Weibull characteristic strength
A	The facet area of the cohesive element
A_0	The characteristic area of the cohesive element
m_0	Weibull modulus of strength distribution
m_a	Weibull modulus for the effective area modification
γ	Power exponent
σ_t	Tensile strength of the material
F	Applied loading force
t	Thickness of the sample

k	Non-dimensional factor for FBD testing
$\dot{\varepsilon}$	The applied strain rate
E	Young's modulus of an alumina ceramic
ν	Poisson's ratio of an alumina ceramic
σ^{in}	The stress of incident waves
v^{in}	The particle velocity of incident waves
σ^{-}	The stress of reflected waves
v^{-}	The particle velocity of reflected waves
σ^{+}	The stress of transmitted waves
v^{+}	The particle velocities of transmitted waves
A_s	The cross sectional area of the specimen
A_b	The cross sectional area of the impact bar and the support bar
E_b	Elastic modulus of the impact bar and the support bar
β	The effective frictional angle

Chapter 1

Introduction

1.1 Motivation

Advanced ceramics are prime candidates for use in armoured vehicles and personal protective equipment [1] due to their notable characteristics, such as low density [2], high hardness [3], and exceptional wear resistance [4]. These properties make them indispensable in protection systems where they endure high deformation rates and complicated dynamic stress conditions during blast and impact scenarios [5, 6]. In ballistic penetration, the brittle nature of ceramics leads to their fracturing and disintegration within a conoidal shape. The subsequent stages of fracture, including fragmentation and the flow of granular material, play a crucial role in energy dissipation, dulling the impact of the projectile and neutralizing its impact [7, 8]. Among the various advanced ceramics, alumina is widely favored for its favourable cost-effectiveness and widespread availability [9, 10]. This thesis focuses on alumina ceramics due to their common application in protection systems and their role as a prime example of oxide-dense ceramics.

To understand the failure mechanisms of advanced ceramics in defense applications, researchers conduct controlled experiments, such as uniaxial compression tests, which are often complemented by detailed imaging techniques [11]. These experiments typically unravel the failure process in stages, starting with fracture (encompassing crack initiation, growth, and coalescence) [12], then fragmentation [13–15], and culminating in granular flow, where some fragments further break down into fine powders [13, 16, 17]. The mechanical behavior of advanced ceramics depends on both strain rate [18] and the stress state [19, 20], revealing complex mechanical mechanisms under different conditions. Various experimental methodologies have been employed to investigate these failure processes, including quasi-static tests using MTS machines [5, 6], a split-Hopkinson

pressure bar (SHPB) for dynamic testing [21], laser shock experiments [22], and ballistic impact assessments [6, 14]. Additionally, exploring the microstructure of advanced ceramics through X-ray computed tomography, transmission electron microscopy, and scanning electron microscopy has been crucial in understanding the mechanisms behind strain-rate- and stress-state-dependent failures [5, 23]. This thesis aims to elucidate these failure mechanisms through an integrated approach that combines experimental research with physics-based numerical modelling.

Numerous computational approaches have been developed to simulate the failure behavior of advanced ceramics. Among them, Johnson and Holmquist have developed several versions of their model, namely JH1 [24], JH2 [25], and JHB [26]. These models are designed to capture the mechanical behavior of brittle materials under conditions of large deformations, rapid strain rates, and high pressures. The JH2 model, in particular, stands out for its application to ceramics, owing to its accuracy and the availability of necessary parameters for simulation [24–27]. This model successfully incorporates the effects of strain rate, hydrostatic pressure, and other relevant factors on material strength [24–26]. However, these models generally fail to accurately represent the post-fracture phenomena, such as fragmentation and granular flow seen in advanced ceramics [28, 29]. To address these limitations, some researchers [29, 30] have turned to discrete element modelling (DEM) to capture the processes of crack development and fragmentation in brittle materials. DEM conceptualizes materials as collections of distinct, interacting particles or blocks, which can be either rigid or deformable [31–33]. This method has been extensively used to study granular materials [30, 32] and structures with joints [29, 31]. The existing body of research underscores the importance of developing models that can accurately depict the post-fracture behaviour of advanced ceramics, particularly focusing on fragmentation and granular flow dynamics [18, 29]. These studies lay the groundwork for further exploration into the post-peak stress responses of such materials, highlighting the ongoing need for advancements in modelling techniques.

1.2 Background and Literature Review

1.2.1 Failure processes in advanced ceramics

Fracture initiation in advanced ceramics under compressive loading is largely attributed to micro-cracks and pores within the material [34]. These imperfections act as stress concentration locations, significantly influencing the material's fracture behaviour [5, 23]. The theoretical framework for understanding compressive failure in brittle materials is often described by the "wing crack model" [35–38], which traces its roots to the

foundational work by Nemat-Nasser and Horii in the 1980s [37, 38]. According to this model, micro-cracks or pores, initially oriented randomly, extend in the direction parallel to the applied uniaxial compressive load. The cracks are driven by the mode I tensile stress at the crack tips [37–40]. Building on the foundational principles of the wing crack model, subsequent studies have introduced additional mechanisms for the macroscopic crack propagation process, including the interactions between cracks [41, 42], the phenomenon of dilatancy [43], and models that integrate sliding and material damage [44, 45]. Despite these advancements, existing models still need help to fully capture the complexities of post-fracture and fragmentation behaviours in ceramics. This thesis addresses these limitations, proposing new insights into the fragmentation processes following fracture in ceramic materials.

Understanding the intricacies of fragmentation processes is crucial for accurately depicting the post-fracture dynamics of advanced ceramics [14, 46]. The work by Grady and Kipp [46] highlighted that the fragmentation phenomenon is intricately linked to the entire crack lifecycle, including nucleation, propagation, and coalescence. Moreover, they pointed out that the size of the fragments is closely tied to the mechanical characteristics of the materials and the loading rates. Further investigations by Hogan et al. [15] identified two principal mechanisms of fragmentation in the context of compression failure in boron carbide, observed through impact and compression testing. They delineated a "microstructure-dependent" fragmentation mechanism, accountable for generating smaller fragments, and a "structure-dependent" fragmentation mechanism, responsible for creating larger fragments due to structural breakdown. The existing limitations of conventional constitutive models (such as JH1, JH2, and JHB [24, 26, 47, 48]) in incorporating these fragmentation processes into their descriptions of failure in advanced ceramics underscore the necessity for a combined approach of numerical and experimental research, as pursued in this thesis.

After the fragmentation process, the collective behaviour of the resulting granular materials comes into play. This granular flow entails the interactions among hundreds or thousands of fragments or particles produced during fragmentation. Key behaviours observed in this phase include pore compaction [49], friction among fragments [50], the formation of force chains [51, 52], and shear-induced dilation [49]. Grady's research [17] on the dynamic response of brittle materials to shock loading introduces a physical model that breaks down the shear failure mechanism within the shock wave into three distinct phases: the initiation and nucleation of fractures, their subsequent growth, and the flow of comminuted material, or granular flow. His findings suggest that further compression of these powder-like particles leads to ultra-fine debris layers within the fracture zones, which retain significant compressive and shear strength. Moreover, the granular flow phase is characterized by particle rotation [53], jamming [54], and local

dilation to make room for the volume increase caused by shear fractures [17]. These processes contribute to localized energy dissipation and a temperature rise. This thesis adopts a novel multi-scale modelling approach to capture both the fragmentation and granular flow dynamics in advanced ceramics. This method, which has not previously been applied to advanced ceramics, includes defining a representative interface area [55] and incorporates factors like compaction and friction [30], providing a comprehensive framework for understanding complex ceramic failure behaviours. Thus, this thesis will consider these characteristics of advanced ceramics by numerical modelling methods.

1.2.2 Experimental methods in advanced ceramics

The mechanical properties and failure mechanisms of advanced ceramics are significantly influenced by the strain rate and the stress state under which they are subjected. This intricate dependency reveals the complex nature of their mechanical behaviour, necessitating a diverse range of experimental techniques to comprehend their responses under various conditions fully. To this end, researchers have developed and utilized multiple methodologies to probe the failure processes inherent to these materials. These methodologies include:

- Quasi-static testing, typically conducted using MTS machines, allows for carefully examining ceramic materials under slowly applied loads, providing insights into their mechanical properties at low strain rates [5, 6]. Such tests are invaluable for establishing baseline mechanical behaviour, enabling comparisons with dynamic testing results to assess the effects of strain rate more comprehensively.
- The Split-Hopkinson Pressure Bar (SHPB) has become a cornerstone methodology for investigating the behaviour of ceramics under high strain rates [11, 21]. The SHPB facilitates the imitation of dynamic events such as impacts or explosions, offering a window into the material responses under conditions often encountered in real-world applications. This method has been instrumental in delineating the dynamic strength and fracture characteristics of ceramics, thereby enhancing our understanding of their performance in protective equipment and structural components.
- Laser shock experiments represent another avant-garde approach, providing a non-contact method for inducing high strain rates in materials. Researchers [22] can generate shock waves within the ceramic by applying intense, short-duration laser pulses, simulating extreme stress conditions. This technique is particularly useful for studying damage onset and crack propagation under high-speed impact scenarios [22, 56, 57].

- Ballistic impact assessments further expand the toolkit for exploring mechanical behaviour of advanced ceramics [6, 14]. By subjecting ceramic samples to impact from high-velocity projectiles, scientists can directly evaluate their resistance to penetration and fracture. Such experiments are crucial for developing ceramics used in armour and protective structures, where material performance under impact is paramount [14, 58].
- Due to the brittle nature of advanced ceramics, the quest to understand their tensile properties has prompted the adoption of indirect testing techniques. Sleeve-fracturing, beam bending, and Brazilian disk tests circumvent the direct application of tensile forces, offering a pragmatic approach to evaluating tensile strength [59, 60]. These approaches bypass the difficulties of direct tensile testing, providing valuable insights into the tensile strength of advanced ceramics.
- Uniaxial compression testing has been instrumental in understanding the compressive strength of advanced ceramics, a crucial attribute for materials used in structural and protective roles [13, 23]. By applying pressure along a single axis until failure, this testing method elucidates the mechanical strength of ceramics, guiding their development for industrial and technological applications where compressive loads are prevalent.
- To comprehend the shear response of advanced ceramics, hydraulic confinement and compression-shear techniques have emerged as a novel experimental approach [11, 21]. These methods simulate the complex stress states ceramics encounter, including combined compression and shear stresses by changing the geometries of specimens, thereby enhancing our understanding of their failure mechanisms under such conditions. Insights from these studies inform the design and improvement of ceramics for applications requiring superior shear strength.

Beyond mechanical testing, exploring the microstructural characteristics of advanced ceramics has proven essential in uncovering the underlying mechanisms of strain-rate- and stress-state-dependent failures. Techniques such as X-ray computed tomography (CT), transmission electron microscopy (TEM), and scanning electron microscopy (SEM) offer insights into the internal structure of these materials. Through detailed imaging and analysis, researchers [5, 11, 23, 61] can identify the presence of micro-cracks, pores, and other features that influence mechanical properties and failure modes. These microstructural investigations complement mechanical testing, providing a holistic understanding of ceramic behaviour that guides the development of more robust and reliable materials.

Together, these diverse experimental methodologies capture the mechanical behaviour of advanced ceramics under various conditions. By integrating findings from mechanical testing with microstructural analysis, researchers are equipped to advance the design and application of ceramics in industries ranging from aerospace to defence [3, 62–64].

1.2.3 Computational methods for describing failure in brittle materials

A wide array of computational techniques has been developed to accurately model the mechanical properties and behaviour of brittle materials. Among these, continuum damage mechanics (CDM) [44, 45], the extended Finite Element Method (XFEM) [65], and the cohesive zone model (CZM) [66] have emerged as particularly influential. The CDM focuses on the initiation and growth of damage within a material, and XFEM facilitates the modelling of discontinuities such as cracks without re-meshing. The CZM, in particular, stands out due to its unique advantages [67], such as generating new surfaces that adhere to the Griffith energy criterion, supporting branching and intersecting cracks, and eliminating the singularities found in linear elastic fracture mechanics. These features have made the CZM a powerful tool for investigating the compression strength of advanced ceramics [68, 69], studying the fragmentation of brittle materials [70], and analyzing various fracture mechanisms [71].

The implementation of the CZM involves creating new fracture surfaces during the simulation process, necessitating the use of numerical contact algorithms. This requirement renders the CZM especially compatible with discretized simulation methods [72]. Building upon this foundation, Munjiza [31] introduced the hybrid finite-discrete element method (HFDEM), a novel computational approach designed to seamlessly integrate the finite element method (FEM) with the discrete element method (DEM). This hybridization allows the modelling of material behaviour to transition from a continuum to a discontinuum [32, 33], effectively capturing the complex damage and failure dynamics [73].

Initially conceived for simulating the behavior of geomaterials [73–75], the HFDEM has since been adapted to model the failure of ceramics as well [33]. Within the HFDEM framework, materials are represented as either two-dimensional triangular or three-dimensional tetrahedral elements, with cohesive elements interlinking these discrete components to simulate arbitrary crack paths [55]. The motion of the discretized system is then resolved using an explicit finite difference time integration scheme, enabling the detailed simulation of fracture initiation, propagation, and the interactions between emergent discrete fragments [55, 72, 76]. Despite its success when applied to geological applications [31–33], the application of HFDEM to advanced ceramics still needs to

be explored, presenting a novel area of investigation that this thesis aims to address. By extending the use of HFDEM to advanced ceramics, this research seeks to unravel new insights into the fracture behaviour and mechanical integrity of these materials, potentially paving the way for innovative applications and improvements in material design.

1.3 Thesis Objectives

The objective of this thesis is to deepen our understanding of the failure mechanisms observed in an advanced ceramic by leveraging a combination of experimental observations and numerical modelling techniques. The ceramic used in this thesis is a commercially available alumina ceramic (CeramTec ALOTEC 98 SB alumina ceramic) widely used in protective applications. Central to this study is developing a model that encapsulates the intricate processes and mechanisms underlying the failure of ceramics, including the initiation and propagation of fractures [38], the damage evolution leading to catastrophic failure [12, 77], and the subsequent fragmentation and granular flow behaviours that emerge post-failure [13–15]. To ensure the reliability and applicability of this model, it will undergo rigorous validation against a suite of high-fidelity experimental data. These experiments, which include uniaxial compression, compression shear, and Brazilian disk tests, will provide critical insights into the stress-strain responses, fracture patterns, and fragmentation characteristics of advanced ceramics. This comprehensive approach bridges theoretical modelling and empirical observations, offering a more nuanced understanding of ceramic failure mechanisms.

1.4 Thesis Goals

The objectives of this thesis are accomplished by completing the following research goals:

- Investigate the essential microstructural characteristics and elemental analysis of the alumina ceramic, such as grain size, impurities and elements, using scanning electron microscopy (SEM), energy-dispersive spectroscopy (EDS), Electron Backscatter Diffraction (EBSD), X-ray microscopy (XRM). These parameters serve as key inputs for modelling efforts and provide a basis for comparison with other materials.
- Conduct strain-rate and stress-state dependent experiments (e.g., Brazilian disk tests, uniaxial compression experiments, and combined compression-shear

experiments) of advanced ceramics coupled with an ultra-high-speed camera that enables the digital image correlation (DIC) technique to resolve the deformation field of the specimen surface during testing. The quasi-static tests are carried out on a standard MTS series 810 servo-hydraulic machine, and the dynamic tests are carried out on a modified version of a split-Hopkinson pressure bar (SHPB) device. The stress-strain curves, deformation evolution (lateral to axial strain ratio), fracture patterns, and post-experimental fragmentation characteristics are used to validate the proposed HFDEM model developed in this thesis.

- Explore the micro-failure mechanisms of the alumina ceramic, and bridge the gap between micro-mechanisms and macroscopic material behaviors. It is necessary to identify key micro-failure mechanisms such as intergranular and transgranular fracture, crack initiation at grain boundaries, and the influence of impurities and pores. Additionally, it is crucial to investigate how these micro-failure mechanisms affect macroscopic properties like tensile strength and compressive strength.
- Develop a theoretical method that predicts mechanical tensile strength, drawing directly from the experimental findings presented in this thesis. This model would incorporate the effects of microstructural features, strain rate, and stress state to describe the strength of alumina ceramics under tensile loading. The theoretical model is calibrated against the experimental results, adjusting parameters to match predicted and observed tensile strengths closely.
- Develop a multi-scale hybrid finite-discrete element model to describe the fracture and fragmentation processes of advanced ceramics. This proposed model accounts for various phenomena and mechanisms that manifest during compressive failure of advanced ceramics, such as 1) fracture initiation and growth via the wing-crack, 2) catastrophic failure via well-chosen damage evolution law, and 3) fragmentation and granular flow behaviour via the hybrid finite-discrete element method. The model is informed and validated by experiments performed in this thesis.
- Utilize experimental data and computational simulations to analyze the impact of material properties, including elastic modulus, fragment size, and flaws in the material on the strength of advanced ceramics. These sensitivity analyses provide a theoretical groundwork for the future design and optimization of advanced ceramic materials, enabling more accurate predictions of material behavior and guiding the development of more efficient ceramic materials.

1.5 Key Contributions

The findings of this thesis will be important to:

- Provide insights into the transition process of the intact advanced ceramic to a fractured state under both stress-state and strain-rate dependent loading. Insights are gained by understanding the crack patterns and damage evolution mechanisms of the fracture process.
- Propose new theoretical models to describe failure mechanisms in advanced ceramics that consider stress-state and strain-rate dependent loading, guided by advanced stress-state and strain-rate dependent experimentation.
- Offer insights into the factors that affect the mechanical performance of advanced ceramics under external loading by bridging their micro-scale mechanisms (e.g., flaws) and macro-scale mechanisms (e.g., fracture and fragmentation processes).
- Provide a better understanding of the relationship between mechanical properties (e.g., shear strength and tensile strength) and the failure process (e.g., fracture and fragmentation) by applying the HFDEM.
- Offer promising avenues for a qualitative and quantitative understanding of the failure mechanisms of advanced ceramics, which serves as theoretical support for further material design, optimization and manufacturing, such as improving the mechanical performance of these materials.

1.6 Thesis Structure

This thesis is structured based off of research published as journal articles presented as individual chapters. Individual author contributions are listed on the title pages of Chapters 2–6. Variable notations may differ across chapters. The chapters are presented in the following order, with a summary included:

- Chapter 1: “Introduction” discusses the background and motivation for studying advanced ceramics, emphasizing their importance in various applications. It provides an overview of the existing challenges and gaps in knowledge that this research aims to address. The chapter sets out the specific objectives of the thesis, detailing the research questions and goals that guide the investigation. Additionally, it outlines the overall contributions to the field made by the thesis,

highlighting the novel insights and advancements achieved. This chapter establishes the context and framework for the subsequent research, setting the stage for the detailed studies presented in the following chapters.

- Chapter 2: “Strain-rate-dependent Compressive and Compression-shear Response of an Alumina Ceramic”. Published in the *Journal of the European Ceramic Society*, as **Jie Zheng**, Min Ji, Zahra Zaiemyekeh, Haoyang Li, and James David Hogan, 2022. This chapter studies the microstructure and properties of CeramTec ALOTEC 98 SB alumina ceramic (CeramTec 98% alumina) through microscopic characterization and mechanical experiments. The rate-dependent strength and failure response of an alumina ceramic are studied under both uniaxial compression and compression-shear loading. To monitor the strain field and the failure process of the alumina ceramic during testing, an ultra-high-speed camera coupled with digital image correlation (DIC) is used to visualize crack initiation and propagation processes and obtain quantitative stress-strain information. A new data processing method is then proposed in this study to calculate the shear components for the compression-shear tests. Validation of the proposed method is confirmed by the shear strain obtained from the DIC analysis with the ultra-high-speed camera. New observations and understandings of failure mechanisms are obtained using the results obtained by the proposed model and the DIC analysis. 1) In compression-shear tests, the shear failure happens before complete failure and shear behaviour plays an important role during the failure process. 2) The equivalent peak stress (strength) of the compression-shear test is smaller than the uniaxial compression one. 3) The directional cracks have a weak influence on the compressive stiffness but have a strong influence on the shear response.
- Chapter 3: “Strain-rate-dependent Tensile Response of an Alumina Ceramic: Experiments and Modelling”. Published in the *International Journal of Impact Engineering*, as **Jie Zheng**, Haoyang Li, and James David Hogan, 2023. In this chapter, the strain-rate-dependent tensile response of a commercial alumina ceramic (CeramTec 98% alumina) is investigated by experimental and modelling methods. The experiments at different loading rates are carried out on a standard MTS machine and a modified split-Hopkinson pressure bar system with flattened Brazilian disk specimens. High-speed imaging coupled with digital image correlation (DIC) is used to measure the strain fields. In the dynamic tests, it is verified that multiple cracks appear simultaneously around the locations of maximum tensile stress and strain. Next, a matching approach based on theoretical models (i.e., the uniform and sinusoidal load models) is proposed to synchronize the stress and strain history curves in time, and the matching results show the tensile cracks are often generated prior to the peak stress as visualized in ultra-high-speed

camera images. This peak stress corresponds to the failure of the sample structure, which is different from the material tensile strength as an inherent material property. The strain-rate-dependent tensile strength of the alumina ceramics is computed with a correction method, and the tensile strength is defined as the tensile stress when the central crack first appears in the ultra-high-speed camera images. Then, a strain-rate-dependent tensile strength model is proposed to describe the tensile strength of the CeramTec 98% alumina and other alumina ceramics in the literature [78–82].

- Chapter 4: “Hybrid Finite-discrete Element Modeling of the mode I Tensile Response of an Alumina Ceramic”. Published in *Modelling*, as **Jie Zheng**, Haoyang Li, and James David Hogan, 2023. In this chapter, we have developed a three-dimensional hybrid finite-discrete element model to investigate the mode I tensile opening failure of the alumina ceramic. This model implicitly considers the flaw system in the material and explicitly shows the macroscopic failure patterns. A single main crack perpendicular to the loading direction is observed during the tensile loading simulation. Some fragments appear near the crack surfaces due to the branching behaviour of the cracks. The tensile strength obtained by our model is consistent with the experimental results from the literature. Once validated with litterateur, the influences of the distribution of the flaw system on the tensile strength and elastic modulus are explored. The simulation results show that the material with more uniform flaw sizes and fewer big flaws has stronger tensile strength and higher elastic modulus.
- Chapter 5: “Advanced Tensile Fracture Analysis of Alumina Ceramics: Integrating Hybrid Finite-discrete Element Modeling with Experimental Insights”. Published in the *Engineering Fracture Mechanics*, as **Jie Zheng**, Haoyang Li, and James David Hogan, 2024. This chapter offers novel insights into the mode I tensile response of an alumina ceramic through the use of computational modelling and the flattened Brazilian disk (FBD) experiments. A modified hybrid finite-discrete element method (HFDEM) is developed, integrating a coupled damage and friction cohesive model and a microscopic stochastic fracture model with a Weibull strength distribution by Monte Carlo simulation. The model is used to simulate direct tensile failure processes under quasi-static loading conditions, providing qualitative and quantitative predictions of direct tensile failure processes of an alumina ceramic. Concurrently, quasi-static flattened Brazilian disk tests (indirect tensile tests) are performed on a standard MTS machine coupled with a high-speed camera. The modified HFDEM model is also applied to reproduce the FBD experiments, and our simulated tensile strength is consistent with the experimental results. The results of the modified HFDEM model show three kinds of phenomena (i.e.,

“underestimation”, “reasonable estimation”, and “overestimation” of the indirect tensile strength) and four different types of associated fracture and fragment patterns of FBD testing. The integration of simulation and experimental results reveal relationships between fracture patterns, fragment geometry, tensile strength, and indirect tensile strength. The fracture and fragmentation patterns derived from our modified HFDEM model can be utilized to analyze the “tensile strength” measured in BD testing.

- Chapter 6: “Modified Hybrid Finite-discrete Element Modeling of Compressive Failure in Alumina Ceramics”. Submitted to *International Journal of Mechanical Sciences* as **Jie Zheng**; Li, HY; Zaiemyekheh, Z; Sun, N.; Sayahlatifi, S.; Chen, ZT and Hogan, JD. 2024. In this chapter, we developed a modified hybrid finite-discrete element model (HFDEM) for alumina ceramics, and the model is validated with quasi-static uniaxial compression experiments coupled with a digital image correlation technique. This model proposed the linear- and power-law cohesive constitutive behaviour to describe the crack nucleation and propagation processes, respectively. Additionally, our model considers the flaw distribution of the material by coupling a microscopic stochastic fracture model. This HFDEM accounts for various phenomena and mechanisms that manifest during compressive failure of advanced ceramics: fracture growth follows the wing-crack mode, catastrophic failure and fragmentation behavior. The proposed model was evaluated by comparing the numerically-predicted quasi-static compressive stress-strain responses to the experimental results. The simulation results demonstrated that the proposed method can predict the mechanical response of the alumina ceramic under uniaxial compressive loading. Once validated, the effects of other mechanical properties (e.g., Poisson’s ratio, elastic modulus, shear strength, and tensile strength) on the compressive stress-strain responses were explored. Notably, the elastic modulus and Poisson’s ratio were found to have a negligible impact on the peak compressive strength during uniaxial compression. Additionally, the impact of increasing tensile strength on compressive strength becomes less significant. Conversely, shear strength significantly affects both the peak compressive strength and the failure strain.
- Chapter 7: "Conclusion" provides a summary of the key scientific contributions and implications of this thesis. It highlights the major advancements and findings, showcasing their significance in the field of advanced ceramics. This chapter delves into how these contributions enhance our understanding of material behaviour and failure mechanisms. In addition, it discusses the broader impact of the research outcomes on material science and engineering applications. Furthermore, this chapter outlines directions for future work, proposing specific areas where

additional research can further enhance understanding and innovation in advanced ceramic materials.

Chapter 2

Strain-rate-dependent Compressive and Compression-shear Response of an Alumina Ceramic

Published as **Jie Zheng**; Ji, M; Zaiemyekheh, Z; Li, HY and Hogan, JD. *Strain-rate-dependent Compressive and Compression-shear Response of an Alumina Ceramic*, Journal of the European Ceramic Society. (2022)

Author	Contributions
Jie Zheng	Conceived the ideas and experimental design of the study; Developed theoretical methodology; Performed experiments/data collection; Carried out the experiments; Data analysis and interpretation; Primary author (drafted the manuscript).
Ji, M	Performed experiments/data collection; Provided revisions to scientific content of manuscript .
Zaiemyekheh, Z	Performed experiments/data collection; Provided revisions to scientific content of manuscript .
Li, HY	Performed experiments/data collection; Provided revisions to scientific content of manuscript .
Hogan, JD	Provided revisions to scientific content of manuscript; Provided stylistic/grammatical revisions to manuscript; Principal investigator

2.1 Abstract

This study assessed the microstructure and properties of CeramTec ALOTEC 98 SB alumina ceramic through microscopic characterization and mechanical experiments. The

rate-dependent strength and failure response of an alumina ceramic were studied under both uniaxial compression and compression-shear loading. Under quasi-static uniaxial compression at rates of 10^{-5} to 10^3 s⁻¹, the strength had an average of 3393 ± 306 MPa, and at dynamic strain rates of 10^2 to 10^3 s⁻¹, the strength ranged from 3763 to 4645 MPa. The CeramTec ALOTEC 98 SB alumina ceramic was found to have greater mechanical properties than other commercial alumina ceramics from the literature (i.e., AD-995). To monitor the strain field and the failure process of the alumina ceramic during testing, an ultra-high-speed camera coupled with digital image correlation (DIC) was used to visualize crack initiation and propagation processes and obtain quantitative stress-strain information. A new data processing method was then proposed in this study to calculate the shear components for the compression-shear tests. Validation of the proposed method was confirmed by the shear strain obtained from the DIC analysis with the ultra-high-speed camera. Using the results obtained by the proposed model and the DIC analysis, new observations and understandings of failure mechanisms are obtained. 1) In compression-shear tests, the shear failure happens before complete failure, and shear behaviour plays an important role during the failure process. 2) The equivalent peak stress (strength) of the compression-shear test is smaller than the uniaxial compression one. 3) The directional cracks have a weak influence on the compressive stiffness but have a strong influence on the shear response.

2.2 Introduction

Advanced ceramics are used as critical structural components in applications of ballistic protection systems because of their superior hardness [3, 62–64] and strength-to-weight ratio [83]. During high velocity impact, ceramics experience different spatially- and temporally-evolving strain rates and stress states, resulting in various failure behaviors (e.g., brittle ceramics fracture and fragment in a conoidal volume) [83]. The effective application of advanced ceramics requires a thorough understanding of their mechanical response and failure behavior at various strain rates and stress states. To date, many efforts in studying the dynamic behavior of ceramics have been made for impact [6], tension [60, 84] and uniaxial compression loading [13, 23, 85, 86], with limited studies on the role of the shear component in dynamic failure under compression-shear loading [87]. This paper will explore both the compression and compression-shear response of an alumina ceramic.

Using a hydraulic confinement technique during compression experiments is one approach in the literature to study the shear-type response of brittle materials [88]. In their studies, Lankford et al. [89] and Anderson et al. [90] studied the dynamic compressive

failure behaviour of silicon carbide at a strain rate of 1800 s^{-1} and confining pressures of 0 MPa to 200 MPa. In other studies, Hogan et al. [15] and Farbaniec et al. [21] investigated the dynamic fracture and fragmentation of boron carbide under biaxial confined compression. Their experimental results revealed the addition of confining pressure effectively suppresses unstable growth of the cracks and delays catastrophic failure. As an outcome of the suppression of failure, the shear strength is increased with increasing hydrostatic pressure, and the effect of strain rate on the strength of advanced ceramics diminishes with the confinement pressure increasing [15, 88]. However, in these experiments, limited efforts were applied to explore the influence of shear behaviour in the failure process [91, 92]. In the current study, we will explore the role of shear behaviour in the failure process under combined compression-shear loading.

Another way to obtain combined compression and shear loading is to use a modified split-Hopkinson Pressure Bar (SHPB) device or to utilize specimen with specially designed geometry structures, as is done in this paper. In their studies, Clifton [93], Baker and Yew [94], and Duff et al. [95] modified the conventional SHPB by adding a torsion device to achieve dynamic compression and shear loading. In related studies, Zheng et al. [96], Xu et al. [97] and Zhou et al. [98] used a compression-shear modified loading device to study rock materials, and Tan et al. [20] applied the same technique to study the dynamic failure of inorganic glass. All of these studies found that these materials exhibit obvious strain rate sensitivity and shear-dependency. Apart from modifying the SHPB device, changing the shape of the specimen is another effective and implementable technique to generate shear stress in standard dynamic compression experiments. For example, Rittel et al. [99] and Zhao et al. [100] developed a special compression-shear specimen which is a cylinder with two diametrically opposed slots. As another example, Xu et al. [87] conducted both static and dynamic compression-shear experiments on rock materials through loading cuboid specimen containing parallel loading faces that are inclined to the loading direction. In their experiment, high-speed photographs were used to monitor the progressive failure process, and the results demonstrated that both shear-dominated failure and localized tensile damage appeared during the failure process, with the splitting failure mode being dominant. Different from confined compression experiments, in the compression-shear experiment of rock materials and glass, researchers [87, 96–98] concluded that the equivalent stress at failure decreases with an increasing shear portion in the stress, with obvious strain-rate effects noted. Despite numerous publications involving rocks in this area, the study of the shear-type behavior of advanced ceramics under compression-shear loading is less common, and this motivates the current study to address the gap in knowledge on the compression-shear behavior of alumina ceramics.

This paper probed the microstructural characteristics and mechanical response of the material under strain rate dependent loading. First, microstructural characterization studies were carried out using scanning electron microscopy, energy-dispersive spectroscopy, Electron Backscatter Diffraction, and X-ray microscopy. This characterization informs about the microscale features and chemical composition of the CeramTec ALOTEC 98 SB alumina ceramic under investigation here. Then, both uniaxial compression and compression-shear testing were carried out on a standard MTS machine at quasi-static strain rates ($10^{-5} \sim 10^{-3}\text{s}^{-1}$) and a split-Hopkinson pressure bar for dynamic strain rates ($10^2 \sim 10^3\text{s}^{-1}$). To monitor the strain field and the failure process of the alumina, an ultra-high-speed digital camera was used in conjunction with digital image correlation (DIC) to visualize the crack initiation-propagation processes and to obtain quantitative stress-strain information. A new data processing method was proposed in this study to calculate the shear strain and stress for the compression-shear tests, based on previous works in the literature [101–103] by now considering the evolution of Poisson’s ratio and compressive stiffness induced by compressive loading. The validation of the proposed method was confirmed by the shear strain measured from the DIC analysis. The results show that the compression and shear responses of the alumina exhibit obvious strain-rate and stress-state-dependent behavior. In the Discussion section, we compare the mechanical properties of the CeramTec ALOTEC 98 SB alumina ceramic with other alumina from the literature [5, 86, 104–110]. We also discuss new observations of shear failure in ceramics made possible through the approaches pursued here. Overall, results from the present study provide a better understanding of the compression-shear failure behavior of alumina, including the effects of strain rate and stress state, which is crucial in the design of next-generation protection materials.

2.3 Experimental methods

In this study, a commercially available alumina ALOTEC 98 SB from CeramTec (which is called CeramTec 98% in this paper), Germany, was studied. The number “98” refers to the alumina content being approximately 98 mass percentage, with the remainder being sintering additives or trace impurities, and this is confirmed in microscopy analysis in section 2.5.1. The specimen was 2.3 mm by 2.7 mm in cross-section and 3.5 mm in length, with tilting angles between parallel ends of 0° (for uniaxial compression tests) and 5° (for compression-shear tests). These sizes were chosen to give the material sufficient time to reach stress equilibrium to achieve more accurate results, as described in details in the literature [6, 86, 104, 111–113]. The shapes of specimens are shown in Figure 2.1. The cuboidal shape was chosen so that digital image correlation analysis could be performed

on the flat surface of the specimen during the test, as well as to better observe dynamic fracture behaviors. The surface of the specimens was sprayed with speckle patterns (with the paint spot size in the range of 20 to 30 μm) using a fine-tipped airbrush to facilitate digital image correlation.

2.3.1 Material characterization

Scanning electron microscopy (SEM), Electron Backscatter Diffraction (EBSD), and energy-dispersive x-ray spectroscopy (EDS) were used to perform the microstructural characterization (such as grain size and defects) and determine the elemental composition on mechanically polished surfaces of the alumina (i.e., polished down to 0.25 μm). A Field Emission SEM (Zeiss Sigma, Oberkochen, Baden-Württemberg, Germany) equipped with EBSD and EDS detectors were used to perform the microstructural and elemental analysis in this study. The electron high tension voltage was set at 20 kV with working distances of approximately 8.5 mm and 13.5 mm for the EDS and EBSD detectors, respectively. The working distances were selected to compensate for the detecting angle of the detectors and to ensure sufficient signal strength. The EDS and EBSD map data were analyzed using the Oxford AZtec software. Mechanically polished samples were coated with 6 nm of carbon to enhance conductivity.

2.3.2 Quasi-static uniaxial compression and compression-shear tests

The quasi-static uniaxial compression and compression-shear tests were carried out using a standard servohydraulic MTS 810 machine. The description of this setup is detailed in previously published papers from the authors [6, 112]. In order to prevent the MTS loading platens from being indented by the alumina samples and fragments, polished tungsten carbide (WC) platens were placed in between the specimen and the loading platens. For uniaxial compression tests (the specimen with tilting angles of 0°), high pressure grease was applied between the surfaces of the WC platen and specimen to eliminate the frictional effect and allow for lateral motion [6, 112]. On the contrary, for the compression-shear tests, no grease was applied to induce tangential force by friction and to make sure no surface sliding occurs between the specimen and platens [87]. In the quasi-static tests, the specimens were compressed under the displacement control setting along the long dimension (3.5mm) at a constant rate in the range of 3.5×10^{-4} to 3.5×10^{-2} mm/s. The force history was recorded by a 100 kN load cell with a background noise of ± 1 N. The strain field of the specimen surface was obtained by digital image correlation (see section 2.3.4 for details), and the strain rates in the axial direction were measured to be in the range of 10^{-5} to 10^{-3} s^{-1} by taking the slope of the digital image

correlation outputted strain history curves. The measured strain rate is an order lower than the setting value (10^{-4} to 10^{-2}), and this is due to the compliance of the loading frame [114].

2.3.3 Dynamic uniaxial compression and compression-shear tests

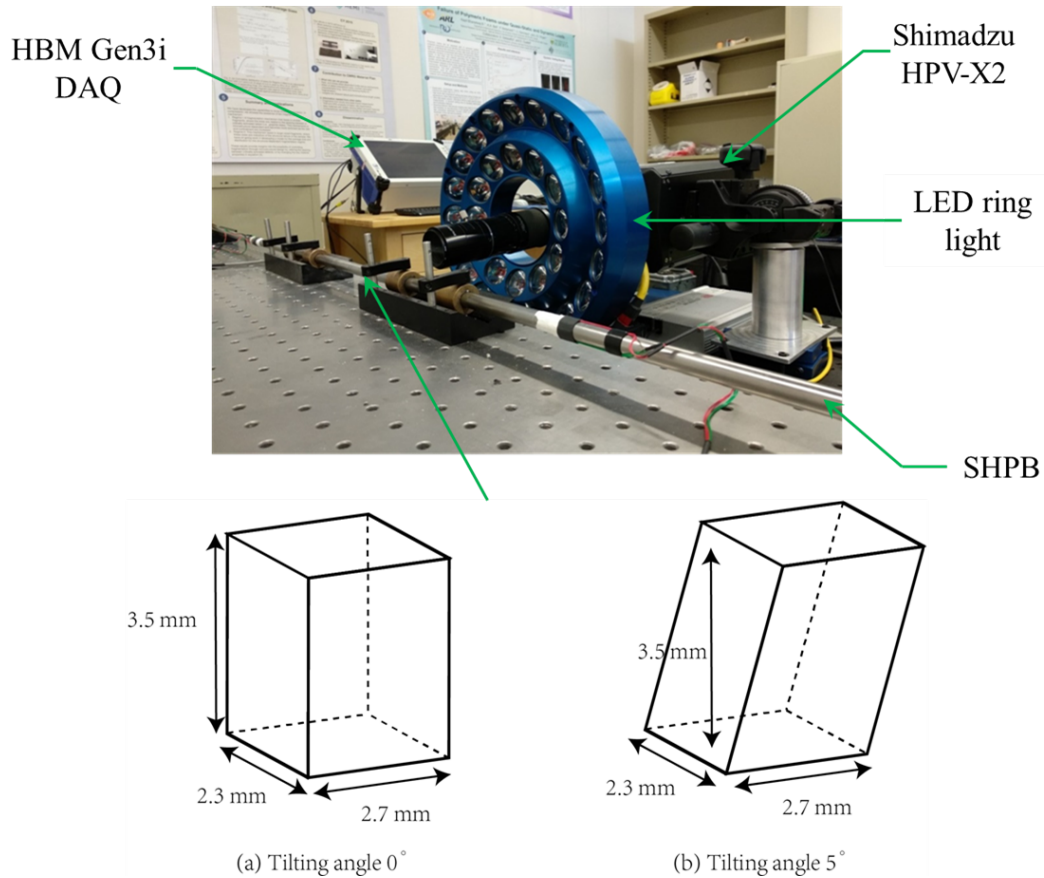


FIGURE 2.1: The split-Hopkinson pressure bar configuration for dynamic testing with an ultra-high-speed camera, a high-speed data acquisition system (DAQ) and an ultra-bright LED ring light. The insert below shows the geometries of the specimen: (a) uniaxial compression specimen with a tilting angle of 0° , and (b) compression-shear specimen with a tilting angle of 5° .

The dynamic uniaxial compression and compression-shear tests were conducted on a modified split-Hopkinson pressure bar (SHPB). The experimental system used in this study was the same as in Koch et al. [104] and Lo et al. [6]. The incident and transmitted bar were 1016 mm and 914 mm in length, respectively, with a diameter of 12.7 mm. The bars were made of hardened C-350 maraging steel with a density of 8080 kg/m^3 , an elastic modulus of 200 GPa, and longitudinal wave velocity of 4975 m/s. The yield strength of the bar was approximately 2.68 GPa which meets the requirements for testing ceramics [115, 116]. Impedance-matched Ti-6Al-4V titanium alloy jacketed tungsten carbide platens were used in the dynamic tests to protect the incident and transmitted

bars from being indented by the hard ceramic samples and fragments [116]. In dynamic uniaxial compression tests, high pressure grease was applied between the protection platens and specimen to reduce friction and allow for free lateral expansion for specimen. Similar to the quasi-static tests, no grease was used in the dynamic compression-shear tests to induce tangential force by friction and to make sure no surface sliding occurs between the specimen and loading devices [87]. The theory of the SHPB system has been well documented by Song and Chen [102], and the nominal axial stress of the specimen is computed using the strain gauge signal from the transmitted bar and the transmitted bar properties.

An HBM Gen3i High-Speed Recorder was employed for the data acquisition at 4 MHz with a Bessel IIR pre-filter to eliminate low frequency noise. In the current experiments, different types of pulse shaping configurations were used to produce near triangular pulses (i.e., tin and high density polyethylene (HDPE)), which is desired in testing linear elastic brittle materials [6]. The pulse shapers reduce the oscillation of the stress pulse due to dispersion effects and ensure the required stress equilibrium is achieved, as recommended in literature [6, 104, 117]. In order to achieve dynamic strain rates ranging from 80 to 850 s^{-1} , we varied the striker length (125 and 304 mm), as well as the types and dimensions of pulse shapers (tin, thin HDPE and thick HDPE), which are summarized in Table 2.1. Figure 2.2 and Figure 2.3 show that the pulse shaping configurations used in the current study can induce uniform deformation across the sample surface and achieve near constant strain rates for the specimens, as is recommended in literature [6]. In all configurations of the setup, the 1-wave passage criterion was verified by comparing the rise time in the incident and transmitted pulses. More details of Figure 2.2 and Figure 2.3 are discussed next in section 2.3.4.

TABLE 2.1: Pulse shaping configurations used in dynamic experiments

Strain Rate (s^{-1})	Material	Pulse Shaper		Striker Length (mm)
		Diameter (mm)	Thickness (mm)	
80 to 150	Tin	3.97	1.59	304
300 to 450	HDPE (thin HDPE)	3.18	1.59	304
500 to 850	HDPE (thick HDPE)	3.18	2.38	125

2.3.4 Digital image correlation

To provide visualization on the specimen surface to monitor the macroscopic deformation, an AOS PROMON U750 high-speed camera with a full resolution of 1280×1024 pixels recording at 5 to 500 frames per second (FPS and its value is determined by the loading rate) was used in quasi-static tests, and an ultra-high-speed camera (Shimadzu HPV-X2) was used in dynamic tests. The Shimadzu HPV-X2 camera has a full resolution of 400

$\times 250$ pixels, and the frame rates used in the tests ranges from 0.5 million to 5 million FPS depending on the pulse shaping configurations used (i.e., affecting the strain rates). An REL Inc. ultra-bright LED ring light was applied to provide sufficient lighting that enhanced imaging and DIC analysis. The exposure time was set at the range of 200 to 500 ns according to the frame rate of the camera and compensation for the lighting.

The DIC technique was applied to obtain the two-dimensional strain information and the failure process of the quasi-static and dynamic experiments by using the VIC-2D V6 software (Correlated Solutions, Inc. USA). During analysis, the surface of the specimen was discretized with a subset size of 31×31 pixels, and a step size of 7 pixels was chosen [6]. The zero-normalized sum of squared differences (ZNSSD) criterion with the optimized 8 tap interpolation scheme was utilized in the analysis.

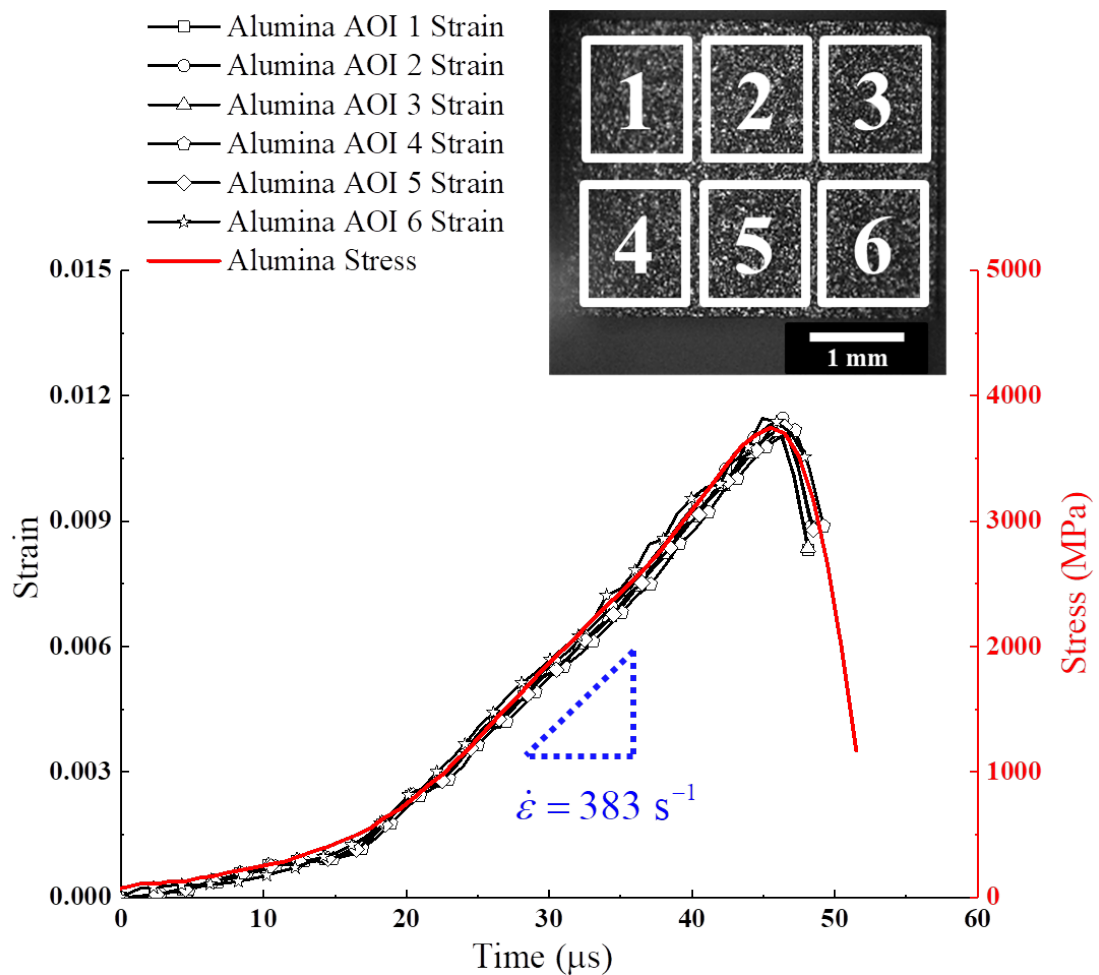


FIGURE 2.2: For specimen under dynamic uniaxial compression, the stress profile obtained from the transmitted gauge and the local strain profiles computed from six different areas of interest (AOI) by DIC are matched in time. The locations of the six AOIs are shown in the inset. The linear portions of the strain-time curves is taken as the strain rate, and the average strain rate in this experiment is approximately 383 s^{-1} .

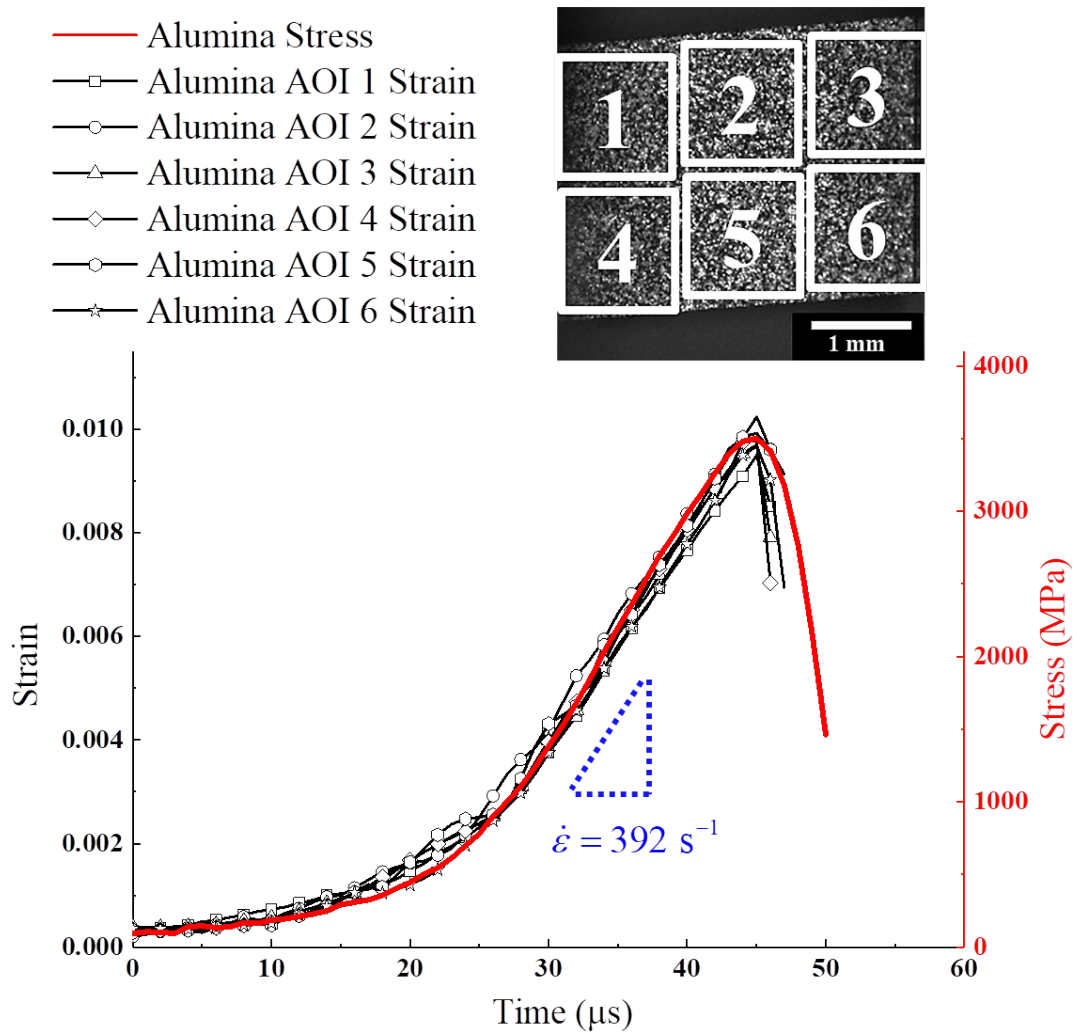


FIGURE 2.3: For specimen under combined dynamic compression and shearing loading, the axial stress profile obtained from the transmitted gauge and the local axial strain profiles computed from six different areas of interest (AOI) by DIC are matched in time. The locations of the six AOIs are shown in the inset. The linear portions of the strain-time curves is taken as the axial strain rate, and the average strain rate in this experiment is approximately 392 s^{-1} . The axial direction is the horizontal direction.

In this study, the engineering strain was computed by DIC analysis, and the slope of the linear portions of the strain-time curves was taken as the strain rate. Figure 2.2 and Figure 2.3 show the representative stress and strain history for the dynamic uniaxial compression and compression-shear tests on the CeramTec 98% alumina, respectively. Six different local areas of interest (AOI) for strain-time are plotted with the stress-time to verify the stress equilibrium of the tests. It is observed that all six strain-time profiles are overlapped with each other, and this indicates that the specimen was deformed uniformly during loading [102]. In addition, the strain profiles were matched well with the stress history curve, which is expected for a typical linear elastic brittle material, and further demonstrates stress equilibrium during loading [6]. Lastly, the stress-strain curves

were obtained by matching the average strain profile with the stress profile generated from the quasi-static and dynamic experiments. The average strain was calculated by averaging across the entire specimen surface.

2.4 Data processing method for combined compression and shear loading

In this section, we propose a new method that includes the force and deformation analysis during the compression-shear tests used to calculate the shear strain and stress based on previous work [101, 102]. This new method considers: 1) the evolution of Poisson's ratio induced by the loading [77, 118] and 2) the damage evolution of the compressive stiffness [12, 118]. The degrees of changes in these elastic properties depends on the material [77]. This proposed method is validated with the DIC measurements in the current study, which will be shown later.

As reference for this analysis, labeled in Figure 2.4a, F_n and F_t are the normal force and the tangential force applied on the specimen, respectively, where the tangential force is induced by friction. In Figure 2.4b, α is the tilting angle of 5° , γ and θ are the shear strain, d is the loading displacement, and h is the length of the specimen. In compression-shear testing, it is difficult to measure the tangential force directly, and so the current study proposes a data processing method to calculate the tangential strain and stress. To do this, our study utilized existing literature [102] to develop some assumptions to calculate the tangential force: 1) there is no surface sliding between the loading device and specimen (i.e., no grease applied between specimen and platen surfaces), as the red dashed line in Figure 2.4b shows, and 2) when the specimen reaches the equilibrium state, the deformation is uniform, and the strain and stress can be determined. Also, it is emphasized that these assumptions are consistent with the observation from images of the ultra-high-speed camera acquired in this study.

When no surface sliding occurs between the specimen and loading devices, and the value of d is extremely small, the normal strain ϵ , the shear strain γ and their incremental form can be expressed as:

$$\epsilon = \frac{d}{h}, \quad \Delta\epsilon = \frac{\Delta d}{h} \quad (2.1)$$

$$\gamma = \theta \approx \frac{d}{h-d} \tan \alpha \approx \frac{d}{h} \tan \alpha, \quad \Delta\gamma \approx \frac{\Delta d}{h} \tan \alpha \quad (2.2)$$

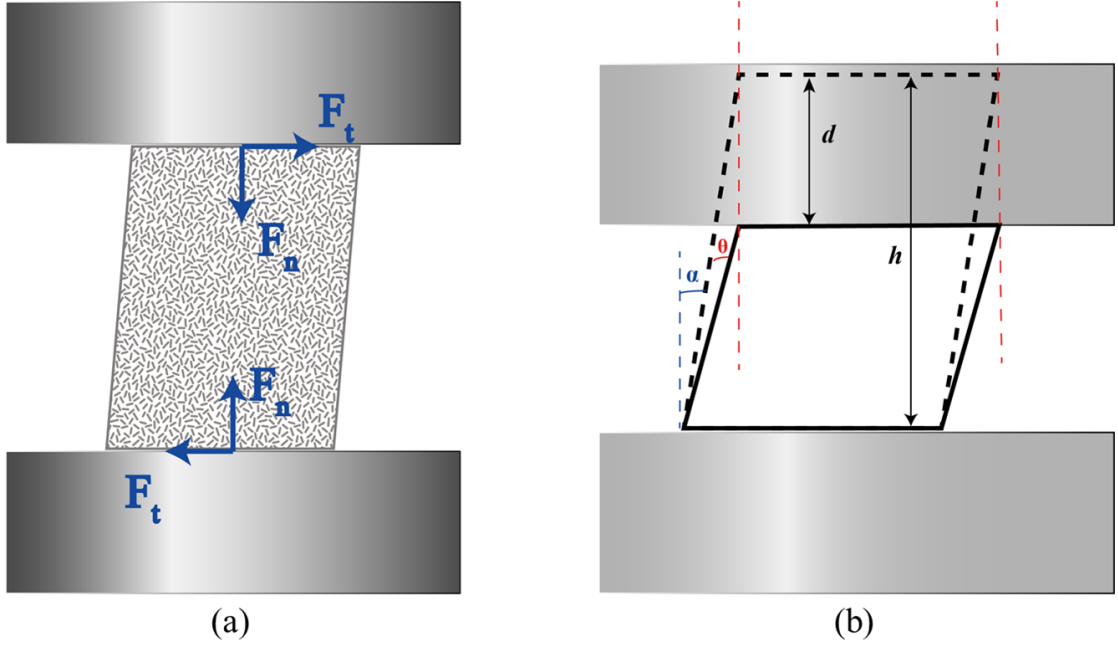


FIGURE 2.4: The analysis of force and deformation of the specimen during compression-shear testing: (a) the force analysis of the specimen, where the specimen is sprayed with a speckle pattern for digital image correlation which allows for measurements of compression and shear strains. F_n and F_t are the normal force and the tangential force applied on the specimen, respectively, where the tangential force is induced by friction. (b) the deformation analysis of the specimen with the assumption that no surface sliding happens, as indicated by the red dashed lines. The black dashed lines demonstrate the initial location of the specimen, and the solid line is the specimen under compression and shear loads. α is the tilting angle of 5° , θ is the shear strain, d is the loading displacement, and h is the length of the specimen.

In a general case, the non-linear constitutive relationship of the alumina is:

$$\Delta\sigma = \frac{E(1-v)}{(1+v)(1-2v)} \cdot \Delta\varepsilon_1 + \frac{E \cdot v}{(1+v)(1-2v)} \cdot (\Delta\varepsilon_2 + \Delta\varepsilon_3) \approx \frac{E(1-v)}{(1+v)(1-2v)} \cdot \Delta\varepsilon \quad (2.3)$$

$$\Delta\tau = G \cdot \Delta\gamma \quad (2.4)$$

where $E = E(\sigma)$ is the elastic modulus, $G = G(\sigma)$ is the shear modulus, and $v = v(\sigma)$ is the Poisson's ratio. Based on the study of Koch et al.[113, 118], E , G and v are regarded as functions of the stress, and their relationship is:

$$G(\sigma) = \frac{E(\sigma)}{2[1+v(\sigma)]} \quad (2.5)$$

The normal force and the tangential force follow:

$$F_n = \sigma \cdot A_s, \quad F_t = \tau \cdot A_s \quad (2.6)$$

where A_s is the cross sectional area of the specimen. As a result of the dependency of the elastic modulus, shear modulus and Poisson's ratio on the stress state and level, the relationship between the tangential and normal force in an incremental form is obtained by combining Equations (2.1) to (2.6):

$$\frac{\Delta F_t}{\Delta F_n} = \frac{G(\sigma)}{E(\sigma)} \cdot \frac{(1+v)(1-2\nu)}{(1-\nu)} \tan \alpha = \frac{[1-2 \cdot \nu(\sigma)] \tan \alpha}{2 \cdot [1-\nu(\sigma)]} \equiv \tan \beta \quad (2.7)$$

Here β is the effective frictional angle of the contact surface of the specimen with the loading devices, and it refers to the ratio of the normal component to the shear component of surface force applied on the specimen. Note here that β is different from tilting angle α .

According to Equation (2.6) and Equation (2.7), increments of compressive and shear stresses in the specimen satisfy:

$$\Delta \sigma = \frac{\Delta F_n}{A_s} \quad (2.8)$$

$$\Delta \tau = \frac{\Delta F_n}{A_s} \frac{[1-2 \cdot \nu(\sigma)] \tan \alpha}{2 \cdot [1-\nu(\sigma)]} \quad (2.9)$$

According to Equation (2.7), the compression and shear force can be obtained by the strain signals measured on the transmitted bar in an incremental form:

$$\Delta F_n = A_b \cdot E_b \cdot \Delta \varepsilon_t(t) \quad (2.10)$$

$$\Delta F_t = A_b \cdot E_b \cdot \frac{[1-2 \cdot \nu(\sigma)] \tan \alpha}{2 \cdot [1-\nu(\sigma)]} \cdot \Delta \varepsilon_t(t) \quad (2.11)$$

where t is the time, A_b and E_b are cross-sectional areas and elastic modulus of the impact bar and the support bar, respectively, and ε_t is the strain signals of the transmitted wave recorded by the strain gauges.

The relative loading displacement d in Figure 2.4b can be determined by DIC analysis, and thus d and its increment are:

$$\Delta d(t) = h \cdot \Delta \varepsilon = h \cdot \Delta \varepsilon(\Delta \varepsilon_0, D_{E_c}) \quad (2.12)$$

$$d(t) = h \cdot \int_0^t [\Delta \varepsilon(\Delta \varepsilon_0, D_{E_c})] dt \quad (2.13)$$

where ε is the axial strain obtained from DIC analysis, D_{E_c} is the damage to the compression stiffness, and ε_0 is the axial strain without any damage. Similarly, according to Equations (2.1) and (2.2), the compressive strain and shear strain in incremental form are expressed as:

$$\Delta\varepsilon(t) = \Delta\varepsilon(\Delta\varepsilon_0, D_{E_c}) = \Delta\varepsilon \quad (2.14)$$

$$\Delta\gamma(t) = \tan \alpha \cdot \Delta\varepsilon(\Delta\varepsilon_0, D_{E_c}) = \tan \alpha \cdot \Delta\varepsilon(t) \quad (2.15)$$

In order to compare the uniaxial compression results and the compression-shear results across the range of strain rates probed here, the equivalent stress and equivalent strain rate are used. The equivalent stress is expressed as:

$$\sigma_e = \sqrt{\frac{1}{2} \left[(\sigma_x - \sigma_y)^2 + (\sigma_x - \sigma_z)^2 + (\sigma_y - \sigma_z)^2 + 6 (\tau_{xy}^2 + \tau_{xz}^2 + \tau_{yz}^2) \right]} \quad (2.16)$$

The equivalent strain rate is analogous to the equivalent stress and is expressed as:

$$\dot{\varepsilon}_e = \sqrt{\frac{1}{2(1+\nu)^2} \left[(\dot{\varepsilon}_x - \dot{\varepsilon}_y)^2 + (\dot{\varepsilon}_x - \dot{\varepsilon}_z)^2 + (\dot{\varepsilon}_y - \dot{\varepsilon}_z)^2 + 6 (\dot{\varepsilon}_{xy}^2 + \dot{\varepsilon}_{xz}^2 + \dot{\varepsilon}_{yz}^2) \right]} \quad (2.17)$$

2.5 Experimental results

2.5.1 Material characterization

The microstructural features of the CeramTec 98% alumina were first investigated by examining the intact material surface. Figure 2.5a is an SEM micrograph showing a typical microstructure of the CeramTec 98% alumina. The grey regions correspond to the alumina phase, and the surface pores can be observed. Some of the porous features in Figure 2.5a are secondary glassy phases that were removed during mechanical polishing [104], confirmed by EDS analysis (shown later). Figure 2.5b shows an EBSD map for the CeramTec 98% alumina, and it shows the grain size and the crystal orientation of the grains at the surface of the sample. Based on the Figure 2.5b, the equivalent circle diameters of grains were determined by using the AZtec Channel 5 software, with an average of $1.85 \pm 0.98 \mu\text{m}$. Specifically, the large standard deviation is associated with the large horizontal high-aspect-ratio grains. Figure 2.6 shows approximately 88% of the grain size (the equivalent circle diameters) distribution is between 0.4 and 2.8 μm , and they are nearly circular small grains. There are also a relatively small number of large horizontal high-aspect-ratio grains with the equivalent circle diameters ranging

from 5 to 8 μm . Next, both small equiaxed and large columnar grains appear to have no preferred crystallographic orientation, and most boundaries are of high misorientation angle ($>15^\circ$). The large grains with higher aspect ratios appear to be more-or-less aligned near-parallel with each other. Lastly, the un-indexed (black) regions in Figure 2.5b are believed to be corresponding to either the pores or regions with impurities. Those impurities can easily form a glassy phase concentrated at the grain boundaries [104, 119], and the impurity analysis has been conducted using the EDS data (shown later).

The X-Ray Microscopy (XRM) was also applied to characterize the defects (pores and impurities) in the sample. XRM scans of the samples were carried out using a ZEISS Xradia Versa 620, with X-ray voltage 100 kV, power 14.02 W and a voxel size of $0.5275 \times 0.5275 \times 0.5275 \mu\text{m}^3$. Only the central volume of the sample (a cylinder with a height of 0.61 mm and a diameter of 0.53 mm) was considered for XRM analysis, as Figure 2.7a and b shows. The Dragonfly Pro software (Object Research Systems, Inc. Canada) was used to explore the data, and the reconstructed pores were filtered by a minimum of 8 voxels (a resolution limit consistent with those used in the literature [5, 120]). The histogram distribution of different defect volumes is shown in Figure 2.7c, and most of the defects are less than $160 \mu\text{m}^3$ in volume. The largest volume of the defect is around $10200 \mu\text{m}^3$ and large defects are infrequent in the sample. The volume percentage of the defects is around 1%.

Next, the elemental composition and impurity distribution are examined using EDS. Figure 2.8 and Table 2.2 show the elemental composition of the CeramTec 98% alumina determined in terms of weight percentage and atomic percentage by EDS. This material is primarily composed of aluminum (atomic 39.52%, weight 52.47%) and oxygen (atomic 59.47%, weight 46.1%) mixed with traces of Mg (atomic 0.49%, weight 0.58%), Si (atomic 0.27%, weight 0.37%), and Ca (atomic 0.25%, weight 0.48%). Carbon is excluded from the concentration calculation since it is likely introduced during sample preparation (mechanical polished with liquid-suspended diamond and carbon coating to enhance conductivity). For pure alumina, the ratios of atomic percentage of aluminum to oxygen should be 2:3, and an excess of oxygen element would indicate oxide contaminants. The distribution of magnesium, calcium and silicon may come from manufacturing process [121]. Overall, the material is confirmed to be single phase α -alumina verified by SEM and EDS.

2.5.2 Strain-rate dependent uniaxial compression tests

In the current study, four quasi-static tests with strain rates ranging from 1.6×10^{-5} to $1.63 \times 10^{-3} \text{ s}^{-1}$ and eleven dynamic tests with the strain rates ranged from 83 to 835

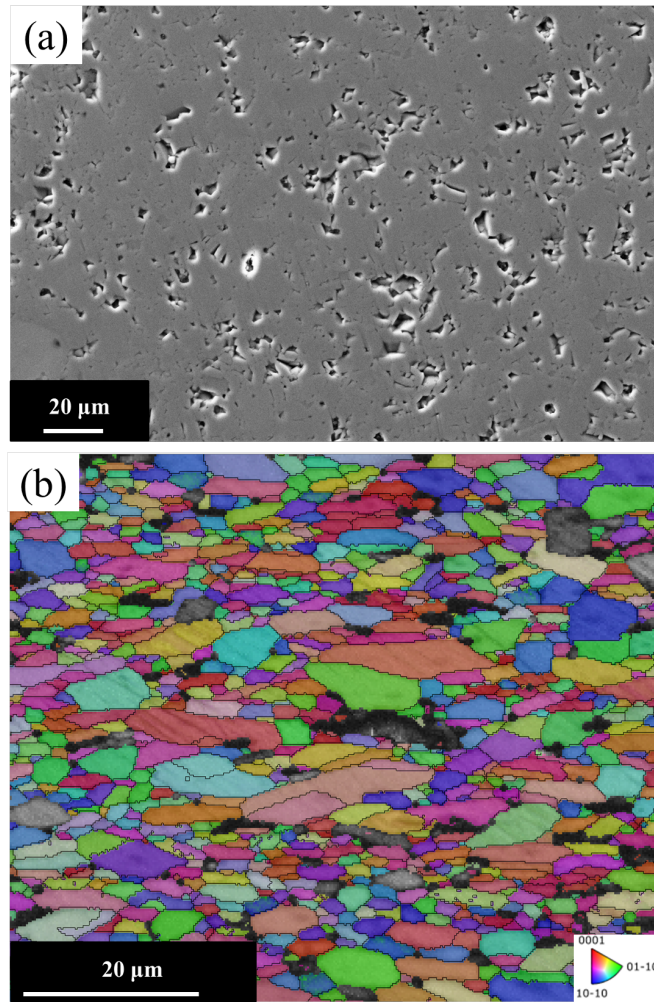


FIGURE 2.5: (a) SEM image of a polished alumina surface which shows the micro-structural features of the alumina. The grey regions correspond to the alumina, and the surface pores can be observed. (b) EBSD maps for the CeramTec 98% alumina, and this map shows the grain size and the crystal orientation of the grains at the surface of the sample.

s^{-1} were performed for the alumina under uniaxial compression. Figure 2.9 shows the representative stress-strain curves where the solid lines represent the uniaxial compression tests. The stress-strain curves are shown as nearly-straight lines. When the stress-strain curves reach the peak value, the specimen failed catastrophically, and the stress drops immediately in both quasi-static and dynamic tests. The Young's modulus and Poisson's ratio remain near-constant before failure, as Figure 2.9 and Figure 2.10 show, and their values are calculated by taking the slope of the stress-strain curve and the lateral-axial strain curve, respectively. Under the quasi-static condition, the Young's modulus has an average of 356 ± 28 GPa, and an average of 380 ± 42 GPa under the dynamic condition. Similarly, the Poisson's ratio has an average of 0.243 ± 0.023 under the quasi-static condition, and 0.226 ± 0.030 under the dynamic condition. A summary of the data is shown in Table 2.3. These properties are consistent with the reported values of alumina

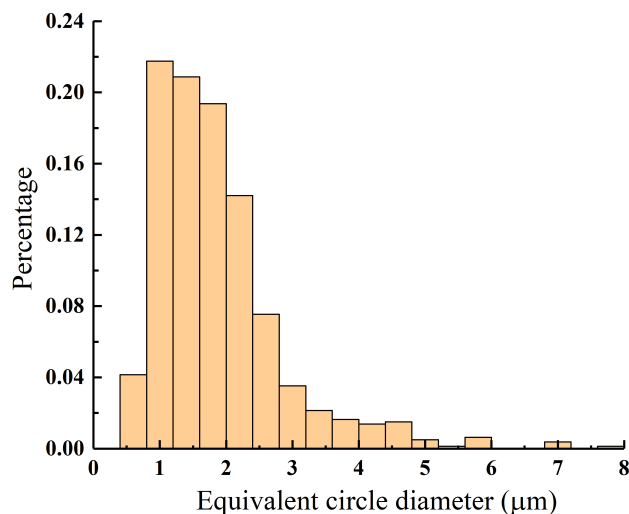


FIGURE 2.6: The histogram distribution of the equivalent circle diameter of the grain in the CeramTec 98% alumina, which is obtained from several regions of the sample. Approximately 88% of the grain size (the equivalent circle diameters) distribution is between 0.4 and 2.8 μm , and they are nearly circular small grains. There are also a relatively small number of large horizontal high-aspect-ratio grains with the equivalent circle diameters ranging from 5 to 8 μm .

TABLE 2.2: Elemental composition of the CeramTec 98% alumina as determined by EDS

Element	Weight (%)	Atomic (%)
O	46.1	59.47
Al	52.47	39.52
Mg	0.58	0.49
Si	0.37	0.27
Ca	0.48	0.25

ceramics [104].

Figure 2.11 shows the relationship of the compressive strength and the strain rate for the CeramTec 98% alumina. From Equation (2.16) and Equation (2.17), the equivalent peak stress and corresponding strain are computed, and their values are also listed in Table 2.3 for clarity. It is observed that the CeramTec 98% alumina shows rate dependence in its compressive strength. For the quasi-static experiments at the strain rates of 1.6×10^{-5} to $1.63 \times 10^{-3} \text{ s}^{-1}$, the compressive strength has an average of $3393 \pm 306 \text{ MPa}$, and the failure strain was $0.88 \pm 0.11\%$. For the dynamic experiments at strain rates of 83 to 835 s^{-1} , the compressive strength has an average of $4126 \pm 297 \text{ MPa}$ (with an average of 4126 MPa) and the failure strain was $1.13 \pm 0.17\%$. In the current study, the CeramTec 98% alumina has approximately a 22% increase in strength across the studied strain rates, and these results are consistent with the recent SHPB results by Koch et al. [104] on

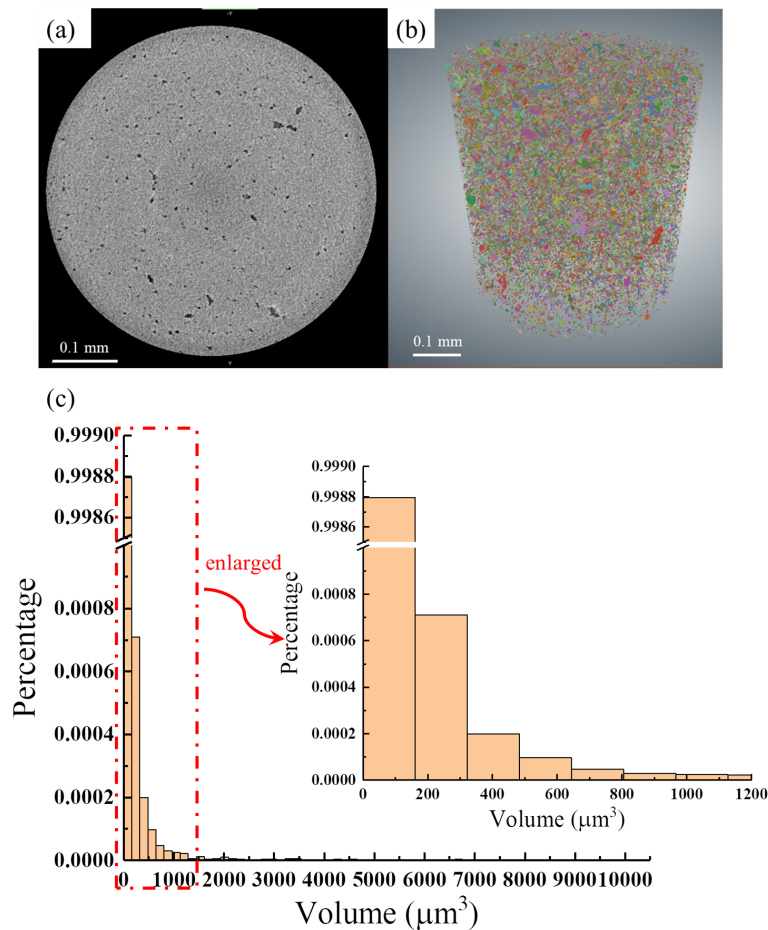


FIGURE 2.7: (a) and (b): The central volume of the sample, a cylinder with a height of 0.61 mm and a diameter of 0.53 mm, was considered for the XRM analysis. The colored volumes in (b) are the defects (pores and impurities) in the sample. (c) The histogram of defects with different size volumes. The volume value of the defects is dominated by small ones (less than $160 \mu m^3$), and large defects are infrequent (the largest volume of the defect is around $10200 \mu m^3$). The histogram of the volumes less than $1200 \mu m^3$ is enlarged in the inset.

the CoorsTek AD-85 (around 30% increase) and AD-995 (around 50% increase) alumina ceramics (see section 2.6.1 for details).

2.5.3 Strain-rate dependent compression-shear tests

In the current study, six quasi-static compression-shear tests with axial strain rates ranging from 1.5×10^{-5} to $1.6 \times 10^{-3} \text{ s}^{-1}$ and nine dynamic compression-shear tests with axial strain rates ranging from 82 to 833 s^{-1} were performed for the alumina. Similar to uniaxial compression results, the axial stress and axial strain curves for the compression-shear tests are shown as nearly-straight dash lines in Figure 2.9 with little softening occurring prior to failure, which corresponds to D_{E_c} in Equation (2.14) in our proposed model. The Young's modulus and Poisson's ratio in the compression-shear

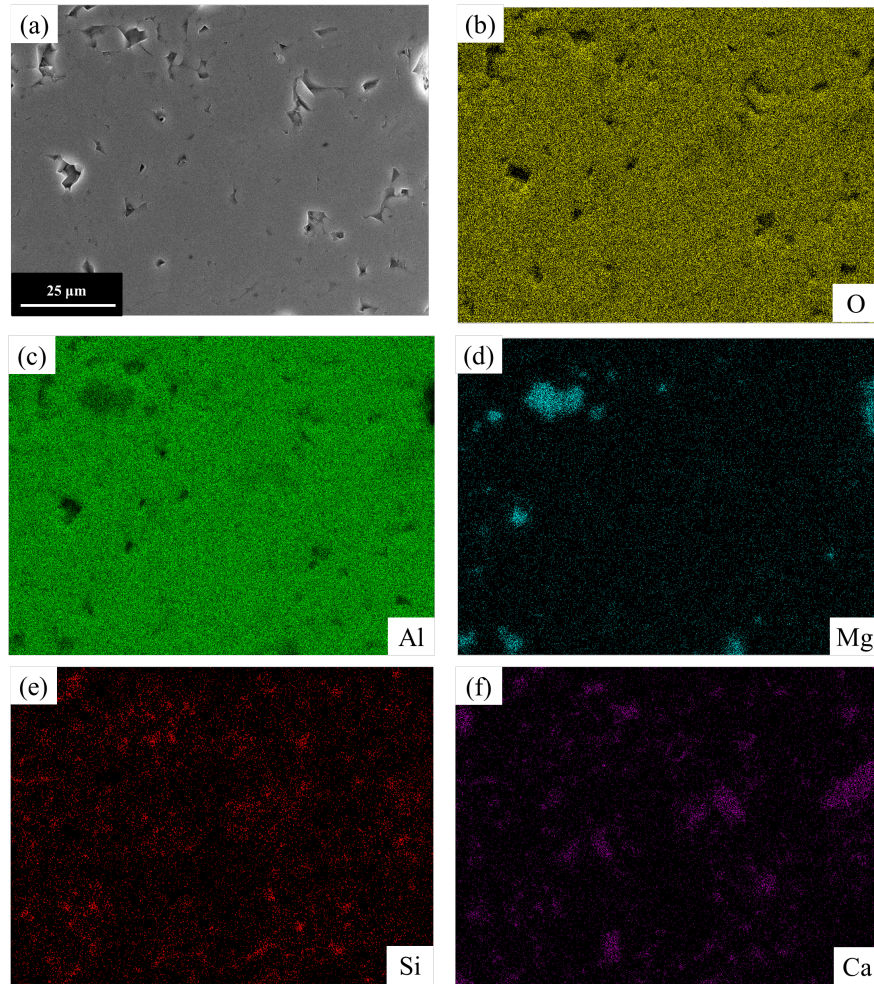


FIGURE 2.8: SEM coupled with EDS investigating the chemical composition of the alumina. (a) SEM micrograph showing a magnified view of a mechanically polished surface of the CeramTec 98% alumina. (b) EDS map of the distribution of oxygen. (c) EDS map of the distribution of aluminum. (d) EDS maps of magnesium element. (e) EDS maps of silicon element. and (f) EDS maps of the calcium element. The magnesium, silicon and calcium elements are present in low quantities.

tests are in the same range as the uniaxial compression tests, as the dash lines in Figure 2.9 and Figure 2.10 show. As before, Table 2.3 lists the data. In order to compare the uniaxial compression and the compression-shear results, the equivalent stress (Equation (2.16)) and equivalent strain rate (Equation (2.17)) are used. Figure 2.11 and Table 2.3 show the equivalent peak stress and the equivalent strain rate of both uniaxial compression and compression-shear tests. It is observed that the equivalent peak stress of the compression-shear tests is smaller than the uniaxial compression one. The significance of these results will be discussed later.

Next, to validate the proposed model in section 2.4 and better understand the role of shear failure on the mechanical response in compression-shear tests, the predicted shear strain calculated by using Equation (2.15) is compared with shear strain obtained by

DIC analysis in Figure 2.12. It is notable in Figure 2.12 that the peak value in the black DIC curve occurs sooner in time than that of the red predicted curve. The red curve in Figure 2.12 is derived from Equation (2.15): $\Delta\gamma(t) = \tan\alpha \cdot \Delta\varepsilon(t)$, whose time is related to the complete failure of the sample. It means the shear failure happens earlier than complete failure. There are also minor differences in time-evolved magnitudes between the DIC results and the model results, which may be induced by different crack and damage evolution, which are themselves strain-rate dependent. More specifically, in quasi-static loading, fewer defects are activated and the evolution of the cracking is considered less interacting [77]. In dynamic loading, multi-cracks are nucleated and grow. As the strain rate is further increased, the density of cracking nucleation increases, and these cracks will interact and coalesce with each other [77]. These rate effects in terms of nucleation, growth, interaction, and coalescence results in differences in damage accumulation behaviors. Altogether, the validation from Figure 2.12 shows the predicted model is in reasonable agreement with the experimental results.

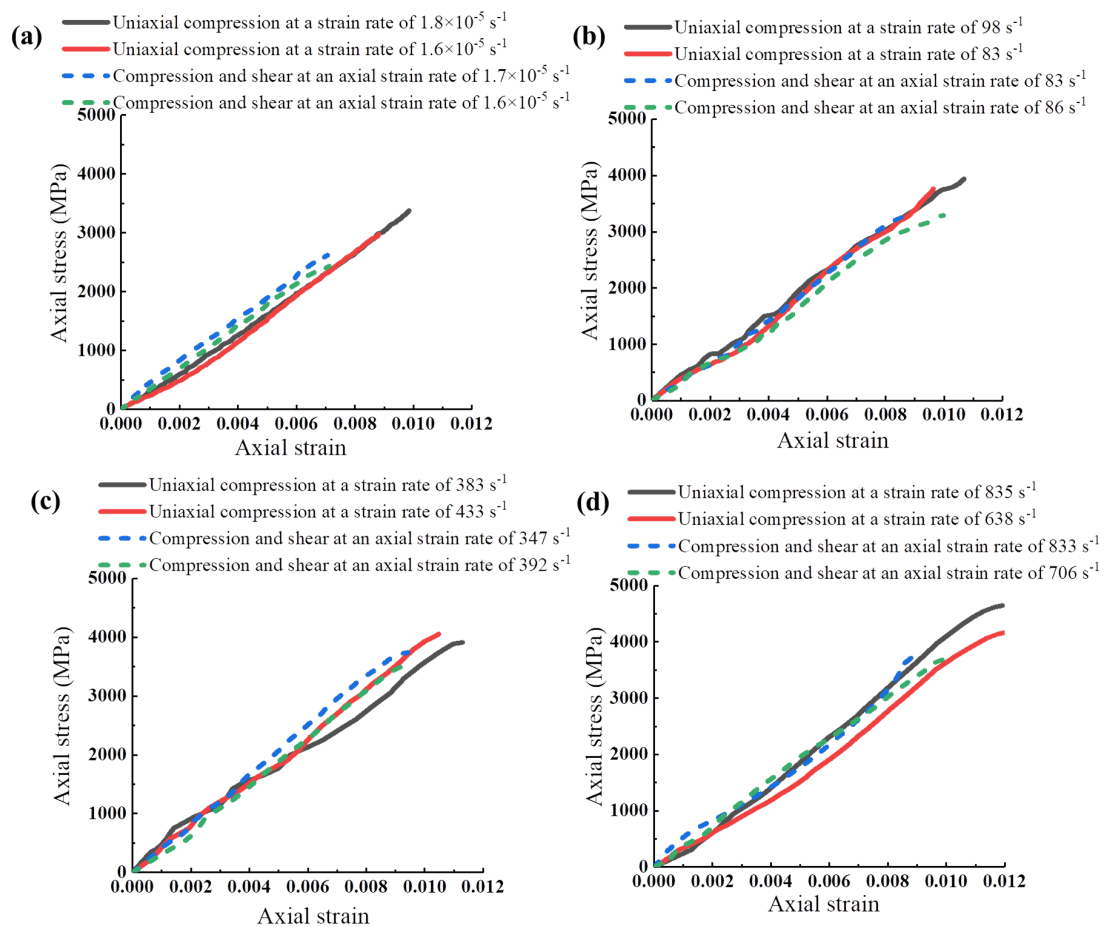


FIGURE 2.9: Representative stress-strain curves in the axial direction at quasi-static and dynamic strain rates (with three different pulse shaping configurations shown in Table 2.1) for the CeramTec 98% alumina. The solid lines correspond to the uniaxial compression tests, and the dashed lines correspond to the compression-shear tests.

Additional summarized data is provided in Table 2.3.

TABLE 2.3: The mechanical properties and responses of the CeramTec 98% alumina

	Young's modulus (GPa)	Poisson's ratio	Axial strain rate (s^{-1})	Equivalent strain rate (s^{-1})	Axial peak stress (MPa)	Equivalent peak stress (MPa)
	349	0.228	1.8×10^{-5}	1.8×10^{-5}	3378	3378
	321	0.257	1.6×10^{-5}	1.6×10^{-5}	2977	2977
	367	0.219	1.54×10^{-3}	1.54×10^{-3}	3691	3691
	388	0.266	1.63×10^{-3}	1.63×10^{-3}	3529	3529
	395	0.203	98	98	3937	3937
	421	0.288	83	83	3763	3763
	403	0.224	93	93	4128	4128
Uniaxial compression test	342	0.261	87	87	3760	3760
	372	0.235	115	115	4074	4074
	311	0.190	383	383	3914	3914
	407	0.216	433	433	4054	4054
	384	0.189	355	355	4593	4593
	411	0.211	835	835	4645	4645
	311	0.226	638	638	4201	4201
	428	0.242	785	785	4318	4318
	358	0.230	1.7×10^{-5}	1.70×10^{-5}	2620	2624
	364	0.247	1.6×10^{-5}	1.60×10^{-5}	2433	2436
	367	0.196	1.5×10^{-5}	1.50×10^{-5}	2656	2660
	342	0.213	1.6×10^{-3}	1.60×10^{-3}	2927	2931
	376	0.23	1.6×10^{-3}	1.60×10^{-3}	2972	2976
	364	0.199	1.6×10^{-3}	1.60×10^{-3}	3090	3095
Compression-shear tests	407	0.198	83	83.2	3278	3283
	396	0.289	86	86.2	3289	3292
	429	0.287	82	82.1	3303	3306
	425	0.249	347	347.6	3743	3748
	405	0.207	392	392.8	3500	3505
	398	0.24	364	364.7	3565	3565
	342	0.216	833	834.6	3720	3725
	353	0.239	706	707.3	3708	3713
	428	0.224	508	508.9	3186	3191

Finally, the time-evolution of surface fracturing is investigated by relating high-speed images acquired during dynamic experiments with stress-time information. In both uniaxial compression and compression-shear tests, the surface cracks are primarily directional cracks in the axial direction (almost parallel to the lateral edge), as Figure 2.13 and Figure 2.14 show.

2.6 Discussion

2.6.1 Microstructure and mechanical properties of comparable alumina ceramics

In this study, the chemical composition, microstructure and mechanical characterization of the CeramTec 98% alumina ceramic have been investigated. In this sub-section, a comparison is made between the CeramTec 98% alumina, the CoorsTek alumina ceramics (AD-85 and AD-995) and others from the literature [5, 86, 104–109]. Comparing microstructures among this study and the CoorsTek alumina, it is found that the CeramTec 98% alumina has fewer intergranular defects (the defect volume fraction is

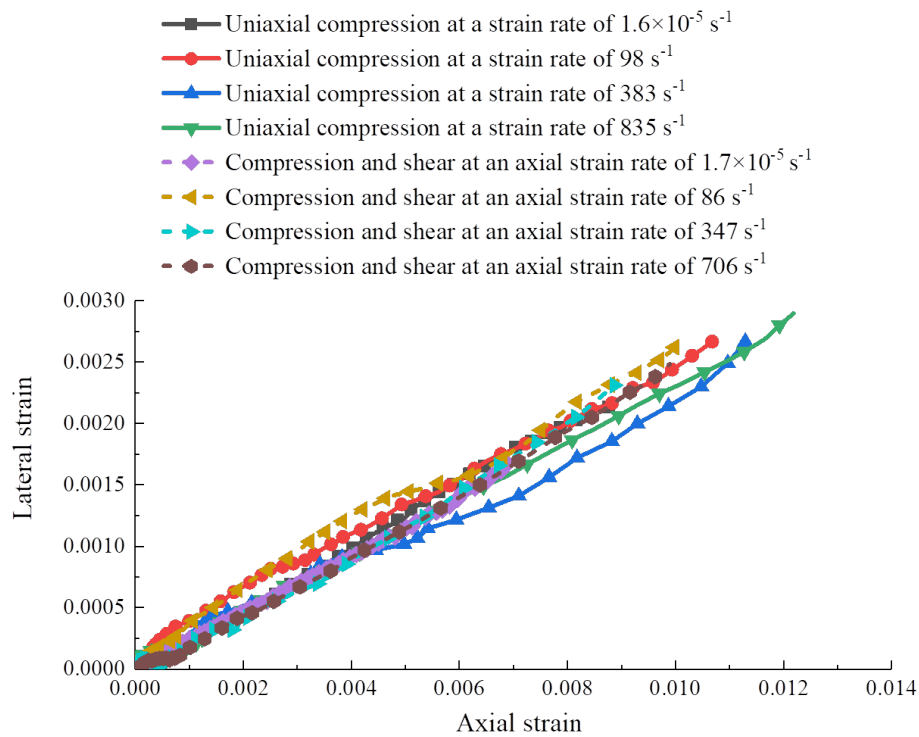


FIGURE 2.10: Representative lateral-axial strain curves at quasi-static and dynamic strain rates (with three different pulse shaping configurations shown in Table 2.1) for the CeramTec 98% alumina. The solid lines correspond to the uniaxial compression tests and the dashed lines correspond to the compression-shear tests, noting little differences between the two types of tests.

around 1%), which is similar to AD-995 (the defect volume fraction is around 1%) but much fewer than AD-85 (the defect volume fraction is around 4%) [5, 104]. Additional previous studies on AD-995 by Lankford et al. [106] demonstrated the AD-995 material has larger and more porosity than the CeramTec 98%, although this conclusion is made on limited available micrographs. In the CERAMSHIELD CAP3 material in Swab et al. [86], there is a greater number of intergranular phases and more frequent porosity features, although the authors do not necessarily quantify the amount or types of phases. These intergranular impurities and pores serve as crack nucleation sites [104], and so are detrimental to material performance. Further, the grain size of the CeramTec 98% alumina (over 88% is between 0.4 and 2.8 μm) is much smaller than that in Coorstek AD-995 ($8 \pm 3 \mu\text{m}$) [104]. In the CERAMSHIELD CAP3 alumina in Swab et al. [86], the grain sizes measured using outlines of their intergranular phases in their SEM images yield sizes of $15.3 \pm 9.7 \mu\text{m}$. These differences are notable because past studies [122, 123] have found ceramics with smaller grain sizes will have better mechanical performance.

To probe these comparisons further, a summary of the uniaxial compression strength of

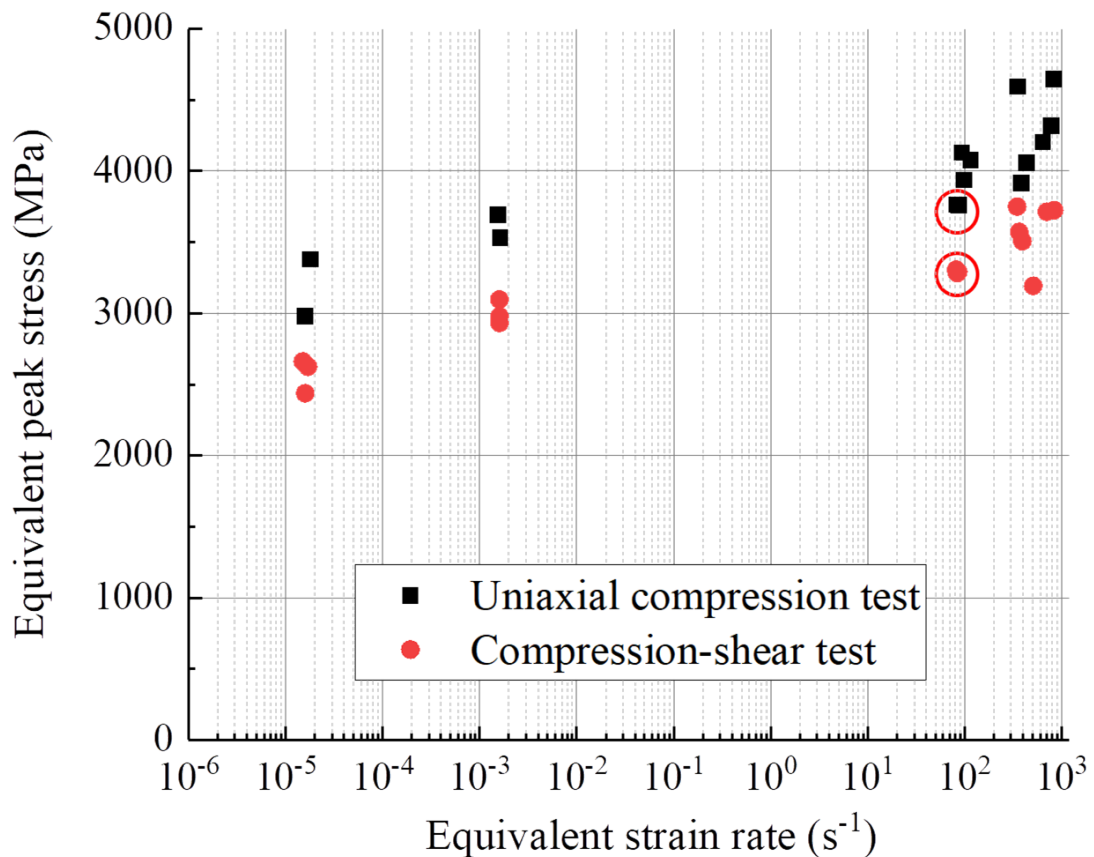


FIGURE 2.11: Semi-log plot of the equivalent peak stress and the equivalent strain rate for the CeramTec 98% alumina. The black rectangle points represent the uniaxial compression tests, and the red circle points represent the compression-shear tests. A black rectangle point in the figure is circled, because there are two points almost overlapped. A red circle point in the figure is circled, because there are three points almost overlapped.

various alumina ceramics under strain rates of $10^{-5} \sim 2500s^{-1}$ [5, 104–110] is shown in Figure 2.15. Note that most commercial names are known, while some are not. Also, we are only making a comparison among test results acquired using cylindrical and cuboidal shaped specimen. In Swab et al. [86], dogbone specimen geometries were used and strength results are higher as described by those authors [5, 104–110], and we do not report their results in Figure 2.15. Here, we observe that the CeramTec 98% alumina has a greater quasi-static compressive strength (3393 ± 306 MPa), and generally greater dynamic strength, when compared with AD-995 (quasi-static strength of 2455 ± 366 MPa) [104–106, 110] and AD-85 (1942 ± 155 MPa) [5, 104]. From a survey of the limited literature involving Young’s modulus measurements, the CeramTec 98% also has a higher experimentally measured Young’s modulus (356 ± 28 GPa) when compared with AD-995 (elastic modulus of 303 ± 31 GPa [104, 106]) and AD-85 (elastic modulus of 221 ± 27 GPa [5, 104]). As highlighted earlier, these improvements in mechanical properties are likely related to the differences of defects and grain sizes [5, 104, 122, 123].

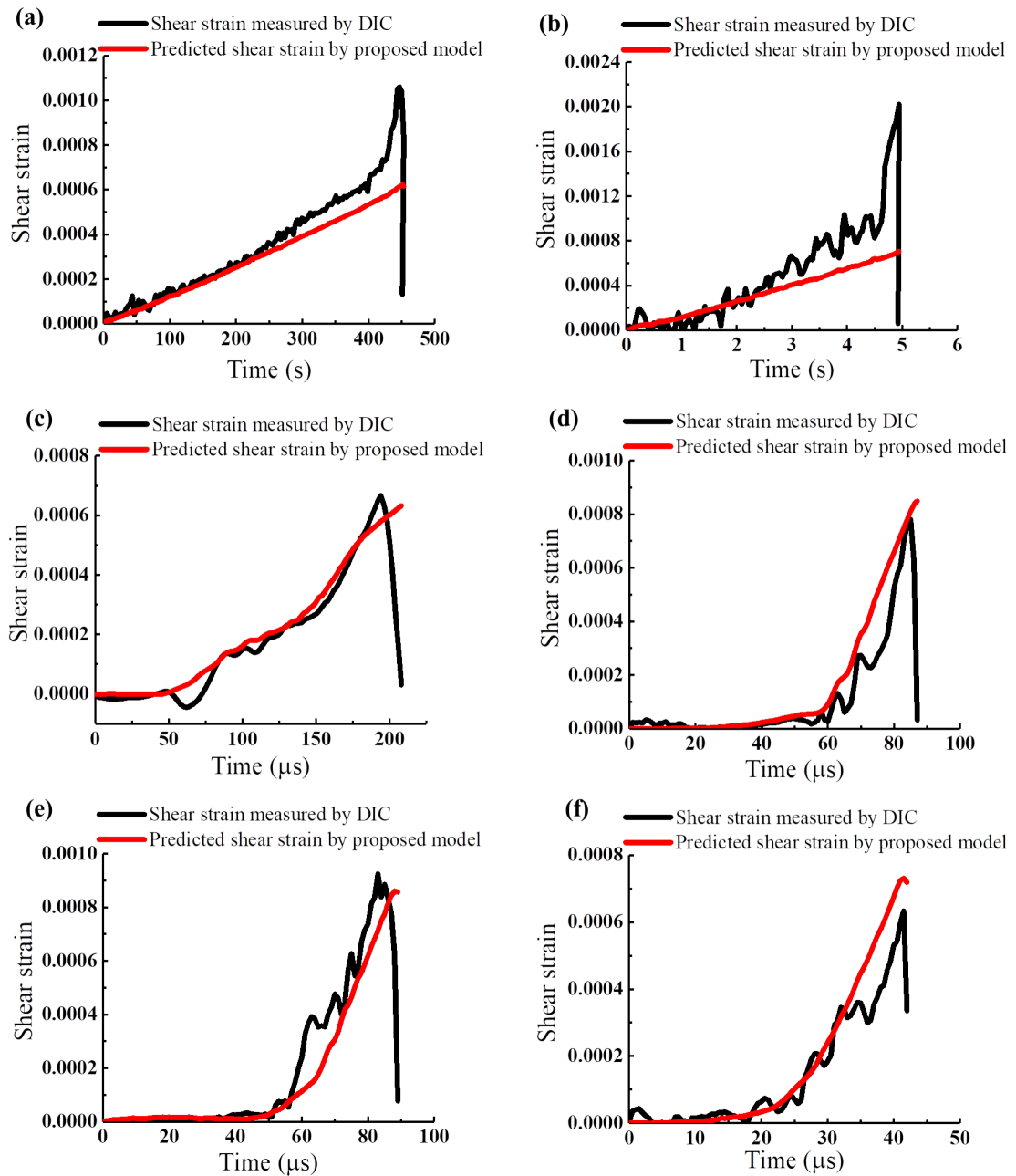


FIGURE 2.12: The shear strain-time curves from compression-shear tests at various strain rates. The black curves are the shear strain obtained from DIC analysis, and the red curves are the predicted shear strain by Equation (2.15): (a) shear strain-time curve at a quasi-static strain rate ($1.6 \times 10^{-5} \text{ s}^{-1}$), (b) shear strain-time curve at a quasi-static strain rate ($1.6 \times 10^{-3} \text{ s}^{-1}$), (c) shear strain-time curve at a strain rate of 83 s^{-1} (tin pulse shaper), (d) shear strain-time curve at a strain rate of 347 s^{-1} (thin HDPE pulse shaper), (e) shear strain-time curve at a strain rate of 392 s^{-1} (thin HDPE pulse shaper), and (f) shear strain-time curve at a strain rate of 706 s^{-1} (thick HDPE pulse shaper).

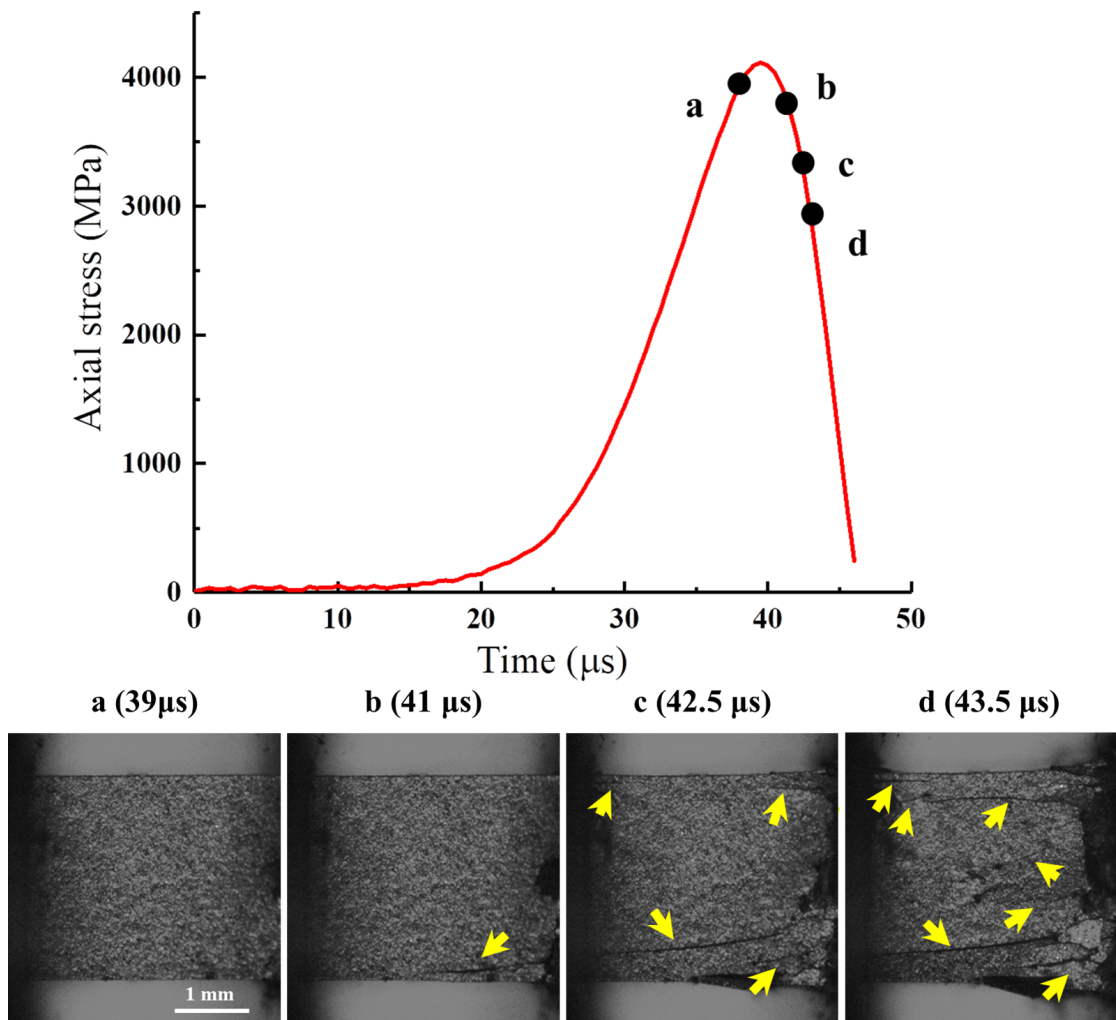


FIGURE 2.13: Time-resolved failure visualization for uniaxial compression test. The strain rate is around 638 s^{-1} . Ultra-high-speed photographs are shown in the inset, and their corresponding points are shown as the black points on the red stress-time curve. The cracks are pointed out by yellow arrows.

2.6.2 Shear-induced failure on mechanical response

In this final sub-section, we discuss the implications of the results in terms of acquiring a better understanding of the role of shear in failure of ceramics. We draw upon mechanical response (i.e., stress-strain response, strain-time curves and rate-dependent strength measurements) presented in the manuscript to articulate the importance of this study in modelling ceramic behavior, especially in impact applications [91, 92].

First, results presented in Figure 2.12 show that shear failure (peak shear strain) in the compression-shear experiments occurs sooner in time than complete failure, and the shear strain evolution is associated with rate effects manifested in shear strain. These rate effects and trends are believed to be related to localized nucleation, growth and interaction of the cracks [77] and crack sliding [43]. In quasi-static tests, the increase

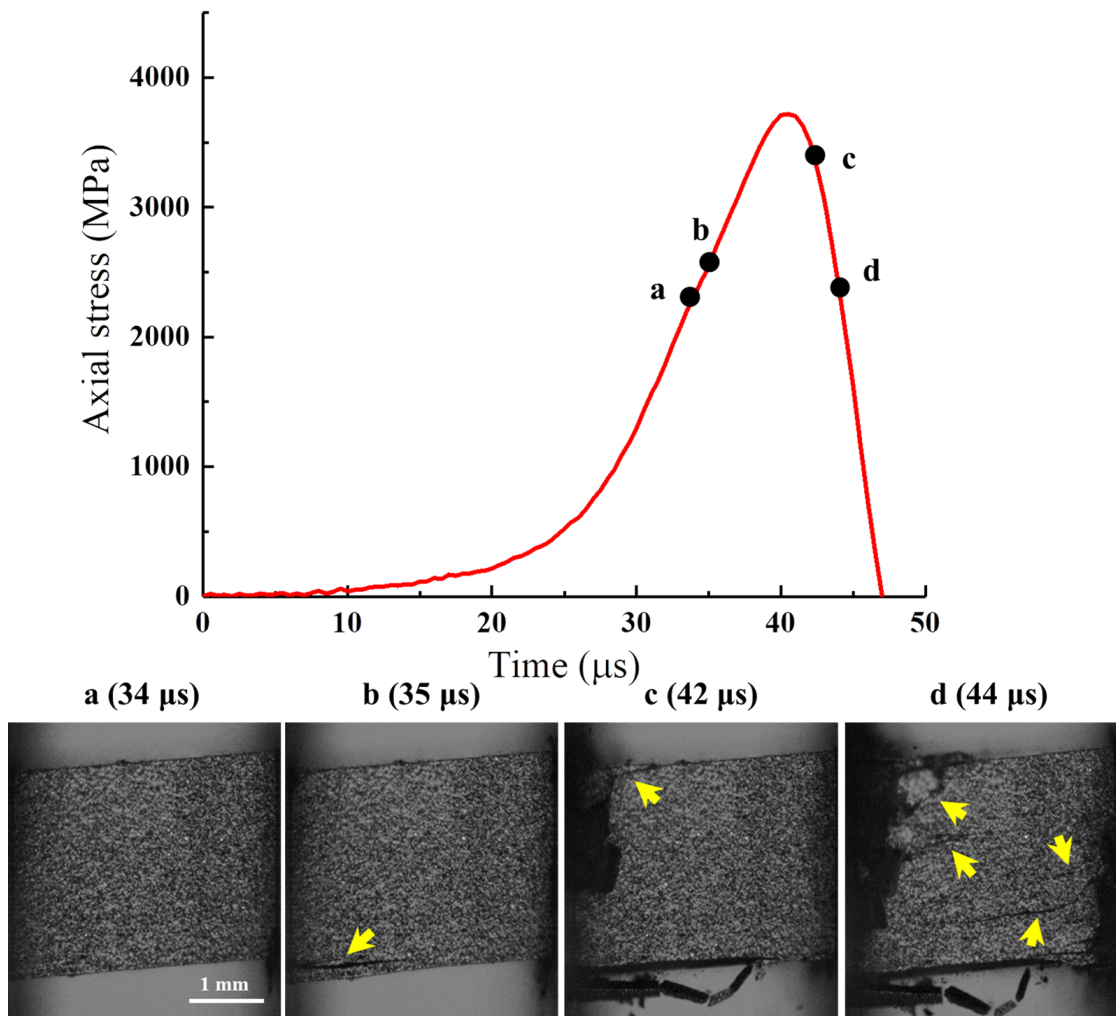


FIGURE 2.14: Time-resolved failure visualization for compression-shear test. The strain rate in the axial direction is around 706 s^{-1} . Ultra-high-speed photographs are shown in the inset, and their corresponding points are shown as the black points on the red stress-time curve. The cracks are pointed out by yellow arrows.

in shear strain is accelerated prior to failure (Figure 2.12a and b), indicating that $\dot{D} \rightarrow +\infty$ prior to catastrophic shear failure [77, 124, 125], where \dot{D} is the damage in shear response. In this damage accumulation and failure process, compression-shear results from this study indicate that directional cracking has a stronger detrimental effect on the shear resistance of the material as indicated by shear strain evolutions (Figure 2.12a and b) when compared with the compressive resistance as indicated by the nearly linear stress-strain curve prior to peak strength (Figure 2.9a). Taken together, these results confirm that shear loading and associated shear damage accumulation play an important role in the failure process of brittle materials. The importance of shear has been noted previously in the literature for uniaxial compressive failure [104, 118, 126] and is a core assumption in the wing crack model [38, 39, 43]. The anisotropic damage evolution is an important consideration in failure modelling of brittle materials [77, 124, 125], where

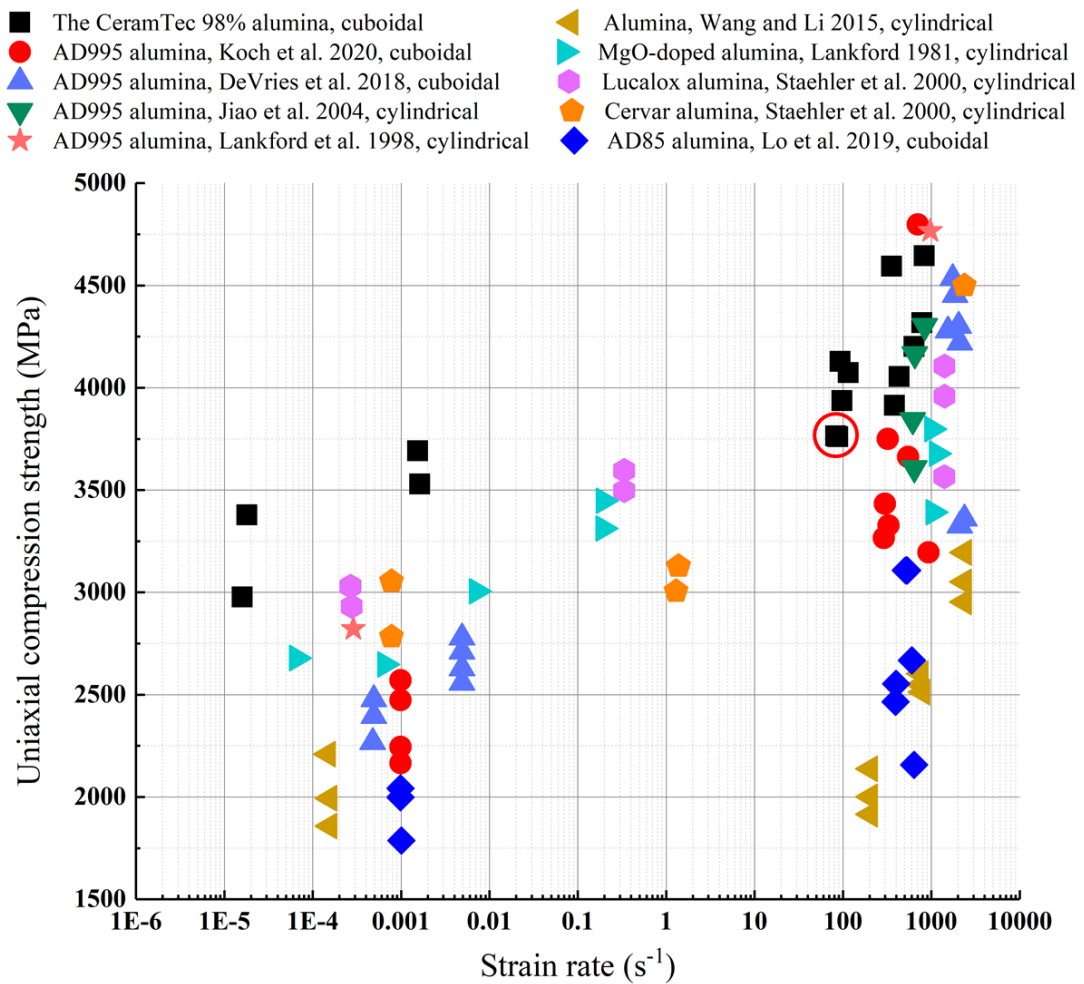


FIGURE 2.15: Summary of uniaxial compression strengths of various alumina ceramics with cylindrical or cuboidal shaped specimen. The black points are the uniaxial compression strength of the CeramTec 98% alumina from this study, and the other colored points are the uniaxial compression strength of other alumina obtained from literature [5, 104–110]. A black rectangle point in the figure is circled because there are two points almost overlapped.

insights into stress-state dependent and non-linear damage forms can be gained from experimental results presented here.

Finally, a key observation from this paper is that the equivalent peak stress in combined compression-shear loading is smaller than that under uniaxial compression (Figure 2.11), which may be related to the earlier shear failure (Figure 2.12) from overall increased damage accumulation and fracturing. As far as the authors are aware, this observation has not yet been made widely for ceramics, with most studies involving combined compression-shear loading occurring in rocks [87, 96, 98] and glass [20]. Based on the new results presented in this paper, it is important to consider stress-state dependent (e.g., combined or history-dependent loading) anisotropic damage accumulation evolution in models [77, 125, 127], and this will be of particular importance when simulating the

response of advanced ceramics in impact and ballistic applications [6, 27, 91, 92, 128–130] where the materials experience spatially- and temporally-evolving combined stress states and strain rates.

2.7 Conclusion

This study assessed the performance of the CeramTec 98% alumina through microscopic characterization, and strain-rate-dependent uniaxial compression and compression-shear experiments. The microscopic characterization and mechanical performance of the CeramTec 98% alumina are compared with some other commercial alumina, and the CeramTec 98% alumina has higher mechanical properties stemming from Figure 2.15. A new data processing method was proposed in this study to calculate the shear components for the compression-shear tests. Validation of the proposed method was confirmed by the shear strain from the DIC analysis. By dealing with the results obtained by the proposed model and the DIC, new observation and understandings are made: 1) The shear failure happens before complete failure, and shear behaviour plays an important role during the failure process in compression-shear tests. 2) The equivalent peak stress (strength) of the compression-shear test is smaller than the uniaxial compression one. 3) The directional cracks have weak influence on the compressive stiffness, but have a strong influence on the shear behaviour.

Chapter 3

Strain-rate-dependent Tensile Response of an Alumina Ceramic: Experiments and Modelling

Published as **Jie Zheng**; Li, HY and Hogan, JD. *Strain-rate-dependent Tensile Response of an Alumina Ceramic: Experiments and Modelling*, International Journal of Impact Engineering (2023).

Author	Contributions
Jie Zheng	Conceived the ideas and experimental design of the study; Performed experiments/data collection; Data analysis and interpretation; Developed theoretical methodology; Primary author (drafted the manuscript)
Li, HY	Provided revisions to scientific content of manuscript
Hogan, JD	Provided revisions to scientific content of manuscript; Provided stylistic/grammatical revisions to manuscript; Principal investigator

3.1 Abstract

The strain-rate-dependent tensile response of a commercial alumina ceramic (CeramTec 98% alumina) is investigated by experimental and modelling methods. The experiments at different loading rates are carried out on a standard MTS machine and a modified split-Hopkinson pressure bar system with flattened Brazilian disk specimens. High-speed imaging coupled with digital image correlation (DIC) is used to measure the strain fields, and this enables us to capture the fracture process and the corresponding stress field

based on theoretical considerations. In the dynamic tests, it is verified that multiple cracks appear simultaneously around the locations of maximum tensile stress and strain. Next, a matching approach based on theoretical models (i.e., the uniform and sinusoidal load models) is proposed to synchronize the stress and strain history curves in time, and the matching results show the tensile cracks are often generated prior to the peak stress as visualized in ultra-high-speed camera images. This peak stress corresponds to the failure of the sample structure, which is different from the material tensile strength as an inherent material property. In this study, we use the term “overloading” to describe the structural failure of the material. The difference between the peak stress and material tensile strength is associated with the time it takes for the crack to propagate, interact, and span the structure during the loading process, which is termed as “time-dependent structural failure”. The strain-rate-dependent tensile strength of the alumina ceramics is computed with a correction method, and the tensile strength is defined as the tensile stress when the central crack first appears in the ultra-high-speed camera images. Then, the fracture surfaces of the alumina fragments are examined by Scanning electron microscopy to explore the fracture mechanism in the failure process. Finally, a strain-rate-dependent tensile strength model is proposed to describe the tensile strength of the CeramTec 98% alumina and other alumina ceramics in the literature.

3.2 Introduction

Advanced ceramics are attractive for use in impact protection applications as a result of their low density, high hardness, and high wear resistance [3]. In the application of armour systems, ceramic materials are used as the first layer to blunt the projectile [131]. Upon impact, the ceramic materials crack and fail because, in part, of the reflected tensile waves generated from the back-free surface of the armour [83]. Thus, the wide application of advanced ceramics requires understanding the deformation and failure mechanisms that manifest under tensile loading. The challenges associated with performing conventional direct tensile tests on advanced ceramics have led to several indirect approaches (e.g., sleeve-fracturing tests, beam bending tests, and Brazilian tests) for assessing the tensile strength of ceramics [59, 60]. Among these testing approaches, the Brazilian testing is suggested for studying the tensile strength of brittle materials for ease of manufacturing [132–135]. To reduce the stress concentration near the loading area, Wang et al. [136–139] introduced two parallel flat ends on the Brazilian disk (termed the flattened Brazilian disk) of rock materials. In the dynamic Brazilian tests, Antonn et al. [140] found that the stress distribution was similar to the quasi-static one, and more dynamic Brazilian disk tests were carried out to investigate the strain-rate-dependent effect on the tensile strength of brittle materials [141–146].

Recently, the flattened Brazilian disk and the split Hopkinson pressure bar (SHPB) are widely used in the literature to characterize the dynamic tensile strength of brittle materials [60, 139, 147–151]. In the dynamic Brazilian disk tests conducted by Mellor and Hawkes [152], the cracks appeared prior to the recorded peak load (“structural strength”), therefore, the tensile strength is likely overestimated without any correction [152]. This overestimation phenomenon is also mentioned in the Brazilian tests of concrete [153] and rock materials [154, 155]. However, little attention has been directed toward solving this problem. In the current study, experimental and theoretical methods are used to unravel the differences between the “structural strength” and the “material tensile strength” in Brazilian disk testing.

To obtain the stress and strain fields, the Brazilian disk test has also been extensively studied coupled with theoretical approaches [156, 157]. For example, Hondros [158] proposed a complete stress solution for the Brazilian disk under uniformly distributed loads, and he assumed the material was linearly elastic, homogeneous, and isotropic. Since then, several studies have investigated the exact solutions of the stress and strain fields to take anisotropy [159, 160] and nonlinear deformation characteristics [161, 162] into account. In recent studies, Markides et al. [156, 163, 164] obtained the full-field solutions for stress and strain in the Brazilian disk under different types of loading distributions (e.g., the uniform and sinusoidal load), and he found that the stress and strain fields away from the disk’s center were influenced by the different applied load. In addition to the mechanical properties, the other topic of interest in Brazilian disk testing is the problem of crack initiation and growth [155]. In some studies [162, 165], researchers hypothesized the central crack would occur first when the maximum tensile stress exceeded its tensile strength, based on the Griffith failure criterion. In other studies [155, 166], researchers thought the tensile cracks might initiate at the location where the tensile strain reached the critical extension strain. In the current study, we use insights from these theoretical studies [156, 163, 164] coupled with experimental methods to explore the fracture process of a CeramTec 98% alumina ceramic in the flattened Brazilian disk (FBD) test configuration.

Building on past works, the current study uses combined experimental and modelling methods to investigate the strain-rate-dependent tensile response of an alumina ceramic. Firstly, quasi-static and dynamic tests are carried out on a standard MTS machine and a modified split-Hopkinson pressure bar (SHPB) system. An ultra-high-speed camera coupled with digital image correlation (DIC) is used to measure the strain field. In Section 3.3.4, analytical solutions proposed by Markides et al. [156, 163, 164] are used to calculate the stress and strain of the Brazilian disk specimen along the vertical diameter based on the Saint-Venant principle [60, 137–139, 147–150]. In the dynamic FBD tests, we find the splitting fracture of the FBD may not be controlled only by the Griffith

failure criterion (the maximum tensile stress), but also by the maximum tensile strain. In Section 3.4.1, by using the proposed matching method in the current study, the “time-dependent structural failure” phenomenon is observed in the dynamic FBD tests of the alumina ceramic, thereby providing insights into the differences between “structural strength” and the “material tensile strength”. Then, the strain-rate-dependent tensile strength of the CeramTec 98% alumina is achieved with a correction method that regards the stress when the central crack first appears as the tensile strength and is compared with other alumina ceramics under different loading rates. The fracture surfaces of the alumina fragments are examined using Scanning electron microscopy (SEM) to explore the failure mechanism in Section 3.4.2. Lastly, a strain-rate-dependent tensile strength model for alumina ceramics is proposed based on the one-dimensional elastic wave theory [81, 101, 102], the Griffith failure criterion [79, 81, 155], and observations made in the current study and spall experiments [81, 167, 168]. Finally, in Section 3.4.3 and Section 3.4.4, this model is validated with the experimental results of the CeramTec 98% alumina and other alumina ceramics (i.e., A94, A98 and A99) [78–82].

3.3 Experimental and modelling methods

3.3.1 Material and specimens

In this study, a commercially available alumina ceramic ALOTEC 98 SB from CeramTec, Germany, is investigated, and it is referred to as CeramTec 98% in this paper. This ceramic has an alumina content of 98 mass percentage, a low porosity of less than 2%, high hardness of 13.5 GPa, a low density of 3.8 g/cm³, Young’s modulus of 335 GPa, and Poisson’s ratio of 0.23. These mechanical properties are provided by the manufacturer [169] and evaluated in our previous studies [11, 61]. The FBD specimen has a diameter of 8 mm and thickness of 4 mm with two parallel flat ends corresponding to the loading angle $2\omega_0 = 20^\circ$, as Figure 3.1 shows. The thickness to the diameter ratio is 0.5, which is recommended in the literature [133, 170]. The surfaces of the specimens were sprayed with speckle patterns to facilitate digital image correlation (DIC) analysis, and the methods are presented in detail later in this section.

3.3.2 The flattened Brazilian disk tests

The quasi-static FBD tests were carried out using a MTS 810 materials testing machine with a ± 100 kN load cell. The specimens were compressed under displacement control at a loading speed in the range of $\sim 10^{-4}$ to $\sim 10^{-2}$ mm/s, and the loading direction of

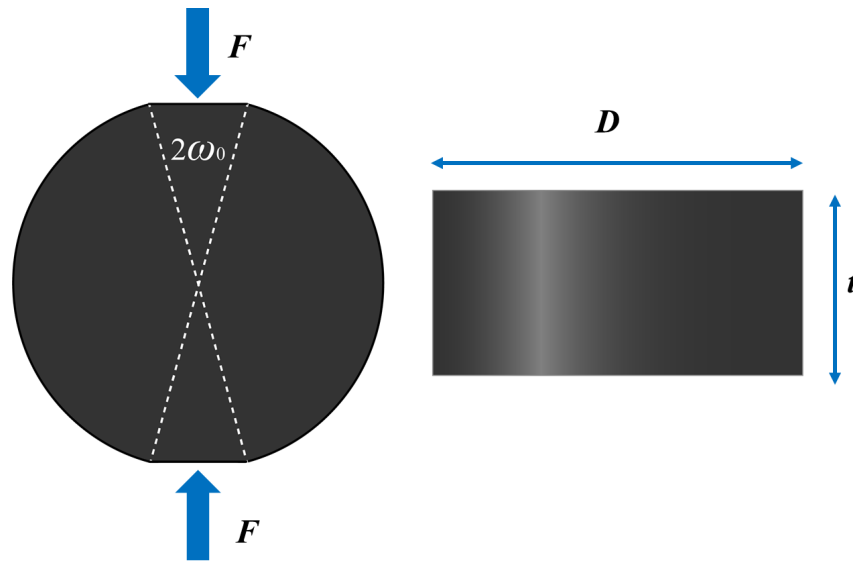


FIGURE 3.1: The schematic diagram of the FBD sample. The diameter D is 8 mm, thickness t is 4 mm, the loading angle $2\omega_0$ is 20° , and F is the applied loading in the test.

F is shown in Figure 3.1. A PROMON U750 high-speed camera with a full resolution of 1280×1024 pixel² was used to monitor the specimen surface during quasi-static testing. The acquisition rate of the camera was set between 5 and 500 frames per second (FPS), and its value is related to the loading speed. In FBD tests, shear failure might occur near the loading zone due to friction between loading platens and specimen [155, 164], as observed in many Brazilian disk tests of rocks [171]. To eliminate the frictional effects and prevent the premature edge failure (shear failure), high-pressure grease was applied between the surfaces of the loading platens and the flat ends of the specimen in both the quasi-static and dynamic FBD tests.

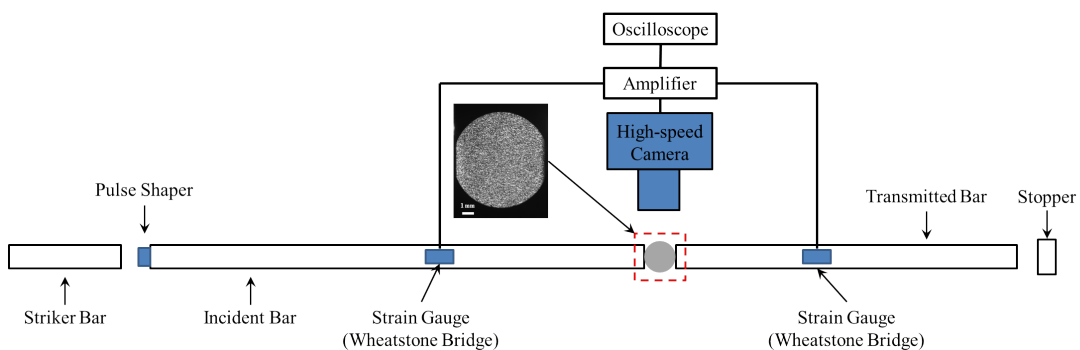


FIGURE 3.2: The split-Hopkinson pressure bar configuration for dynamic testing. This figure shows the schematics of the experimental setup and the typical camera view of an FBD sample.

Figure 3.2 shows the dynamic FBD test setup, and these were conducted using a 12.7mm diameter split-Hopkinson compression bar synchronized with an ultra-high-speed camera.

The incident and transmitted bars were made from hardened C-350 maraging steel with an elastic modulus of 200 GPa and a density of 8080 kg/m³, and they are 1016 mm and 914 mm in length, respectively. The experimental system used in this study was the same as in Koch et al. [104] and Lo et al. [6]. In addition, a long striker (304 mm in length) was chosen to provide a loading pulse recommended in literature [149, 172] to realize the dynamic force equilibrium and to maintain the equilibrium status until specimen failure. The pulse shapers (i.e., tin, high density polyethylene (HDPE), and paper) were also used in the dynamic test to control the rise time and profile of the incident pulse and achieve a constant strain rate [6, 11, 149]. In this study, the tin and HDPE pulse shapers are 1.59 mm in thickness and 3.97 mm in diameter, and the paper pulse shaper is 0.1 mm in thickness and 3.97 mm in diameter. During the dynamic tests, the images were recorded by a Shimadzu HPV X-2 ultra-high-speed camera with a SIGMA F2.8EX DG MACRO OS lens with a full resolution of 400 × 250 pixel² and a focal length of 105 mm. To monitor the specimen surface with different strain rates, the exposure time was chosen in the range of 200 to 500 ns, and the framing rate was selected in the range of 0.5 to 2 million fps.

Two strain gauges (Micro 184 Measurements CEA-13-250UN-350) on the incident and transmission bars were used to measure the incoming, reflected, and transmitted pulses. An HBM Gen3i High-Speed Recorder was employed for the data acquisition from the strain gauges at 4 MHz with a Bessel IIR pre-filter to eliminate low-frequency noise. For the theory of the SHPB system, the stress wave propagation analysis has been well documented by Song and Chen [102]. Using the strain gauge signal, the dynamic loading applied to the specimen was computed from the classical one-dimensional wave propagation theory [173, 174], as we will now explain.

In all the dynamic tests of the current study, force equilibrium was achieved. For example, Figure 3.3 shows a representative force equilibrium plot comparing the force applied to the specimen surface in contact with the incident bar F_{in} (obtained from the incident and reflected signals) and the force on the specimen surface in contact with the transmitted bar F_{out} (obtained directly from the transmitted signal). A factor R_f is used to evaluate the relative difference between F_{in} and F_{out} [60, 111, 149]:

$$R_f = 2 \left| \frac{F_{in} - F_{out}}{F_{in} + F_{out}} \right| \quad (3.1)$$

In Figure 3.3, R_f has a higher value at the beginning and then drops dramatically with an average value of $R_{f,mean} = 0.034$ starting around 18 μ s during the loading process in the dynamic FBD test. The evolution of R_f in the current study is similar to the observations in the experimental studies of Khosravani et al. [149] and Zhang et al. [60, 175]. As a result, our experimental results satisfy the criterion for force equilibrium

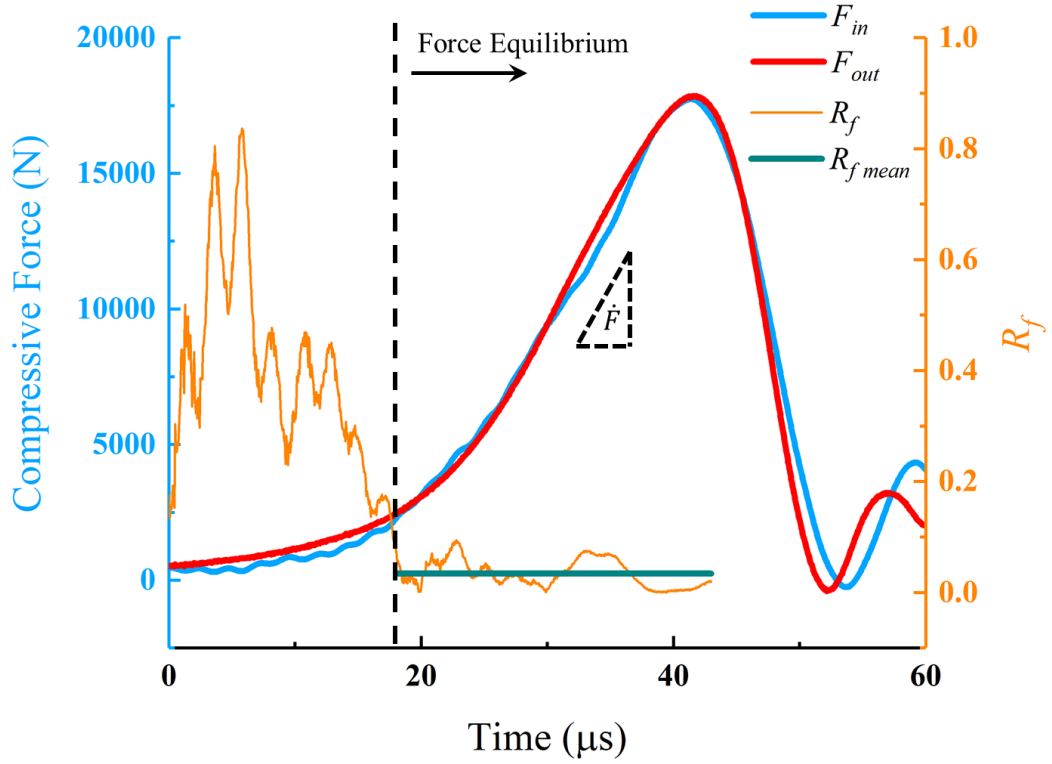


FIGURE 3.3: The check for force equilibrium in the dynamic FBD test. The F_{in} is the incident bar force obtained from the incident and reflected signals. The F_{out} is the transmitted bar force obtained from the transmitted signal. R_f is a factor related to the force equilibrium. R_{fmean} is the mean value of R_f during the loading process in the dynamic FBD test when the force equilibrium is achieved. Finally, the \dot{F} is the loading rate obtained from the slope of the loading curve.

in brittle materials (less than 5%) [60, 149, 176] during the loading process in the dynamic FBD tests. Thus, a good force equilibrium was achieved during the loading process in the dynamic FBD test at around $18 \mu\text{s}$. Due to the linear increase of the loading force, a constant loading rate $\dot{F} = 8.69 \times 10^8 \text{ N/s}$ can be determined by the slope of the force-time curve in Figure 3.3.

Finally, the engineering strain was obtained from DIC analysis. In the current study, a commercial software, VIC2D V6 (Irmo, South Carolina, USA), was used for the DIC analysis in both quasi-static and dynamic experiments. During analysis, according to the different loading rates, the area of interest was discretized into a subset size between 23×23 and $31 \times 31 \text{ pixel}^2$ and step sizes between 3 and 5 pixels to minimize the correlation error, as recommended in literature [60, 82, 131, 177]. The zero-normalized sum of squared differences (ZNSSD) criterion with the optimized eight-tap interpolation scheme was utilized in the analysis. Pre-filtering of images was done with a low-pass filter,

and subset weighting was done via a Gaussian weighting, as recommended in literature [6, 112].

3.3.3 Post-mortem fractographic analysis

The microstructure of the as-received CeramTec 98% alumina had been investigated in our previous study [11] by Scanning electron microscopy (SEM), Electron Backscatter Diffraction (EBSD), energy-dispersive x-ray spectroscopy (EDS), and X-Ray Microscopy (XRM) methods. In this study, post-mortem fracture surfaces of tested samples were studied by SEM analysis. This analysis was carried out using a Zeiss Sigma machine (Oberkochen, Baden-Württemberg, Germany). The micrographs were obtained using an In-Lens (IL) detector. The machine was operated with the electron high tension voltage at 10 kV and a working distance of ~ 5 mm.

3.3.4 Theoretical considerations

In addition to obtaining the strain field by DIC analysis, the current study uses a theoretical approach to estimate and explore the stress and strain fields during FBD testing. The stress and strain used in the current study are the nominal stress and engineering strain because the failure deformation of the alumina ceramic is small (i.e., failure strain < 0.003). There is no direct analytical solution of the stress and strain fields for the FBD geometry, but the equivalent method based on the Saint-Venant principle can give an approximate analytical solution of the stress and strain fields near the disk's center [136–138]. For example, based on the equivalent uniformly distributed load in Figure 3.4, the tensile strength, σ_t , at the center of the FBD sample is given by Wang et al. [138]:

$$\sigma_t = k \frac{2F}{\pi D t} \quad (3.2)$$

where σ_t is the tensile strength in the radial direction (xx), D and t are the diameter and thickness of the sample, and k is a non-dimensional factor depending on the loading angle whose value is 0.9644 when $2\omega_0 = 20^\circ$. In the literature, this equivalent uniformly distributed load method was used to give an approximate solution for the FBD tests in both quasi-static [136–138] and dynamic [60, 139, 147–150] conditions.

In the literature, researchers have also been interested in the stress and strain distribution along the vertical diameter (denoted as y-axis in Figure 3.4) [155, 157, 178], which is parallel to the loading direction. These stress and strain fields away from the disk's center are influenced by the exact distribution of the applied load [164, 178], which may affect tensile crack initiation [155]. To investigate the influence of the load distribution,

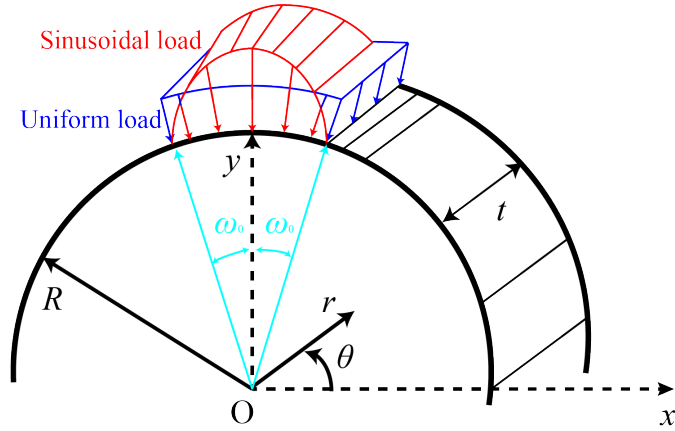


FIGURE 3.4: Schematic representation of two kinds of loading types exerted on the disk, and these equivalent methods can provide an approximate analytical solution for the FBD tests [138]. The blue load is the equivalent uniformly distributed load and the red load is the equivalent sinusoidal distributed load. The $2\omega_0$ is the loading angle, and its value is the same as that in an FBD with $2\omega_0 = 20^\circ$. R and t are the radius and thickness of the sample, respectively, and their values are the same as the FBD. (r, θ) is an arbitrary point on the sample in polar coordinates.

both uniform and non-uniform (i.e., sinusoidal) distributed loads are selected in the current study to predict the stress and strain along the vertical diameter, as Figure 3.4 shows schematically.

For the equivalent uniformly distributed load in Figure 3.4, the stress along the vertical diameter is given by Markides et al. [156]:

$$\sigma_{rr} = \frac{p}{\pi} \left[2\omega_0 + \arctan \left(\frac{R \cos \omega_0 - r \sin \theta}{R \sin \omega_0 - r \cos \theta} \right) + \arctan \left(\frac{R \cos \omega_0 + r \sin \theta}{R \sin \omega_0 + r \cos \theta} \right) + \right. \\ \left. \arctan \left(\frac{R \cos \omega_0 - r \sin \theta}{R \sin \omega_0 + r \cos \theta} \right) + \arctan \left(\frac{R \cos \omega_0 + r \sin \theta}{R \sin \omega_0 - r \cos \theta} \right) - 2\pi - \right. \\ \left. R^2(R^2 - r^2) \left(\frac{\sin 2(\theta - \omega_0)}{R^4 + 2(rR)^2 \cos 2(\theta - \omega_0) + r^4} - \frac{\sin 2(\theta + \omega_0)}{R^4 + 2(rR)^2 \cos 2(\theta + \omega_0) + r^4} \right) \right] \quad (3.3)$$

$$\begin{aligned}
\sigma_{\theta\theta} = \frac{p}{\pi} & \left[2\omega_0 + \arctan\left(\frac{R \cos \omega_0 - r \sin \theta}{R \sin \omega_0 - r \cos \theta}\right) + \arctan\left(\frac{R \cos \omega_0 + r \sin \theta}{R \sin \omega_0 + r \cos \theta}\right) + \right. \\
& \arctan\left(\frac{R \cos \omega_0 - r \sin \theta}{R \sin \omega_0 + r \cos \theta}\right) + \arctan\left(\frac{R \cos \omega_0 + r \sin \theta}{R \sin \omega_0 - r \cos \theta}\right) - 2\pi + \\
& \left. R^2(R^2 - r^2) \left(\frac{\sin 2(\theta - \omega_0)}{R^4 + 2(rR)^2 \cos 2(\theta - \omega_0) + r^4} - \frac{\sin 2(\theta + \omega_0)}{R^4 + 2(rR)^2 \cos 2(\theta + \omega_0) + r^4} \right) \right]
\end{aligned} \tag{3.4}$$

with

$$p = \frac{F}{2Rt \sin \omega_0} \tag{3.5}$$

where F is the total force applied to the specimen, $\theta = 90^\circ$, and r is in the range of 0 to 4 mm as we are interested in the values from the center to the outer edge of the disk. σ_{rr} and $\sigma_{\theta\theta}$ are two normal stress in polar coordinates, and they can be transformed into the Cartesian coordinates: $\sigma_{yy} = \sigma_{rr}$ and $\sigma_{xx} = \sigma_{\theta\theta}$ with $x = 0$ and y in the range of 0 to 4 mm. The ω_0 is the loading angle, and its value is the same as the one in FBD $2\omega_0 = 20^\circ$. R and t are the radius and thickness of the sample, respectively, which are both 4 mm.

Next, in one study of dynamic FBD tests, Wang et al. [139] found the stress distribution is non-uniform at the two flat ends of the specimen. The sinusoidal load model considered the contact and deformation between the specimen and loading device by assuming a non-uniform distribution of radial pressure [163]. Although, it is generally accepted that the different types of load distributions would not seriously influence the stress or strain field at the center of the Brazilian disk [138, 164], but this condition is not appropriate for the area far away from the center along the vertical diameter in Figure 3.4 [164]. In the current study, we investigate the influence of the loading distribution on the stress and strain field along the vertical diameter ($x = 0$ and y in the range of 0 to 4 mm for the equivalent sample in Figure 3.4). For the equivalent sinusoidal distributed load, the stress along the vertical diameter is given by Markides et al. [163]:

$$\begin{aligned}
\sigma_{rr} = \frac{c}{2\pi} & \left\{ -4\omega_0 \cos \omega_0 + \frac{(R^2 - r^2)^2}{2Rr^3} \right. \\
& \cos \theta \left(\ln \sqrt{\frac{R^2 + r^2 - 2Rr \sin(\theta - \omega_0)}{R^2 + r^2 - 2Rr \sin(\theta + \omega_0)}} - \ln \sqrt{\frac{R^2 + r^2 + 2Rr \sin(\theta - \omega_0)}{R^2 + r^2 + 2Rr \sin(\theta + \omega_0)}} \right) + \\
& \left(\frac{r^4 + 4R^2r^2 - R^4}{2Rr^3} \sin \theta - 2 \cos \omega_0 \right) (\arg(t_1 - z) - \arg(t_2 - z)) - \\
& \left(\frac{r^4 + 4R^2r^2 - R^4}{2Rr^3} \sin \theta + 2 \cos \omega_0 \right) (\arg(t_1 + z) - \arg(t_2 + z)) + \frac{R^2 - r^2}{r} \\
& \left[\left(\frac{r^2 \cos 2\theta - R^2}{2Rr} + \cos \omega_0 \sin \theta \right) \left(\frac{R \sin \omega_0 - r \cos \theta}{R^2 + r^2 - 2Rr \sin(\theta + \omega_0)} + \frac{R \sin \omega_0 + r \cos \theta}{R^2 + r^2 - 2Rr \sin(\theta - \omega_0)} \right) - \right. \\
& \left(\frac{r \sin 2\theta}{2R} - \cos \omega_0 \cos \theta \right) \left(\frac{-R \cos \omega_0 + r \sin \theta}{R^2 + r^2 - 2Rr \sin(\theta + \omega_0)} + \frac{R \cos \omega_0 - r \sin \theta}{R^2 + r^2 - 2Rr \sin(\theta - \omega_0)} \right) + \\
& \left(\frac{r^2 \cos 2\theta - R^2}{2Rr} - \cos \omega_0 \sin \theta \right) \left(\frac{R \sin \omega_0 + r \cos \theta}{R^2 + r^2 + 2Rr \sin(\theta + \omega_0)} + \frac{R \sin \omega_0 - r \cos \theta}{R^2 + r^2 + 2Rr \sin(\theta - \omega_0)} \right) - \\
& \left. \left(\frac{r \sin 2\theta}{2R} + \cos \omega_0 \cos \theta \right) \left(\frac{-R \cos \omega_0 - r \sin \theta}{R^2 + r^2 + 2Rr \sin(\theta + \omega_0)} + \frac{R \cos \omega_0 + r \sin \theta}{R^2 + r^2 + 2Rr \sin(\theta - \omega_0)} \right) \right] \left. \right\}
\end{aligned} \tag{3.6}$$

$$\begin{aligned}
\sigma_{\theta\theta} = & \frac{c}{2\pi} \left\{ -4\omega_0 \cos \omega_0 + \frac{3r^4 - 2R^2r^2 - R^4}{2Rr^3} \right. \\
& \cos \theta \left(\ln \sqrt{\frac{R^2 + r^2 - 2Rr \sin(\theta - \omega_0)}{R^2 + r^2 - 2Rr \sin(\theta + \omega_0)}} - \ln \sqrt{\frac{R^2 + r^2 + 2Rr \sin(\theta - \omega_0)}{R^2 + r^2 + 2Rr \sin(\theta + \omega_0)}} \right) + \\
& \left(\frac{3r^4 + R^4}{2Rr^3} \sin \theta - 2 \cos \omega_0 \right) (\arg(t_1 - z) - \arg(t_2 - z)) - \\
& \left(\frac{3r^4 + R^4}{2Rr^3} \sin \theta + 2 \cos \omega_0 \right) (\arg(t_1 + z) - \arg(t_2 + z)) - \frac{R^2 - r^2}{r} \\
& \left[\left(\frac{r^2 \cos 2\theta - R^2}{2Rr} + \cos \omega_0 \sin \theta \right) \left(\frac{R \sin \omega_0 - r \cos \theta}{R^2 + r^2 - 2Rr \sin(\theta + \omega_0)} + \frac{R \sin \omega_0 + r \cos \theta}{R^2 + r^2 - 2Rr \sin(\theta - \omega_0)} \right) - \right. \\
& \left(\frac{r \sin 2\theta}{2R} - \cos \omega_0 \cos \theta \right) \left(\frac{-R \cos \omega_0 + r \sin \theta}{R^2 + r^2 - 2Rr \sin(\theta + \omega_0)} + \frac{R \cos \omega_0 - r \sin \theta}{R^2 + r^2 - 2Rr \sin(\theta - \omega_0)} \right) + \\
& \left(\frac{r^2 \cos 2\theta - R^2}{2Rr} - \cos \omega_0 \sin \theta \right) \left(\frac{R \sin \omega_0 + r \cos \theta}{R^2 + r^2 + 2Rr \sin(\theta + \omega_0)} + \frac{R \sin \omega_0 - r \cos \theta}{R^2 + r^2 + 2Rr \sin(\theta - \omega_0)} \right) - \\
& \left. \left(\frac{r \sin 2\theta}{2R} + \cos \omega_0 \cos \theta \right) \left(\frac{-R \cos \omega_0 - r \sin \theta}{R^2 + r^2 + 2Rr \sin(\theta + \omega_0)} + \frac{R \cos \omega_0 + r \sin \theta}{R^2 + r^2 + 2Rr \sin(\theta - \omega_0)} \right) \right] \left. \right\} \quad (3.7)
\end{aligned}$$

with

$$\begin{aligned}
c &= \frac{F}{2Rt(\sin \omega_0 - \omega_0 \cos \omega_0)}; \\
\arg(t_1 - z) &= \arctan \left(\frac{R \cos \omega_0 - r \sin \theta}{R \sin \omega_0 - r \cos \theta} \right); \\
\arg(t_1 + z) &= \pi + \arctan \left(\frac{R \cos \omega_0 + r \sin \theta}{R \sin \omega_0 + r \cos \theta} \right); \\
\arg(t_2 - z) &= \pi - \arctan \left(\frac{R \cos \omega_0 - r \sin \theta}{R \sin \omega_0 + r \cos \theta} \right); \\
\arg(t_2 + z) &= \pi - \arctan \left(\frac{R \cos \omega_0 + r \sin \theta}{R \sin \omega_0 - r \cos \theta} \right).
\end{aligned} \quad (3.8)$$

Our study only focuses on the vertical diameter (or y-axis) in Figure 3.4, thus $\theta = 90^\circ$ (or $x=0$) and r (or y) is in the range of 0 to 4 mm. In the later part of this paper, the Cartesian coordinates are used to describe the stress and strain fields, thus $\sigma_{xx} = \sigma_{\theta\theta}$ and $\sigma_{yy} = \sigma_{rr}$ in Equations (3.3), (3.4), (3.6) and (3.7) with $y = r$ (in the range of 0 to 4 mm) and $x = 0$ (corresponding to $\theta = 90^\circ$).

Figure 3.5 shows the stress distribution along the vertical diameter (denoted as y-axis in Figure 3.4) under a total compressive force $F = 5.25$ kN using the above-mentioned

models. It should be noted that when the force equilibrium is realized in the experiment, the stress and strain distribution in the dynamic test is considered the same as the quasi-static [139, 176, 179]. Thus, based on the force equilibrium in Figure 3.3, the total compressive force $F = 5.25$ kN is selected for both quasi-static and dynamic tests. Figure 3.5 shows that the uniform and sinusoidal load models compute the same tensile stress at the disk's center ($x = 0$ and $y = 0$), but differences appear when the location is away from the center (around $x = 0$ and $y > 2.5$ mm). The maximum tensile stress σ_{xx} appears at the disk's center, and the tensile stress decreases slightly within 3 mm but drops dramatically when y is larger than 3 mm. This result is consistent with the conclusion made by Markides et al. [163] that the stress field around the center region ($x = 0$ and $y < 2.5$ mm in the current study) is insensitive to the exact loading application mode, but the critical differences appear near the loading vicinity ($x = 0$ and $y > 2.5$ mm in the current study).

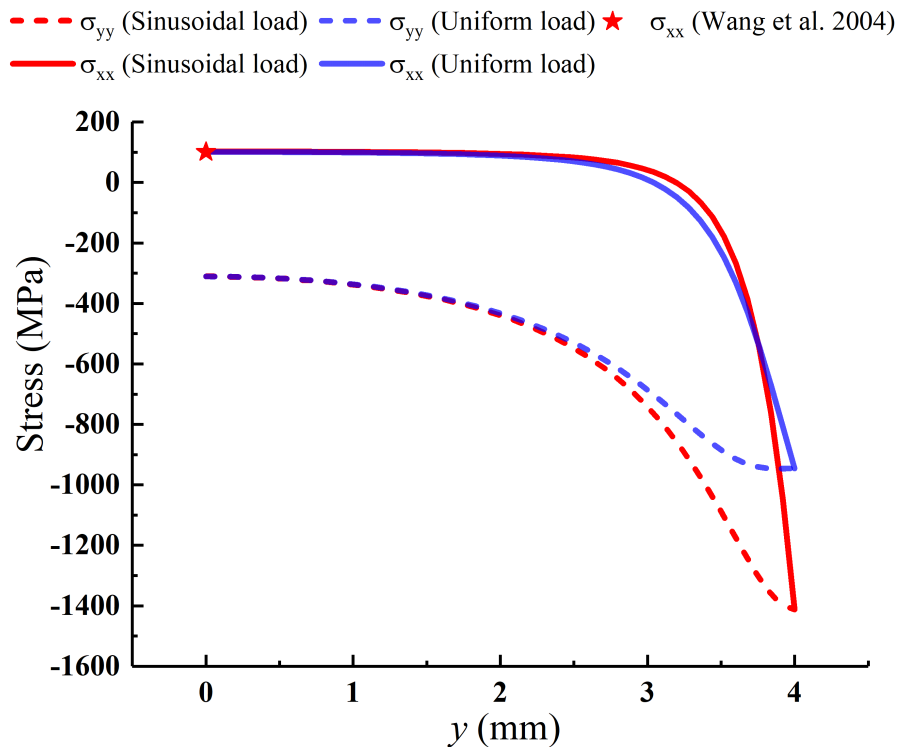


FIGURE 3.5: The stress distribution along the vertical diameter under a total compressive force of $F = 5.25$ kN obtained by different models. The σ_{yy} and σ_{xx} curves under uniform load are obtained by Equations (3.3) and (3.4) [156], and the σ_{yy} and σ_{xx} curves assuming a sinusoidal load are obtained by Equations (3.6) and (3.7) [163]. The point of σ_{xx} is obtained by Equation (3.2) [136–138].

3.3.5 The strain-rate-dependent tensile strength model

In this section, we reveal the relationship between strain rate and tensile strength for alumina ceramics based on one-dimensional elastic wave theory [81, 101, 102]. The model proposed here is also based on the post-mortem fractographic analysis made in the current study (discussed in Section 3.4.4) that failure processes of alumina is governed by the intergranular and transgranular micro-cracks, and the experimental observations of spall tests [81, 167, 168] that the failure process of alumina ceramics began with a single initial crack when encountered by the first reflected tensile pulse, although other secondary cracks appeared subsequently by the later reflected pulse. Thus, the dynamic tensile strength of alumina ceramics is dominated by the defects that generate the single primary initial crack. The experimental results presented in Gálvez et al. [79] and Díaz-Rubio et al. [81] followed the Griffith failure criterion that the specimen failed at the point where the tensile stress exceeded the material tensile strength [155]. From this and considering a square tensile incident pulse passing through a potential cracking section with defects (e.g., micro-crack), the reflected and transmitted waves would be generated due to discontinuity, according to:

$$\begin{aligned}\sigma^{in} &= -\rho \cdot c \cdot v^{in} \\ \sigma^{-} &= \rho \cdot c \cdot v^{-} \\ \sigma^{+} &= -\rho \cdot c \cdot v^{+}\end{aligned}\tag{3.9}$$

where $\sigma^{in}, v^{in}, \sigma^{-}, v^{-}, \sigma^{+}$ and v^{+} are the stresses and particle velocities of incident, reflected and transmitted waves at the interface of the potential cracking section inside the sample, respectively. An equilibrium is achieved at the two sides of the flaw prior to failure when:

$$\sigma^{+} = \sigma^{in} + \sigma^{-}\tag{3.10}$$

Also, we assume that the strength of the flaw decreases due to the opening of the flaw, and this assumption is based on the linear degradation law [68]:

$$\sigma^{+} = \sigma_{cr} \left(1 - \frac{\delta}{\delta_{cr}}\right)\tag{3.11}$$

where σ_{cr} is the critical stress leading the material to degrade. Later in the strain-rate-dependent tensile strength model (Equation (3.18)), we would find the value of σ_{cr} equals the quasi-static tensile strength, which is determined experimentally. δ_{cr} is the critical micro-crack opening displacement, and the material fails when $\delta = \delta_{cr}$. Finally, we have the relationship linking the crack opening displacements and particle velocities

at the interface of the potential cracking section inside of the sample [81, 101, 102]:

$$\dot{\delta} = v^+ - (v^{in} + v^-) \quad (3.12)$$

Combining Equations (3.9) to (3.12), we define::

$$\dot{\sigma}^+ = \frac{2\sigma_{cr}}{\rho \cdot c \cdot \delta_{cr}} (\sigma^+ - \sigma^{in}) \quad (3.13)$$

whose solution to the ordinary differential Equation (3.13) is:

$$\sigma^+ = \sigma^{in} + (\sigma_{cr} - \sigma^{in}) \cdot e^{\frac{t}{t_c}} \quad (3.14)$$

where t_c is a constant value related to the material properties:

$$t_c = \frac{\rho \cdot c \cdot \delta_{cr}}{2\sigma_{cr}} \quad (3.15)$$

From this, we determine that failure results in $\sigma^+ = 0$ and $\delta = \delta_{cr}$ at a time $t = \tau$, where τ is defined as the time to fail. Equation (3.14) becomes:

$$\sigma_0 = \sigma^{in} = \sigma_{cr} \cdot \frac{e^{\tau/t_c}}{e^{\tau/t_c} - 1} \quad (3.16)$$

where σ_0 is the tensile strength associated with failure from the initial flaw.

The time τ is the failure time of a square pulse. In this study, the loading force is a triangle pulse with a constant strain rate $\dot{\epsilon}$. The empirical transformation that converts the strain rate of a triangle pulse ($\dot{\epsilon}$) to the equivalent failure time of a square pulse (τ) is given by the linear regression method [180]:

$$\frac{\tau}{t_c} = a \cdot \dot{\epsilon}^{-0.5} \quad (3.17)$$

Here, a is a constant factor associated with the strain rate sensitivity (discussed in Section 3.4.4), and its value can be obtained by curve fitting with the experimental results.

Finally, by combining Equations (3.16) and (3.17), we define a relationship describing the strain-rate-dependent tensile strength of alumina ceramics:

$$\sigma_0 = \sigma_{cr} \cdot \frac{e^{a \cdot \dot{\epsilon}^{-0.5}}}{e^{a \cdot \dot{\epsilon}^{-0.5}} - 1} \quad (3.18)$$

As a limiting case for quasi-static conditions, $\dot{\epsilon}$ is a extremely small value and the quasi-static tensile strength is $\sigma_0 = \sigma_{cr}$ based on Equation (3.18). In Section 3.4.4,

we apply this strain-rate-dependent tensile strength model (Equation (3.18)) to the experimental results from this study and the literature [78–81].

3.4 Results and discussion

Figure 3.6 shows typical experimentally measured tensile stress and strain history curves for the disk's center in a dynamic test. The stress history curve at the disk's center is obtained from the force curve in Figure 3.3, as well as using the models proposed in Equations (3.4) and (3.7) assuming both a uniform and sinusoidal distributed load. These two models (Equations (3.4) and (3.7)) can obtain the same stress history curve at the disk's center, which is mentioned in Figure 3.5. The strain history in Figure 3.6 is obtained experimentally by DIC, where a rapid increase in strain is observed at around 70 μs . This rapid increasing turning point corresponds to the onset of a crack at the center of the disk in the dynamic FBD test (more details are discussed in Section 3.4.2). Some studies [149, 152] have noted that correlating the peak stress and the onset of the center crack (i.e., the turning point in Figure 3.6) may lead to overestimation of tensile strength. The current study proposes a new matching method to solve the overestimation problem and determine the tensile strength as the stress when the central crack first occurs.

3.4.1 The temporally- and spatially-evolving strain components

In these experiments, the loading history $F(t_1)$ is obtained from the SHPB or MTS system with the recorded time t_1 , and the DIC system can measure the strain history $\varepsilon(t_2)$ at the disk's center with a different recorded time t_2 . The matching method proposed here is to determine the delay time t_0 between the recorded time t_1 and t_2 from the two different systems. In the current study, we use the strain history of the disk's center to carry out the matching. The theoretical results of the uniform and sinusoidal loading models are the same for the disk's center; thus, we can choose either the uniform or sinusoidal loading model (Equations (3.4) and (3.7)) to calculate the predicted results at the disk's center. The method is described as follows:

1. Based on the experimental method, the loading history $F(t_1)$ is obtained from the SHPB or MTS system with the recorded time t_1 , and the DIC system can measure the strain history $\varepsilon(t_2)$ with a different recorded time t_2 ;
2. Next, the theoretical stress history curve $\sigma(t_1)$ for the disk's center can be obtained by the loading history $F(t_1)$ and assuming a uniform or sinusoidal loading model;

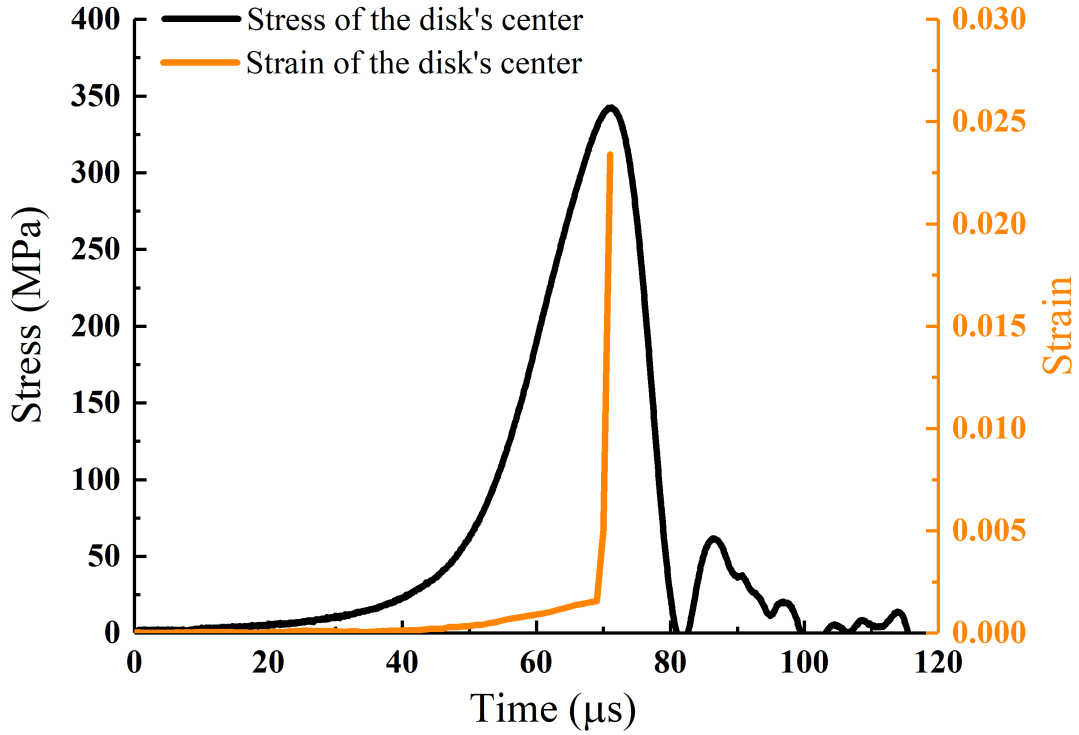


FIGURE 3.6: An example of the tensile stress (σ_{xx}) and strain (ε_{xx}) history of the disk's center ($x = 0$ and $y = 0$ mm) in a dynamic test. Here, the stress and strain curves are in different system times, the SHPB or MTS system time and the DIC system time, respectively.

3. Then, the theoretical strain history curve $\varepsilon(t_1)$ can be estimated by adopting Hooke's law generalized for isotropic linear-elastic materials;
4. Then, the theoretical results $\varepsilon(t_1)$ can be matched with the DIC strain history curve $\varepsilon(t_2)$ in time to find out the delay time t_0 .
5. Lastly, the $\varepsilon(t_1 - t_0)$, $\sigma(t_1 - t_0)$ and $F(t_1 - t_0)$ obtained from the SHPB or MTS system are matched with $\varepsilon(t_2)$ obtained from the DIC system.

Based on the matching method, Figure 3.7 compares the theoretically calculated strain components with experimental results for the disk's center during the loading period in the dynamic FBD test with a loading rate of $\dot{F} = 8.69 \times 10^8$ N/s. From Figure 3.7, it is observed that the experimental results are consistent with the theoretical predictions, with the main difference appearing around $70 \mu s$, where the DIC strain component increases (for ε_{xx}) or decreases (for ε_{yy}) rapidly prior to the peak predicted strain and stress. This is due to the fast expansion from cracking at the disk's center that occurs at around $70 \mu s$ (more details about the cracking are discussed in Section 3.4.2).

The discrepancies between the theoretical and experimental strains are relatively small before $70 \mu\text{s}$, and the material behaves linear-elastically. As an outcome of the linearly increasing part in the tensile strain curve, a constant tensile strain rate of $\dot{\varepsilon} = 91 \text{ s}^{-1}$ can be determined by the slope of the ε_{xx} history curve in Figure 3.7a. In the current study, all the tensile strain rates ($\dot{\varepsilon}$) are calculated for the disk center ($x = 0$ and $y = 0$), and their values are obtained from the slope of the ε_{xx} history curve.

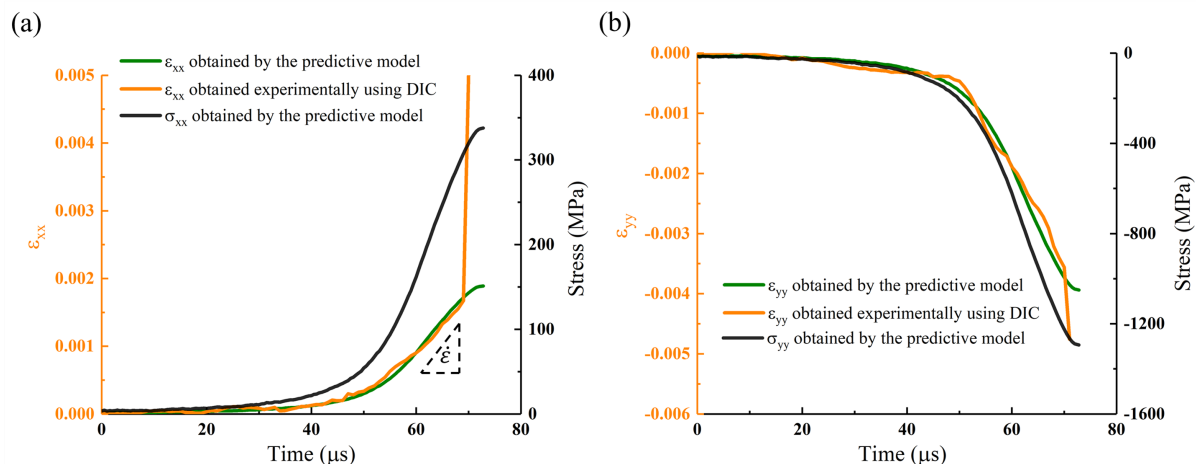


FIGURE 3.7: The DIC strain vs. predicted strain for the disk's center ($x = 0$ and $y = 0$) of the FBD sample in a dynamic test with a loading rate of $\dot{F} = 8.69 \times 10^8 \text{ N/s}$. The predicted strain is obtained by Equations (3.4) and (3.7) and Hooke's law. The DIC strain history $\varepsilon_{xx}(t_2)$ in (a) is the same as that in Figure 3.6, and here we only show some part of it for the value of $\varepsilon_{xx}(t_2)$ within 0.005. The $\dot{\varepsilon}$ is the tensile strain rate calculated from the slope of $\varepsilon_{xx}(t_1 - t_0)$ obtained by the theoretical model. The stress history curves are also shown in the figures, and the stress history $\sigma(t_1 - t_0)$ is matched with the DIC strain history $\varepsilon_{xx}(t_2)$ in time.

In addition to investigating the *temporally-evolving* strain components shown in Figure 3.7, the current study also investigates the *spatially-evolving* strain components along the vertical diameter (the y-axis with $x = 0 \text{ mm}$) under a total compressive force of $F = 5.25 \text{ kN}$, as Figure 3.8a and b show for ε_{xx} and Figure 3.8 c and d show for ε_{yy} . The force $F = 5.25 \text{ kN}$ is selected because force equilibrium is achieved under this condition, as Figure 3.3 shows. When the force equilibrium is achieved, the stress and strain distribution in the dynamic test is considered the same as in the quasi-static test [139, 176, 179].

First, Figure 3.8a shows the distribution of ε_{xx} along the vertical diameter (the y-axis with $x = 0 \text{ mm}$) under a total compressive force of $F = 5.25 \text{ kN}$, where the blue and red curves are obtained by assuming the uniform and sinusoidal loading models. For the two curves of ε_{xx} , it can be seen that the tensile strain will increase slightly along y from the center to the loading area and then drop dramatically. Specifically, the two curves of ε_{xx} are almost the same within $y = 2.5 \text{ mm}$, but the difference becomes larger when y is

greater than 2.5 mm, as the inset in Figure 3.8a shows. In addition, experimental results from quasi-static (Qs) and dynamic (Dyn) testing are plotted in Figure 3.8a, and the following number in the legend is the loading rate obtained from the slope of the loading curve (shown in Figure 3.3). Although the maximum tensile stress is located at the disk's center ($x = 0, y = 0$ mm) as Figure 3.5 shows, the maximum tensile strain occurs away from the disk's center as Figure 3.8a shows. In the uniform loading model, the maximum tensile strain appears at approximately $x = 0, y = 2.5$ mm, which is approximately 13% greater than the value at the disk's center. Similarly, in the sinusoidal loading model, the location of the maximum tensile strain is around $x = 0, y = 2.8$ mm, and its value is around 27% greater than the tensile strain at the disk's center. Averaging across all the experimental results, the maximum tensile strain is located between $y = 2$ and 3.2 mm with $x = 0$ mm, and its value is around 17% to 40% greater than the tensile strain at the disk's center. To better demonstrate the location of the maximum tensile strains, Figure 3.8b shows the full tensile strain (ε_{xx}) field of a sample under a total compressive force of $F = 5.25$ kN in the "Qs 7.55×10^2 N/s" test. It is observed that a band with large tensile strain appears along the y-axis, with the maximum tensile strain being 0.00073 at around $x = 0, y = 2.9$ mm when compared with 0.00053 at the disk center. This observation justifies the model prediction. The strain component ε_{yy} along the vertical diameter is also shown in Figure 3.8c. Similarly, the two curves of ε_{yy} obtained from the two models are almost the same within $y = 2.5$ mm, but the difference becomes larger when y is higher than 2.5 mm. According to the experimental results, ε_{yy} decreases faster than the results of the predictive models. In addition, the full strain (ε_{yy}) field of the sample in the "Qs 7.55×10^2 N/s" test is shown in Figure 3.8 d. It is observed that the maximum compressive strain is near the loading vicinity ($x = 0$ and $y > 3$ mm), which justifies the model prediction.

Overall, by comparing the predictive curves obtained by the two models with the experimental results in Figure 3.8, we find that both the uniform and sinusoidal loading models are consistent with the experimental results within $y < 2.5$ mm. However, the differences become large when $y > 2.5$ mm. The discrepancies between the theoretical and experimental results may come from: 1) the real load distribution is complicated and different from the uniform and sinusoidal load distribution [136–138]; 2) the material microstructure is not homogeneous and the defects inside the material may have significant effects on stress and strain distributions [155]. In this paper, the main purpose of comparing the results of two models and experiments is to show that the loading distribution would affect both the values and locations of the maximum tensile strain along the vertical diameter, but has almost no influence on the area near the disk's center where the maximum tensile stress exists.

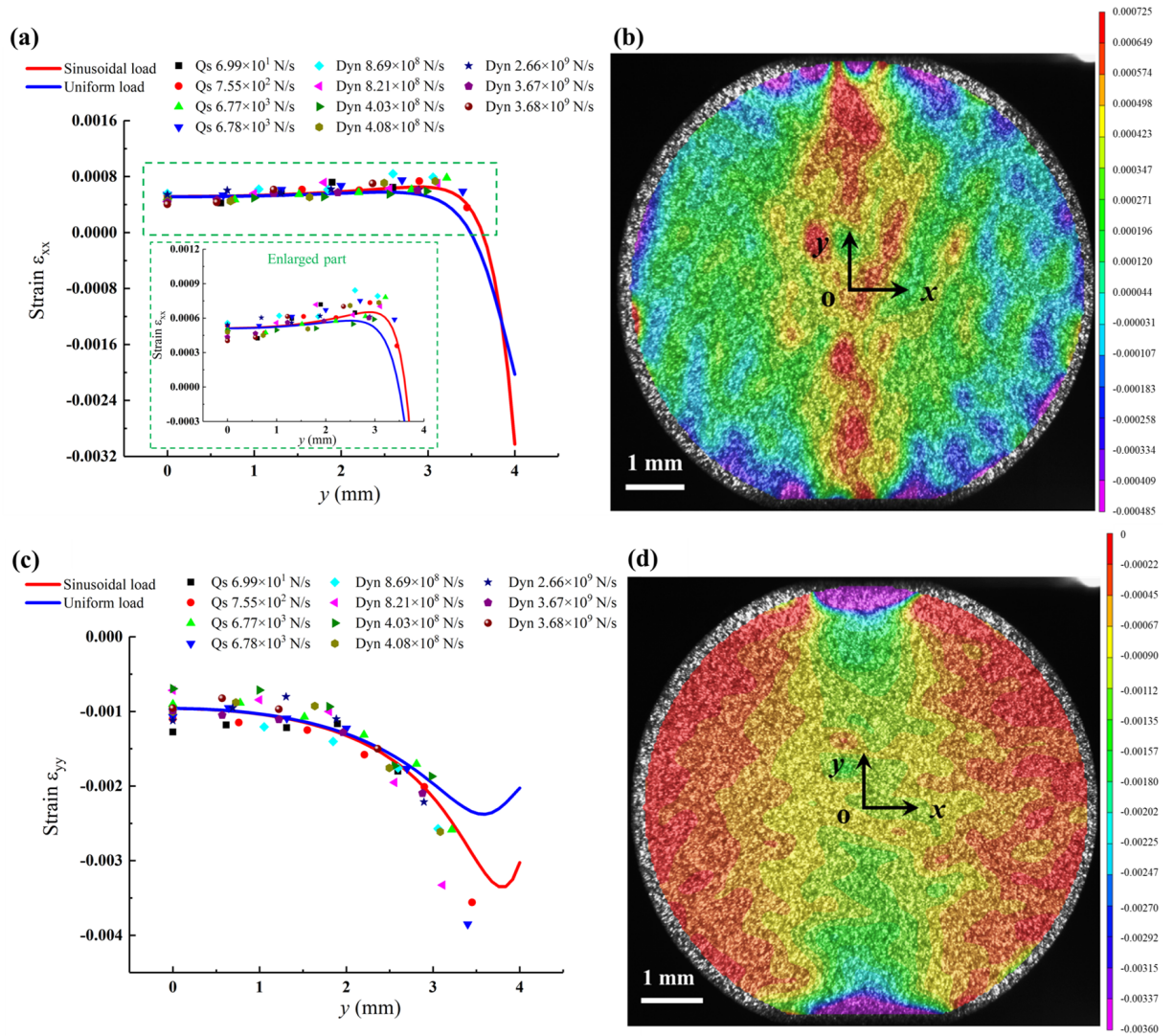


FIGURE 3.8: This figure shows ϵ_{xx} and ϵ_{yy} distributions under a total compressive force of $F = 5.25$ kN. a) The blue and red curves are the ϵ_{xx} distribution along the vertical diameter ($x = 0$ and $y = 0$ to 4 mm) obtained from the uniform (Equation (3.4)) and sinusoidal (Equation (3.7)) loading models. The points in the figure are obtained from experimental results with different loading rates. b) The ϵ_{xx} field of the sample surface obtained from the “Qs 7.55×10^2 N/s” test. c) This figure includes the ϵ_{yy} distribution along the vertical diameter ($x = 0$ and $y = 0$ to 4 mm) obtained from the uniform Equation (3.3) and sinusoidal Equation (3.6) loading models, and the points are obtained from experiments with different loading rates. d) The ϵ_{yy} field of the sample surface in the “Qs 7.55×10^2 N/s” test.

The phenomenon that the locations of maximum tensile stress and maximum tensile strain are different along the compressive diametral line has also been observed in Brazilian disk tests involving polymethylmethacrylate (PMMA) material [164] and rock materials [155, 171]. This phenomenon occurs because the material is in a local biaxial stress state along the vertical diameter, which is the main disadvantage of using BD tests to calculate the tensile strength [181]. The different locations of the maximum stress and strain and their linkages to the crack initiation location in the BD test has been a topic of

interest in the literature [155, 162, 165]. In some studies [162, 165], researchers thought the central crack would occur first when the maximum tensile stress exceeds its tensile strength based on the Griffith failure criterion. For example, in one study involving the dynamic FBD tests of rock material, Wang et al. [139] had found the location of crack initiation is the center of the FBD sample with a loading angle $2\omega_0=20^\circ$ (the same as the current study) by using strain gauges. However, in other studies [155, 166], researchers postulated that the tensile cracks might initiate at the location where the tensile strain reaches the critical extension strain. To investigate the crack initiation location of the alumina ceramic, in the current study, an ultra-high-speed camera is used to monitor the surface cracks in the dynamic FBD tests. Based on this, in the following section, we will unravel the relationship between the loading distribution, maximum tensile stress, maximum tensile strain, and crack initiation in the dynamic tests.

3.4.2 The fracture process of the FBD sample in a dynamic test

Here, we explore the fracture process of the FBD sample in the dynamic test. The reason why we do not show the fracture process of the quasi-static tests is that our quasi-static camera is not fast enough to capture the process. An appropriate speed camera could be triggered manually to capture the quasi-static fracture process, such as in Swab et al. [182]. However, we were unsuccessful in using our ultra-high-speed camera in capturing meaningful data in the quasi-static experiments. The fracture processes happen in μs [182, 183], which is extremely short compared with the loading time (e.g., seconds) in the quasi-static tests; therefore, triggering is challenging. While this is the case, we do note that the fracture processes have almost no influence on the strain and stress history in quasi-static conditions, which will be fully discussed in Section 3.4.3. Included in Figure 3.9 are time-resolved images showing the fracture process of a disk and the associated DIC contours with a loading rate of $\dot{F} = 8.69 \times 10^8 \text{ N/s}$ imaging at 1M fps. At $69 \mu\text{s}$, no crack is observed on the sample surface in Figure 3.9a and d. However, in Figure 3.9b and e, four cracks appear simultaneously at $70 \mu\text{s}$ at around $x = 0$, $y = 0 \text{ mm}$ and $x = 0$, $y = \pm 2.5 \text{ mm}$; these are pointed out by the yellow arrows in Figure 3.9e. The locations of maximum tensile stress is around $x = 0$ and $y = 0 \text{ mm}$ and maximum tensile strain is around $x = 0$ and $y = 2.5 \text{ mm}$ in the “Dyn $8.69 \times 10^8 \text{ N/s}$ ” test, shown in Figure 3.5 and Figure 3.8a. In all the dynamic tests, it is observed that multiple cracks appear simultaneously around the locations of maximum tensile stress and strain. This observation suggests that the splitting fracture of a Brazilian disk may not be controlled only by the Griffith failure criterion (the maximum tensile stress), but also by the maximum tensile strain in dynamic tests [155].

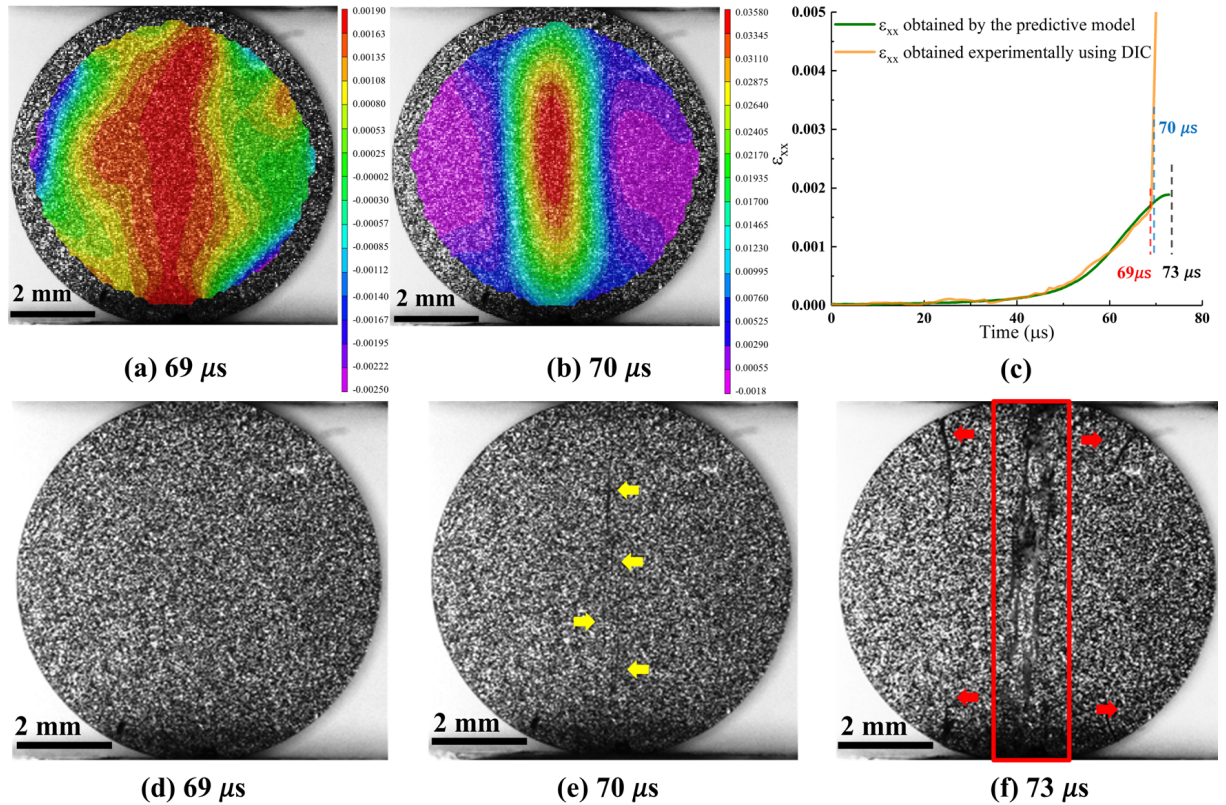


FIGURE 3.9: This figure shows the fracture process of the FBD sample in a dynamic test with a loading rate of $\dot{F} = 8.69 \times 10^8$ N/s. a) and b) are the tensile strain (ε_{xx}) field of the sample at 69 and 70 μ s, respectively; c) is the ε_{xx} history curves of the disk's center obtained by DIC and the predictive model, which are from Figure 3.7a; d), e) and f) are the fracture process of the FBD sample obtained by the ultra-high-speed camera. The yellow arrows in e) are main cracks, and the red arrows in f) are secondary cracks. The fragmentation process is found in the red rectangle zone.

Figure 3.5 previously showed that the location of the maximum tensile *stress* is at the disk's center, and its value is weakly influenced by the types of loading distribution. However, the types of loading distribution are important for determining the location and the value of the maximum tensile *strain* theoretically. For example, the value of the maximum tensile strain in the uniform loading model is smaller than that in the sinusoidal loading model, and their locations are different, as Figure 3.8a shows. Thus, the loading configurations (or the types of loading distribution) should be carefully considered in the dynamic BD tests for advanced ceramics through experimental design (e.g., specimen geometry and/or setup modification) to prevent cracks induced by the maximum tensile strain appearing early and affecting the central crack [139]. According to Figure 3.8a, applying a uniformly distributed load can better limit the maximum tensile strain. Various efforts have been made in the literature to obtain a uniformly distributed load by experimental methods. For example, Yu et al.[184] designed special spacers with a 20° arc angle to improve the contact between the specimen and spacers in order to generate a uniform stress distribution. In a separate study, Swab et al. [185]

placed a piece of grafoil between the specimen and load platens to promote a uniform stress distribution along the contact interface.

3.4.3 Unraveling structure vs. material failure

Now, we explore the difference between the tensile strength (material failure) and structural failure, especially in the dynamic tests. The current study will still use the crack at the disk's center (the location of the maximum stress) to determine the material's tensile strength of the FBD samples. This is because: 1) the crack at the disk's center based on the Griffith failure criterion is widely accepted and used to determine the tensile strength in the dynamic FBD tests for brittle materials, including advanced ceramics [60, 139, 147–150]; 2) the location of maximum stress is at the disk's center and is independent of the types of loading distribution (see Figure 3.5); and 3) the stress and strain at the disk's center is insensitive to the types of loading distribution as the results of the uniform and sinusoidal loading model are the same at the disk's center (see Figure 3.8). The theoretical results of the uniform and sinusoidal loading models are the same for the disk's center; thus, we can choose either the uniform or sinusoidal loading model (Equations (3.4) and (3.7)) to calculate the predictive results (i.e., stress and strain) at the disk's center.

In the dynamic tests, the central crack may occur before the recorded peak stress is reached. Using the peak load to calculate the tensile strength without any correction might lead to overestimating the strength [149, 176]. To avoid the overestimation problem, we define the tensile stress when the central crack first occurs to be the tensile strength of the alumina ceramics. To identify when the central crack first appears, the tensile strain evolution and fracture process are investigated. In addition to the time-resolved images showing the fracture process in the disk, Figure 3.9 also includes the temporally-evolving tensile strain of the disk's center (Figure 3.9c). Here, we observe the tensile strain (ε_{xx}) obtained by DIC analysis is consistent with the results predicted by the model at 69 μs , and no crack is observed on the sample surface as Figure 3.9d shows. However, at 70 μs in Figure 3.9c, the tensile strain (ε_{xx}) obtained by the DIC analysis increases rapidly, and the central crack occurs at 70 μs in Figure 3.9e. Thus, we take the tensile stress $\sigma_{xx} = 320.6$ MPa at 70 μs as the indirect tensile strength with the tensile strain rate of $\dot{\varepsilon} = 91$ s^{-1} for the disk's center. It is observed that the tensile strength is smaller than the peak stress, which occurs at 73 μs , as Figure 3.9c and Figure 3.7a show. According to Hooke's law, the predictive tensile strain history is obtained from the loading (or stress) history, and their peak values occur at the same time. In Figure 3.9f, it can also be observed that the cracks continue to propagate, interact and generate fragments at around 73 μs in the dynamic FBD test. In the

literature [176, 186], it has been noted that during the fracture and fragmentation process in the compression loading period, the absorbed energy contributes to the generation of new surfaces, the number and size of fragments, and the kinetic energy of moving fragments. Thus, the peak loading (or stress) at around $73 \mu\text{s}$ in Figure 3.9c is related to fracture and fragmentation processes (the structural failure), which is higher than the material tensile strength. The phenomena that the peak loading stress is higher than the material tensile strength has been referred to as the “overloading” phenomena in the literature [149]. Here, we observe that the difference between the peak loading stress and material tensile strength is associated with the time it takes for the fracture to propagate and span the structure during the loading process. In the current study, we define this fracture evolution and fragmentation process happening during the loading process as the “time-dependent structural failure” phenomenon.

Next, we explore the “overloading” phenomenon observed in the experiments with different strain rates. Figure 3.10 shows four representative examples comparing the predictive strain components with DIC results for the disk’s center. Figure 3.10a and b show that the predictive strain components are consistent with DIC results, and the failure occurs when the peak load is reached in quasi-static tests. The “overloading” phenomena is not observed in the quasi-static loading condition because the fracture and fragmentation processes happen in μs [183], and the “time-dependent structural failure” is extremely short compared with the loading time (e.g., seconds) in the quasi-static tests. Thus, in the quasi-static tests, the “time-dependent structural failure” phenomenon can be reasonably ignored, and we identify the peak stress as the tensile strength [136, 137]. In the dynamic tests, Figure 3.10c and d show that there is a rapid increase in the experimentally measured tensile strain prior to the peak stress (or peak predictive strain). The rapid increase in the experimentally measured tensile strain is associated with the “structural-dependent failure”, and this process results in the “overloading” phenomena in all the dynamic tests.

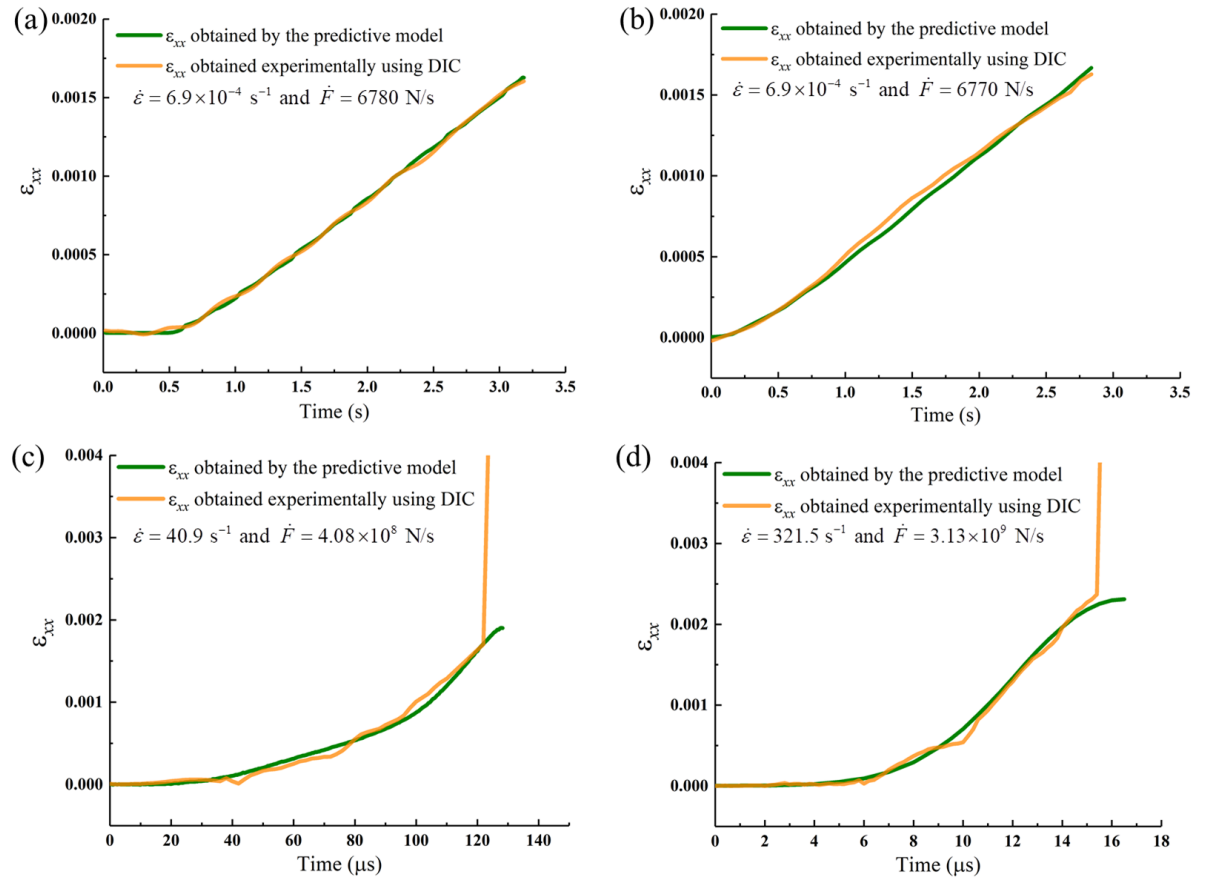


FIGURE 3.10: The DIC tensile strain history vs. predictive tensile strain history for the disk's center in the FBD test with various loading rates. The predictive tensile strain history is obtained theoretically using Equations (3.4) and (3.7) and Hooke's law. The tensile strain rates $\dot{\epsilon}$ and loading rates \dot{F} are listed in the legend. In this figure, a) and b) are quasi-static experimental results, and c) and d) are dynamic experimental results.

The disadvantage of this time-matching method to determine the material tensile strength is related to the challenge of determining the delay time between the measured tensile strength and the peak stress. It means this method requires sophisticated data acquisition and ultra-high-speed camera systems. In addition, this method requires the first-appearing crack to be at the disk center, which means more tests should be performed to satisfy this requirement.

3.4.4 Strain-rate-dependent tensile strength and post-mortem fractographic analysis

For each strain rate, we run at least three tests, and the variability on experimental results (e.g., the strain rate and tensile strength) is now summarized in Table 3.1. The experiments include quasi-static and dynamic tests with different pulse shapers (i.e., tin,

HDPE and paper) for achieving various strain rates. In Table 3.1, the strain rate is calculated from the slope of the tensile strain-time history at the disk's center (shown in Figure 3.7); the loading rate is obtained from the slope of the loading curve (shown in Figure 3.3); the peak stress at the disk's center is calculated by Equations (3.4) and (3.7) which obtain the same results for the disk's center; the material tensile stress is determined by the tensile stress when the central crack first occurs, and its corresponding tensile strain is listed as the "tensile strain when the central crack first appears". In all the quasi-static tests, the peak stress is the same as the material tensile strength without observing the "overloading" phenomenon. However, the "overloading" phenomenon is observed in all dynamic testing leading to tensile strength lower than the peak stress.

TABLE 3.1: The experimental results of the FBD tests under different loading rates

	Strain rate (s^{-1})	Loading rate (N/s)	Peak stress (MPa)	Material tensile strength (MPa)	Tensile strain when the central crack first appears
Quasi-static tests	7×10^{-6}	69.9	292.1	292.1	0.00157
	7.8×10^{-5}	755	324.9	324.9	0.00185
	7.8×10^{-5}	754	277.5	277.5	0.00153
	7.5×10^{-5}	738	271.4	271.4	0.00151
	6.9×10^{-4}	6780	321.7	321.7	0.00163
	6.9×10^{-4}	6770	329.8	329.8	0.00171
Dynamic tests (pulse shaper: tin)	40.9	4.08×10^8	340.2	324.5	0.00176
	42.1	4.03×10^8	332.4	321.2	0.00182
	40.7	4.02×10^8	333.3	316.1	0.00171
Dynamic tests (pulse shaper: HDPE)	91.4	8.69×10^8	337.8	320.6	0.00179
	71	6.72×10^8	357.2	334.1	0.00186
	85.4	8.21×10^8	335.1	316.7	0.00169
Dynamic tests (pulse shaper: paper)	321.5	3.13×10^9	413.1	399.1	0.00241
	321.7	3.08×10^9	383.7	371.3	0.00192
	385.5	3.67×10^9	413.4	400.2	0.00252
	387	3.68×10^9	395.7	383.7	0.00194

Next, post-mortem fractographic analysis is used to investigate the microstructural fracture mechanisms of the CeramTec 98% alumina under quasi-static and dynamic indirect tension loading. Figure 3.11a and b show the fracture surfaces taken from quasi-static tests. The rough fracture surface consists of sharp edges, indicating intergranular cracking is the dominant failure mechanism. Intergranular-type fracture has been commonly observed in alumina materials because of the relatively weak interfacial strength [107, 187]. In addition, pores resulting from the impurity phase (e.g., oxide contaminants of Mg, Si and Ca [11]) pullout and cleavages are observed on large flat grain surfaces. For the CeramTec 98% alumina under dynamic loading in Figure 3.11c and d, the intergranular fractures result in the uneven fracture surface, but more transgranular micro-cracks span across the grains. Besides cleavages and pores, micro-crack branching can be observed in Figure 3.11d. Overall, the fracture

mode transitions from mainly intergranular fracture under quasi-static loading to both intergranular and transgranular fracture under dynamic loading in indirect tension experiments.

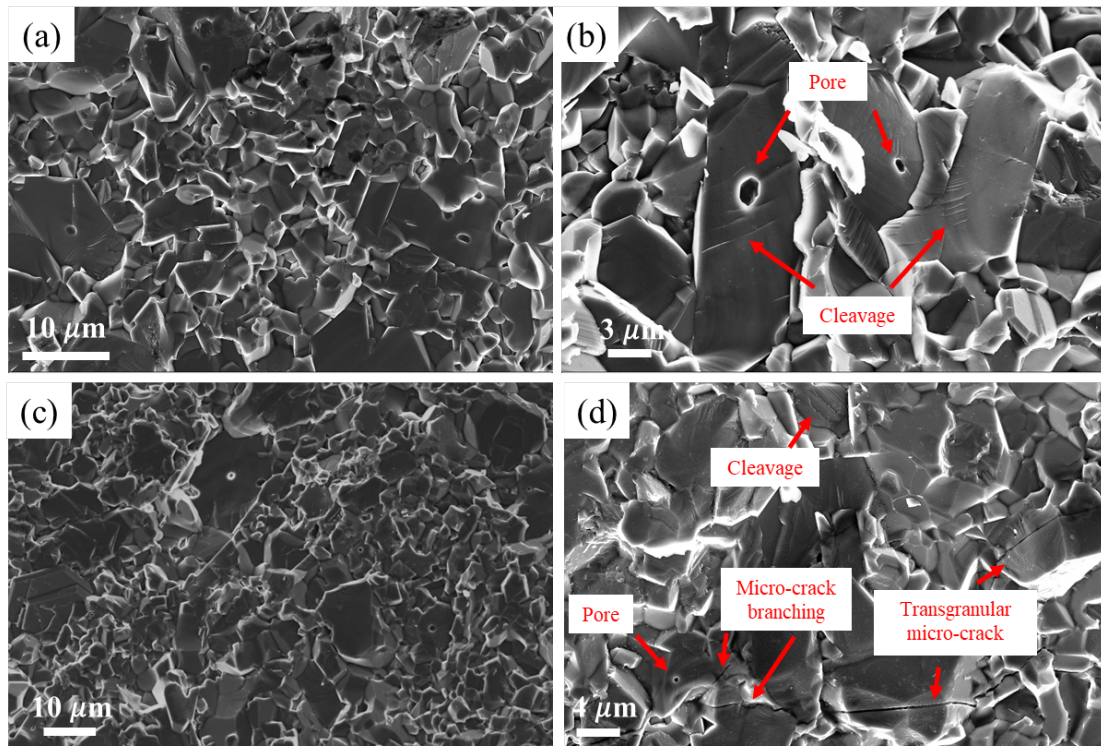


FIGURE 3.11: SEM images of the fracture surface of the CeramTec 98% alumina by the indirect tension tests. a) and b) are quasi-static experimental results, where the fracture surface is rough and full of sharp edges, indicating intergranular cracking is the dominant failure mechanism. c) and d) are dynamic experimental results, and the failure process is governed by a mixed-mode of intergranular and transgranular fracture. Pores and cleavages are observed in both quasi-static and dynamic tests.

Figure 3.12 shows the strain-rate-dependent tensile strength of various alumina ceramics, and the legend lists the testing types, the material names, and the corresponding literature citation. The red points in Figure 3.12 are the tensile strength of the CeramTec 98% alumina considered in this study under strain rates between 10^{-6} and 400 s^{-1} . It is found that the tensile strength variability is large in the quasi-static tests, and the level of scattering tends to decrease with higher loading rates for the CeramTec 98% alumina. This is because, in quasi-static conditions, the brittle material follows the weakest link hypothesis, and the mechanical properties of the local weakest sites of different samples (e.g., the relatively weak interfacial strength in Figure 3.11b) are more variable [107, 187, 188]. But in dynamic conditions with higher loading rates, more micro-cracks are nucleated (shown in Figure 3.11d), which results in a smaller scattering effect [107, 188, 189]. Figure 3.12 also shows the tensile strength of other alumina ceramics under different strain rates [78–82]. Note that most tensile strength values

are known, while some are given with the average values and error bars depending on how they were presented in their original publication. The additional alumina ceramics from the literature [78–81] are manufactured by Morgan Matroc with different purities of 94% (A94), 98% (A98), and 99.5% (A99). From Figure 3.12, it is observed that the CeramTec 98% alumina has greater tensile strength than other alumina ceramics across all strain rates, especially in the quasi-static tests.

Then, we apply the strain-rate-dependent tensile strength model (Equation (3.18)) proposed in the current study to the experimental results of the CeramTec 98% alumina and other alumina ceramics [78–81]. Note that this model is based on the one-dimensional elastic wave theory, and thus, this model is only applicable for the uniaxial tension condition. Although the tensile strength obtained from the FBD or BD experiments in our study are evaluated in a state of biaxial stress, and it is widely accepted that the FBD or BD experimental results can be used as the uniaxial (one-dimensional) tensile strength [78, 79, 81]. In the current study, we also calculate the tensile strength with a correction method to determine the tensile strength as the stress when the central crack first occurs. This tensile strength does not include the fracture propagation and interaction process (“time-dependent structural failure”), which satisfies the “single crack initiation” criteria in the proposed model. The black dash curve in Figure 3.12 is the strain-rate-dependent tensile strength model for the CeramTec 98% alumina with $\sigma_{cr} = 314$ MPa and $a = 31$ in Equation (3.18). The black full curve in Figure 3.12 is the model for the A94, A98 and A99 with $\sigma_{cr} = 181$ MPa and $a = 15$ in Equation (3.18). It is observed that the tensile strength at lower strain rates remains nearly constant, and its value equals to σ_{cr} . When the strain rate is higher than a static-dynamic transition strain rate [190], the tensile strength will increase rapidly, as has also been observed in other models [191, 192]. The transition strain rates of the different alumina ceramics are discussed later in this section.

Next, it is observed that there are some differences between the proposed model for A94, A98 and A99 and the values measured at high strain rates in Figure 3.12. First, this is because the model is fitted to all three types of alumina ceramics, with each ceramic having a different microstructure, purity, and expected material properties based on these differences [23, 191]. Second, their strengths are determined by two kinds of experiments (i.e., dynamic Brazilian disk tests at a strain rate of around 40 s^{-1} and spall tests at a strain rate of around 1000 s^{-1}). In the dynamic Brazilian disk tests, the “overloading” phenomenon may lead to an overestimation of the tensile strength at around 40 s^{-1} , which explains that the experimental data is higher than our model. For the spall tests at around 1000 s^{-1} , the elastic wave dispersion in cylindrical rods (e.g., material dispersion and geometrical dispersion) may cause the decrease of the peak pulse observed in a typical spall test of a ceramic material [193]. Furthermore, microstructural effects [81] will also manifest differently between the Brazilian disk and spall tests given they are

performed under different stress states. The data denoted by the red dashed rectangle in Figure 3.12 lie outside of the model prediction because their strengths are lower than those of the same material at a lower strain rate. These data are still included in the Figure 3.12 for completeness. Overall, the proposed model is mostly consistent with experimental results from the current study and the literature [78–82].

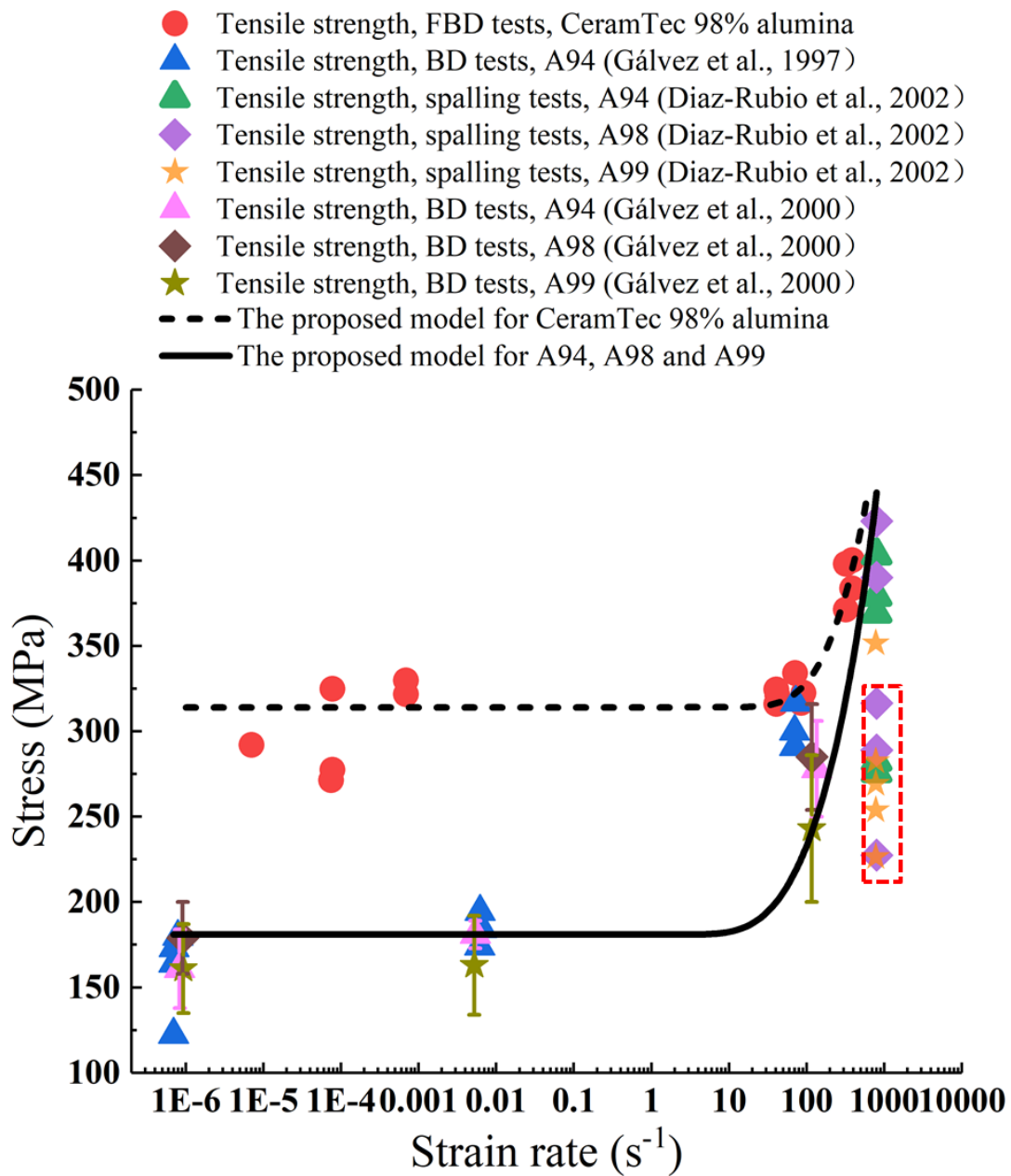


FIGURE 3.12: Strain-rate-dependent tensile strength of various alumina ceramics. The red points are the material tensile strength of the CeramTec 98% alumina studied here. The other colored points are the tensile strength of different alumina obtained from literature [78–82]. The legend includes the testing types, the material names, and the corresponding literature citation. The black dash curve in the figure is the strain-rate-dependent tensile strength model for the CeramTec 98% alumina with $\sigma_{cr} = 314$ MPa and $a = 31$ in Equation (3.18). The black full curve in the figure is the model for the A94, A98 and A99 with $\sigma_{cr} = 181$ MPa and $a = 15$ in Equation (3.18). A red dash rectangle is used to denote some data because their strengths are lower than those of the same material at a lower strain rate. These data lie outside the model prediction but are still included in the figure for completeness.

To describe the strain-rate-dependent tensile behavior of alumina ceramics in a general form, the tensile strength σ_0 in Equation (3.18) is normalized by the characteristic stress

σ_{cr} and the applied strain rate $\dot{\epsilon}$ by the characteristic factor a^2 :

$$\sigma_0^* = \frac{e^{\dot{\epsilon}_*^{-0.5}}}{e^{\dot{\epsilon}_*^{-0.5}} - 1} \quad (3.19)$$

with

$$\sigma_0^* = \frac{\sigma_0}{\sigma_{cr}}, \dot{\epsilon}_* = \frac{\dot{\epsilon}}{a^2} \quad (3.20)$$

Figure 3.13 describes the strain-rate-dependent tensile behavior of all alumina ceramics in the normalized form. The black curve in Figure 3.13 is the normalized strain-rate-dependent tensile strength model for alumina ceramics obtained by Equation (3.19). The colored points are the normalized tensile strength of various alumina ceramics with different normalized strain rates obtained from experiments [78–82]. Broadly, it is observed that the normalized tensile strength of alumina ceramics would remain nearly constant below a transition strain rate (around $\dot{\epsilon} = 0.04a^2$), while a rapid increase in strength develops as the strain rate increases above the transition strain rate. The transition strain rate for the CeramTec 98% alumina is around 39 s^{-1} , and is around 9 s^{-1} for the A94, A98, and A99 alumina. According to Equation (3.20) and Figure 3.13, the alumina becomes more rate sensitive when the transition strain rate ($0.04a^2$) is smaller. Thus, a is the factor associated with the strain rate sensitivity of the materials, and the CeramTec 98% alumina shows less rate sensitivity than the other alumina ceramics (i.e., A94, A98 and A99). Overall, this model can describe the strain-rate-dependent tensile behavior of alumina ceramics in a general form, and this has implications if one wanted to implement such strain-rate-dependent tensile model into higher scale constitutive models (e.g., Johnson–Holmquist–Beissel model [26]).

Finally, the limitations of this strain-rate-dependent tensile strength model are that the model is only applicable for the uniaxial tension condition, and the tensile failure should satisfy the “single crack initiation” criteria. In addition, this model does not consider temperature effects and cannot be applied to higher strain rate experiments (e.g., laser shock tests).

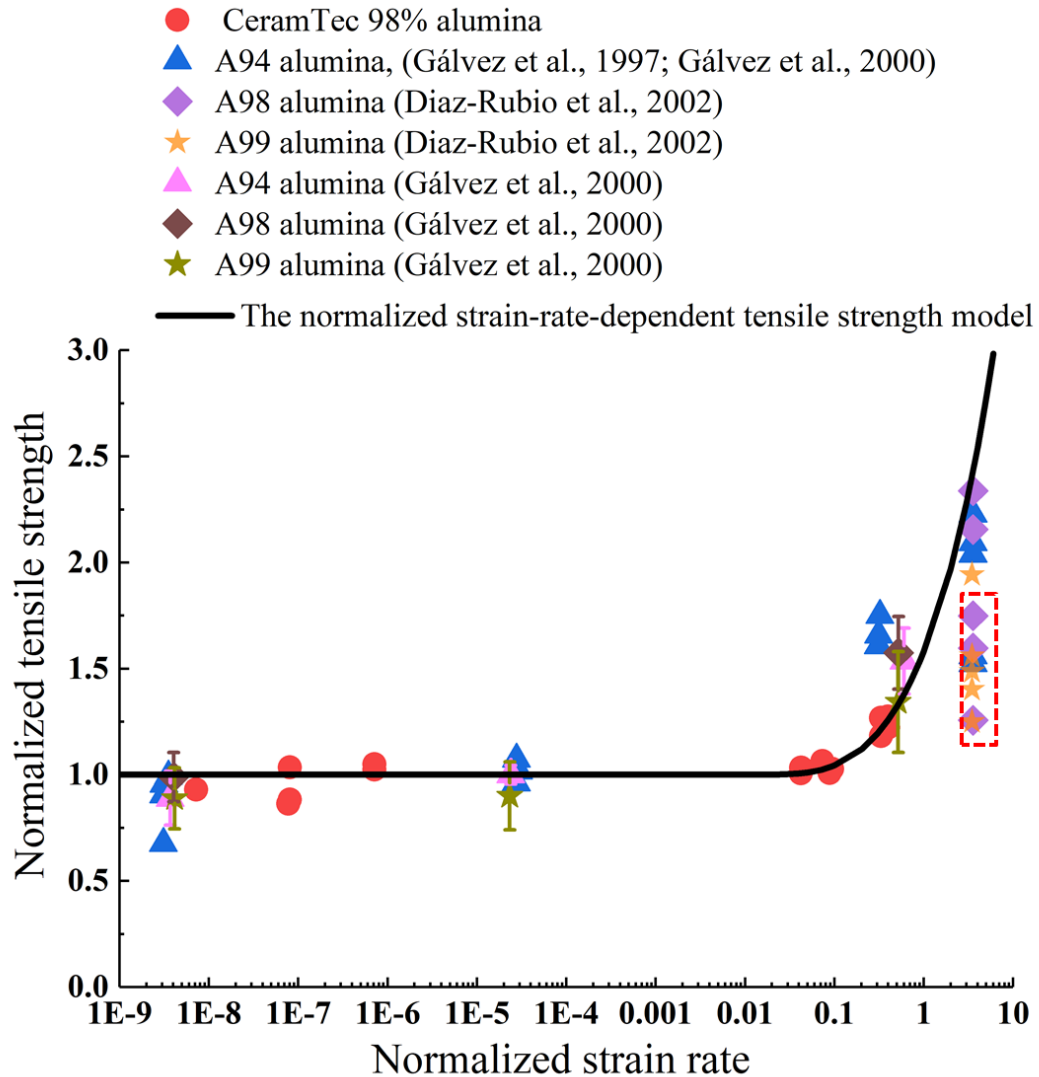


FIGURE 3.13: The relationship between the normalized tensile strength and normalized strain rates of various alumina ceramics. The black curve is the normalized strain-rate-dependent tensile strength model obtained by Equation (3.19). The red points are the normalized tensile strength of the CeramTec 98% alumina. The other colored points are the normalized tensile strength of different alumina obtained from literature [78–82]. The experimental data is normalized by Equation (3.20). A red dash rectangle is used to denote some data because their strengths are lower than those of the same material at a lower strain rate. These data lie outside the model prediction but are still included in the figure for completeness.

3.5 Conclusion

In this study, experimental and modelling methods are used to investigate the strain-rate-dependent tensile response of an alumina ceramic. Several key outcomes are obtained:

1. The locations of maximum tensile stress and maximum tensile strain are different along the compressive diametral line, and the loading distribution affects both the value and location of the maximum tensile strain along the vertical diameter, but has little influence on the area near the disk's center where the maximum tensile stress occurs;
2. In the dynamic tests, multiple cracks appear simultaneously around the locations of maximum tensile stress and strain, and this observation means that the splitting fracture of a Brazilian disk may not be controlled only by the Griffith failure criterion (the maximum tensile stress), but also by the maximum tensile strain;
3. In the dynamic tests, cracks appear prior to the recorded peak load, and the peak stress corresponding to the failure of the sample structure is different from the tensile strength of the material, which is referred to as the "overloading" phenomenon;
4. The difference between the peak stress and material tensile strength is associated with the time it takes for the crack to propagate, interact, and span the structure during the loading process, which is referred to as "time-dependent structural failure";
5. The strain-rate-dependent tensile strength of the alumina ceramics is achieved with a correction method, which is determined by the tensile stress when the central crack first occurs;
6. The fracture mode transitions from mainly intergranular fracture under quasi-static loading conditions to both intergranular and transgranular fracture under dynamic loading in indirect tension experiments.
7. A strain-rate-dependent tensile strength model for alumina ceramics is proposed based on one-dimensional elastic wave theory, the Griffith failure criterion, and experimental observations. This model is consistent with the experimental results of the CeramTec 98% and other alumina ceramics (i.e., A94, A98 and A99).

Chapter 4

Hybrid Finite-discrete Element Modeling of the Mode I Tensile Response of an Alumina Ceramic

Published as **Jie Zheng**; Li, HY and Hogan, JD. *Hybrid Finite-Discrete Element Modeling of the Mode I Tensile Response of an Alumina Ceramic*, Modelling (2023).

Author	Contribution
Jie Zheng	Conceived the ideas and experimental design of the study; Performed experiments/data collection; Data analysis and interpretation; Developed theoretical methodology; Primary author (drafted the manuscript)
Li, HY	Provided revisions to scientific content of manuscript
Hogan, JD	Provided revisions to scientific content of manuscript; Provided stylistic/grammatical revisions to manuscript; Principal investigator

4.1 Abstract

We have developed a three-dimensional hybrid finite-discrete element model to investigate the mode I tensile opening failure of the alumina ceramic. This model implicitly considers the flaw system in the material and explicitly shows the macroscopic failure patterns. A single main crack perpendicular to the loading direction is observed during the tensile loading simulation. Some fragments appear near the crack surfaces due to the branching behaviour of the cracks. The tensile strength obtained by our model is consistent with the experimental results from the literature. Once validated with

litterateur, the influences of the distribution of the flaw system on the tensile strength and elastic modulus are explored. The simulation results show that the material with more uniform flaw sizes and fewer big flaws has stronger tensile strength and higher elastic modulus.

4.2 Introduction

Advanced ceramics are often used as structural components in shielding applications [194–197] because of their desirable properties, such as low density [83], high hardness [3], and high wear resistance [4]. In ballistic applications, the role of the ceramic upon impact is to blunt the projectile [58, 198, 199] and to distribute the load [198]. During impact, pre-existing micro-cracks or pores in ceramics serve as stress concentration sites [34], which significantly affect fracture behaviour [5, 23, 200, 201]. The relationships between microstructure and failure processes have been widely investigated [5, 13–15, 202, 203]. For example, Munro [202] and Nohut [203] found that the strength of alumina ceramics is limited by the distribution of flaws in the material, and the Weibull analysis could be used to characterize both the strength and the flaw system. Recently, Lo et al. [5] studied the microstructural and mechanical variability of AD85 alumina, and they found the flaw characterization (e.g. pore size, spatial distribution, orientation, and morphology) significantly influences the mechanical response of the alumina ceramic. In a separate study, Hogan et al. [13–15] identified the relationship between microstructure and fragment size by observing impact and compression experiments of ceramics. To better understand the failure mechanisms of advanced ceramics, controlled experiments such as uniaxial compression, beam bending tests, and Brazilian disk experiments are often coupled with advanced high-speed imaging [6, 59, 60, 86, 204–208]. In these experiments, the mode I tensile opening cracks are widely accepted as an important failure mode of advanced ceramics [35–39]. However, direct tension tests is a challenge for advanced ceramics because of their brittleness. In the current study, the mode I tensile behaviour of an alumina ceramic is investigated. The widespread use of high-purity alumina (Al_2O_3) as body armor material is due to its beneficial combination of favorable ballistic properties, affordability, and well-established manufacturing processes [209]. A significant number of studies have been conducted with the objective of enhancing the performance of alumina ceramics [209–212]. These ceramics are usually produced through various sintering techniques such as flash sintering (FS) [212], hot-pressing sintering (HPS) [210], and spark plasma sintering (SPS) [209]. The trend of 3D printing ceramics is gradually becoming more prevalent, offering multiple methods for production [209]. Some of the most common methods include stereo lithography, which involves curing photo-curable binder loaded ceramic pastes, and selective laser sintering,

involving laser sintering of green powder beds [209]. Other techniques such as modified inkjet printing and binder jetting are also utilized in ceramic material production [211]. These different manufacturing methods would affect alumina ceramic's microstructure (e.g., flaw system). However, these experimental studies are limited by manufacturing technologies and testing methods for the direct tension performance of ceramics. For example, many factors (e.g., additives [212], debinding step [210] and temperature [209]) can affect the internal flaws and mechanical performance of ceramics in sintering manufacturing, which is complex [211]. In addition, exploring the influence of flaw systems on direct tensile performance is expensive and challenging [211, 213]. To overcome these challenges, in the current study, the inherent microstructural flaws based on experimental studies [202, 203, 214] are applied to the numerical modelling method to explore the mode I tensile behaviour of an alumina ceramic.

Numerous numerical models have been established to describe the failure behaviour of brittle materials. These include the continuum damage mechanics (CDM) [44, 45], the extended Finite Element Method (XFEM) [65], virtual crack closure technique (VCCT) [215–217], and the cohesive zone method (CZM) [66]. The CDM method utilizes damage parameters to explain the failure process but cannot capture crack-induced discontinuities [31]. VCCT, on the other hand, can simulate pre-defined crack propagation by imposing constraints on the nodes at crack edges but requires re-meshing [215–217]. XFEM avoids mesh refinement and reconstruction by modifying the displacement approximation function in conventional FEM with an enrichment function term [65]. While these methods can model progressive cracking behaviour, they necessitate additional limitations, such as external criteria for discontinuous displacement enrichment [65], re-meshing requirements [215–217], and complex model pre-definitions [215–217]. Additionally, these methods cannot effectively address complex cracking problems, including crack intersection, coalescence, and branching. The CZM has several advantages over the other methods, including 1) creating new surfaces to generate cracks, 2) allowing for branched and intersecting cracks, and 3) eliminating the singularity present in linear elastic fracture mechanics [67]. In the literature [68, 69], the CZM framework has been applied to study the strength of advanced ceramics, dynamic fracture events [71], and fragmentation of brittle materials [70]. In the CZM method, new surfaces are created when the fracture occurs, and these new faces require numerical contact algorithms, which makes CZM ideally suited for discretized methods [72]. To address the mutually interacting separate fragments in fracture processes, Munjiza [31] developed an innovative numerical approach called the hybrid finite-discrete element method (HFDEM). One distinct feature of the HFDEM is that it is able to capture the transition from a continuum (e.g. finite element method) to a discontinuous-based method (e.g. discrete element method) [32, 33] to overcome the inability of these

methods to capture progressive damage and failure processes in brittle materials (e.g., geomaterials [73–75] and ceramics [33]). In HFDEM, materials are often discretized as triangle elements (two-dimensional) or tetrahedral elements (three-dimensional), and cohesive elements are utilized to connect these discrete elements to represent the potential arbitrary crack path [55]. In addition, the use of tetrahedral elements offers the advantage of generating more potential fracture surfaces when compared with hexahedron elements, which make the results using tetrahedral element more reliable [30, 31, 55, 126, 218]. Then, an explicit finite difference time integration scheme is applied to solve the motion of the discretized system [31]. Recently, HFDEM has been used in modelling brittle materials under different loading conditions, as it can explicitly describe the process of fracture nucleation and growth, as well as the interaction of newly-created discrete fragments [55, 72, 76]. In the current study, the HFDEM is applied to investigate the failure process of the alumina ceramic.

Motivated by these previous studies, this paper aims to develop a three-dimensional HFDEM model to investigate the mode I tensile opening failure of the alumina ceramic. This method is focused on the macroscopic failure process accounting for the flaw system with an implicit method. The material is assumed to have Weibull distributed initial flaws, making its failure mode stochastic. The failure of the specimen is simulated through the nucleation and propagation of these cracks generated by flaws. Limited experimental results are available for the direct tension problems, owing to the challenges posed by testing, such as specimen gripping and alignment [219]. The indirect tensile strength from our previous study is used [208], and the simulation results show reasonable agreement with the experimental results. The influence of flaw system on the tensile strength is also investigated. Overall, the current study provides new insight into the mode I tensile fracture behaviour of alumina ceramic.

4.3 Computational approach

In this section, a three-dimensional hybrid finite-discrete element method (HFDEM) is established to describe the failure process of brittle materials, and then applied to the alumina ceramic. First, we develop the main features of the cohesive law to represent the mode I tensile response of brittle materials. Second, the distribution of the flaw system [202, 203, 214] is considered in this model. Finally, the model is implemented with a FORTRAN vectorized user-material (VUMAT) subroutine in ABAQUS/Explicit to solve the model numerically.

4.3.1 The cohesive law

An extensive account of the HFDEM theories and their finite element implementation can be found in [31–33, 73–75, 220]. In this section, we summarize the main features of the cohesive law used in the current study:

$$\boldsymbol{\sigma} = (1 - D)\mathbf{K}\boldsymbol{\delta} \quad (4.1)$$

with

$$\boldsymbol{\sigma} = \begin{bmatrix} \sigma_1 \\ \tau_1 \\ \tau_2 \end{bmatrix}, \quad \mathbf{K} = \begin{bmatrix} K_1 & 0 & 0 \\ 0 & K_2 & 0 \\ 0 & 0 & K_3 \end{bmatrix}, \quad \boldsymbol{\delta} = \begin{bmatrix} \delta_1 \\ \delta_2 \\ \delta_3 \end{bmatrix}$$

where $\boldsymbol{\sigma}$ represents the interface stress, σ_1 is the normal stress, and τ_1 and τ_2 are the shear stresses in the other two directions. D is a scalar damage parameter of the REA, where $D = 0$ is the intact state, and $D = 1$ represents a fully damaged state. \mathbf{K} is the penalty stiffness of the interface where subscript 1 represents the normal direction, and subscripts 2 and 3 represent the two shear directions. $\boldsymbol{\delta}$ represents relative displacements.

Linear irreversible cohesive law is widely used for the decaying response of brittle materials, such as rocks [55, 72, 76] and ceramics [69, 220–222]. For a damage value in the range of $0 \sim 1$, the damage evolution can be expressed as:

$$D = \max\left\{0, \min\left\{1 - \left(\frac{\delta_c - \delta_e}{\delta_c - \delta_m^0}\right), 1\right\}\right\} \quad (4.2)$$

where δ_e is the effective relative displacement ($\delta_e = \sqrt{\delta_1^2 + \delta_2^2 + \delta_3^2}$), and δ_c represents the critical displacement when interface failure occurs. δ_m^0 is the relative displacement when the damage initiates under mixed mode loading, which is obtained by:

$$\delta_m^0 = \sqrt{\frac{(\delta_1^0)^2 (1 + \beta^2) \delta_2^0 \delta_3^0}{\delta_2^0 \delta_3^0 + \beta^2 (\delta_1^0)^2}} \quad \text{and} \quad \beta = \frac{\sqrt{\delta_2^2 + \delta_3^2}}{\delta_1} \quad (4.3)$$

$$\delta_1^0 = \frac{\sigma_1^0}{K_1}, \quad \delta_2^0 = \delta_3^0 = \frac{\tau_1^0}{K_2} = \frac{\tau_2^0}{K_3} \quad (4.4)$$

where σ_1^0 , τ_1^0 , and τ_2^0 are the strengths in the normal and two shear directions under pure mode loading, and δ_1^0 , δ_2^0 and δ_3^0 are the corresponding displacements.

Until here, the only unknown parameter in Equation (4.2) is the critical displacement δ_c . In the cohesive zone method, mode II and mode III fracture is often regarded as the

same due to a lack of mode III mechanical property information [223]. Thus, the mixed mode energy-based failure function [224] can be expressed as:

$$\left(\frac{G_1}{G_1^c}\right)^\gamma + \left(\frac{G_{\text{shear}}}{G_{\text{shear}}^c}\right)^\gamma = 1 \quad (4.5)$$

where G_{shear}^c is the critical shearing energy release rate with $G_{\text{shear}}^c = G_2^c = G_3^c$, and G_1^c , G_2^c and G_3^c terms are the fracture energies under pure mode loading. The G_{shear} is the energy dissipation rate by shearing, which is sum of the energy release by the mixed mode II and III crack, $G_{\text{shear}} = G_2 + G_3$, and the G_2 and G_3 are given in Equation (4.6). A quadratic $\gamma = 2$ failure criteria is frequently chosen according to the mixed mode experimental results [224, 225] and so it is used here. For the cohesive interface, the energy dissipation rates are:

$$G_i = \int \sigma_i d\delta_i \quad (i = 1, 2, 3) \quad (4.6)$$

In HFDEM model proposed in this current study, the bonding stresses transferred by the material are functions of the relative displacements across the crack elements, and this is illustrated in Figure 4.1 for the mode I tensile response.

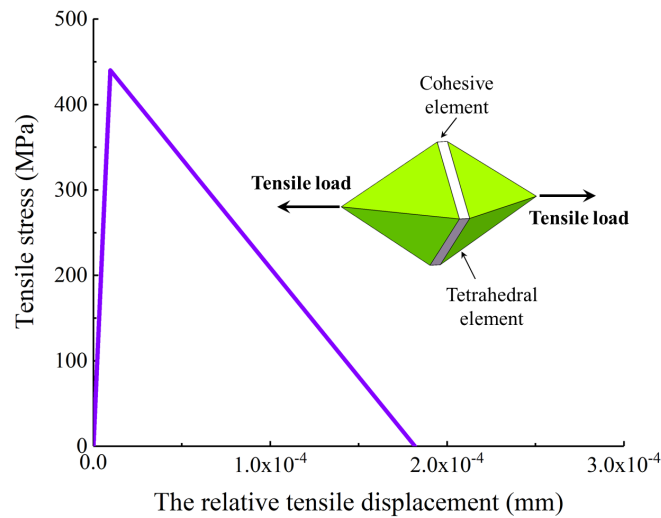


FIGURE 4.1: The mode I constitutive behaviour of the cohesive element with $K_1 = 4.6 \times 10^7$ N/mm³, $\sigma_0 = 440$ MPa, and $G_1^c = 0.04$ N/mm. In the inset figure, a cohesive (crack) element is interspersed throughout two tetrahedral elements.

4.3.2 The microscopic stochastic fracture model

For brittle materials such as ceramics, the strength is limited by the distribution of flaws in the material specimen, and any flaw in the material can serve as an origin of a crack [202]. The Weibull strength distribution is widely used in ceramics to characterize the influence of flaws statistically [202, 203, 214].

$$P(\sigma, V) = 1 - \exp \left[-\frac{V}{V_0} \left(\frac{\sigma}{\sigma_0} \right)^m \right] \quad (4.7)$$

where $P(\sigma, V)$ is the cumulative failure probability of an alumina ceramic, V is the volume of the investigated component, V_0 is the characteristic volume, σ is the applied stress, m is the Weibull modulus, and σ_0 is the Weibull characteristic strength.

In HDFEM, the cohesive elements represent the intrinsic and extrinsic flaws [55]. Thus, Weibull's statistical strength theory [203] is applied to cohesive elements to show the stochastic properties of the alumina ceramics. In the recent study by Daphalapurkar et al. [222], a modified microscopic facet-strength probability distribution based on Equation (4.7) is applied to the dynamically introduced cohesive method.

$$f(\sigma) = \frac{m_0}{\sigma_0} \left(\frac{A}{A_0} \right)^{\frac{m_0}{m_a}} \left(\frac{\sigma}{\sigma_0} \right)^{m_0-1} \exp \left[\left(\frac{A}{A_0} \right)^{\frac{m_0}{m_a}} \cdot \left(\frac{\sigma}{\sigma_0} \right)^{m_0} \right] \quad (4.8)$$

where A is the facet area of the cohesive element, A_0 is the characteristic area; m_0 is the Weibull modulus of strength distribution, and m_a is the Weibull modulus for the effective area modification. In the current study, we applied the microscopic facet-strength probability model to the pre-inserted cohesive method to represent the flaws in the material. Monte Carlo simulations generate the strength data affected by flaws according to Equation (4.8).

Figure 4.2 shows a Monte Carlo simulation for Weibull's statistical strength distribution of cohesive elements with $m_0 = 11.0$, $m_a = -11.0$, $\sigma_0 = 440.0$, $A = 0.01268$ and $A_0 = 0.013$. The percentage of low-strength cohesive elements (below 350 MPa) is around 7.9%, which is associated with the big flaws in the material. The rest of the cohesive elements (around 92.1 %) have strong strength (between 350 and 530 MPa), which corresponds to the material with smaller flaws. The Weibull statistical model for failure has been adapted to fit within the cohesive element framework by incorporating the following assumptions: 1) The pre-inserted cohesive elements in the finite element mesh are treated as potential locations for flaws. 2) When the tensile stress applied on a facet exceeds its strength, the flaw in that location becomes a microcrack. The cohesive

elements with low strength will activate at nearly negligible loads and can be considered as intrinsic microcracks.

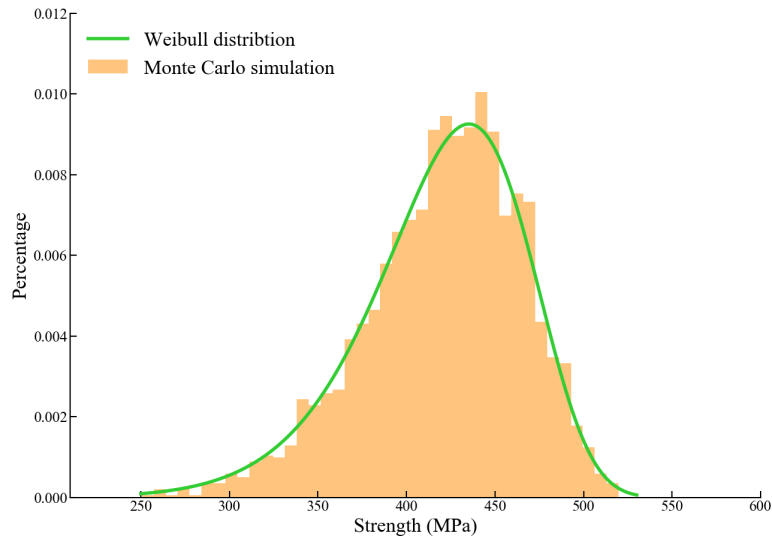


FIGURE 4.2: The green line is Weibull’s statistical strength distribution of cohesive elements obtained from Equation (4.8) with $m_0 = 11.0$, $m_a = -11.0$, $\sigma_0 = 440.0$, $A = 0.01268$ and $A_0 = 0.013$. The orange bar is the statistics of the facet strength of the cohesive element with random flaws generated by Monte Carlo simulations. The percentage of low-strength cohesive elements (below 350 MPa) is around 7.9%, which is associated with the big flaws in the material. The rest of the cohesive elements (around 92.1 %) have strong strength (between 350 and 530 MPa), which corresponds to the material with smaller flaws.

4.4 The hybrid finite-discrete element method

The hybrid finite-discrete element method is an advanced numerical method that combines continuum mechanics methods with the discrete element method (DEM) algorithms to solve complicated crack problems involving multiple interacting deformable bodies [31–33]. In HFDEM, the specimens are considered a collection of elastic bulk elements connected by cohesive elements [31]. The cohesive elements represent the inherent flaws in the specimens, which become the potential cracks during the loading process, and are also referred to as “crack elements” in HFDEM [55]. When $D=1$, the crack element is completely broken, and the cohesive element is deleted from the model, which generates new crack surfaces. In the HFDEM model, cohesive elements introduce a well-defined length scale into the material description, and are consequently sensitive to the size of the element [226]. In the current study, the physical and statistical model (Equation (4.8)) has introduced an internal microstructural length scale (A_0) into our HFDEM model, and thus regularizes the problem in terms of mesh convergence. This technique (Equation (4.8)) has been applied to the dynamically introduced cohesive method and demonstrated the effectiveness of mesh convergence [221, 222]. However, this

technique (Equation (4.8)) has not been used in the pre-inserted cohesive method before, and we use the pre-inserted cohesive method considering the physical and statistical model (Equation (4.8)) to simulate the mode I tensile behaviour in this paper.

4.4.1 Modeling mode I failure considering distributed flaws

In this study, the mechanical properties of the CeramTec 98% are provided by the manufacturer [169] and evaluated in our previous studies [11, 61, 208]. This CeramTech ceramic has an alumina content of 98 mass percentage, a low porosity of less than 2%, a high hardness of 13.5 GPa, a low density of 3.8 g/cm³, Young's modulus of $E = 335$ GPa, and Poisson's ratio of $\nu = 0.23$. For the physical and statistical model [11, 61, 202, 203, 208, 214], the Weibull modulus of the strength distribution is $m_0 = 11$, the Weibull modulus for the effective area modification is $m_a = -11$, the Weibull characteristic strength is $\sigma_0 = 440$ MPa, the characteristic area is $A_0 = 0.013$ mm², and mode I fracture energy is $G_c = 0.04$ N/mm, which are summarized in Table 4.1.

TABLE 4.1: The properties of CeramTec 98% alumina for the HFDEM model

The mechanical properties of the CeramTec 98% alumina	
Porosity	< 2%
Hardness	13.5 (GPa)
Density	3.8 (g/cm ³)
Young's modulus	335 (GPa)
Poisson's ratio	0.23
The properties for the microscopic stochastic fracture model	
Weibull modulus of the strength distribution	11
Weibull modulus for the effective area modification	-11
Weibull characteristic strength	440 (MPa)
Characteristic area	0.013 (mm ²)
Mode I fracture energy	0.04 (N/mm)

The simulation sample for the mesh sensitivity analysis is a ceramic block with dimensions $L_x = 1.5$ mm, $L_y = 0.5$ mm, and $L_z = 2.5$ mm. In the simulations, a fixed-displacement boundary condition is implemented to the bottom, and the specimen is free to expand or contract freely in the lateral direction. The loading process is performed by imposing a velocity boundary condition in the z-direction to mimic the direct tension loading. The boundary velocity, v_0 , is fixed to 1 mm/s, which is a

quasi-static direct tension loading. This model has also been also employed by Zhou and Molinari [221] to study mesh sensitivity. In the literature [218, 226], various studies have focused on the influence of mesh size on the mechanical response of brittle materials, and the upper limit of mesh size for advanced ceramics is suggested to be around 0.3 mm. In addition, experimentally determined fragment sizes for ceramics [13, 15] can also guide in choosing the element size because each tetrahedral elastic element acts as a potential fragment generated in the post-fracture process in the HFDEM model. In their experimental study, Hogan et al. [15] measured more than 1500 ceramic fragments generated by quasi-static uniaxial compression. According to their measurements, most of the fragments are between 0.01 and 1 mm in size, and over 70% of the fragments are larger than 0.1 mm [13]. With this taken into account, the current study focuses on capturing the macroscopic failure (fracture and fragmentation process) numerically, therefore, we performed simulations with mesh sizes of 0.075, 0.1, 0.15, and 0.25 mm to confirm that there was minimal sensitivity. Monte Carlo simulations are carried out to simulate the variety of the specimen strength because of the different flaw distributions inherent to the samples. Three numerical tests are performed for each simulation case (fixed mesh and material parameters). The facet area of the cohesive element is $A = 0.00336 \text{ mm}^2$ for mesh sizes of 0.075 mm, $A = 0.00611 \text{ mm}^2$ for mesh sizes of 0.1 mm, $A = 0.01268 \text{ mm}^2$ for mesh sizes of 0.15 mm, and $A = 0.038 \text{ mm}^2$ for mesh sizes of 0.25 mm, which are summarized in Table 4.2.

TABLE 4.2: Statistics of four FEM meshes

Validation models	Average mesh size (mm)	Average facet area (mm^2)
Case 1	0.25	0.038
Case 2	0.15	0.01268
Case 3	0.1	0.00611
Case 4	0.075	0.00336

The stable time step used in the current study satisfies the criteria given by [222]:

$$\Delta t_{stable} \leq \alpha \left(\frac{l_e}{c} \right) \quad (4.9)$$

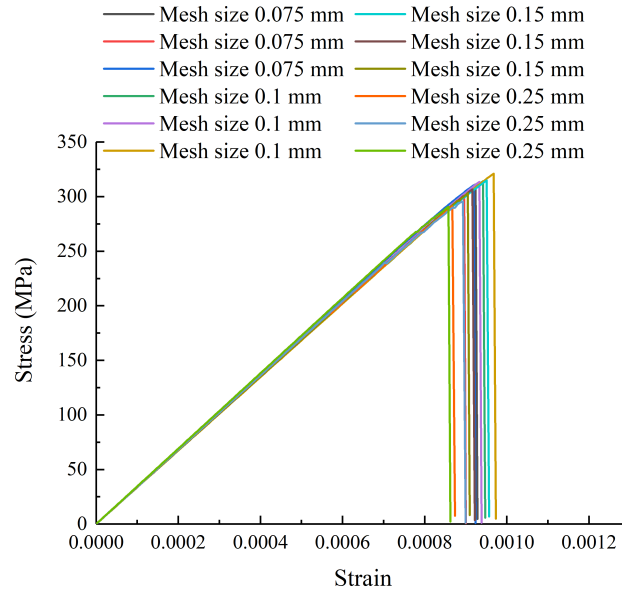
where c is the wave speed in the alumina ceramic, l_e is the smallest element size, and α is a factor whose value is 0.1 or less. This stable time step is able to resolve the two kinds of time-scales. The first time-scale is the response time associated with the cohesive law, and is given by [227]:

$$t_0 = \frac{E G_c}{c \sigma_0^2} \quad (4.10)$$

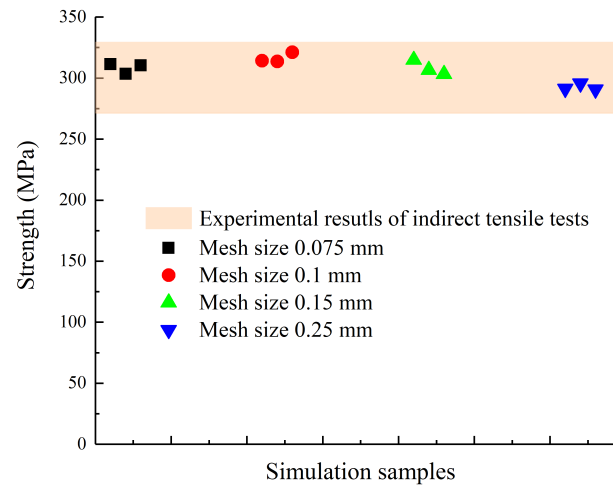
The other time-scale is associated with the time required for complete decohesion of the cohesive law [222]:

$$t_c = \left(\frac{\delta_c}{c\dot{\epsilon}} \right)^{0.5} \quad (4.11)$$

where $\dot{\epsilon}$ is the applied strain rate, and δ_c is the critical crack opening displacement.



(a)



(b)

FIGURE 4.3: a) Variation of engineering stress-strain response of the CeramTec 98% alumina during the direct tension simulations with four kinds of mesh sizes. b) The shaded region is the tensile strength of the CeramTec 98% obtained by Brazilian disk experiments [208], and the dots are the simulation results with four kinds of mesh sizes.

Figure 4.3a illustrates the tensile stress and strain evolution of the alumina under quasi-static direct tension loading. The stress increases linearly during the loading process with a constant strain rate until catastrophic failure occurs. The variety of the tensile strength in the simulations with the same mesh size is due to the different flaws in the materials generated by Monte Carlo simulations. The peak stresses of the four kinds of simulation with different mesh sizes are consistent with the experimental results [208], and the difference of simulated stress-strain responses are within 7% (see Figure 4.3b). Although the difference in stress (or strain) states between indirect and direct tension samples, the difficulties inherent in conducting conventional direct tensile tests on advanced ceramics have resulted in using indirect methods, such as Brazilian tests, for evaluating their tensile strength [59, 60, 208]. Our previous investigation [208] involved the application of an experimental approach coupled with a theoretical method to determine the tensile strength of alumina ceramic materials, which makes the obtained tensile strength more reliable.

Next, the failure pattern of the simulation with four different mesh sizes is shown in Figure 4.4. A horizontal crack perpendicular to the loading direction is observed during the loading process. The single main crack causes catastrophic failure at the low loading rate. Some fragments appear near the crack surfaces due to the branching behaviour of the crack. The fracture process of simulation results under the tensile loading is consistent with the observation in brittle materials [228–231]. The origins of fractures can stem from either internal volume flaws (such as cracks, pores, uneven density, and composition variations) or surface flaws (like cracks from machining, surface pits, and voids) [231]. In the current study, we consider the tensile characteristics in the loading direction based on the statistical studies of flaws for alumina ceramics [202, 203, 214]. However, the flaws on the sample surfaces and the influence of the flaws on shear or compression directions are not considered. In brittle materials, fracture in brittle materials occurs due to the application of stress to the critical flaws in the material leading to unstable propagation of that cracks. When subjected to direct tension testing, the crack at the origin expands approximately perpendicular to the principal tensile stress and spreads symmetrically from the origin in a uniform stress field. The fracture processes include crack surface creation, fragment release, and the main crack splits into multiple branches [231]. In the simulation, the branching phenomenon is more pronounced for the samples with smaller mesh sizes, and this is because each cohesive element associated with flaws is a potential source of microcracking in the material. The smaller meshed sample has more cohesive elements (or crack elements) with critical strength in the material. The increase in the number of crack initiation sources naturally promotes branching behaviour [228–231]. Overall, our model is mesh-independent based on qualitative (e.g., failure patterns) and quantitative (e.g., stress-strain curves) evaluations.

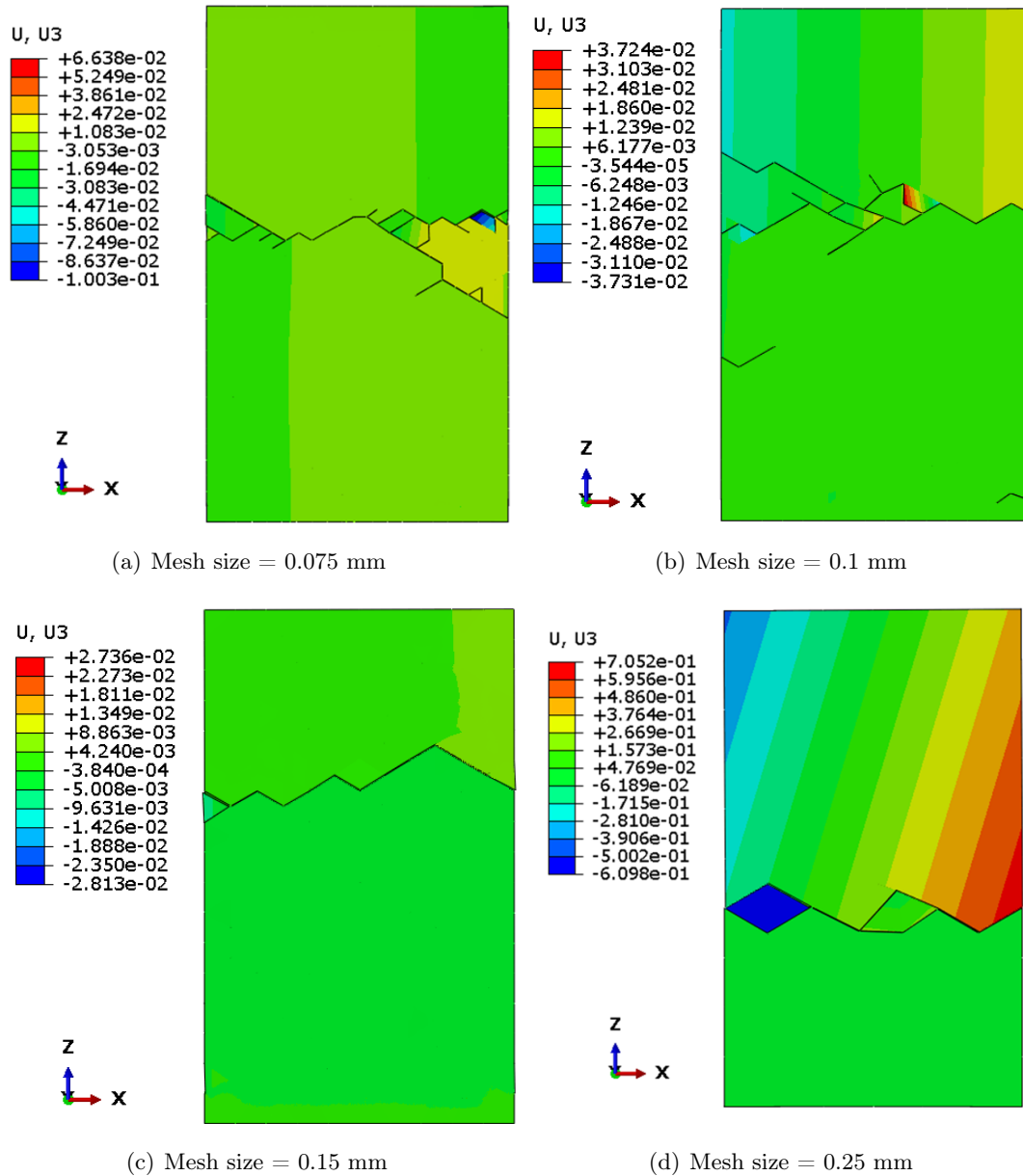


FIGURE 4.4: The failure pattern of the samples with different mesh sizes. The legends in the figure correspond to the displacement of the samples in the z-direction (U_3). It is observed that a horizontal crack perpendicular to the loading direction is generated during the loading process. The single main crack causes catastrophic failure. In some cases, the main crack may split into multiple branches. Some fragments appear near the crack surfaces due to the branching behaviour of the cracks.

4.4.2 The effect of flaw distribution

In recent years, the influences of cohesive parameters (i.g., cohesive strength and the critical energy release rate) on the mechanical response of brittle materials have been widely investigated [55, 72, 76, 126]. However, limited numerical studies focused on the influence of the distribution of the flaw systems. The influence of the flaw systems in

materials on the strength at the quasi-static loading rate has traditionally been related to the size of the largest flaw in the material based on experimental studies [222, 232]. Moreover, researchers found that the distribution of the flaw systems is also significant to the elasticity and strength of ceramic materials [233, 234]. In the current study, we consider the different Weibull distributions of the flaw system with five choices of Weibull modulus $m_0 = 9, 10, 11, 12,$ and 13 [202]. Figure 4.5 shows that the percentage of low-strength cohesive elements (below 350 MPa) is around 12.2% for $m_0 = 9$, 9.9% for $m_0 = 10$, 7.9% for $m_0 = 11$, 6.4% for $m_0 = 12$, and 5.1% for $m_0 = 13$. This means the higher value of m_0 corresponds to more uniform flaw sizes with fewer big flaws, and a smaller m_0 physically represents a more heterogeneous material with a higher amount of bigger flaws.

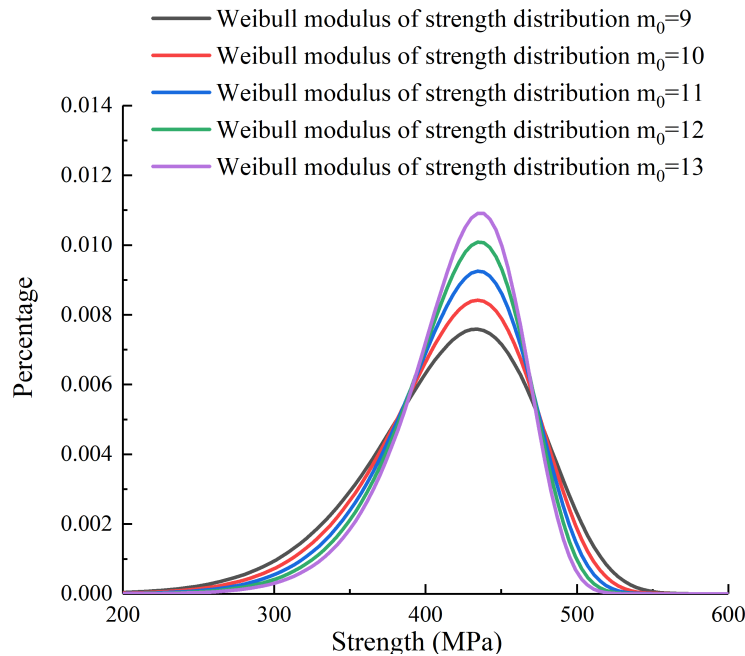
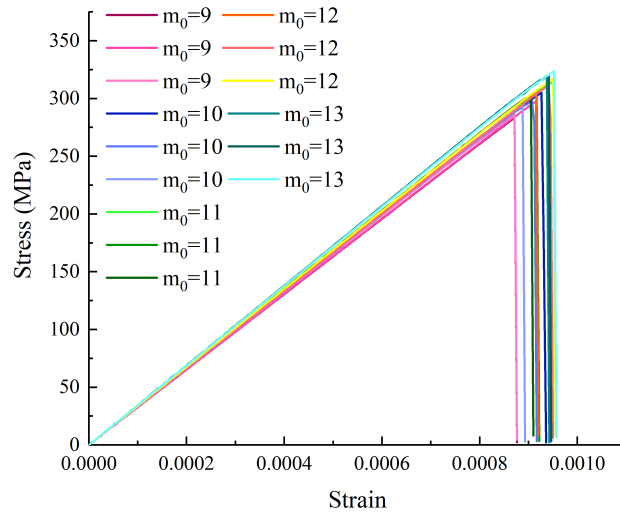


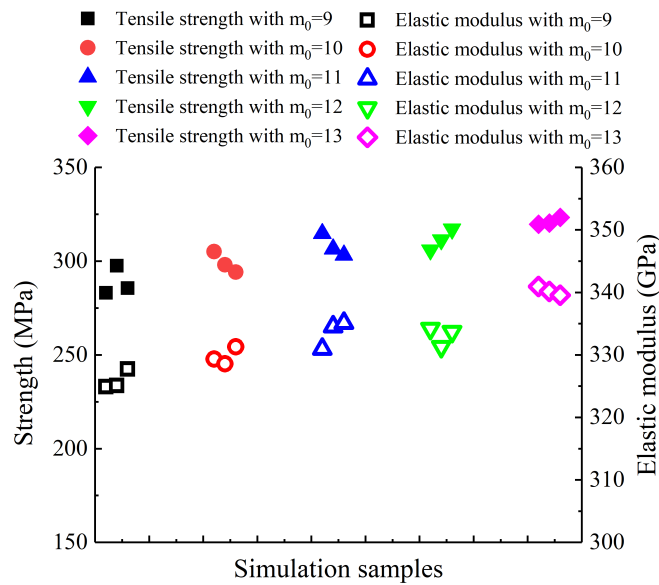
FIGURE 4.5: Microscopic strength distributions with different Weibull modulus ($m_0 = 9, 10, 11, 12,$ and 13).

Figure 4.6a shows the tensile stress-strain curves during the constant low strain-rate loading, and Figure 6(b) summarizes the tensile strength and elastic modulus obtained by simulation with five different Weibull modulus. It is observed that material with smaller m_0 (i.e., more heterogeneous material with a higher number of bigger flaws) exhibits lower tensile strength and elastic modulus. This agrees with the experimental observation [233, 235] that both the strength limit and elasticity moduli decrease with a higher percentage of big flaws. This is because the strength of a ceramic specimen is not only determined by the existing critical flaws in the material [77] but also by the flaw distribution [202, 203, 214]. Next, Figure 4.7 shows that the failure pattern is

consistent with Figure 4.4, for which a single main crack perpendicular to the loading direction is generated during the loading process. Some fragments appear near the crack surfaces due to the branching behaviour of the cracks. The branching phenomenon is more pronounced for the material with a smaller m_0 value. This is because the material has more critical flaws with larger sizes, and these flaws are activated during the loading process. The increase in the number of crack initiation sources naturally stimulates the branching behaviour.



(a)



(b)

FIGURE 4.6: a) The engineering stress-strain response of the CeramTec 98% alumina during the direct tension simulations with different Weibull modulus ($m_0 = 9, 10, 11, 12, \text{ and } 13$). b) The full dots are the tensile strength and the hollow dots are the elastic modulus obtained by simulation with five different Weibull modulus.

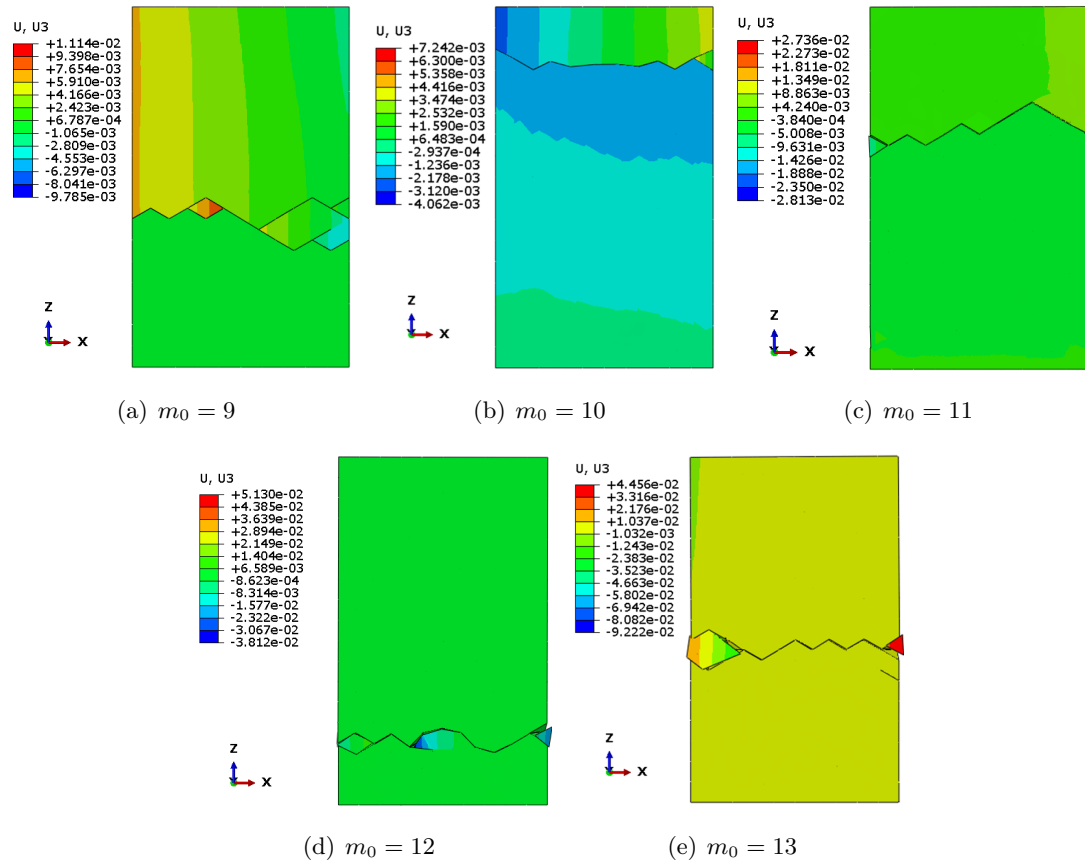


FIGURE 4.7: The failure pattern of the simulation results with different Weibull modulus ($m_0 = 9, 10, 11, 12,$ and 13). The U_3 legend in the figure indicates the displacement of the samples in the z -direction. The failure pattern is consistent with Figure 4.4, a horizontal crack forms perpendicularly to the loading direction during the loading process, ultimately leading to a catastrophic failure caused by the single main crack. In certain instances, the main crack can divide into multiple branches, resulting in fragments near the crack surfaces due to the crack's branching behaviour.

4.5 Conclusion

We performed a three-dimensional HFDEM model to investigate the mode I tensile opening failure of the alumina ceramic. In this model, the ceramic material was divided into two parts: bulk material regions, represented by tetrahedral elements, and pre-inserted cohesive elements that appear at the interfaces (facets) between tetrahedral elements. The bulk material was linear, homogeneous, and isotropic elasticity, while the behaviour of the micro-cracks was described using cohesive elements. A microscopic stochastic fracture model is developed considering a random distribution of internal flaws in the material. The microscopic stochastic fracture model, including a Weibull strength distribution, is adapted to fit within the HFDEM model. Our model implicitly considered the tensile failure processes related to the flaw system in the material and

explicitly showed the macroscopic failure patterns. This model is mesh-independent based on qualitative (e.g., failure patterns) and quantitative (e.g., stress-strain curves) evaluations. The tensile strength obtained by our model is consistent with the indirect tensile testing results from our previous study [208]. In the simulation, micro-cracks nucleated randomly within the sample and grew, eventually merging, leading to the catastrophic failure of the specimen. A single main crack perpendicular to the loading direction is observed during the tensile loading process. Some fragments appear near the crack surfaces due to the branching behaviour of the crack. Furthermore, the influences of the flaw system distribution on the tensile strength and elastic modulus are explored. The simulation results show that the material with more uniform flaw sizes and fewer big flaws has stronger tensile strength and higher elastic modulus. Overall, applying this new model provides theoretical guidance for future material design and optimization.

Chapter 5

Advanced Tensile Fracture Analysis of Alumina Ceramics: Integrating Hybrid Finite-discrete Element Modeling with Experimental Insights

Published as **Jie Zheng**; Li, HY and Hogan, JD. *Advanced Tensile Fracture Analysis of Alumina Ceramics: Integrating Hybrid Finite-discrete Element Modeling with Experimental Insights*, Engineering Fracture Mechanics (2024).

Author	Contribution
Jie Zheng	Conceived the ideas and experimental design of the study; Performed experiments/data collection; Data analysis and interpretation; Developed theoretical methodology; Primary author (drafted the manuscript)
Li, HY	Provided revisions to scientific content of manuscript
Hogan, JD	Provided revisions to scientific content of manuscript; Provided stylistic/grammatical revisions to manuscript; Principal investigator

5.1 Abstract

This study offers novel insights into the mode I tensile response of an alumina ceramic through the use of computational modelling and the flattened Brazilian disk (FBD)

experiments. A modified hybrid finite-discrete element method (HFDEM) is developed, integrating a coupled damage and friction cohesive model and a microscopic stochastic fracture model with a Weibull strength distribution by Monte Carlo simulation. The model is used to simulate direct tensile failure processes under quasi-static loading conditions, providing qualitative and quantitative predictions of direct tensile failure processes of an alumina ceramic. Concurrently, quasi-static flattened Brazilian disk tests (indirect tensile tests) are performed on a standard MTS machine coupled with a high-speed camera. The modified HFDEM model is also applied to reproduce the FBD experiments, and our simulated tensile strength is consistent with the experimental results. The results of the modified HFDEM model show three kinds of phenomena (i.e., “underestimation”, “reasonable estimation”, and “overestimation” of the indirect tensile strength) and four different types of associated fracture and fragment patterns of FBD testing. The integration of simulation and experimental results reveal relationships between fracture patterns, fragment geometry, tensile strength, and indirect tensile strength. The fracture and fragmentation patterns derived from our modified HFDEM model can be utilized to analyze the “tensile strength” measured in BD testing. Overall, this research offers important insights and direction for future Brazilian disk experiments and tensile strength assessments, enhancing our comprehension of ceramic failure mechanisms under tensile loadings.

5.2 Introduction

The emergence and development of advanced ceramics have significantly influenced the effectiveness of impact protection in various applications such as aircraft [236], tanks [197], and bulletproof body armors [11]. This is due to their exceptional properties such as high wear resistance [4], high hardness [200], and low density [208]. In protection systems, ceramic materials often serve as the front layer to blunt the projectile [131], but they tend to crack and fail upon impact partly due to reflected tensile waves generated from the back-free surface of the target [83]. Moreover, most ceramics are brittle and exhibit low tensile strength simultaneously [237]. Therefore, for applications such as ballistic protection [83, 197] and debris shielding in aerospace and space applications [236, 238], it is necessary to conduct research on ceramic materials to optimize lightweight structures, especially regarding the deformation and failure mechanisms that occur under tensile loading.

Due to the difficulties in conducting traditional direct tensile tests on advanced ceramics, alternative indirect methods have been developed to assess their tensile strength, such as sleeve-fracturing tests [239], beam bending tests [240, 241], and Brazilian disk tests

[149, 185, 242]. Among these methods, the Brazilian disk method is particularly recommended for studying the tensile strength of brittle materials due to its ease of implementation [135, 242]. The Brazilian disk testing approach is suitable for brittle materials that have significantly higher compressive strengths than tensile strengths [86, 243], and has been applied to, for example, alumina ceramics [61, 192, 208], silicon carbide [244], and glass ceramics [60]. To reduce stress concentration near the loading area, Wang et al. [136–139] modified the Brazilian disk test by adding two parallel flat ends that are subjected to the experimental loading, which is called the flattened Brazilian disk. The flattened Brazilian disk has been noted to achieve better contact with loading devices compared to the technology using curved loading platens [164]. The flattened Brazilian disk test has been widely recognized in recent scholarly works [60, 61, 147, 151, 208, 242] as a Brazilian disk method for determining the tensile strength of brittle materials. Thus, our study uses flattened Brazilian disk testing to investigate the mode I tensile response of an alumina ceramic. The Brazilian disk method induces a bi-axial stress state (i.e., vertically compressive and horizontally tensile when the loading direction is vertical) that causes the sample to fracture under tension at the disk's center, typically resulting in a clean breakage along the loaded diameter and resulting in splitting the disk into two halves [245]. An important and basic assumption for determining the indirect tensile strength by the Brazilian disk method is that the vertically compressive stress (or intermediate principal stress) does not influence the disk fracture [155]. Despite the widespread use of the Brazilian disk method for determining the tensile strength of brittle materials, varying research findings have led to inconsistent conclusions regarding the correlation between the tensile strength obtained through the Brazilian disk method and direct uniaxial tensile tests [155]. For example, Coviello et al. [246] and Swab et al. [185] have found that the Brazilian disk method might underestimate the tensile strength of certain materials. Conversely, other studies have suggested that the Brazilian disk method effectively determines the tensile strength of brittle materials, as noted in the studies by Zhang et al. [60] and Khosravani et al. [149]. In other studies, many researchers maintain that the Brazilian disk method tends to overestimate tensile strength, as indicated in the investigations by Li et al. [155] and Zheng et al. [208]. Currently, limited studies focus on the root cause of these arguments of “underestimation” and “overestimation” phenomena in BD testing [155]. In this study, we implement a comprehensive computational model to compare the tensile strength obtained by the Brazilian disk and direct tensile simulations and investigate the mechanisms behind the “underestimation” and “overestimation” phenomena observed in the Brazilian disk method.

Computational models are important for capturing the mechanisms that control the performance of a given brittle material [247–249]. In the literature, several models

have been developed to investigate the failure process of brittle materials, which include continuum damage mechanics (CDM) [250, 251], the extended Finite Element Method (XFEM) [65], virtual crack closure technique (VCCT) [216, 217], and the cohesive zone method (CZM) [66, 252]. CDM uses damage parameters to explain failure but cannot model crack-induced discontinuities [250, 251]. VCCT can simulate crack propagation by imposing constraints on nodes at crack edges. However, it requires computationally expensive re-meshing in order to capture the stress field around the crack tip [216, 217]. XFEM, on the other hand, avoids mesh refinement and reconstruction by modifying the displacement approximation function with an enrichment term, but with the limitations of capturing multiple interacted deformable bodies [65]. The CZM approach offers several benefits over other discussed methods, including the capability to create new surfaces to initiate cracks, enabling the modelling of crack branching and interaction, and eliminating the singularity that exists in linear elastic fracture mechanics [68, 69]. Due to these advantages, the CZM has been widely used to investigate the strength of advanced ceramics [68, 69], fracture behaviour [71], and fragmentation processes [70]. Recently, Munjiza et al. [31] developed the hybrid finite-discrete element method (HFDEM), a pioneering numerical approach based on the CZM. The HFDEM method creates new surfaces when cracks occur, and numerical contact algorithms are introduced to manage these new faces. For such reasons, the HFDEM is particularly suitable for geomaterials [55, 73, 74] and ceramic materials [33, 253]. For example, Mahabadi et al. [73] attributed the failure mechanism of these brittle materials to the development of macro-cracks generated from pre-existing internal flaws and defects, and these pre-existing internal flaws and defects are represented by cohesive elements in HFDEM. Mahabadi et al. [55] also found that the use of tetrahedral elements provides an advantage over hexahedron elements by generating more potential fracture surfaces, leading to more reliable results. Recently, Daphalapurkar et al. [222] and Zheng et al. [253] modified the HFDEM by considering a random distribution of internal flaws for ceramic materials. In their modified HFDEM, micro-cracks randomly nucleated within the ceramics, grew, and interacted, resulting in catastrophic failure. Based on the modified HFDEM [222, 253] and experimental flaw system results [202, 203, 214, 254], the current study will integrate the HFDEM with a Weibull distribution of flaw systems in alumina ceramics to investigate the fracture behaviour. In the fragmentation process of HFDEM, researchers [68, 126] observed that fragments can still maintain contact with friction force persisting under compression-and-shear loading, and they have assumed that the shear strength of cohesive elements remains constant without degradation for ceramics. To overcome the limitation of the assumption, our study also integrates the coupled damage and friction cohesive model [255] with the modified HFDEM model. Thus, our study involves the integration of the hybrid finite-discrete element method (HFDEM), a microscopic stochastic fracture model based on a Weibull distribution, and the coupled damage and

friction cohesive model to explore the mode I tensile behaviour of an alumina ceramic (i.e., the direct tension and Brazilian disk tests).

This paper presents a combined experimental and computational method to investigate the mode I tensile response of an alumina ceramic. In Section 5.3, a modified HFDEM is developed by integrating the hybrid finite-discrete element method and the coupled damage and friction cohesive model. To account for the random distribution of internal flaws in the material, a microscopic stochastic fracture model, featuring a Weibull strength distribution, is developed and integrated into the HFDEM model. In Section 5.4, the proposed model is applied to simulate the direct tensile failure of an alumina ceramic under quasi-static loading conditions. In Section 5.5, quasi-static indirect tensile tests are performed using flattened Brazilian disks, and the failure process was monitored using a high-speed camera. In addition, the HFDEM simulation is applied to a Brazilian disk test setup, and our tensile strength predictions agreed with experimental findings. The validated Brazilian disk HFDEM model is then utilized to explore the mechanisms governing the “underestimation” and “overestimation” phenomena and compare them with direct tensile simulations. These simulated and experimental results reveal the relationship between fracture patterns, fragment geometry, tensile strength, and indirect tensile strength. Overall, the findings from this study provide valuable insights and guidance for future Brazilian Disk experiments and tensile strength evaluations, thereby deepening our understanding of ceramic material behaviors and failure mechanisms under tensile stress.

5.3 Computational approach

This section presents the development of a modified hybrid finite-discrete element method (HFDEM). In Section 5.3.1, the constitutive response of alumina is represented by a three-dimensional (3D) coupled damage and friction law of the cohesive zone method based on the works of literature [74, 252, 255, 256]. In Section 5.3.2, a microscopic stochastic fracture model [222, 253, 257] is incorporated to consider the random distribution of internal flaws in the material observed in experiments [202, 203, 214]. This model incorporates a Weibull strength distribution, designed to represent flaws in the material [222, 253], and is tailored to integrate with the modified HFDEM model.

5.3.1 The coupled damage and friction cohesive model

An extensive account of the theory of HFDEM and its finite element implementation can be found in [33, 73, 74, 220]. In this section, we summarize the main features of the

cohesive law used in the current study. In their work, Alfano and Sacco [255] proposed a cohesive zone method that combined interface damage and friction. They partitioned a unit representative elementary area (REA) of the interface into two parts: the damaged part, D , and the undamaged part, $(1-D)$, and their model only accounted for friction in the damaged part when the material was under compressive loading. Building on the two-dimensional model proposed by Alfano and Sacco [255], we extend the model in this study for a three-dimensional system:

$$\boldsymbol{\sigma} = (1 - D)\mathbf{K}\boldsymbol{\delta} + D\boldsymbol{\sigma}^d \quad (5.1)$$

with

$$\boldsymbol{\sigma} = \begin{bmatrix} \sigma_1 \\ \tau_1 \\ \tau_2 \end{bmatrix}, \quad \mathbf{K} = \begin{bmatrix} K_1 & 0 & 0 \\ 0 & K_2 & 0 \\ 0 & 0 & K_3 \end{bmatrix}, \quad \boldsymbol{\delta} = \begin{bmatrix} \delta_1 \\ \delta_2 \\ \delta_3 \end{bmatrix}, \quad \boldsymbol{\sigma}^d = \begin{bmatrix} \sigma_1^d \\ \tau_1^d \\ \tau_2^d \end{bmatrix}$$

where $\boldsymbol{\sigma}$ represents the interface stress, σ_1 is the normal stress, and τ_1 and τ_2 are the shear stresses in the other two directions. D is a scalar damage parameter of the REA, where $D = 0$ is the intact state and $D = 1$ represents a fully damaged state. \mathbf{K} is the penalty stiffness of the interface, where subscript 1 represents the normal direction, and subscripts 2 and 3 represent the two shear directions. $\boldsymbol{\delta}$ represents relative displacements, and $\boldsymbol{\sigma}^d$ is the stress in the damaged part, which follows the Coulomb friction law [256] defined by:

$$\sigma_1^d = \frac{(|K_1\delta_1| - K_1\delta_1)}{2}, \quad \tau^d = \begin{bmatrix} \tau_1^d \\ \tau_2^d \end{bmatrix} = \begin{bmatrix} K_2(\delta_2 - \delta_2^{di}) \\ K_3(\delta_3 - \delta_3^{di}) \end{bmatrix} \quad (5.2)$$

with

$$\dot{\delta}_n^{di} = \dot{\lambda} \frac{\tau_n^d}{|\tau^d|} \quad (n=1, 2)$$

accompanying with the extra Kuhn-Tucker conditions [255]:

$$\mu\sigma_1^d + |\tau^d| \leq 0, \quad \dot{\lambda} \geq 0, \quad \dot{\lambda}(\mu\sigma_1^d + |\tau^d|) = 0 \quad (5.3)$$

where μ is the coefficient of friction and λ is an internal variable.

A linear irreversible cohesive law is widely used for the decaying response of brittle materials, such as rocks [55, 76] and ceramics [69, 220–222]. For a damage value in the

range of 0 to 1, the damage evolution can be expressed as:

$$D = \max\{0, \min\{1 - \left(\frac{\delta_c - \delta_e}{\delta_c - \delta_m^0}\right), 1\}\} \quad (5.4)$$

where δ_e is the effective relative displacement, $\delta_e = \sqrt{\delta_1^2 + \delta_2^2 + \delta_3^2}$, and δ_c represents the critical displacement when interface failure occurs. δ_m^0 is the relative displacement when the damage initiates under mixed mode loading, which is obtained by:

$$\delta_m^0 = \sqrt{\frac{(\delta_1^0)^2 (1 + \beta^2) \delta_2^0 \delta_3^0}{\delta_2^0 \delta_3^0 + \beta^2 (\delta_1^0)^2}} \quad \text{and} \quad \beta = \frac{\sqrt{\delta_2^2 + \delta_3^2}}{\delta_1} \quad (5.5)$$

Until here, the only unknown parameter in Equation (5.4) is the critical displacement, δ_c . In the cohesive zone method, mode II and mode III fracture is often regarded as the same due to a lack of mode III mechanical property information [223]. Thus, the mixed mode energy-based failure function [224] can be expressed as:

$$\left(\frac{G_1}{G_1^c}\right)^\gamma + \left(\frac{G_{\text{shear}}}{G_{\text{shear}}^c}\right)^\gamma = 1 \quad (5.6)$$

where G_{shear}^c is the critical shearing energy release rate with $G_{\text{shear}}^c = G_2^c = G_3^c$, and G_1^c , G_2^c and G_3^c terms are the fracture energies under pure mode loading. The G_{shear} is the energy dissipation rate by shearing, which is the sum of the energy release by the mixed mode II and III crack, $G_{\text{shear}} = G_2 + G_3$, and G_2 and G_3 are given in Equation (5.7). A quadratic failure criteria with $\gamma = 2$ is frequently chosen according to the mixed mode experimental results [224, 225] and so it is used here. For the cohesive interface, the energy dissipation rates are:

$$G_i = \int \sigma_i d\delta_i \quad (i = 1, 2, 3) \quad (5.7)$$

5.3.2 The microscopic stochastic fracture model

Ceramics usually contain pre-existing flaws such as micro-cracks, pores, and impurities that act as stress concentration sites during the loading process [5, 11, 34, 258]. These flaws may serve as the origin of a crack [201, 202]. To characterize the statistical influence of flaws in alumina ceramics, the Weibull strength distribution is widely used [202, 203, 214], and defined as

$$P(\sigma, V) = 1 - \exp\left[-\frac{V}{V_0} \left(\frac{\sigma}{\sigma_0}\right)^m\right] \quad (5.8)$$

where $P(\sigma, V)$ is the cumulative failure probability of a alumina ceramic, V is the volume of the investigated component, V_0 is the characteristic volume, σ is the applied stress, m is the Weibull modulus, and σ_0 is the Weibull characteristic strength.

The use of cohesive elements in HDFEM enables the representation of pre-existing intrinsic defects in ceramics [55]. As a result, the stochastic properties of alumina ceramics can be demonstrated by applying Weibull's statistical strength theory [203] to these cohesive elements. In recent studies by Daphalapurkar et al. [222] and Zheng et al. [253], a modified microscopic facet-strength probability distribution, based on Equation (5.8), has been applied to cohesive elements as:

$$f(\sigma) = \frac{m_0}{\sigma_0} \left(\frac{A}{A_0} \right)^{\frac{m_0}{m_a}} \left(\frac{\sigma}{\sigma_0} \right)^{m_0-1} \exp \left[\left(\frac{A}{A_0} \right)^{\frac{m_0}{m_a}} \cdot \left(\frac{\sigma}{\sigma_0} \right)^{m_0} \right] \quad (5.9)$$

where A is the facet area of the cohesive element, A_0 is the characteristic area, m_0 is the Weibull modulus of strength distribution, and m_a is the Weibull modulus for the effective area modification. The current study utilizes the microscopic stochastic fracture model to represent material flaws through the pre-inserted cohesive elements in HFDEM. The mechanical properties of cohesive elements affected by flaws are generated using Monte Carlo simulations by Equation (5.9).

5.4 The hybrid finite-discrete element model (HFDEM)

This section applies the HFDEM to a commercially available alumina ceramic ALOTEC 98 SB from CeramTec, Germany, referred to as CeramTec 98% alumina throughout this study. First, we use the modified HFDEM considering the coupled damage and friction law and the microscopic stochastic fracture model to show the constitutive behavior of the CeramTec 98% alumina by using a user-material (VUMAT) Fortran user-subroutine in ABAQUS/Explicit software in Section 5.4.1. Next, the modified HFDEM is applied to simulate the direct tension behavior of the CeramTec 98% alumina in quasi-static loading conditions in Section 5.4.2. In the direct tension simulation, the influence of mesh size and loading rate on the modified HFDEM is investigated.

5.4.1 Material properties and HFDEM

The mechanical properties of CeramTec 98% alumina have been previously evaluated by the manufacturer and other studies [11, 61, 208]. Table 5.1 shows the ceramic material has 98% alumina content by mass, less than 2% porosity, a hardness of 13.5 GPa, a density of

3.8 g/cm³, Young's modulus of 335 GPa, Poisson's ratio of 0.23, and friction coefficient of 0.4. The microscopic stochastic fracture model used in this study incorporates a Weibull modulus of strength distribution of $m_0 = 11$, a Weibull modulus for the effective area modification of $m_a = -11$, a Weibull characteristic tensile strength of $\sigma_0 = 440$ MPa, and a characteristic area of $A_0 = 0.013$ mm² as evaluated by the studies [11, 61, 202, 203, 208, 214, 253].

TABLE 5.1: The properties of CeramTec 98% alumina for the HFDEM model

The mechanical properties of the CeramTec 98% alumina		
Porosity	< 2%	[11, 61]
Hardness	13.5 (GPa)	[11, 61]
Density	3.8 (g/cm ³)	[11, 61]
Young's modulus	335 (GPa)	[11, 61]
Poisson's ratio	0.23	[11, 61]
Friction coefficient	0.4	[11, 61]
The properties for the microscopic stochastic fracture model		
Weibull modulus of the strength distribution	11	[214, 253]
Weibull modulus for the effective area modification	-11	[214, 253]
Weibull characteristic tensile strength	440 (MPa)	[214, 253]
Characteristic area	0.013 (mm ²)	[214, 253]
Mode I fracture energy	0.04 (N/mm)	[214, 253]

The hybrid finite-discrete element method (HFDEM) is an advanced numerical technique that integrates continuum mechanics approaches with discrete element method (DEM) algorithms to address complex fracture and fragmentation issues involving multiple interacting deformable bodies [33]. In this method, specimens are treated as elastic bulk elements connected by cohesive elements. These cohesive elements embody the inherent flaws in the specimens, which may turn into potential cracks during loading, and are also known as "crack elements" within the HFDEM framework [55]. Figure 5.1a and b show the mechanical response of the cohesive element of the CeramTec 98% alumina obtained by Equation (5.1) and Table 5.1. In accordance with Tabiei and Zhang [259] and Wang et al. [260], the penalty stiffness values for Equation (5.1) are selected as $K_1 = 4.6 \times 10^7$ N/mm³.

The cohesive stress transferred by the material is a function of the relative displacements across the crack elements. When D equals to 1, the crack element is entirely broken, resulting in the removal of the cohesive element from the model and the creation of new

crack surfaces. Subsequently, elastic elements separate from the specimen, producing fragments. Figure 5.1a shows the tensile response of the cohesive elements following the bilinear cohesive law. This law is popularly used to simulate the fracture of brittle materials [33, 73, 74, 253, 260].

Next, many studies [68, 126] have assumed that the shear strength of cohesive elements remains constant as the relative shear displacement increases in the BD simulation. In our current study, we emphasized the coupled damage and friction cohesive model under compression and shear loading conditions to explain this assumption. We propose that friction can contribute to sufficient residual strength in shear. For example, the shear strength mentioned in Figure 5.1b is more than three times the tensile strength. Equation (5.1) illustrates that when the material is subjected to compression-shear loading, the friction effect becomes active in the damaged part of the cohesive element. Figure 5.1b describes the shear response under constant compressive loading, showing an initial linear increase in shear stress followed by a nonlinear response when the friction effect becomes significant. It is observed that the peak shear stress increases with higher compressive loading, and this phenomenon is also observed in confined compression experiments in the literature [13, 15]. When the damage value (D in Equation (5.1)) reaches 1, the materials fail, but the fragments can still maintain contact with frictional force persisting between elastic elements as Figure 5.1b shows.

In this study, we have incorporated a physical and statistical model known as the “microscopic stochastic fracture model” (Equation (5.9)) into the HFDEM model. This model has been applied to advanced ceramics when representing flaws in the material [202, 203, 214, 221, 222, 253]. Figure 5.1c is a Monte Carlo simulation of Equation (5.9), illustrating Weibull’s statistical strength distribution of cohesive elements, with parameters $m_0 = 11.0$, $m_a = -11.0$, $\sigma_0 = 440.0$ MPa, $A = 0.01268$ mm² and $A_0 = 0.013$ mm². These parameters are chosen based on the literature [202, 203, 214, 221, 222, 253]. Figure 5.1d shows the cumulative probability distribution of the tensile strength of cohesive elements. Figure 5.1d demonstrates that approximately 7.9% of the cohesive elements have low strength (below 350 MPa), indicating the presence of significant flaws in the material. The remaining cohesive elements (approximately 92.1%) exhibit higher strength values (ranging from 350 to 530 MPa), indicating the portion of the representative volume with smaller or fewer flaws. A comprehensive explanation of the physical significance of this microscopic stochastic fracture model can be found in the studies by Daphalapurkar et al. [222] and Zheng et al. [253], which is omitted here. The modified HFDEM model is numerically solved in the current study using a user-material (VUMAT) Fortran user-subroutine in ABAQUS/Explicit software.

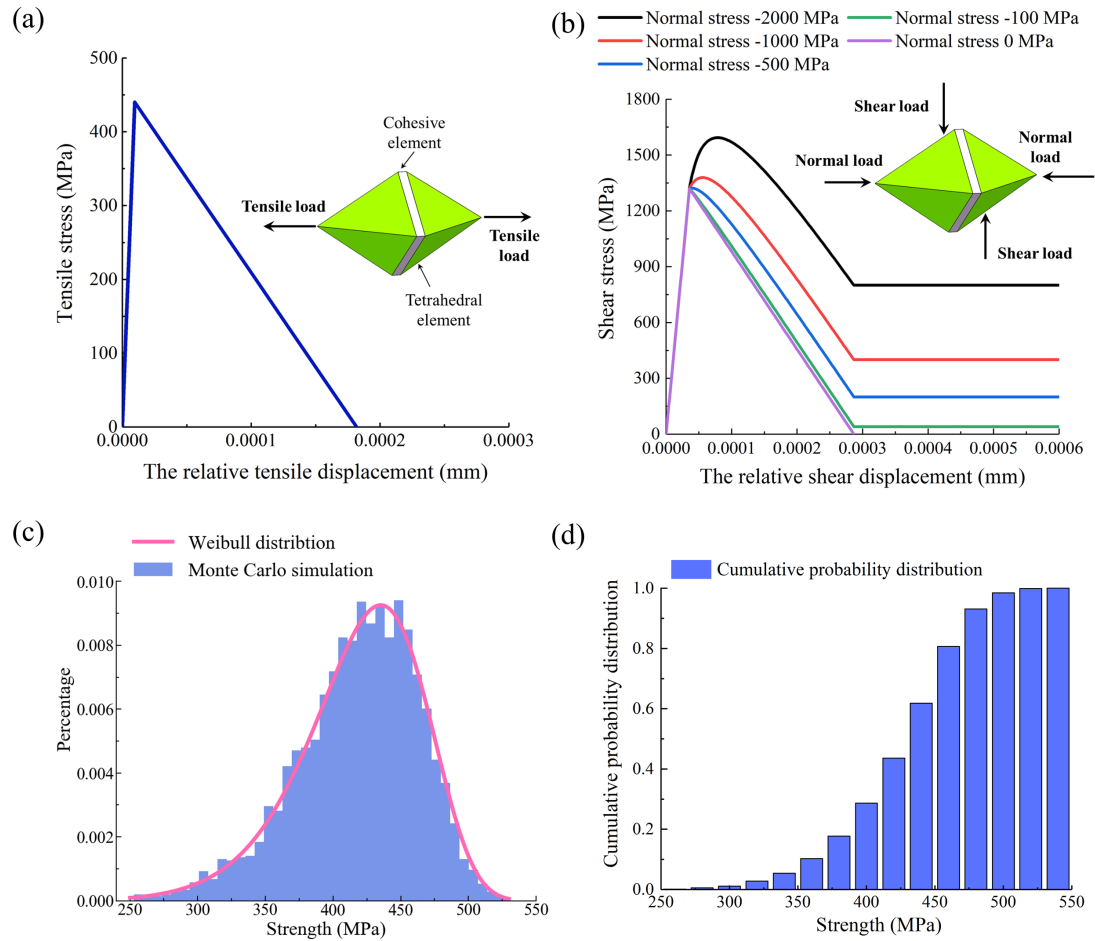


FIGURE 5.1: a) The blue line is the mode I constitutive behaviour of the cohesive element under tensile loading derived from Equation (5.1) and Table 5.1, and the inset figure shows the loading state of the cohesive element. b) The curves are the mode II constitutive behaviour of the cohesive element under compression-shear loading derived from Equation (5.1) and Table 5.1, and the inset figure shows the loading state of the cohesive element. c) The purple line depicts a Weibull's statistical strength distribution by Equation (5.9). The blue bar is the statistical data related to the facet strength of the cohesive elements generated by the Monte Carlo simulations. d) The cumulative probability distribution obtained from the Monte Carlo simulations shown in (c).

5.4.2 The direct tension HFDEM model

The hybrid finite-discrete element method combines continuum mechanics methods and discrete element algorithms to solve complex fracture and fragmentation problems that involve multiple interacting deformable bodies [33]. The elastic elements could be separated from the specimen during the loading process which generates fragments. The element size dictates the minimum fragment size in the post-fracture process of the HFDEM model. Hogan et al. [13, 15] shows the fragment sizes of advanced ceramic were between 0.01 and 1 mm, and most of (over 70%) the fragments were larger than 0.1 mm in the experimental observation. So, we pick four kinds of mesh sizes (0.075,

0.1, 0.15, and 0.25 mm) to verify the mesh sensitivity for the direct tension model. The direct tension HFDEM model used in the current study is a ceramic rectangular block with dimensions $L_x = 1.5$ mm, $L_y = 0.5$ mm, and $L_z = 2.5$ mm. This model has also been used to study the tensile response of advanced ceramics by Zhou and Molinari [221] and Zheng et al. [253]. For each mesh size with fixed input material parameters, three numerical simulations were carried out with the Monte Carlo method to show the variety of the specimen strength due to the stochastic flaws (e.g. impurities, pores and micro-cracks) in the material [5, 11, 202, 203, 214]. The facet area of the cohesive element in Equation (5.9), denoted by A , is provided in Table 5.2 for different mesh sizes. For mesh sizes of 0.075 mm, the area is 0.00336 mm²; for mesh sizes of 0.1 mm, the area is 0.00611 mm²; for mesh sizes of 0.15 mm, the area is 0.01268 mm²; and for mesh sizes of 0.25 mm, the area is 0.038 mm². In the simulation, direct tensile loading is applied in the z-direction by imposing a velocity boundary condition. For the mesh size sensitivity analysis, the velocity boundary is set to be 2.5 mm/s. Furthermore, four kinds of different velocity boundary conditions are chosen as $v_0 = 0.05, 0.25, 2.5$ and 25 mm/s to show that the tensile strength is a constant value under quasi-static loading conditions. To save calculation time, the simulation with different velocity boundary conditions employed 0.15 mm tetrahedral elements and a maximum time step of 5×10^{-7} ms. This time step size was used to maintain numerical stability [218].

TABLE 5.2: Input parameters for the four different mesh sizes

Validation models	Average mesh size (mm)	Average facet area (mm ²)
Case 1	0.075	0.00336
Case 2	0.1	0.00611
Case 3	0.15	0.01268
Case 4	0.25	0.038

Figure 5.2a is the summary of the tensile strength of the CeramTec 98% alumina in quasi-static loading conditions. The points in the Figure 5.2a is the simulated direct tensile strength with four kinds of mesh sizes (0.075, 0.1, 0.15, and 0.25 mm), and the variety of the tensile strength in each mesh size is because of the stochastic flaws generated by Monte Carlo simulations of Equation (5.9). The purple shaded area is the indirect tensile strength obtained by the quasi-static flattened Brazilian disk (FBD) testing, which will be discussed in Section 5.5.1. It is observed that the simulated tensile strength using different mesh sizes is consistent with the experimental results, and the difference in simulated tensile strength is within 6%. Figure 5.2b compares tensile strength under four kinds of velocity boundary conditions (25, 2.5, 0.25 and 0.05mm/s) with the mesh size of 0.15 mm, and the results show that a strain rate up to at least 10 s^{-1} does not influence tensile strength in quasi-static loading conditions. Next, the crack patterns for four different mesh sizes are presented in Figure 5.2c to Figure 5.2f. These figures reveal

consistent behavior across all direct tensile simulations, with a main crack propagating horizontally and perpendicular to the principal tensile stress. Additionally, fragments are observed to generate around the horizontal cracks. This crack pattern aligns with the mode I failure process observed in experiments and simulations involving brittle materials [228–230]. Generally, the fracture process involves the generation of crack surfaces, the release of fragments, and the splitting of the main crack into multiple branches [229]. According to Figure 5.2c to Figure 5.2f, the branching phenomenon is more pronounced in cases with smaller mesh sizes. This is attributed to the increased number of critical cohesive elements that are activated during the loading process in simulated samples with smaller mesh sizes. Consequently, a greater number of crack initiation sources naturally promotes more severe branching behavior [228–230]. Overall, this demonstrates that our HFDEM model can qualitatively (e.g., crack patterns) and quantitatively (e.g., tensile strength) predict the mode I failure process of the alumina ceramic.

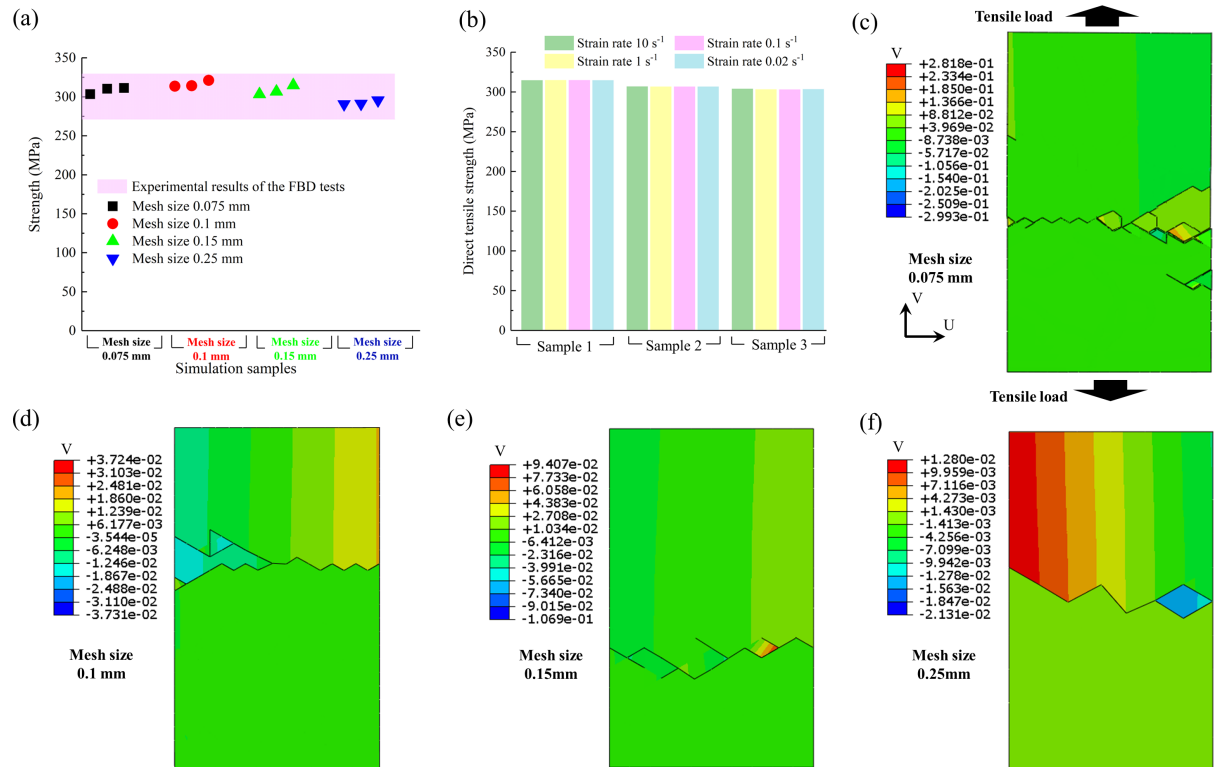


FIGURE 5.2: a) The purple-shaded area represents the indirect tensile strength of the CeramTec 98% alumina obtained by the FBD experiments in Section 5.5.1. The plotted points correspond to simulation results obtained using four distinct mesh sizes. b) The bar graph represents the tensile strength simulated by three distinct samples under four different tensile loading rates in quasi-static loading conditions. c)-f) The results show the vertical displacement field and the crack patterns across four distinct mesh sizes. Notably, a horizontal crack perpendicular to the loading direction is generated. In certain instances, this primary crack might bifurcate into several branches. The black arrows in c) show the tensile loading direction.

5.5 Experiments and numerical simulation of indirect tensile testing

In this section, we use experimental and HFDEM methods to study the indirect tensile behaviour of the CeramTec 98% alumina by FBD testing. The FBD tests are also called indirect tensile tests in this paper. First, the experimental method, process, and results are introduced in Section 5.5.1. Next, the modified HFDEM is applied to the indirect tensile tests in Section 5.5.2. By comparing the simulated indirect tensile results with the direct tensile results, the “underestimation”, “reasonable estimation”, and “overestimation” phenomena of the indirect tensile strength are interpreted in the HFDEM simulation. These simulation results are consistent with the experimental observation in our study and literature [155, 185, 208]. Then, the fracture patterns and fragment geometry of the indirect tensile tests are investigated to reveal their relationship with tensile strength and indirect tensile strength in Section 5.5.3.

5.5.1 Experimental method and results of FBD testing

In the current study, the flattened Brazilian disk (FBD) tests involving CeramTec 98% alumina are performed using a MTS 810 materials testing machine, as Figure 5.3a shows. The FBD specimen has a diameter of 8 mm and thickness of 4 mm with two parallel flat ends corresponding to the loading angle $2\omega_0 = 20^\circ$, shown in Figure 5.3b and c. The thickness-to-diameter ratio is 0.5, which is recommended in the literature [170]. The specimens are compressed under displacement control at a loading speed in the range of $\sim 10^{-4}$ to $\sim 10^{-2}$ mm/s. The force history is recorded by a 100 kN load cell with a background noise of approximately ± 1 N. An AOS PROMON U750 high-speed (HS) camera is used to visualize the specimen surface and monitor the macroscopic deformation at a full resolution of 1280 by 1024 pixels. The acquisition rate of the camera is set between 5 and 500 frames per second (FPS), and its value is related to the loading speed. In FBD tests, shear failure might occur near the loading zone due to friction between loading platens and specimen [155, 164]. To reduce the frictional effects and prevent premature edge failure (shear failure), high-pressure grease is applied between the surfaces of the loading platens and the flat ends of the specimen, as done in many previous experimental papers [61, 112–114, 164, 208].

For the quasi-static experiments, we perform six tests, and the variability of experimental results (i.e., loading rate, strain rate, tensile strength) is summarized in Table 5.3. In Table 5.3, the strain rate is calculated from the slope of the tensile strain-time history at the disk’s center; the loading rate is obtained from the slope of the loading curve;

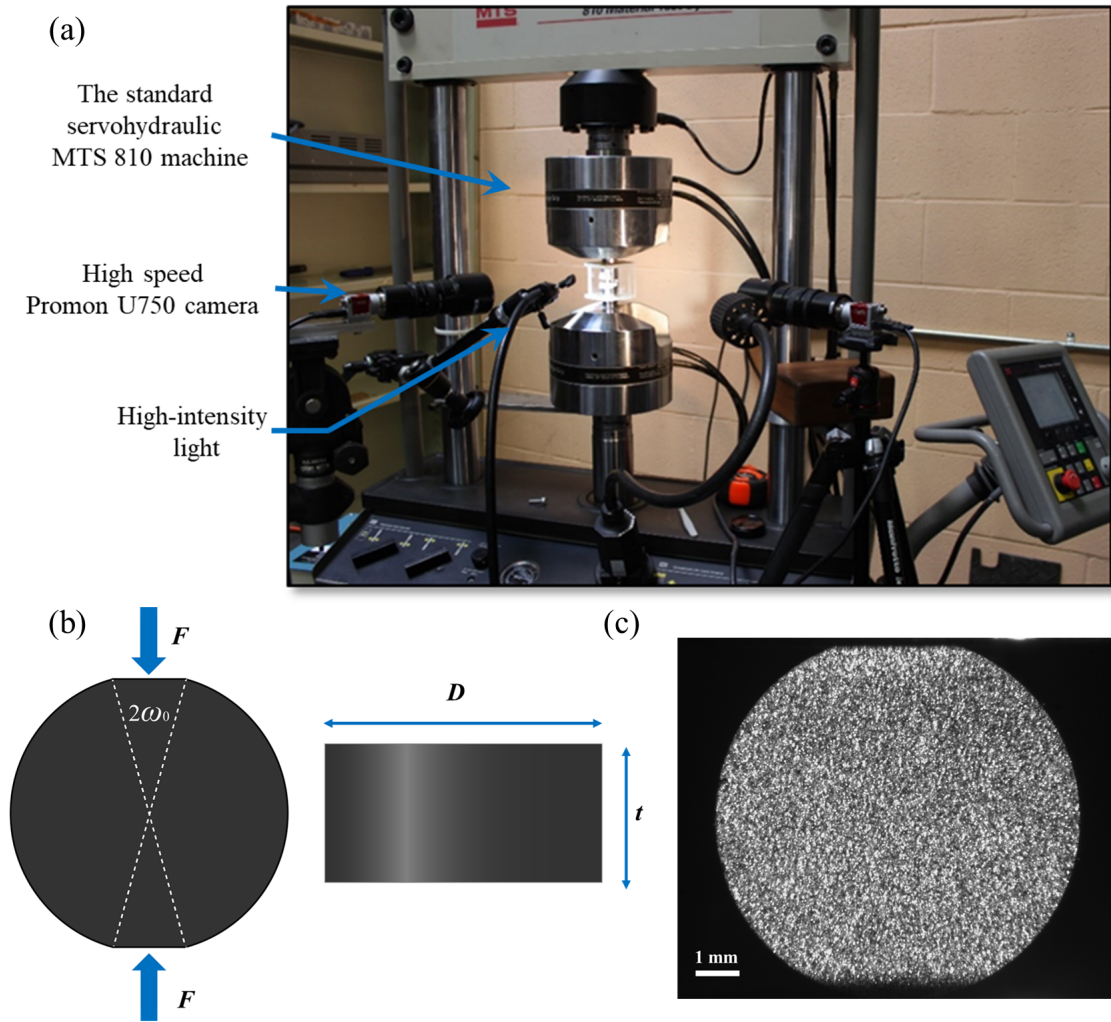


FIGURE 5.3: a) The flattened Brazilian disk (FBD) tests are performed using a MTS 810 material testing machine coupled with a high-intensity light and a high-speed (HS) camera. b) The schematic diagram of the FBD sample. The diameter D is 8 mm, thickness t is 4 mm, the loading angle $2\omega_0$ is 20° , and F is the applied loading during the test. c) The specimen is sprayed with speckle patterns to facilitate digital image correlation measurements.

the material tensile stress is determined by the tensile stress when the central crack first occurs. The tensile strength, σ_t , was proposed by Wang et al. [138]:

$$\sigma_t = k \frac{2F}{\pi D t} \quad (5.10)$$

where σ_t is the tensile strength of the material, and F is the applied loading force. D and t are the diameter and thickness of the sample, and k is a non-dimensional factor depending on the loading angle whose value is 0.9644 when $2\omega_0 = 20^\circ$ [138, 208]. It is observed that the material tensile strength is a nearly constant value under the quasi-static loading conditions in the range of 300.6 ± 29.2 MPa, which is consistent with the results from literature [61, 192, 208].

TABLE 5.3: The experimental results of the FBD tests

Strain rate (s ⁻¹)	Loading rate (N/s)	Material tensile strength (MPa)
7×10^{-6}	69.9	292.1
7.8×10^{-5}	755	324.9
7.8×10^{-5}	754	277.5
7.5×10^{-5}	738	271.4
6.9×10^{-4}	6780	321.7
6.9×10^{-4}	6770	329.8

5.5.2 The numerical simulation of FBD testing

The HFDEM model is employed for FBD testing, also referred to as the indirect tension simulation in this paper. To optimize computational time, we select a slice measuring 0.3 mm, approximately 1/13th of the thickness of the actual experimental specimen, as Rena et al. used in their study [68]. The remaining geometric parameters, including diameter and loading angle, match those of the specimen presented in Figure 5.3. Our model comprises of roughly 35,000 tetrahedral elements and 66,000 cohesive elements, with a selected mesh size of 0.15 mm. We impose plane strain boundary conditions on this model, which is also utilized in the indirect tension studies by Rena et al. [68] and Li and Wong [155]. Within our simulation, loading is applied at a constant velocity of 10 mm/s, in accordance with Figure 5.3b. The maximum time step is set at 3.6×10^{-10} s, following the methodology of Camacho and Ortiz [218]. The simulation incorporates the mechanical properties of CeramTec 98% alumina, as summarized in Table 5.1 and Figure 5.1. The shear strength is estimated to be approximately three times the tensile strength according to Markides et al. [163], leading us to select six cases with $\tau = 2.5, 3, 3.5, 4.0, 5.0$ and 8.0σ . For each case, we conduct three numerical simulations using a Monte Carlo approach to illustrate the specimen's variability. In our study, each simulation takes roughly 120 hours to complete; utilizing computing hardware equipped with an Intel Xeon CPU E5-2650 v4 @2.2 GHz with 24 cores and 48 threads.

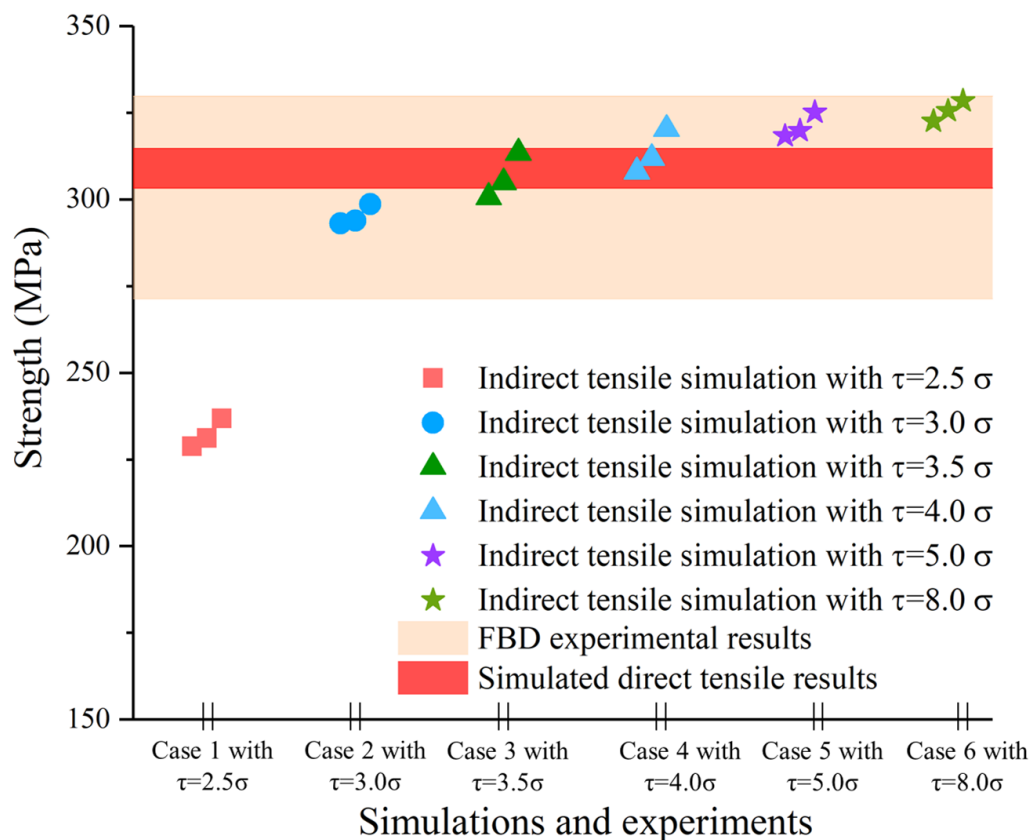


FIGURE 5.4: The area shaded in pink signifies the indirect tensile strength of CeramTec 98% alumina, as documented in Table 5.3. The area shaded in red corresponds to the simulated direct tensile strength derived using a 0.15 mm mesh size, as detailed in Figure 5.2. The points plotted on the graph represent the tensile strength from the HFDEM simulations of FBD testing (also known as indirect tension simulation) using a 0.15 mm mesh size, which are carried out with six different shear strengths.

Figure 5.4 presents a comparison of tensile strength values obtained from indirect tensile simulations, FBD experiments, and direct tensile simulations. The data demonstrates that the tensile strength derived from FBD experiments exhibits more variability than that from direct tensile simulations. In terms of the indirect simulations, case 1 with $\tau = 2.5\sigma$ and case 2 with $\tau = 3\sigma$ result in an underestimation of tensile strength when compared with direct tensile simulations. On the other hand, case 3 with $\tau = 3.5\sigma$ and case 4 with $\tau = 4.0\sigma$ yield reasonably accurate estimations. Interestingly, case 5 with $\tau = 5.0\sigma$ and case 6 with $\tau = 8.0\sigma$ overestimate the tensile strength in comparison to the direct tensile simulations. These distinct phenomena (underestimation, reasonable estimation, and overestimation) suggest that the indirectly obtained tensile strength via FBD testing is significantly influenced by the failure strength of the disk structure, which has been reported in previous studies [155, 185, 208]. This indicates that the aforementioned phenomena correlate with the fracture patterns and fragments observed

in the FBD testing. The specific nature of this relationship is further elucidated in the following section.

5.5.3 The fracture patterns and fragmentation

The Brazilian disk test assumes that the material's tensile strength can be evaluated by initiating a fracture along the diametrical plane when subjected to a compressive load applied along the diameter. This is because most brittle materials fail at their uniaxial tensile strength in the biaxial stress fields of BD testing [261]. The verification of the BD test is usually based on the fracture initiation process captured by a high-speed camera. For example, Swab et al. [185] and Gui et al. [262] used visual examination and photogrammetric analysis methods to capture the fracture patterns, as shown in Figure 5.5. They found that besides the fracture along the diametrical plane, some cracks were also generated at the loading interface. Swab et al. [185] observed that fracture initiation occurred at the loading points, deviating from the expected process in a valid Brazilian disk test where fracture typically initiates in the middle portion of the diameter. In these invalid tests [185], the loading point cracks led to a triple cleft fracture, and the measured tensile strength was lower than the true tensile strength, which is termed the “underestimation” phenomenon in this paper. However, in the case of advanced ceramics possessing high stiffness and strength, the initiation and propagation of cracks occur within microseconds [182]. This is significantly shorter than the loading time (e.g., seconds) in quasi-static tests [208]. Given that the camera used in the quasi-static tests is very hard to capture the fracture process because of the very fast failure process, we employ a combination of experimental methods and numerical simulations to investigate the relationship between the fracture patterns, fragment, and the phenomena of “underestimation”, “reasonable estimation”, and “overestimation”.

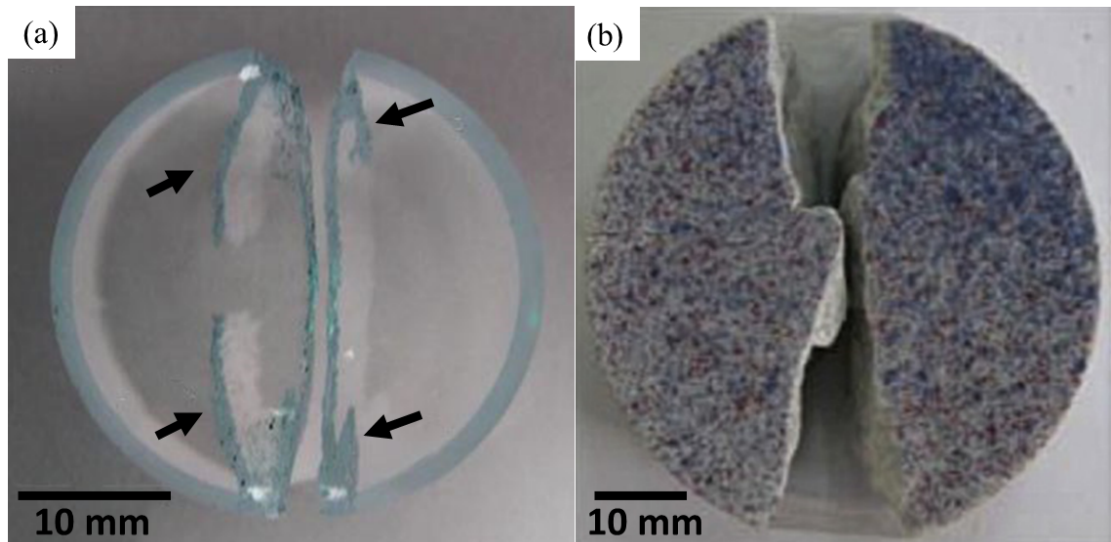


FIGURE 5.5: Fracture patterns observed in the BD tests of a) a coarse-grained, hot-pressed magnesium aluminate spinel by Swab et al. [185] and b) a rock material by Gui et al. [262]. The black arrows in (a) show some cracks initiated from the load application points.

The findings from our indirect tensile simulation reveal four distinct types of fracture and fragmentation patterns, which are illustrated in Figures 5.6 to 5.9. Specifically, in the indirect tensile simulation of case 1 where $\tau = 2.5 \sigma$, Figure 5.6a demonstrates the formation of two cracks at the loading points. However, these cracks do not extend along the central diametral plane but tend to curve slightly out of this plane in the mid-region. As depicted in Figure 5.6b, the sample divides into three primary fragments. These fracture patterns and fragmentation fail to meet the criteria that necessitate the disk to fail at its tensile strength in the biaxial stress fields located at the central diametral plane during FBD testing [261]. Consequently, case 1 represents an unsuccessful FBD test, resulting in a significantly underestimated indirect tensile strength.

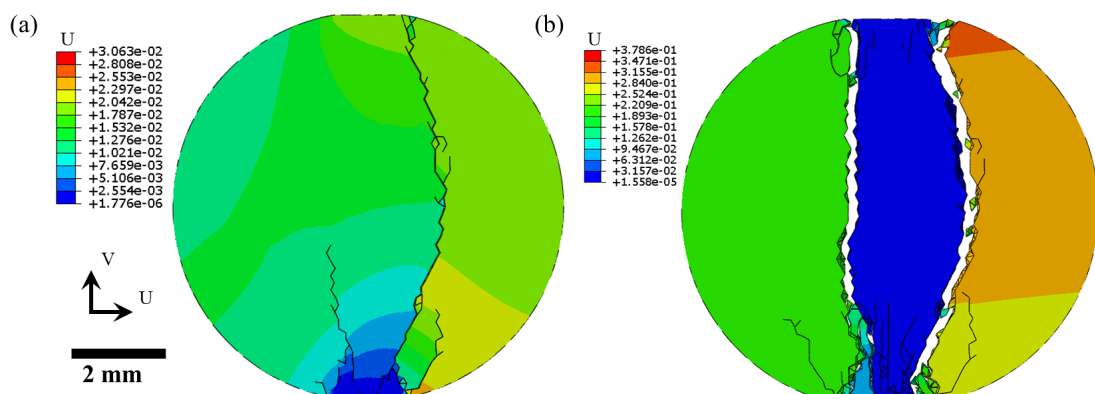


FIGURE 5.6: Fracture patterns and fragmentation observed in the indirect simulation of case 1 with $\tau = 2.5 \sigma$. a) two cracks are generated at the loading points. b) the sample breaks into three primary fragments in the simulation.

Figure 5.7a and b illustrate the fracture pattern and fragments from the indirect tensile simulation in case 2, where $\tau = 3 \sigma$. As observed in Figure 5.7a, two types of cracks emerge simultaneously: a central crack traversing along the central diametral plane and four curved loading point cracks. Notably, the loading point cracks exhibit a slight curvature rather than forming straight lines. These cracks are preliminary indications of the triple cleft fracture pattern frequently observed in BD testing [185, 262], as shown in Figure 5.5. Figure 5.7b depicts that more fragments are generated compared with case 1. A notable bulge is seen in the middle of the fracture surface for the two side fragments, caused by the curved loading point cracks. The shape of these simulated fragments aligns with the fragments from our FBD experiments, as shown in Figure 5.7c. This triple cleft fracture pattern and associated fragments are the most commonly observed in our FBD experiments. However, their measured indirect tensile strength is still slightly underestimated (see Figure 5.4).

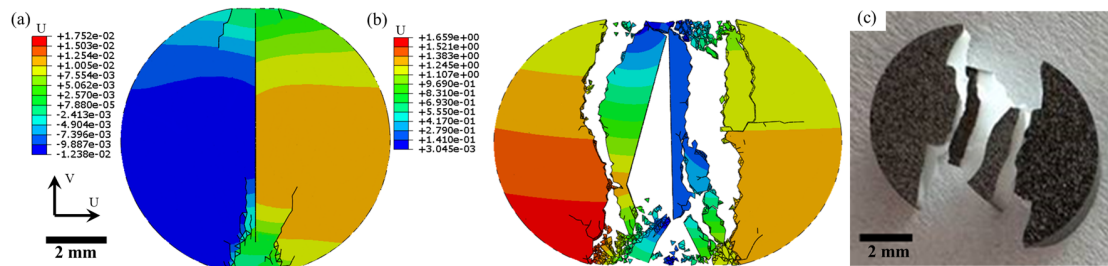


FIGURE 5.7: Fracture pattern and fragments observed in the indirect simulation of case 2 with $\tau = 3 \sigma$. a) Two kinds of cracks emerge simultaneously: the central crack along the central diametral plane and the loading point cracks. b) Fragments generated in the indirect simulation of case 2 with $\tau = 3 \sigma$. c) Fragments generated in the FBD testing.

For the indirect tensile simulations in case 3 with $\tau = 3.5 \sigma$, and case 4 with $\tau = 4.0 \sigma$, both of them can reasonably estimate the tensile strength. Additionally, they exhibit identical fracture patterns and fragments, as shown in Figure 5.8. These fracture patterns and fragments bear a resemblance to those in Figure 5.7. The only discernible difference lies in the loading point cracks, which are straighter than those in Figure 5.7, resulting in straight cracks for the two side fragments with a more flat fracture surface.

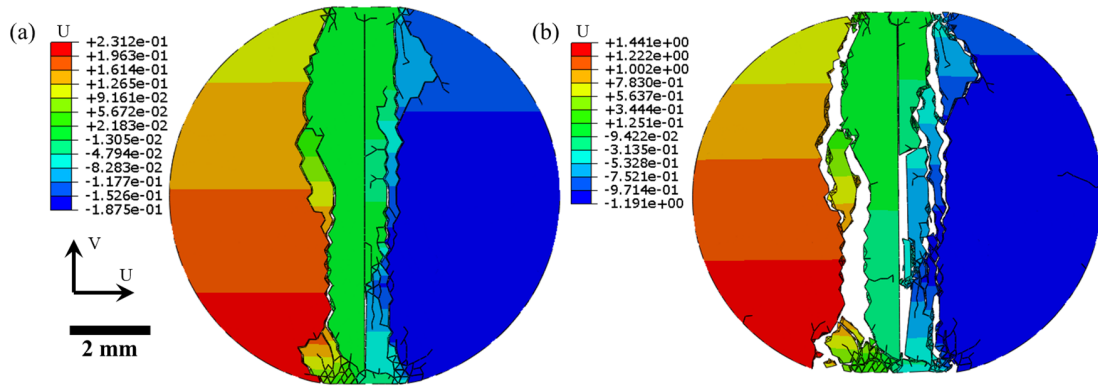


FIGURE 5.8: Fracture pattern and fragments observed in the indirect simulations of case 3 with $\tau = 3.5 \sigma$ and case 4 with $\tau = 4.0 \sigma$. a) Two kinds of cracks emerge simultaneously: the central crack along the central diametral plane and the straight loading point cracks. b) Fragments generated in the indirect simulation.

The fracture and fragment patterns derived from our indirect simulations for case 5 with $\tau = 5.0 \sigma$ and case 6 with $\tau = 8.0 \sigma$ are shown in Figure 5.9. In both simulations (Figure 5.9a) and the experiment (Figure 5.9d), it is observed that the central crack running along the central diametral plane appears first. Subsequently, the loading point cracks and secondary cracks emerge, as shown in Figure 5.9b and e. It is noteworthy that these loading point cracks are straight as opposed to curved. Figure 5.9c and f display the fragments obtained through simulation and experiments, respectively, which agrees well with each other. Observations reveal that these fragments consist of four quarter-circles and some long strip-shaped fragments. This occurs because the failure load is considerably higher, which results in more fragments, and subsequently overestimates the tensile strength.

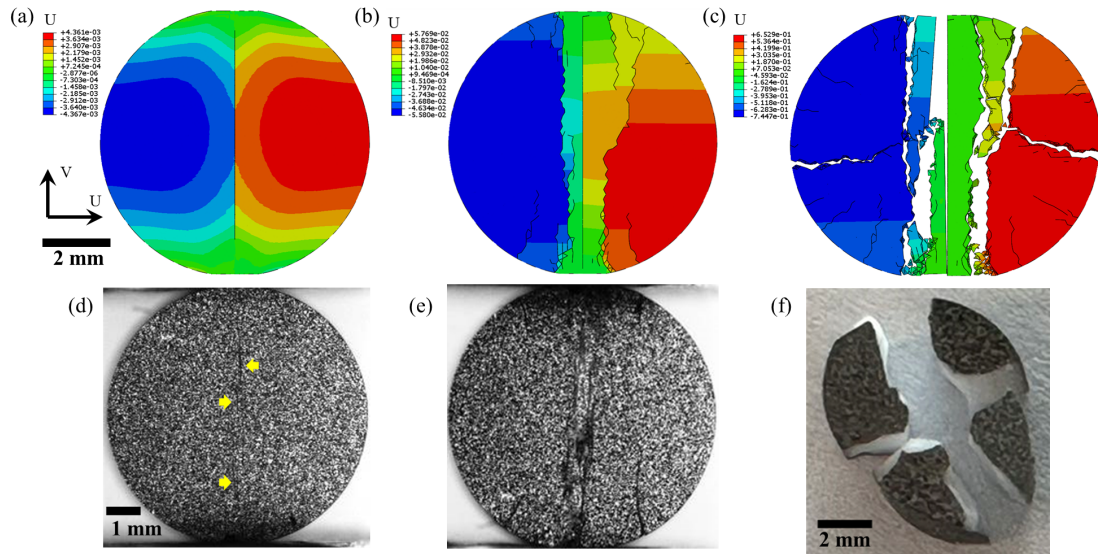


FIGURE 5.9: Fracture pattern and fragments observed in the indirect simulation of case 5 with $\tau = 5.0 \sigma$ and case 6 with $\tau = 8.0 \sigma$. a) and d) are the central crack running along the central diametral plane that appears in the indirect simulation and FBD experiment respectively, and the yellow arrows in d) highlight the central cracks observed in the experiment. b) and e) are three kinds of cracks, including the central crack, the secondary crack and the loading point crack, observed in the indirect simulation and FBD experiment respectively. c) and f) are fragments generated in the indirect simulation and FBD experiment respectively.

By comparing Figures 5.6 to 5.9, we found the three kinds of phenomena (“underestimation”, “reasonable estimation”, and “overestimation” of the tensile strength) are related to the competition between the central crack and loading point cracks. The Brazilian disk specimen is expected to split along the compressive diametral line, where a central crack forms due to tensile stress. However, in many brittle materials, particularly the alumina ceramics investigated in this study, the compressive stress concentration near the loading platen may induce early shear failure fractures, resulting in cracks at the loading points [155]. These loading point cracks have a significant influence on the results of Brazilian disk tests. According to our simulated results (Figures 5.6 and 5.7), brittle materials with weak shear strength tend to develop curved cracks at the loading points. In these scenarios, the “tensile strength” calculated from test results is typically lower than the actual value. When materials possess strong shear strength, the loading point cracks are straight (Figures 5.8 and 5.9), leading to a “reasonable estimation” or “overestimation” of the tensile strength. Furthermore, additional secondary and horizontal cracks are noted in cases of “overestimation” of tensile strength, corresponding to the structural failure of the Brazilian Disk (BD) samples, as shown in Figure 5.9.

The fracture process in advanced ceramics typically occurs rapidly, making it difficult to capture crack patterns. Therefore, the current study suggests using the geometry of the fragments as a means to analyze the measured “tensile strength”. Specifically, our study

finds four different kinds of fragments obtained using the modified HFDEM model. 1) When the BD sample breaks into three primary fragments due to curved loading point cracks without a central crack, resulting in the side fragments resembling crescent moons, it signifies invalid testing and a significantly underestimated tensile strength. 2) If the BD sample splits into two primary fragments and some long strip-shaped fragments because of curved loading point cracks and a central crack, which creates a noticeable bulge in the middle of the two fragments, this indicates an underestimated tensile strength. 3) If the BD sample breaks into two primary fragments and several long strip-shaped fragments due to straight loading point cracks and a central crack, leaving the two main fragments with flat fracture surfaces, it suggests a reasonable estimated tensile strength. 4) When the BD sample breaks into four quarter-circle fragments and multiple long strip-shaped fragments, resulting from straight loading point cracks, a central crack, secondary cracks, and horizontal cracks, it indicates an overestimation of tensile strength. Thus, these results provide a solid foundation for guiding future Brazilian disk experiment interpretation and tensile strength assessments in brittle materials.

5.6 Conclusion

This paper presents the development and implementation of a modified hybrid finite-discrete element method to investigate the mode I tensile response of alumina ceramics, including direct and indirect tensile simulation. Additionally, the flattened Brazilian disk experiments under the quasi-static loading condition are carried out to support the computational modelling.

The computational method developed in the current study integrates a hybrid finite-discrete element method with a coupled damage and friction cohesive model, which provides a sufficient residual shear strength for the materials under compression-and-shear loading due to friction. To quantify the statistical variability of the micro-flaws in the alumina ceramics, a microscopic stochastic fracture model based on a Weibull distribution and Monte Carlo simulation is integrated into the modified HFDEM method. This modified HFDEM is subsequently applied to simulate direct tensile failure processes of the CeramTec 98% alumina under quasi-static loading. The simulation results show that the modified HFDEM can qualitatively (e.g., crack patterns) and quantitatively (e.g., tensile strength) reproduce the direct tensile failure process of an alumina ceramic.

The modified HFDEM is applied to reproduce the flattened Brazilian disk experiments. By comparing the simulated indirect tensile strength with direct tensile strength, the model for the Brazilian disk shows three kinds of phenomena: “underestimation”,

“reasonable estimation”, and “overestimation” of the tensile strength, as Figure 5.4 shows. The HFDEM model is then utilized to investigate the mechanisms behind these three kinds of phenomena. The simulated results show the mechanism is related to the competition between loading point cracks and the central crack, as Figures 5.6 to 5.9 shows.

The validation of the modified HFDEM is performed with FBD experiments. The consistent findings from our simulations and experiments elucidate the relationship between fracture patterns, fragment geometry, and indirect tensile strength. We observe that: 1) When the curved loading point cracks appear without a central crack, it leads to a notably underestimated indirect tensile strength, as Figure 5.6 shows. 2) The triple cleft fracture pattern (characterized by the central crack and bulges in the middle of the fracture surface for the two side fragments) corresponds to an underestimated indirect tensile strength, as Figure 5.7 shows. 3) Having a straight central crack and a clean fracture surface for the two side fragments results in a reasonable estimation of the indirect tensile strength, as Figure 5.8 shows. 4) The presence of a central crack, the secondary cracks, and four quarter-circle fragments lead to an overestimation of the indirect tensile strength, as Figure 5.9 shows. From these results, the fracture and fragmentation patterns obtained by our modified HFDEM mode can be used to analyze the measured “tensile strength” by BD testing.

Chapter 6

Modified Hybrid Finite-discrete Element Modeling of Compressive Failure in Alumina Ceramics

Submitted as **Jie Zheng**; Li, HY; Zaiemyekheh, Z; Sun, N.; Sayahlatifi, S.; Chen, ZT and Hogan, JD. *Modified Hybrid Finite-discrete Element Modeling of Compressive Failure in Alumina Ceramics*, International Journal of Mechanical Sciences (2024).

Author	Contributions
Jie Zheng	Conceived the ideas and experimental design of the study; Developed theoretical methodology; Performed experiments/data collection; Carried out the experiments; Data analysis and interpretation; Primary author (drafted the manuscript).
Li, HY	Provided revisions to scientific content of manuscript
Zaiemyekheh, Z	Provided revisions to scientific content of manuscript
Sun, N	Provided revisions to scientific content of manuscript
Sayahlatifi, S	Provided revisions to scientific content of manuscript
Chen, ZT	Provided revisions to scientific content of manuscript
Hogan, JD	Provided revisions to scientific content of manuscript; Provided stylistic/grammatical revisions to manuscript; Principal investigator

6.1 Abstract

This paper developed a modified hybrid finite-discrete element model (HFDEM) for alumina ceramics, and the model is validated with quasi-static uniaxial compression

experiments coupled with a digital image correlation technique. This model proposed the linear- and power-law cohesive constitutive behaviour to describe the crack nucleation and propagation processes, respectively. Additionally, our model considered the flaw distribution of the material by coupling a microscopic stochastic fracture model. This HFDEM accounted for various phenomena and mechanisms that manifest during compressive failure of advanced ceramics: fracture growth follows the wing-crack-type failure mode, catastrophic failure and fragmentation behavior. The proposed model was validated by comparing the simulated quasi-static compressive stress-strain responses to the experimental results, demonstrating that the method can accurately predict the mechanical response of the alumina ceramic under uniaxial compressive loading. Once validated, the effects of other mechanical properties (e.g., Poisson's ratio, elastic modulus, shear strength, and tensile strength) on the compressive stress-strain responses were explored. Notably, the elastic modulus and Poisson's ratio were found to have a negligible impact on the peak compressive strength during uniaxial compression. Additionally, the impact of increasing tensile strength on compressive strength becomes less significant. Conversely, shear strength significantly affects both the peak compressive strength and the failure strain. Overall, this study provides a qualitative (e.g., fracture and fragmentation behaviour) and quantitative (e.g., stress-strain response) understanding of alumina ceramic under quasi-static uniaxial compressive loading and provides a theoretical guidance for future material design and optimization.

6.2 Introduction

Advanced ceramics are often used as critical structural components in protection [197] and aerospace applications [195] for their desirable properties, such as low density [83], high hardness [3], and high wear resistance [4]. In ballistic applications, the role of the ceramic upon impact is to fracture the tip of the incoming projectile [58, 198, 199] and to distribute the load [198], followed by progressive erosion of the projectile and fragmentation process of the ceramic [8, 263]. During impact, various failure mechanisms (e.g., fracture [197] and granular flow [46]) are activated and evolve spatially and temporally to dissipate energy [264]. To better understand these mechanisms, controlled experiments like uniaxial compression experiments are performed with imaging [6]. In the initial phase of uniaxial compression, pre-existing micro-cracks or pores in ceramics serve as stress concentration sites [34], which have significant effects on fracture and failure processes [5, 23]. Recently, Nohut [203] discovered that the distribution of flaws within the material significantly affected the strength of alumina ceramics, and he suggested that a Weibull distribution analysis can effectively describe the material strength and its flaw system. In a related study, Lo et al. [5] thoroughly examined the microstructural

and mechanical properties of AD85 alumina. Their findings highlighted that the detailed characteristics of flaws, encompassing aspects like pore size, spatial distribution, orientation, and morphology, significantly influenced the mechanical performance of alumina ceramics. Conceptually, the evolution of flaws in advanced ceramics is often described using the “wing crack model” [35, 36, 38], where micro-cracks of random orientation grow parallel to the compressive loading direction as a consequence of the resolved mode I tensile opening failure at the crack tip [37, 39]. In the literature, various models of macroscopic crack propagation have been proposed based on the wing-crack model, such as crack interaction [41, 42], dilatancy [43], and coupled sliding and damage models [44, 45]. However, these models do not include the post-fracture behavior (e.g., fragmentation) of advanced ceramics. This study proposes a modified hybrid finite-discrete element model to build on these past works and improve upon their limitations by considering both the fracture and fragmentation processes. The modified hybrid finite-discrete element model developed in this study also considers the inherent microstructural flaws of an alumina ceramic based on experiments [11, 203, 214] and numerical studies [222, 253].

The ability to capture the fragmentation process in simulation is important as it is the next dominant phase of study to understand the post-fracture behaviour of advanced ceramics after crack initiation and fracture growth [14]. For example, Grady and Kipp [46] found that all three fracture stages (crack nucleation, crack propagation, and crack coalescence) would influence the fragmentation process, and the fragmentation size was associated with mechanical properties of the material and loading rate. Later, Hogan et al. [13–15] identified two distinct fragmentation mechanisms by observing impact and compression experiments of advanced ceramics: the first fragmentation mechanism was “microstructure-dependent” that was responsible for the relatively smaller fragments produced during loading ($<100 \mu\text{m}$), and the other mechanism was the “structure-dependent” fragmentation mechanism that produced relatively larger fragments ($>100 \mu\text{m}$). For lower loading rates, especially under the quasi-static loading condition, “structure-dependent” fragmentation was found to be the dominant mechanism, and the fragment size was relatively large [13]. Thus, our study focuses on the “structure-dependent” fragmentation mechanism for quasi-static experiments through implementing the modified hybrid finite-discrete element model proposed in the current study. In addition to the structural-scale fragments, frictional sliding is another mechanism observed in the fragmentation process of advanced ceramics. In their study, Hu et al. [258] obtained a direct conclusion that the compressive strength is related to frictional sliding when they studied the compressive failure of aluminum nitride. In a separate study, Nicewicz et al. [265] also found experimentally that compaction and frictional interactions played an important role in the breakage of alumina ceramic. The

limitation in considering fragmentation processes in conventional numerical methods and the lack of consideration of the frictional sliding on the compressive strength of advanced ceramics motivate our current joint numerical and experimental investigation.

Besides the experimental studies mentioned above, numerous computational models have been established to describe the behaviour of brittle materials in the past studies. These include the continuum damage mechanics (CDM) [44, 45], the extended Finite Element Method (XFEM) [65], and the cohesive zone model (CZM) [66]. The CZM has a number of advantages over the other methods, including: 1) creating new surfaces following the Griffith energy criterion, 2) allowing for branched and intersecting cracks, and 3) the removal of the singularity presented in linear elastic fracture mechanics [67]. The CZM has been applied to study the compressive response of advanced ceramics [68, 69], dynamic fracture [71], and fragmentation of brittle materials [70]. In the CZM method, new surfaces are created when a crack occurs, and these new faces require numerical contact algorithms, which makes CZM ideally suited for discretized methods [72]. Furthermore, to address the mutually interacting separate fragments in fracture processes, Munjiza [31] developed an innovative numerical approach, known as the hybrid finite-discrete element method (HFDEM). One distinct feature of the HFDEM is that it models the transition from a continuum (e.g. finite element method) to a discontinuous-based method (e.g. discrete element method) [32, 33] to overcome the inability of these methods to capture progressive damage and failure processes in rock materials [73]. The HFDEM approach was initially developed to simulate geomaterials [73–75]. However, more recently, this method has been extended to simulate the failure of ceramics [33]. In HFDEM, materials are often discretized as triangle elements (two-dimensional) or tetrahedral elements (three-dimensional), and cohesive elements are utilized to connect these discrete elements to represent the potential arbitrary crack path [55]. Then, an explicit finite difference time integration scheme is applied to solve the motion of the discretized system [31]. Currently, HFDEM is popularly used in geological materials, as it can explicitly capture the process of fracture nucleation and growth, as well as the interaction of newly-created discrete fragments [55, 72, 76]. To date, limited studies have applied three-dimensional HFDEM to advanced ceramics, which is pursued in this paper.

Motivated by these previous studies, this paper aims to develop a modified three-dimensional HFDEM model to describe the fracture and fragmentation processes of an alumina ceramic. This method focuses on macroscopic failure, and accounts for various mechanisms that manifest during compressive failure of advanced ceramics: 1) fracture growth via the wing-crack model [35, 36, 38], 2) catastrophic failure [266], and 3) the “structure-dependent” fragmentation process [15]. To guide model development, quasi-static uniaxial compression experiments of alumina ceramic are performed coupled with the digital image correlation (DIC) technique to resolve small strains and obtain

2D field information. The stress-strain responses and the corresponding ratio of axial to lateral strain are obtained, and these experimental results are used to validate the numerical model. Once validated, this model is applied to provide theoretical guidance for material development and improvement. Specifically, the model explores the effect and variation of mechanical properties (e.g., Young's modulus, Poisson's ratio, tensile and shear strength) on the failure of alumina ceramics, and links between these properties and microstructural features that may be controlled via manufacturing [209, 211, 212].

6.3 Experimental methods and results

In this study, experiments on alumina ceramics were performed under uniaxial quasi-static conditions to study variability in stress-strain and Poisson's ratio evolution. In the experiments, a commercially available alumina ALOTEC 98 SB from CeramTec (which is called CeramTec 98% in this paper), Germany, was studied. The number "98" refers to the alumina content being approximately 98% in mass percentage, with the remainder being sintering additives or trace impurities. The test specimen was cuboids with dimensions of $2.3 \times 2.7 \times 3.5$ mm used for mechanical testing, as shown in Figure 6.1. Cuboid was selected to enable better imaging and digital image correlation (DIC) analysis. In the figure, the loading platen and base platen are observed on the top and bottom of the image, and the speckle pattern that is used for DIC (discussed later) is observed on the specimen surface. This section will give brief and relevant information about the material and experiments, with additional details found in Zheng et al. [11].

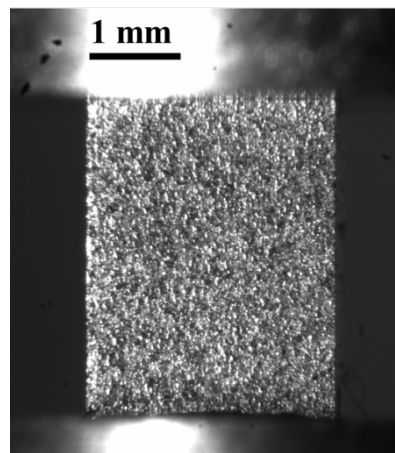


FIGURE 6.1: The alumina ceramic sample under a quasi-static uniaxial compression experiment, sprayed with a speckle pattern necessary for DIC measurements of axial and lateral strains.

6.3.1 Experimental method

A standard MTS series 810 servo-hydraulic machine was used to conduct the quasi-static uniaxial compression tests. The specimens were compressed along the vertical direction in Figure 6.1 under a displacement control setting with a nominal strain rate of $\sim 10^{-4}$ s⁻¹. The force history was recorded by a 100 kN load cell with a background noise of approximately ± 1 N, and the engineering stresses were computed by dividing the measured force by the cross-sectional area of tested specimens. Protective tungsten carbide jacketed platens were used to prevent indentation into the machine, as being used in the literature [112–114]. High-pressure grease was applied between the specimen and loading platens to reduce friction and allow for free lateral expansion. The data acquisition rate of the MTS machine was set at 30 Hz. An AOS PROMON U750 high-speed (HS) camera was used to provide visualization on the specimen surface to monitor the macroscopic deformation at 100 frames per second (FPS) at a full resolution of 1280 by 1024 pixels.

DIC analysis was used to obtain the two-dimensional strain information (i.e., axial and lateral strains) during the experiments. These strains were matched in time with the stress calculated from the MTS machine to acquire complete stress-strain curves for each experiment. As shown in Figure 6.1, the specimens were sprayed with speckle patterns (with the paint spot size between 20 and 30 μm) using a fine-tipped airbrush to facilitate correlation, as done in previous papers [112, 113]. VIC2D (V6 2018) software was employed to perform the DIC analysis. During the analysis, the surface of the sample was discretized with a subset size of 31 by 31 pixels and a step size of 7 pixels. The zero-normalized sum of squared differences (ZNSSD) criterion and the optimized 8-tap interpolation scheme were used to perform correlation analysis to obtain the engineering strain. The current work follows the experimental methodologists used in previously published papers on brittle materials by Li et al. [112], Zheng et al. [11], and Zaiemyekeh et al. [267].

6.3.2 Experimental results

Figure 6.2a shows the stress-strain response of the alumina ceramic obtained from the quasi-static uniaxial compression experiments. The strain rates are obtained by a linear fit of the strain-time data, which ranged from 1.6×10^{-5} to 1.6×10^{-3} s⁻¹. The peak compressive stress is found to be 3.39 ± 0.31 GPa at a corresponding failure strain of 0.99 ± 0.1 %. Young's modulus is obtained by calculating the slope of the stress-strain curve for all specimens, which ranges from 345 GPa to 388 GPa, with an average of 362 ± 20 GPa.

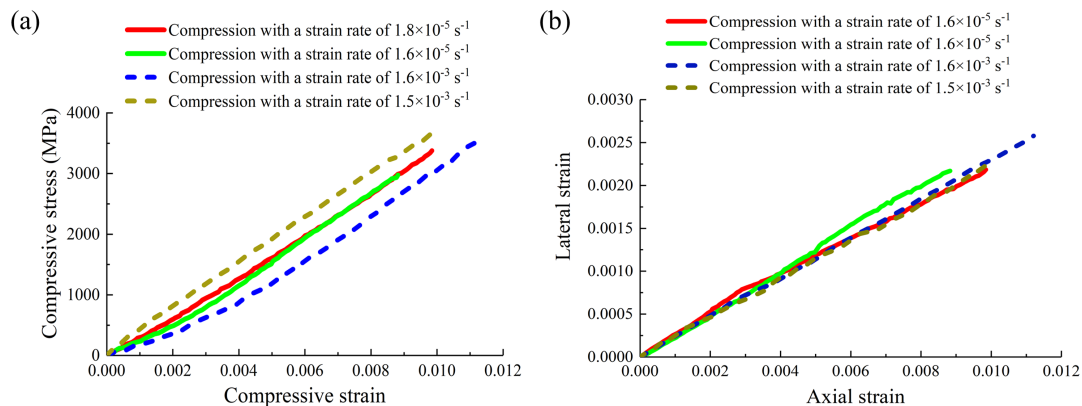


FIGURE 6.2: (a) The engineering axial stress-strain curves of alumina ceramic specimens under quasi-static uniaxial compressive loading at strain rates of 1.6×10^{-5} to $1.6 \times 10^{-3} \text{ s}^{-1}$. (b) Lateral and axial strain curves obtained from the DIC analysis are used to determine Poisson's ratio of the material.

For Poisson's ratio as an important material parameter, there is still an argument about whether Poisson's ratio of ceramics varies during the loading process [77, 268, 269]. In one study, Wang and Ramesh [268] noted an evolution of Poisson's ratio in SiC-N during dynamic uniaxial compression experiments. However, in experiments involving AlON, Paliwal et al. [269] did not observe such a phenomenon, and they regarded Poisson's ratio as constant during the loading process [77]. In the present work, we plot the lateral versus axial strain response for all experiments (see Figure 6.2b). It is observed that the ratio of lateral to axial strain of alumina ceramic can be considered as constant during the quasi-static uniaxial compression, whose slope (Poisson's ratio) ranges from 0.22 to 0.26 with an average of 0.24 ± 0.02 , which is in good agreement with the valued reported for other alumina ceramics [11, 61, 113, 202].

6.4 Computational approach

In this section, a modified hybrid finite-discrete element method (HFDEM) is proposed to describe the failure process of brittle materials under quasi-static uniaxial loading and then applied to the alumina ceramic. First, a three-dimensional (3D) coupled damage and friction law of the cohesive zone method is selected to represent the constitutive response of brittle materials [255, 256]. Next, two types of damage evolution law, linear- and power-law characteristics, are presented to model the catastrophic failure of brittle materials observed in the experiments [77, 240, 241]. Then, to solve the problem numerically, the model is implemented with a user-material (VUMAT) Fortran user-subroutine in ABAQUS/Explicit. Finally, the modified hybrid finite-discrete element method is presented [31–33].

6.4.1 The coupled damage and friction law of the cohesive zone method

Alfano and Sacco [255] proposed a modified cohesive zone model that integrated interface damage with friction, dividing a unit representative elementary area (REA) of the interface into a damaged part (D) and an undamaged part ($1-D$). In their approach, friction was considered only within the damaged portion when the REA experienced compressive loading.

Expanding upon the two-dimensional model introduced by Alfano and Sacco [255], we have developed an extension of this model to accommodate a three-dimensional system:

$$\boldsymbol{\sigma} = (1 - D)\mathbf{K}\boldsymbol{\delta} + D\boldsymbol{\sigma}^d \quad (6.1)$$

with

$$\boldsymbol{\sigma} = \begin{bmatrix} \sigma_1 \\ \tau_1 \\ \tau_2 \end{bmatrix}, \quad \mathbf{K} = \begin{bmatrix} K_1 & 0 & 0 \\ 0 & K_2 & 0 \\ 0 & 0 & K_3 \end{bmatrix}, \quad \boldsymbol{\delta} = \begin{bmatrix} \delta_1 \\ \delta_2 \\ \delta_3 \end{bmatrix}, \quad \boldsymbol{\sigma}^d = \begin{bmatrix} \sigma_1^d \\ \tau_1^d \\ \tau_2^d \end{bmatrix}$$

In this context, $\boldsymbol{\sigma}$ denotes the interface stress, with σ_1 representing the normal stress, and τ_1 and τ_2 indicating the shear stresses in two orthogonal directions. D is the scalar damage parameter of the REA, where $D = 0$ signifies an intact state and $D = 1$ indicates a fully damaged state. \mathbf{K} is the cohesive stiffness at the interface, with subscript 1 for the normal direction and subscripts 2 and 3 for the shear directions. $\boldsymbol{\delta}$ symbolizes relative displacements, and $\boldsymbol{\sigma}^d$ is the stress within the damaged portion, governed by the Coulomb friction law, as defined by:

$$\sigma_1^d = \frac{(|K_1\delta_1| - K_1\delta_1)}{2}, \quad \tau^d = \begin{bmatrix} \tau_1^d \\ \tau_2^d \end{bmatrix} = \begin{bmatrix} K_2 \left(\delta_2 - \delta_2^{di} \right) \\ K_3 \left(\delta_3 - \delta_3^{di} \right) \end{bmatrix} \quad (6.2)$$

with

$$\dot{\delta}_n^{di} = \dot{\lambda} \frac{\tau_n^d}{|\tau^d|} \quad (n=1, 2)$$

accompanied by the additional Kuhn-Tucker conditions [255]:

$$\mu\sigma_1^d + |\tau^d| \leq 0, \quad \dot{\lambda} \geq 0, \quad \dot{\lambda} \left(\mu\sigma_1^d + |\tau^d| \right) = 0 \quad (6.3)$$

where μ represents the coefficient of friction, and λ is an internal variable.

6.4.2 Damage evolution with linear- and power-law characteristic

Catastrophic failure is a typical failure characteristic of brittle materials. Hao et al. [270] reported a specific precursor of catastrophic failure in rock experiments, which they called “a power-law singularity of responses”. This characteristic has also been observed in experiments involving ceramics [77, 240, 241]. To account for the characteristic of “catastrophic failure” in the present study, the damage evolution model defines the failure as being reached when the damage evolution satisfies the following criterion:

$$\left[\frac{\partial D}{\partial \delta_e} \right]_{\delta_e=\delta_c} \rightarrow +\infty \quad \text{and} \quad \left[\frac{\partial \delta_e}{\partial D} \right]_{\delta_e=\delta_c} \rightarrow 0 \quad (6.4)$$

where δ_e is the effective relative displacement ($\delta_e = \sqrt{\delta_1^2 + \delta_2^2 + \delta_3^2}$), and δ_c represents the critical displacement when interface failure occurs. Based on the assumption that δ_e is continuous and can be derived by damage D before D reaches 1, δ_e can be expanded using a Taylor series to:

$$\delta_e = \delta_c + \left[\frac{\partial \delta_e}{\partial D} \right]_{\delta_e=\delta_c} (D_c - D) + \frac{1}{2} \left[\frac{\partial^2 \delta_e}{\partial D^2} \right]_{\delta_e=\delta_c} (D_c - D)^2 + O(D^2) \quad (6.5)$$

Neglecting the high-order term in Equation (6.5) and substituting Equation (6.4) into Equation (6.5), the damage evolution can be expressed as a function of the effective relative displacement δ_e :

$$D = D_c - \sqrt{-2 \left[\frac{\partial^2 \delta_e}{\partial D^2} \right]_{\delta_e=\delta_c}} (\delta_c - \delta_e)^{1/2} = D_c - C(\delta_c - \delta_e)^{1/2} \quad (6.6)$$

with

$$C = \sqrt{-2 \left[\frac{\partial^2 \delta_e}{\partial D^2} \right]_{\delta_e=\delta_c}} \quad \text{and} \quad D_c = 1$$

where the constant value C can be obtained from three-point-bending experiments [240, 241]. We use a power law damage evolution form [271] to replace the calculation process of the constant value C :

$$D = 1 - \left(\frac{\delta_c - \delta_e}{\delta_c - \delta_m^0} \right)^\alpha = 1 - (\delta_c - \delta_m^0)^{-\alpha} (\delta_c - \delta_e)^\alpha \quad (6.7)$$

Comparing Equation (6.6) with the power law damage evolution in Equation (6.7), it can be determined that $\alpha = 0.5$ in Equation (6.7), and $C = (\delta_c - \delta_e)^{0.5}$ in Equation (6.6) for “a power-law singularity of responses” [77, 240, 241, 270]. It should be noted that

if $\alpha = 1$, this model degrades into a linear damage evolution, which is utilized in many studies of brittle materials [74, 75, 126, 253]. For a damage value in the range of 0 to 1, the damage evolution can be expressed as:

$$D = \max\left\{0, \min\left\{1 - \left(\frac{\delta_c - \delta_e}{\delta_c - \delta_m^0}\right)^\alpha, 1\right\}\right\} \quad (6.8)$$

where $\alpha = 1$ for the linear-law characteristic, and $\alpha = 0.5$ for the power-law characteristic. The δ_m^0 is the relative displacement when the damage initiates under mixed mode loading, which is obtained by:

$$\delta_m^0 = \sqrt{\frac{(\delta_1^0)^2 (1 + \beta^2) \delta_2^0 \delta_3^0}{\delta_2^0 \delta_3^0 + \beta^2 (\delta_1^0)^2}} \quad \text{and} \quad \beta = \frac{\sqrt{\delta_2^2 + \delta_3^2}}{\delta_1} \quad (6.9)$$

So far, the only unknown parameter in Equation (6.8) is the critical displacement δ_c , which can be determined by the Griffith energy criterion [271]. In the cohesive zone method, mode II and mode III fracture is often regarded as the same due to a lack of mode III mechanical property information [223]. Thus, the mixed mode energy-based failure function [224] can be expressed as:

$$\left(\frac{G_1}{G_1^c}\right)^\gamma + \left(\frac{G_{\text{shear}}}{G_{\text{shear}}^c}\right)^\gamma = 1 \quad (6.10)$$

where G_{shear}^c is the critical shearing energy release rate with $G_{\text{shear}}^c = G_2^c = G_3^c$, and G_1^c , G_2^c and G_3^c terms are the fracture energies under pure mode loading. The G_{shear} is the energy dissipation rate by shearing, which is the sum of the energy released by the mixed mode II and III crack, $G_{\text{shear}} = G_2 + G_3$, and the G_2 and G_3 are given in Equation (6.11). A quadratic $\gamma = 2$ failure criteria is frequently chosen according to the mixed mode experimental results [224, 225] and is used here.

For the cohesive interface, the energy dissipation rates are defined as follows:

$$G_i = \int \sigma_i d\delta_i \quad (i = 1, 2, 3) \quad (6.11)$$

In the following section, the formulated cohesive laws are integrated into the hybrid finite-discrete element method and incorporated into a user subroutine using FORTRAN. Simulations are conducted using the commercial finite element software ABAQUS/Explicit and their results are compared with experimental data.

6.4.3 The microscopic stochastic fracture model

In brittle materials such as ceramics, strength is limited by the distribution of flaws within the materials, with each flaw potentially initiating a crack [202]. The Weibull strength distribution method has been extensively used in ceramics to assess the effects of these flaws statistically [202, 203, 214], which is defined as follows:

$$P(\sigma, V) = 1 - \exp \left[-\frac{V}{V_0} \left(\frac{\sigma}{\sigma_0} \right)^m \right] \quad (6.12)$$

where $P(\sigma, V)$ denotes the cumulative failure probability of an alumina ceramic, V represents the volume of the component under investigation, V_0 is the characteristic volume, σ indicates the applied stress, m is the Weibull modulus, and σ_0 is the characteristic strength according to Weibull's definition.

In the HDFEM, cohesive elements are used to model flaws [55]. Our study employs Weibull's statistical strength theory [203] combined with cohesive elements to capture the influence of the distribution of stochastic spatial flaws in alumina ceramics. Daphalapurkar et al. [222] recently applied a modified microscopic facet-strength probability distribution, based on Equation (6.12), to the cohesive element method:

$$f(\sigma) = \frac{m_0}{\sigma_0} \left(\frac{A}{A_0} \right)^{\frac{m_0}{m_a}} \left(\frac{\sigma}{\sigma_0} \right)^{m_0-1} \exp \left[\left(\frac{A}{A_0} \right)^{\frac{m_0}{m_a}} \cdot \left(\frac{\sigma}{\sigma_0} \right)^{m_0} \right] \quad (6.13)$$

where A represents the facet area of the cohesive element, A_0 denotes the characteristic area, m_0 is the Weibull modulus for strength distribution, and m_a signifies the Weibull modulus related to the effective area modification. In this study, we applied the microscopic facet-strength probability model with the pre-inserted cohesive method to represent material flaws. We generated strength data impacted by stochastic flaws through Monte Carlo simulations, following the flaw distribution equation (Equation (6.13)).

6.4.4 The modified hybrid finite-discrete element method

In the HFDEM, specimens are modelled as an assembly of elastic bulk elements interconnected by cohesive elements, simulating inherent material flaws that evolve into potential cracks under load, termed "crack elements" [31, 55]. A crack element is considered completely fractured and removed from the model when its damage parameter D equals 1, creating new crack surfaces. Consequently, elastic elements detach, forming fragments that maintain contact and exhibit friction under compressive loads. In

the modified HFDEM model proposed in this study, the cohesive stresses transmitted by the material are dependent on the relative displacements across crack elements. This fracture behaviour is demonstrated for mode I in Figure 6.3 and for mode II in Figure 6.4, aligning with the mechanical characteristics of alumina ceramic as specified in Table 6.1. Subsequent descriptions of Figures 6.3 and 6.4 will occur in the following paragraphs. In Table 6.1, the “basic mechanical properties” are derived from experiments and the manufacturer [11, 61, 208]. The “fracture properties” are sourced from previous studies [253, 272], and the “properties for the microscopic stochastic fracture model” are evaluated by literature [202, 203, 214].

TABLE 6.1: Mechanical and fracture properties of the alumina ceramic

	Parameters	Notation	Value	
The basic mechanical properties of the elastic bulk element	Density	ρ	3800 kg/m ³	[11, 61]
	Young’s modulus	E	362±20 GPa	[11, 61]
	Poisson’s ratio	ν	0.24±0.02	[11, 61]
The fracture properties of the crack element	Weibull characteristic tensile strength	σ_0	440 MPa	[253, 272]
	The model I fracture energy	G_1^c	0.04 N/mm	[253, 272]
	The friction coefficient	μ	0.4	[253, 272]
	The tensile penalty stiffness of cohesive element	K_1	4.6×10 ¹⁶ N/m ³	[253, 272]
The properties for the microscopic stochastic fracture model	Weibull modulus of the strength distribution	m_0	11	[214, 253]
	Weibull modulus for the effective area modification	m_a	-11	[214, 253]
	Characteristic area	A_0	0.013 mm ²	[214, 253]

Figure 6.3 illustrates the evolution of tensile stress adheres to the linear law and power law forms for the catastrophic failure of brittle materials. The linear law is indicated by $\alpha = 1$ in Equation (6.8), while the power law is denoted by $\alpha = 0.5$ in the same equation. A comparison between the decreasing stress with the linear law and power law damage evolution reveals that, near the point of critical displacement, the decrease in stress according to the power law is significantly sharper than that of the linear law. Notably, the damage rate of the power-law becomes infinite at critical displacement (δ_c). While the linear cohesive law is widely applied in modelling brittle materials [126, 218, 253], studies focusing on power-law damage evolution in such materials are scarce.

In Figure 6.4, the mode II constitutive behavior of the cohesive element is shown using the coupled damage and friction law. The mode II fracture properties used in Figure 6.4 are recommended by our previous study of the CeramTec 98% [272], which are seven times greater than those of mode I in Table 6.1. The pure shear behaviour indicated by the dashed curves is similar to the tensile response in Figure 6.3, where the stress decreases according to the power law is significantly faster than that with the linear law. The solid curves in Figure 6.4 demonstrate the shear response of the cohesive element under a compressive stress of 1000 MPa. Comparing the pure shear with the compression-shear behavior, it is noted that the area under the solid curves exceeds that under the dashed curves, indicating the shear response under compressive load consumes more energy than the pure shear response for both linear and power laws. This increased

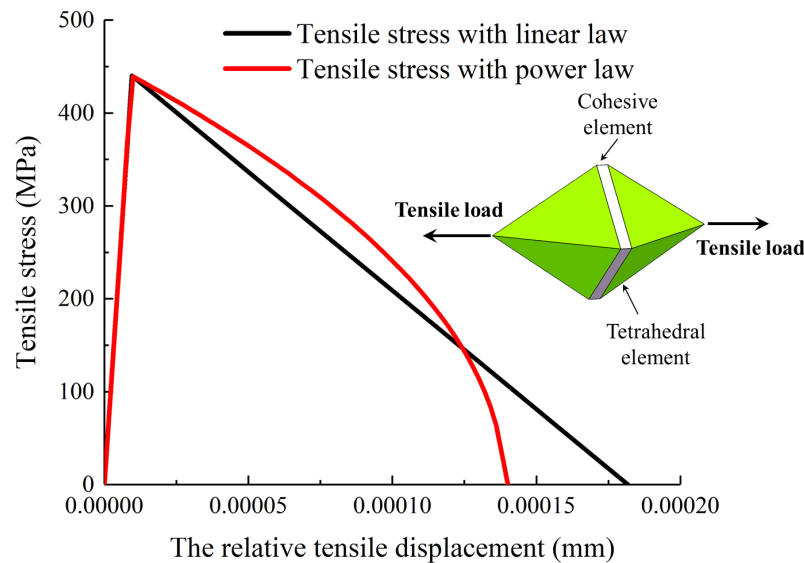


FIGURE 6.3: The mode I constitutive behaviour of the cohesive element is obtained from a validation model (shown as the inset in the figure). In this validation model, a cohesive (crack) element is interspersed throughout two tetrahedral elastic elements. The black line represents the linear cohesive law, and the red curves represent the cohesive law developed in the present study with power-law characteristics.

energy consumption is attributed to friction providing significant residual strength to the material's shear strength during degradation. Furthermore, when the relative shear displacement surpasses the critical displacement under compression-shear conditions, the shear residual strength maintains a constant value due to friction, aligning with the extended Mohr–Coulomb model proposed by Shafiq and Subhash [88]. This frictional residual shear strength, as derived from the coupled damage and friction law, validates the assumption in prior studies [126, 218] that the shear strength of cohesive elements remains unaltered with increasing relative shear displacement under compression-shear conditions. Based on the constitutive behavior of the cohesive elements, friction can enhance the shear strength under compression, thereby inhibiting mode II cracks and favouring the formation of mode I cracks, which evolve into micro “wing-cracks”. These cracks consistently align parallel to the direction of compressive loading when there is no lateral confinement, a phenomenon corroborated by numerical studies [44, 45, 126] and experiments [13, 15] for brittle materials.

Figure 6.5 shows a Monte Carlo simulation using the microscopic stochastic fracture model for the strength distribution of cohesive elements, showing that around 7.9 % of these elements, indicative of significant flaws, have low tensile strength (below 350 MPa). In contrast, a vast majority (92.1 %) exhibit higher tensile strength (350 to 530 MPa), implying smaller flaws. This adaptation of the microscopic stochastic fracture model

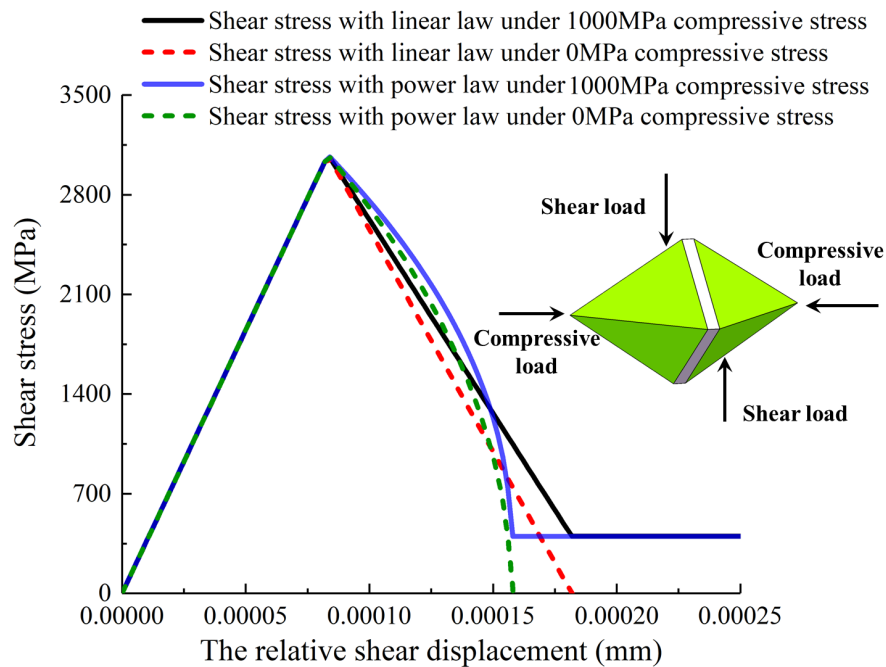


FIGURE 6.4: The mode II constitutive behaviour of the cohesive element is illustrated in terms of the tangential bonding stresses (or shear stress) versus the relative shear displacement. The dash curves show the pure shear behaviour, and the solid curves represent the shear behaviour of the cohesive element subjected to a compressive stress of 1000 MPa.

within the cohesive element framework indicates that: 1) cohesive elements inserted a priori act as potential sites for flaws, and 2) the stress exceeding a certain threshold transforms these flaws into microcracks.

6.5 The comparison between linear- and power-law simulation results

In the previous section, we introduced a modified HFDEM approach, which incorporates a coupled damage and friction model, linear and power-law damage evolution, and a microscopic stochastic fracture model. Following this, the alumina ceramic's response to quasi-static uniaxial compression is simulated using ABAQUS finite element software using a VUMAT subroutine. This modified HFDEM method is then validated against experimental data from quasi-static uniaxial compression tests.

First, the mesh size is carefully chosen based on the physical considerations and computational costs. Several studies [218, 226] indicated that the optimal mesh size for simulating the mechanical behavior of brittle materials, particularly advanced ceramics, should be at most 0.3 mm. This guidance aligns with experimental findings on alumina

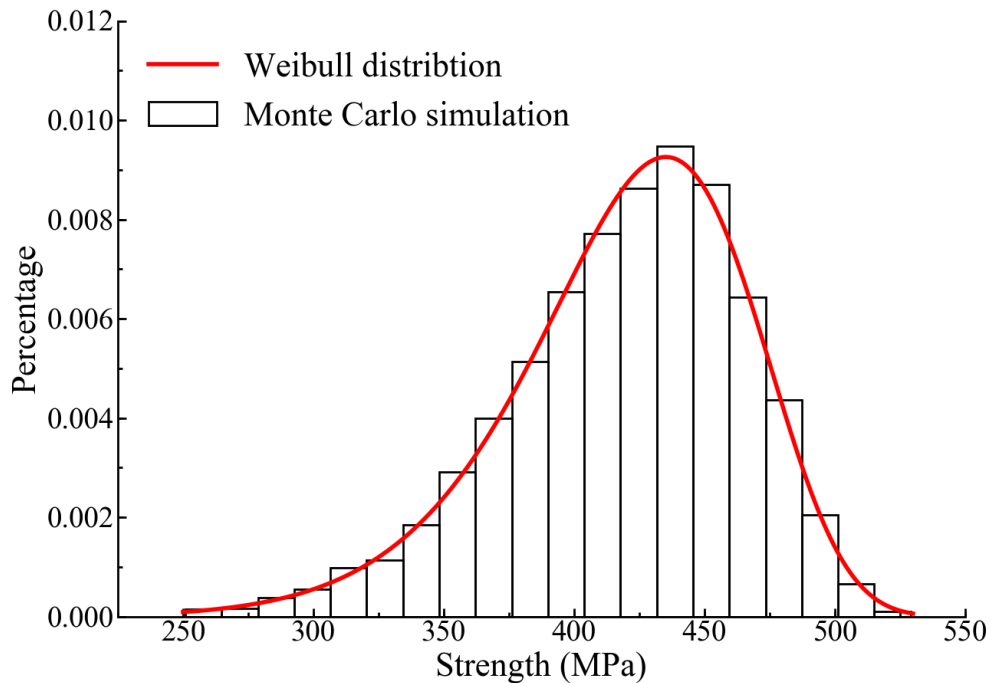


FIGURE 6.5: The red curve represents the Weibull statistical strength distribution of cohesive elements, derived from Equation (6.13), featuring parameters $m_0 = 11.0$, $m_a = -11.0$, $\sigma_0 = 440.0$, $A = 0.01268$, and $A_0 = 0.013$. The grey bar illustrates the strength statistics of cohesive elements with randomly generated flaws, as determined by Monte Carlo simulations.

ceramic fragmentation [13, 15], suggesting that each elastic element within the model could represent a potential fragment in the post-fracture scenario. For example, Hogan et al. [13, 15] documented the characteristics of over 1500 ceramic fragments resulting from quasi-static uniaxial compression tests. Their findings revealed that more than 70% of these fragments exceeded 0.1 mm in size, categorizing them as “structure-dominated fragments”. Drawing on insights from published research [13, 15, 68, 218, 226] and our prior mesh sensitivity analysis of the modified HFDEM [253, 272], we selected an element size of 0.15 mm, paired with a maximum time step of 5×10^{-7} ms for our simulations. The mesh convergence analysis has been conducted in our prior research [253]. This configuration resulted in the model comprising approximately 110,000 tetrahedral elastic elements and 210,000 cohesive elements, ensuring an accurate representation of the material’s response.

In our simulations, we implemented a fixed-displacement boundary condition on the foundation platen to allow lateral expansion or contraction of the sample, closely replicating the experimental conditions (shown in Figure 6.1), where high-pressure grease enabled unimpeded movement at the specimen-platen interface. The application of load was simulated through a velocity boundary condition on the loading platen, an approach that aligns with the methodology employed by Molladavoodi et al. [45] on

uniaxial compression. This technique ensures that our simulations are consistent with experimental conditions.

6.5.1 The stress-strain response

To study the ability of this model to capture the stress-strain response of alumina ceramic under quasi-static uniaxial compression, the linear- and power-law simulation results are compared with experimental results. The input parameters of the alumina ceramic are provided in Table 6.1, and the mode II fracture properties of the reference input parameters are chosen around seven or eight times greater than those of mode I [272]. We carried out three Monte Carlo simulations for each condition to consider the randomness of the flaws in the alumina ceramics, and there are twelve simulations for the linear- and power-law versions of the HFDEM model in this comparison section.

The outcomes of the simulation results are summarized in Figure 6.6. The stress-strain responses from the three Monte Carlo simulations consistently align for each condition with the same input parameters. The average compressive strength calculated by the HFDEM model shows the following results: 2.89 ± 0.06 GPa for the linear damage evolution law when the shear strength is seven times the tensile strength ($\sigma = 7\tau$); 3.27 ± 0.05 GPa for the linear damage evolution law with $\sigma = 8\tau$; 2.65 ± 0.01 GPa for the power damage evolution law with $\sigma = 7\tau$; and 3.02 ± 0.02 GPa for the power damage evolution law with $\sigma = 8\tau$. The elastic modulus obtained by all the simulation results is between 355 and 366 GPa. By comparing the results obtained by linear- and power-law, it is observed that the stress and strain response of linear law is more brittle than the power law. The results of the power-law simulation exhibit a softening process when the stress reaches its peak value. This occurs due to the distinct failure modes (fracture and failure processes) governed by the two different types of damage evolution laws (the linear- and power-law). These two failure modes are further discussed in the subsequent subsection. Due to the different failure modes, the compressive strength obtained by the linear damage evolution law is higher than that by the power law.

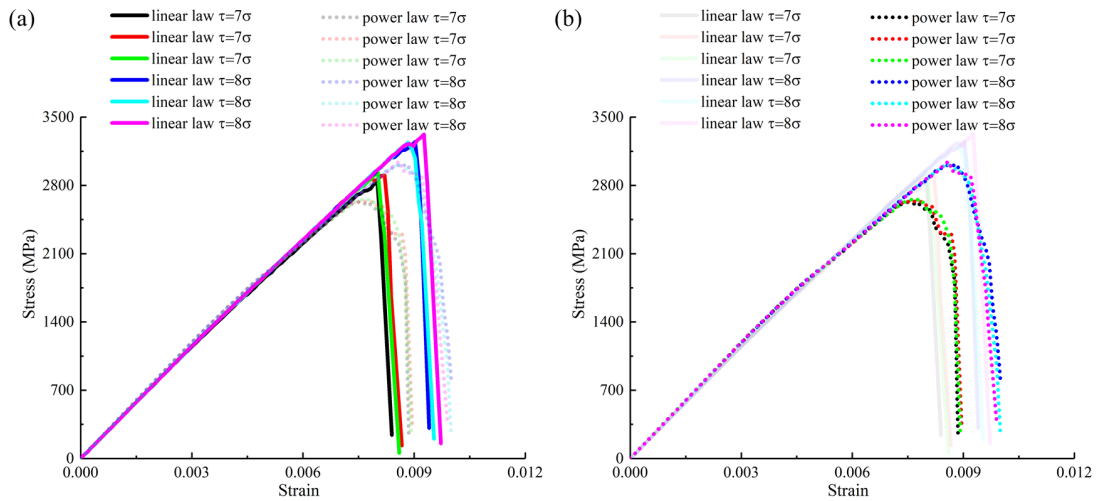


FIGURE 6.6: Variation in the engineering stress-strain response of alumina ceramic obtained by the HFDEM model with linear and power damage evolution laws. Results using the linear damage evolution law are presented as solid curves, and those using the power damage evolution law are depicted with dashed curves. a) The power damage evolution law results are shown as transparent. b) The linear damage evolution law results are displayed transparently.

6.5.2 The fracture and fragmentation processes

Observing the fracture and fragmentation processes experimentally is challenging because the fracture and fragmentation processes of advanced ceramics happen in microseconds [61], which is beyond the frame rate of most of the cameras. However, these processes can be effectively examined through simulations by capturing the spatio-temporal evolution of failure with a smaller time step. Results from the current HFDEM model, as illustrated in Figures 6.7 and 6.9, provide insights into the fracture and fragmentation characteristics observed during the quasi-static compressive failure of the alumina ceramic. Figure 6.7 is the representative failure process of the linear damage evolution law corresponding to the red solid curve in Figure 6.6. Figure 6.9 represents the failure process of power damage evolution law corresponding to the red dash curve in Figure 6.6. The crack modes in Figures 6.7 and 6.9 are consistent with the wing-crack-type failure mode [113], where cracks grow parallel to the compressive loading direction. The common fracture and fragmentation characteristics of the simulation results shown in Figures 6.7 and 6.9 are:

1. Before the peak compressive stress, at ϵ_1 , there exists a small axial crack on the surface of the specimen, which is oriented in the loading direction. This axial crack can be seen before the maximum stress is reached. These oriented cracks obtained by the HFDEM is consistent with the wing-crack-type failure mode.

2. Then, more axial cracks are generated simultaneously near the peak compressive stress, and they continue to grow to dissipate the strain energy at ε_2 .
3. At ε_3 , after the peak compressive stress, transverse cracks are observed, which are perpendicular to the compressive loading direction. These transverse cracks occur mainly due to the buckling of the columns formed from the span-wise propagation of the axial cracks generated at earlier strains, which has also been observed in experimental research by Ashby and Hallam [273]. Later, these axial and transverse cracks propagate rapidly across the specimen, and they coalesce with each other. As a consequence, more and more fragments are generated due to the interaction and coalescence of axial and transverse cracks. Finally, two kinds of fragments are generated: 1) elongated fragments that have higher aspect ratios, and 2) blocky fragments with aspect ratios close to 1. These two types of fragments agree well with observations in Hogan et al. [14].

However, there are differences between the fracture and fragmentation characteristics of Figures 6.7 and 6.9, which are attributed to the implementation of the linear- and power-laws. It is observed in the linear damage evolution failure process (Figure 6.7) that the crack initiates from the corner of the specimen at the strain of ε_1 , and then the fracture growth and fragmentation process begins from the top of the specimen shown at the strain of ε_2 . The fracture and fragmentation processes in Figure 6.7 are consistent with the experimental observation in the current study shown in Figure 6.8. In Figure 6.9 of the power damage evolution failure process, the crack is initiating from the middle part of the specimen at the strain of ε_1 and ε_2 . The fracture and fragmentation processes in Figure 6.9 are consistent with the experimental observation shown in Figure 6.10 [267].

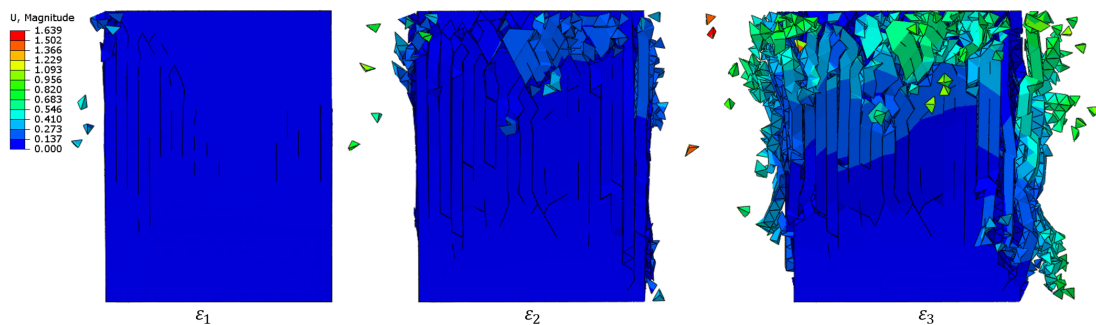


FIGURE 6.7: The fracture and fragmentation process of alumina ceramic of the linear damage evolution law at three different representative strain points, which are shown in the red solid curve of Figure 6.6. These three strain points (ε_1 , ε_2 and ε_3) correspond to the average strain of 0.75%, 0.80% and 0.84%. To better observe the cracks on the specimen surface, we use the displacement legend for the three images, and the unit here is mm.

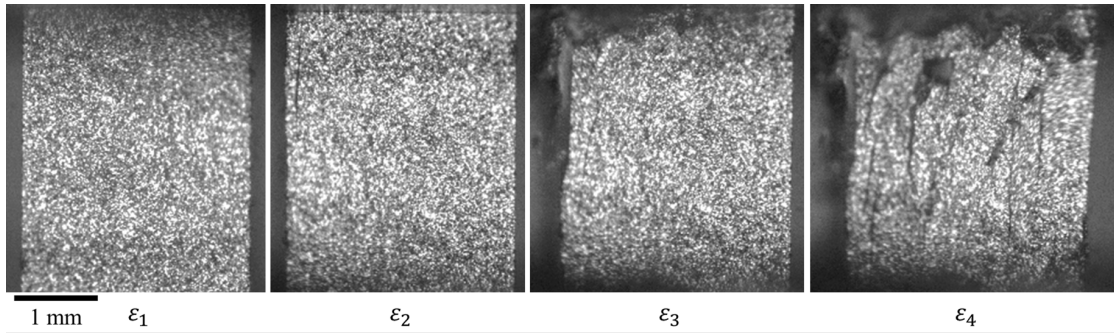


FIGURE 6.8: The fracture and fragmentation process of an alumina ceramic in the current experiments. The strain points (ε_1 and ε_2) correspond to the average strain of 0.84% and 0.86%. At the strain of ε_3 and ε_4 , the DIC loses correlation due to the appearance of cracks.

Altogether, the current model can reasonably capture both the stress-strain response (shown in Figure 6.6) and the fracture-fragmentation processes (shown in Figure 6.7) under quasi-static compressive loading conditions. The simulation results also show various phenomena and mechanisms that manifest during compressive failure of advanced ceramics: 1) the fracture growth follows the wing-crack-type failure mode [35, 36, 38], 2) catastrophic failure of brittle materials [266], and 3) the “structure-dependent” fragmentation process [15]. Next, we explore the effects of varying mechanical properties on the compressive response of the material towards guiding future materials design.

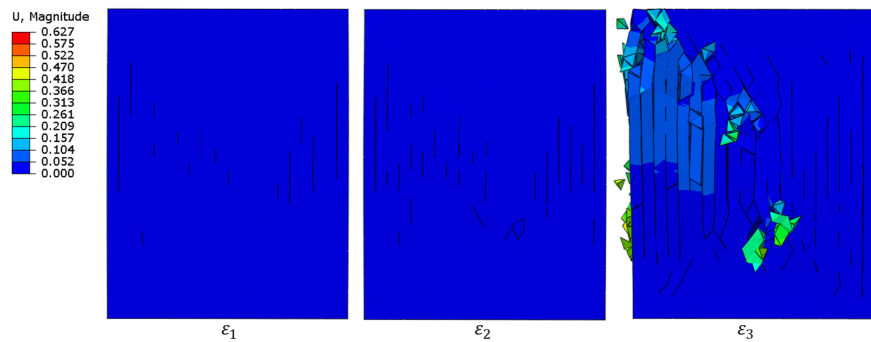


FIGURE 6.9: The fracture and fragmentation process of alumina ceramic of the power damage evolution law at three different representative strain points, which are shown in the red dash curve of Figure 6.6. These three strain points (ε_1 , ε_2 and ε_3) correspond to the average strain of 0.72%, 0.76% and 0.81%. To better observe the cracks on the specimen surface, we use the displacement legend for the three images, and the unit here is mm.

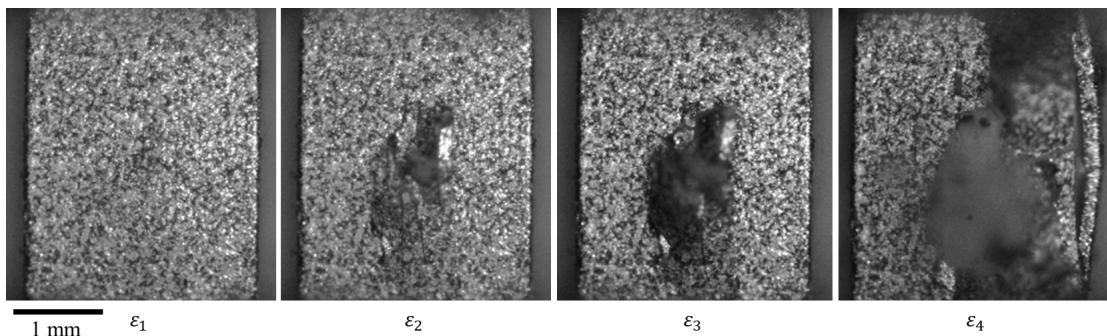


FIGURE 6.10: The fracture and fragmentation process of an alumina ceramic [267]. The strain point (ε_1) correspond to the average strain of 0.75%. At the strain of ε_2 , ε_3 and ε_4 , the DIC loses correlation due to the appearance of cracks.

6.6 Results and discussion

Recently, researchers have explored several manufacturing techniques to improve the mechanical properties of alumina ceramic, such as exploring the role of sintering temperature and pressure-assisted compaction on properties [274–277] and the use of additive manufacturing [211, 267]. Specifically, these techniques have been shown to enhance the elastic modulus, Poisson’s ratio, tensile strength, and shear strength of alumina ceramics. However, the extent to which these properties influence the stress-strain response is not yet fully understood; this section aims to provide more insights into the role of properties on structural performance (i.e., stress-strain). In the following sub-sections, we will explore the effects of various mechanical properties of alumina ceramic on compressive strength by using the linear damage evolution law, which is more consistent with our experimental results than the power law. The mechanical properties of the red reference curve shown in Figure 6.6 are used as the reference input parameters for the subsequent parametric studies, listed in Table 6.1. The mode II fracture properties of the reference input parameters are chosen as seven times greater than those of mode I [272].

The mechanical and fracture properties, which serve as inputs to the model, are studied individually. The variation of mechanical properties investigated in this section is divided into two groups. The first group includes the properties of the elastic bulk elements which are Young’s modulus and Poisson’s ratio in the model, and these are named the “basic mechanical properties” in Table 6.1. Physically motivated by various studies in the literature [275–277], we assume that Poisson’s ratio ν may vary between 0.22 and 0.26, and that the elastic modulus E varies between 340 and 390 GPa. The second group of interest includes the “fracture properties” of the crack elements, and these are the tensile and shear strengths. It is appropriate to assume that the fracture properties

of alumina ceramic will be improved continuously as advancements in manufacturing progress [278–281]. Here, we assume the tensile strength σ_0 increases from 440 to 700 MPa, and the shear strength increases from 5 to 8 times the tensile strength, which were values used in previous studies involving alumina ceramics [272, 282, 283].

6.6.1 The effect of basic mechanical properties

First, we explore the influence of Poisson’s ratio on the stress-strain response in Figure 6.11 by setting its values between 0.22 and 0.26, while the other properties remain the same as the ones used to generate the red reference curve shown in Figure 6.6. This exploration is motivated by previous studies [77, 268, 269] on the role of Poisson’s ratio in failure. As Figure 6.11 shows, the peak compressive stresses and corresponding strains are almost identical throughout this range of Poisson’s ratio, with an average of 2.93 ± 0.01 GPa at a failure strain of $0.8 \pm 0.01\%$. According to these results, it is concluded that the compressive strength in this model is insensitive to Poisson’s ratio. This may not be surprising under quasi-static uniaxial compression conditions studied here where mode I fracture dominates [35–38], as the effect of Poisson’s ratio becomes more important for multi-axial loading (e.g., confined compression [21]).

Next, we explore the effect of Young’s modulus on the stress-strain results in Figure 6.12. This is motivated by the study of Sairam et al. [274], who noted that higher manufacturing temperatures and heating rates increase the elastic modulus of sintered ceramic. In Figure 6.12, the simulation results show that by varying the elastic modulus from 340 to 390 GPa, the failure strain at the peak stress increases from 0.75% to 0.84%. In contrast, the change in the peak compressive strength is negligible over these changes (with an average of 2.94 ± 0.02 GPa). This conclusion is consistent with the experimental result shown in Figure 6.2. Lastly, it should be noted that this conclusion is valid for a small range of Young’s modulus with the other properties unchanged. In reality, if Young’s modulus changes over a larger range, the density, fracture toughness, and other properties would likely change because of the significant shifts in microstructures or phases [274]; however, this interplay was not considered in this study.

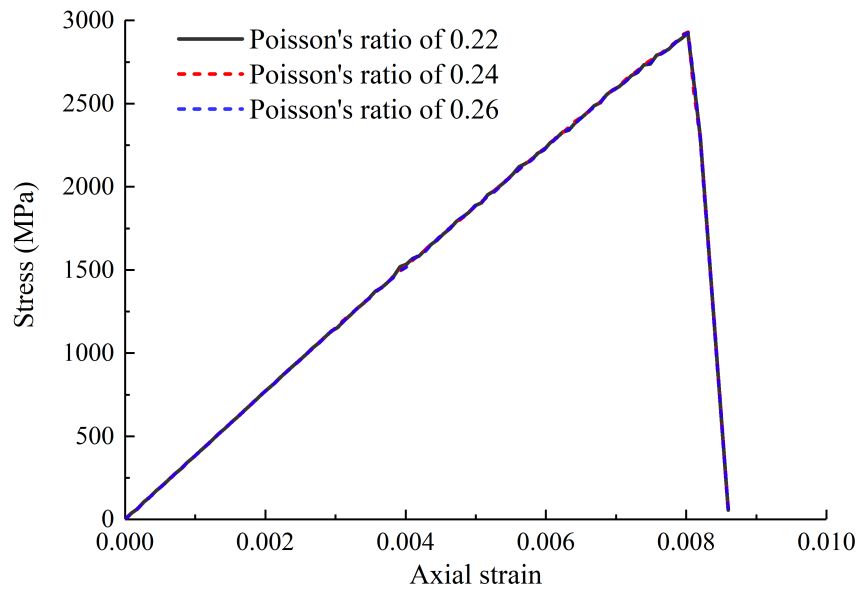


FIGURE 6.11: The predicted engineering stress-strain behavior of alumina ceramic for various Poisson's ratio ν while the other properties remain the same as the ones used to generate the red reference curve shown in Figure 6.6. The changes in the stress-strain curves are negligible over these values of ν .

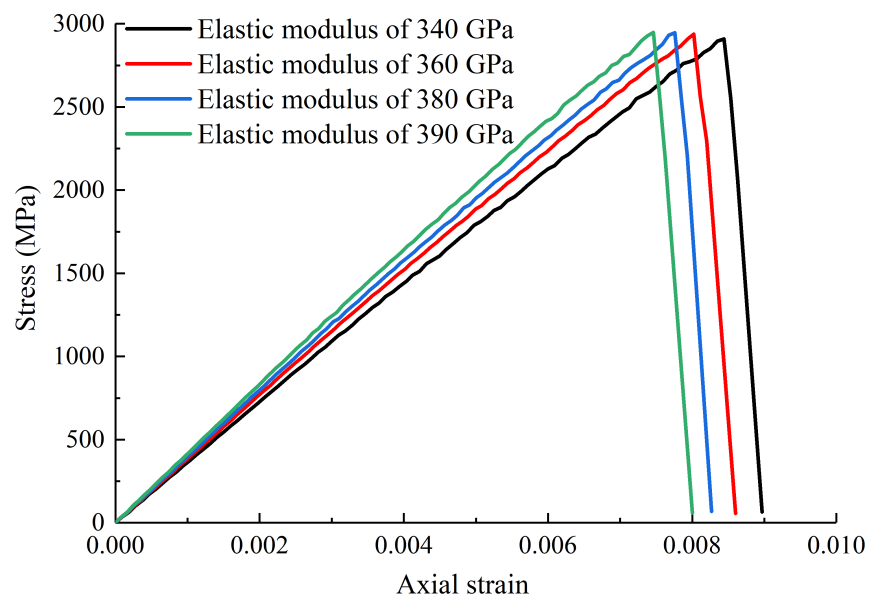


FIGURE 6.12: The predicted engineering stress-strain behavior of alumina ceramic for various elastic modulus E , while the other properties are set to the reference values. According to these curves, the failure strain is affected by the change in stiffness, but the change in the peak compressive stress is minor over these values of E .

6.6.2 The effect of fracture properties

Figure 6.13 illustrates the influence of shear strength, set at 5 to 8 times the tensile strength, on the stress-strain response, with all other properties maintained at their reference values. Three Monte Carlo simulations are conducted for each specified shear strength condition. A black curve connecting them represents the average values and corresponding standard deviations from these simulations. It is observed that by increasing the shear strength by 60% (from 5 to 8 times the tensile strength), there is an increase in the peak stress of 44% (from 2.27 to 3.27 GPa) and an increase in the failure strain of 47.5% (from 0.61 to 0.90%) corresponding to the peak stress. The relationship between the shear strength and compressive failure strength is almost linear (see the black curve in Figure 6.13).

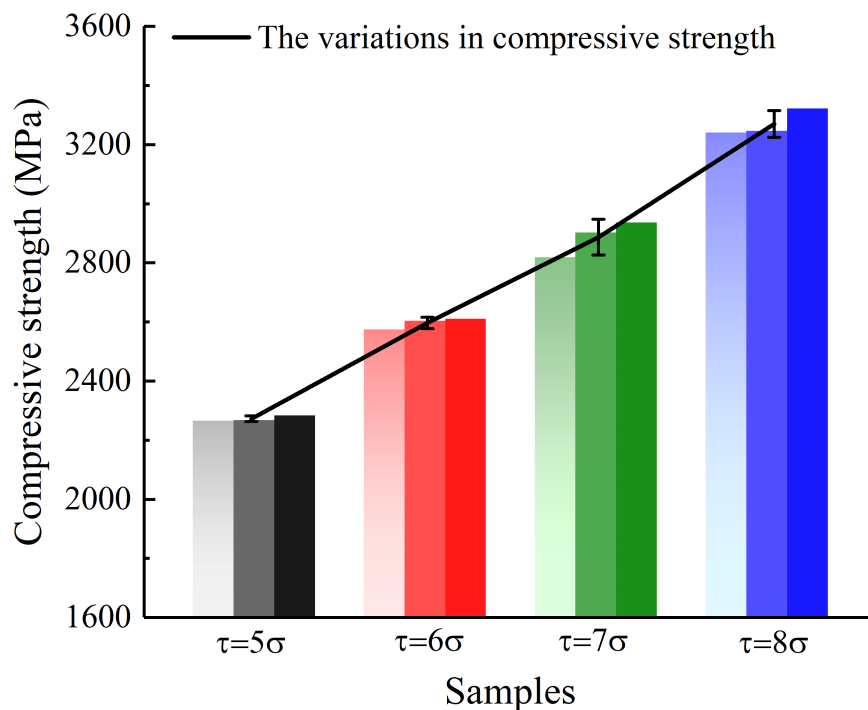


FIGURE 6.13: The predicted compressive strength of alumina ceramic for various shear strengths while the other properties are set to the reference values. The compressive strength increases with higher shear strength.

Next, Figure 6.14 shows the influence of the Weibull characteristic tensile strength on the stress-strain response while the other properties are set to the reference values. Similarly, for each specified tensile strength condition, three Monte Carlo simulations are conducted. The average value and corresponding standard deviation of each specified tensile strength condition are connected by a black curve. As observed, the effect of increasing the Weibull characteristic tensile strength on compressive strength appears to

be weakened. By increasing the tensile strength by 59% (from 440 to 700 MPa), there is an increase in the peak stress of only 23% (from 2.89 to 3.55 GPa) and an increase in the corresponding failure strain of 23.7% (from 0.80 to 0.99%).

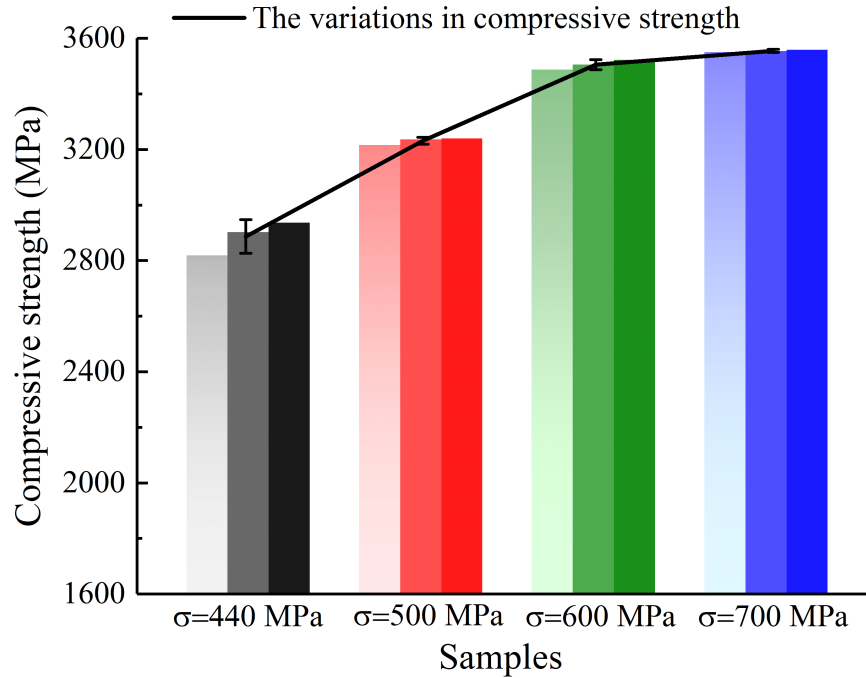


FIGURE 6.14: The predicted compressive strength of alumina ceramic for various Weibull characteristic tensile strengths, while the other properties are set to the reference values. The impact of increasing the Weibull characteristic tensile strength on the compressive strength is weakened.

In the literature [35, 36, 38], the compressive failure of alumina ceramic is attributed to the wing cracks. Interestingly, according to Figure 6.13 and Figure 6.14, the influence of the tensile strength on the compressive strength gradually decreases when the tensile strength increases, as well, the compressive strength is more sensitive to the shear strength than the tensile strength. The central role of wing crack formation in compressive failure aligns well with the observations presented in Figure 6.13 [126]. It is believed that the linear relationship between the shear strength and compressive failure strength follows the idea that shear damage must first occur for wing cracks to form [45, 126]. Thus, the shear strength is strongly correlated to the compressive strength.

In addition, Sadowski and Samborski [284] found there exists a significant difference between the tensile and compressive strength of porous ceramics. They concluded that for tensile loading, the wing cracks were open and became unstable after initiation, while under compression, the wing cracks had a closed region, and the main resistance for the growth of the crack was the shear resistant force. The correlation between the compressive and tensile strength values are weak because they are governed by different

failure mechanisms. In their numerical study, Warner and Molinari [126] obtained a similar conclusion by explaining that the compressive strength is sensitive to the shear strength. Altogether, these observations are consistent with the results obtained in the current study, and the simulation results and discussions presented in this section provide theoretical guidance to perform material design and optimization in the future.

6.7 Conclusion

The purpose of this study was to better understand the mechanical behaviour of alumina ceramics under quasi-static uniaxial compressive loading by developing a modelling framework that accounts for various failure phenomena and mechanisms (i.e., fracture growth via the wing-crack-type failure mode, catastrophic failure, and fragmentation behaviour). First, quasi-static compressive stress-strain curves were obtained experimentally using DIC techniques. Then, a modified hybrid finite discrete element model was employed to study the crack nucleation, propagation, and fragmentation process of the alumina ceramic. This model included three main failure phenomena and mechanisms of the alumina ceramic: 1) the fracture growth follows the wing-crack-type failure mode by using a three-dimensional (3D) coupled damage and friction law of the cohesive zone method, 2) the catastrophic failure was modelled using a type of damage evolution law with linear- and power-law characteristic, and 3) a microscopic stochastic fracture model described the fracture and fragmentation behaviour of the materials.

The modified HDFEM model was validated with experimental results from quasi-static uniaxial compression tests, and it was demonstrated that the presented model could reasonably predict the mechanical response of alumina ceramics under quasi-static uniaxial compression while accounting for variability in mechanical properties. Namely, it was shown that the results of our modified HFDEM model were in good agreement with the experimental results in terms of qualitative (e.g., fracture-fragmentation behaviour and patterns shown in Figures 6.7 to 6.10) and quantitative (e.g., stress-strain curves shown in Figure 6.6) properties of the advanced ceramics under quasi-static uniaxial compression. Once the model was validated, the influences of different parameters, such as Poisson's ratio (shown in Figure 6.11), elastic modulus (shown in Figure 6.12), tensile strength (shown in Figure 6.14), and shear strength (shown in Figure 6.13), on the compressive behaviour were explored and discussed. Interestingly, elastic modulus and Poisson's ratio were shown to have negligible effect on the peak compressive strength in uniaxial compression. The influence of tensile strength on compressive strength

diminishes as the tensile strength increases, and notably, the compressive strength is more sensitive to shear strength than to tensile strength.

Chapter 7

Concluding Remarks

7.1 Summary

This thesis aims to investigate the fracture and fragmentation behavior of alumina ceramics under various stress-state and strain-rate conditions, using both experimental and computational methodologies. Experimentally, this thesis has pushed the boundaries of traditional testing methods by integrating high-speed imaging and digital image correlation techniques with dynamic testing frameworks such as the modified Kolsky bar setup. These advanced experimental techniques have provided unprecedented insights into the real-time fracture processes of ceramics. In addition, advanced microscopy techniques, including high-resolution scanning electron microscopy, high-resolution X-ray tomography, and energy-dispersive X-ray spectroscopy, have been used to investigate the microstructural characteristics, chemical compositions, and microstructure-dependent deformation and failure mechanisms. The development and validation of the modified hybrid finite-discrete element model (HFDEM) stand out as a cornerstone achievement of this thesis. This model has demonstrated remarkable success in accurately simulating the complex behaviors of alumina ceramics, including the initiation and propagation of cracks, and their subsequent evolution into fragments. The ability of the HFDEM to predict these dynamics across different scales and under various loading conditions marks a significant progression in the field of computational materials science, offering a powerful tool for engineers and researchers.

This thesis achieves its objective of providing a better understanding of the effects of microstructure, stress state, and strain rate on the fracture and fragmentation behavior of alumina ceramic materials in the form of five peer-reviewed papers (Chapters 2, 3, 4, 5 and 6). The key results from the works are summarized below for further emphasis:

1. The mechanical performance of the CeramTec 98% alumina is evaluated through detailed microscopic characterization and strain-rate-dependent uniaxial compression and compression-shear experiments. A novel data processing method was introduced to accurately calculate shear components during compression-shear tests, validated against shear strain measurements obtained from DIC analysis. Analyzing results from the proposed model and DIC data yielded several new insights. Shear failure occurs before complete structural failure, indicating that shear behavior plays a critical role in the failure process during compression-shear tests. The equivalent peak stress (strength) observed in compression-shear tests is lower than that in uniaxial compression tests. Directional cracks minimally influence compressive stiffness but significantly affect shear behavior. These findings underscore the importance of considering shear effects in the mechanical assessment of alumina ceramics, particularly for applications involving complex loading scenarios.
2. The strain-rate-dependent tensile response of an alumina ceramic was explored by experimental and modeling methods. The locations of maximum tensile stress and strain differ along the compressive diametral line. Dynamic tests revealed that multiple cracks often appear simultaneously around the areas of maximum stress and strain, suggesting that the splitting fracture of a Brazilian disk is influenced not only by the Griffith failure criterion (maximum tensile stress) but also by maximum tensile strain. Moreover, cracks were observed before the recorded peak load, indicating that the peak stress corresponding to the structural failure of the samples differs from the material's tensile strength. This difference is linked to the time required for cracks to propagate, interact, and span the structure. The strain-rate-dependent tensile strength of alumina ceramics was determined using a correction method based on the tensile stress at the initial occurrence of the central crack. In addition, a strain-rate-dependent tensile strength model for alumina ceramics, consistent with experimental results for CeramTec 98% and other type (A94, A98, A99) alumina ceramics, was proposed based on one-dimensional elastic wave theory, the Griffith failure criterion, and experimental observations.
3. A microscopic stochastic fracture model, incorporating a Weibull strength distribution, was integrated into the HFDEM framework, taking into account a random distribution of internal flaws. This model seamlessly combines the tensile failure processes related to the internal flaw system with the macroscopic failure patterns observed during simulations. The validity of the model is supported by both qualitative (e.g., failure patterns) and quantitative (e.g., stress-strain curves) assessments, proving it to be mesh-independent. The tensile strength predictions from our model align with the indirect tensile testing results. During simulations,

micro-cracks nucleated randomly and grew within the sample, eventually coalescing and leading to catastrophic failure. Typically, a single main crack perpendicular to the loading direction was observed, accompanied by some fragments near the crack surfaces due to branching behavior. Additionally, the influence of flaw distribution on the tensile strength and elastic modulus was examined. Results indicated that materials with more uniformly sized flaws and fewer large flaws displayed enhanced tensile strength and a higher elastic modulus.

4. The proposed computational model integrated a hybrid finite-discrete element approach with a coupled damage and friction cohesive model. It also incorporated a microscopic stochastic fracture model based on the Weibull distribution of micro-flaws in the ceramics. This model successfully simulated the direct tensile failure processes of CeramTec 98% alumina, demonstrating both qualitative (e.g., crack patterns) and quantitative (e.g., tensile strength) results. The modified HFDEM was also utilized to replicate the flattened Brazilian disk experiments, comparing simulated indirect tensile strength with direct tensile strength and identifying phenomena of underestimation, reasonable estimation, and overestimation. Analysis revealed that these differences were linked to the interplay between loading point cracks and central cracks. Validation efforts involving FBD experiments had confirmed the consistency of our simulation findings with experimental observations, highlighting a clear relationship between fracture patterns, fragment geometry, and indirect tensile strength. These findings allow the HFDEM to provide a robust framework for analyzing the measured tensile strength in Brazilian disk testing, thereby enhancing our understanding of the indirect tensile behaviour of ceramic materials.
5. A hybrid finite discrete element model (HFDEM) was utilized to examine the processes of crack nucleation, propagation, and fragmentation in alumina ceramics. This model incorporated a three-dimensional coupled damage and friction law of the cohesive zone method to simulate fracture growth, a damage evolution law with linear and power-law characteristics for modeling catastrophic failure, and a microscopic stochastic fracture model to describe the fracture and fragmentation behavior. The HFDEM model was validated against experimental results from quasi-static uniaxial compression tests, demonstrating its ability to accurately predict the mechanical response of alumina ceramics, capturing both qualitative (e.g., fracture-fragmentation behavior and patterns) and quantitative (e.g., stress-strain curves) aspects. After validation, the influence of various parameters such as elastic modulus, Poisson's ratio, tensile strength, and shear strength was investigated. It was found that while elastic modulus and Poisson's ratio

had negligible effects on peak compression strength, shear strength significantly influenced both peak compression strength and failure strain.

7.2 Future works and recommendations

The research carried out in this thesis has significantly advanced our understanding of the fracture mechanics and failure behaviors of alumina ceramics under various stress conditions. However, several avenues remain open for further exploration to extend these findings and enhance the applicability of the developed models. The following recommendations are proposed for future research:

1. Future studies should include a broader range of ceramic materials to validate the generalizability of the developed models. Investigating different ceramics, such as boron carbide [6] and silicon carbide [285], could provide insights into the unique behaviors of these materials and enhance the robustness of the modeling approaches.
2. The models developed in this thesis primarily focus on mechanical stress responses. Including environmental factors such as temperature, humidity, and corrosive environments could significantly impact the predictive capabilities of these models, particularly for applications in harsh operational conditions [286].
3. Incorporating machine learning techniques to analyze experimental data and predict failure modes could significantly streamline the development of predictive models [287, 288]. Machine learning could also assist in identifying patterns and dependencies not immediately apparent through traditional analysis methods.
4. Modify the SHPB system to facilitate the study of material behavior at intermediate strain rates and to allow for a broader range of stress states, including impact [27] and confined dynamic compression [21].
5. While the current study largely assumes isotropic material properties, some advanced ceramics can exhibit anisotropic behaviors depending on their processing and microstructural orientation [289]. Future studies should consider the anisotropic properties of ceramics to more accurately predict their performance in real-world applications.

Bibliography

- [1] Ramdayal Yadav, Mino Naebe, Xungai Wang, and Balasubramanian Kandasubramanian. Body armour materials: from steel to contemporary biomimetic systems. *RSC advances*, 6(116):115145–115174, 2016.
- [2] Eugene Medvedovski. Ballistic performance of armour ceramics: Influence of design and structure. part 1. *Ceramics International*, 36(7):2103–2115, 2010.
- [3] Marc Anglada. Assessment of mechanical properties of ceramic materials. In *Advances in Ceramic Biomaterials*, pages 83–109. Elsevier, 2017.
- [4] Min-Soo Suh, Young-Hun Chae, and Seock-Sam Kim. Friction and wear behavior of structural ceramics sliding against zirconia. *Wear*, 264(9-10):800–806, 2008.
- [5] Calvin Lo, Tomoko Sano, and James D Hogan. Microstructural and mechanical characterization of variability in porous advanced ceramics using x-ray computed tomography and digital image correlation. *Materials Characterization*, 158:109929, 2019.
- [6] Calvin Lo, Haoyang Li, Geneviève Toussaint, and James D Hogan. On the evaluation of mechanical properties and ballistic performance of two variants of boron carbide. *International Journal of Impact Engineering*, 152:103846, 2021.
- [7] Andreas Krell, Elmar Strassburger, Thomas Hutzler, and Jens Klimke. Single and polycrystalline transparent ceramic armor with different crystal structure. *Journal of the American Ceramic Society*, 96(9):2718–2721, 2013.
- [8] Andreas Krell and Elmar Strassburger. Order of influences on the ballistic resistance of armor ceramics and single crystals. *Materials Science and Engineering: A*, 597:422–430, 2014.
- [9] Alexander B Dresch, Janio Venturini, Sabrina Arcaro, Oscar RK Montedo, and Carlos P Bergmann. Ballistic ceramics and analysis of their mechanical properties for armour applications: A review. *Ceramics International*, 2020.

- [10] J Jiusti, EH Kammer, L Neckel, NJ Lóh, W Trindade, AO Silva, ORK Montedo, and A De Noni Jr. Ballistic performance of al₂o₃ mosaic armors with gap-filling materials. *Ceramics International*, 43(2):2697–2704, 2017.
- [11] Jie Zheng, Min Ji, Zahra Zaiemyek, Haoyang Li, and James D Hogan. Strain-rate-dependent compressive and compression-shear response of an alumina ceramic. *Journal of the European Ceramic Society*, 42:7516–7527, 2022.
- [12] Chengyi Huang, Ghatu Subhash, and Stanley J Vitton. A dynamic damage growth model for uniaxial compressive response of rock aggregates. *Mechanics of materials*, 34(5):267–277, 2002.
- [13] James David Hogan, Lukasz Farbaniec, Nitin Daphalapurkar, and KT Ramesh. On compressive brittle fragmentation. *Journal of the American Ceramic Society*, 99(6):2159–2169, 2016.
- [14] James David Hogan, Lukasz Farbaniec, Debjoy Mallick, Vladislav Domnich, Kanak Kuwelkar, Tomoko Sano, James W McCauley, and Kaliat T Ramesh. Fragmentation of an advanced ceramic under ballistic impact: mechanisms and microstructure. *International journal of impact engineering*, 102:47–54, 2017.
- [15] James D Hogan, Lukasz Farbaniec, Matt Shaeffer, and KT Ramesh. The effects of microstructure and confinement on the compressive fragmentation of an advanced ceramic. *Journal of the American Ceramic Society*, 98(3):902–912, 2015.
- [16] DR Curran, L Seaman, T Cooper, and DA Shockey. Micromechanical model for comminution and granular flow of brittle material under high strain rate application to penetration of ceramic targets. *International Journal of Impact Engineering*, 13(1):53–83, 1993.
- [17] DE Grady. Dynamic failure in brittle solids. Technical report, Sandia National Labs., Albuquerque, NM (United States), 1994.
- [18] DE Grady. Shock-wave compression of brittle solids. *Mechanics of Materials*, 29(3-4):181–203, 1998.
- [19] Xu Nie, Weinong W Chen, Xin Sun, and Douglas W Templeton. Dynamic failure of borosilicate glass under compression/shear loading experiments. *Journal of the American Ceramic Society*, 90(8):2556–2562, 2007.
- [20] Shengzhi Tan, Xiaohu Yao, Shuchang Long, Xiaoqing Zhang, and Shuguang Zang. Static and dynamic strength of soda-lime glass under combined compression-shear loading. *Journal of Non-Crystalline Solids*, 516:14–25, 2019.

- [21] L Farbaniec, JD Hogan, KY Xie, M Shaeffer, KJ Hemker, and KT Ramesh. Damage evolution of hot-pressed boron carbide under confined dynamic compression. *International Journal of Impact Engineering*, 99:75–84, 2017.
- [22] Debjoy D Mallick and KT Ramesh. Dynamic fragmentation of boron carbide using laser-driven flyers. *International Journal of Impact Engineering*, 136:103416, 2020.
- [23] James David Hogan, Lukasz Farbaniec, Tomoko Sano, Matthew Shaeffer, and KT Ramesh. The effects of defects on the uniaxial compressive strength and failure of an advanced ceramic. *Acta Materialia*, 102:263–272, 2016.
- [24] Timothy J Holmquist and Gordon R Johnson. Response of silicon carbide to high velocity impact. *Journal of applied physics*, 91(9):5858–5866, 2002.
- [25] Gordon R Johnson and Tim J Holmquist. Response of boron carbide subjected to large strains, high strain rates, and high pressures. *Journal of applied physics*, 85(12):8060–8073, 1999.
- [26] Gordon R Johnson, Timothy J Holmquist, and Stephen R Beissel. Response of aluminum nitride (including a phase change) to large strains, high strain rates, and high pressures. *Journal of Applied Physics*, 94(3):1639–1646, 2003.
- [27] Geneviève Toussaint and Ioannis Polyzois. Steel spheres impact on alumina ceramic tiles: Experiments and finite element simulations. *International Journal of Applied Ceramic Technology*, 16(6):2131–2152, 2019.
- [28] XF Li, QB Zhang, HB Li, and J Zhao. Grain-based discrete element method (gb-dem) modelling of multi-scale fracturing in rocks under dynamic loading. *Rock Mechanics and Rock Engineering*, 51(12):3785–3817, 2018.
- [29] RJ Wu and HB Li. Effect of material properties and strain rate on fragmentation of anisotropic rock. *Advances in Civil Engineering*, 2020, 2020.
- [30] Andrea Lisjak, Daniel Figi, and Giovanni Grasselli. Fracture development around deep underground excavations: Insights from fdem modelling. *Journal of Rock Mechanics and Geotechnical Engineering*, 6(6):493–505, 2014.
- [31] Antonio A Munjiza. *The combined finite-discrete element method*. John Wiley & Sons, 2004.
- [32] Huaming An, Jianjun Shi, Xin Zheng, and Xuguang Wang. Hybrid finite-discrete element method modelling of brazilian disc tests. In *2016 International Conference on Civil, Transportation and Environment*, pages 371–377. Atlantis Press, 2016.

- [33] Zainorizuan Mohd Jaini, Yuan Tian Feng, Shahrul Niza Mokhatar, and Mazlan Abu Seman. Numerical homogenization of protective ceramic composite layers using the hybrid finite-discrete element methods. *International Journal of Integrated Engineering*, 5(2), 2013.
- [34] Roy Arrowood and James Lankford. Compressive fracture processes in an alumina-glass composite. *Journal of materials science*, 22(10):3737–3744, 1987.
- [35] WF Brace and EG Bombolakis. A note on brittle crack growth in compression. *Journal of Geophysical Research*, 68(12):3709–3713, 1963.
- [36] WB Bradley and AS Kobayashi. An investigation of propagating cracks by dynamic photoelasticity. *Experimental Mechanics*, 10(3):106–113, 1970.
- [37] S Nemat-Nasser and H Horii. Compression-induced nonplanar crack extension with application to splitting, exfoliation, and rockburst. *Journal of Geophysical Research: Solid Earth*, 87(B8):6805–6821, 1982.
- [38] H Horii and S Nemat-Nasser. Compression-induced microcrack growth in brittle solids: Axial splitting and shear failure. *Journal of Geophysical Research: Solid Earth*, 90(B4):3105–3125, 1985.
- [39] S Nemat-Nasser and H Horii. Rock failure in compression. *International Journal of Engineering Science*, 22(8-10):999–1011, 1984.
- [40] Hong Wang and KT Ramesh. Dynamic strength and fragmentation of hot-pressed silicon carbide under uniaxial compression. *Acta Materialia*, 52(2):355–367, 2004.
- [41] H Deng and S Nemat-Nasser. Microcrack arrays in isotropic solids. *Mechanics of materials*, 13(1):15–36, 1992.
- [42] H Deng and S Nemat-Nasser. Microcrack interaction and shear fault failure. *International Journal of Damage Mechanics*, 3(1):3–37, 1994.
- [43] S Nemat-Nasser and M Obata. A microcrack model of dilatancy in brittle materials. 1988.
- [44] Guangli Hu, Junwei Liu, Lori Graham-Brady, and KT Ramesh. A 3D mechanistic model for brittle materials containing evolving flaw distributions under dynamic multiaxial loading. *Journal of the Mechanics and Physics of Solids*, 78:269–297, 2015.
- [45] Mohammad Hossein Ahmadi and Hamed Molladavoodi. A micromechanical sliding-damage model under dynamic compressive loading. *Periodica Polytechnica Civil Engineering*, 63(1):168–183, 2019.

- [46] DE Grady and ME Kipp. Mechanisms of dynamic fragmentation: factors governing fragment size. *Mechanics of Materials*, 4(3-4):311–320, 1985.
- [47] Timothy J Holmquist and Gordon R Johnson. A computational constitutive model for glass subjected to large strains, high strain rates and high pressures. *Journal of Applied Mechanics*, 78(5), 2011.
- [48] Timothy J Holmquist, Gordon R Johnson, and Charles A Gerlach. An improved computational constitutive model for glass. *Philosophical Transactions of the Royal Society A: Mathematical, Physical and Engineering Sciences*, 375(2085):20160182, 2017.
- [49] JH Curran and MM Carroll. Shear stress enhancement of void compaction. *Journal of Geophysical Research: Solid Earth*, 84(B3):1105–1112, 1979.
- [50] J Zhou, S Long, Q Wang, and AD Dinsmore. Measurement of forces inside a three-dimensional pile of frictionless droplets. *Science*, 312(5780):1631–1633, 2006.
- [51] Mohammad Saadatfar, Adrian P Sheppard, Tim J Senden, and Alexandre J Kabla. Mapping forces in a 3d elastic assembly of grains. *Journal of the Mechanics and Physics of Solids*, 60(1):55–66, 2012.
- [52] RC Hurley, SA Hall, JE Andrade, and J Wright. Quantifying interparticle forces and heterogeneity in 3d granular materials. *Physical review letters*, 117(9):098005, 2016.
- [53] C Zhai, EB Herbold, SA Hall, and RC Hurley. Particle rotations and energy dissipation during mechanical compression of granular materials. *Journal of the Mechanics and Physics of Solids*, 129:19–38, 2019.
- [54] Andrea J Liu and Sidney R Nagel. The jamming transition and the marginally jammed solid. *Annu. Rev. Condens. Matter Phys.*, 1(1):347–369, 2010.
- [55] Omid Mahabadi, Patrick Kaifosh, Paul Marschall, and Tim Vietor. Three-dimensional fdem numerical simulation of failure processes observed in opalinus clay laboratory samples. *Journal of Rock Mechanics and Geotechnical Engineering*, 6(6):591–606, 2014.
- [56] M Boustie, JP Cuq Lelandais, L Berthe, and R Ecault. Laser shocks: A tool for experimental simulation of damage into materials. In *AIP Conference Proceedings*, volume 1464, pages 310–316. American Institute of Physics, 2012.
- [57] Alberto Morena and Lorenzo Peroni. Numerical simulations of laser-induced shock experiments on graphite. *Materials*, 14(22):7079, 2021.

- [58] RL Woodward, WA Gooch Jr, RG O'donnell, WJ Perciballi, BJ Baxter, and SD Pattie. A study of fragmentation in the ballistic impact of ceramics. *International Journal of Impact Engineering*, 15(5):605–618, 1994.
- [59] Yajie Dai, Yawei Li, Xiaofeng Xu, Qingyou Zhu, Wen Yan, Shengli Jin, and Harald Harmuth. Fracture behaviour of magnesia refractory materials in tension with the brazilian test. *Journal of the European Ceramic Society*, 39(16):5433–5441, 2019.
- [60] L Zhang, D Townsend, N Petrinic, and A Pellegrino. Loading mode and lateral confinement dependent dynamic fracture of a glass ceramic macor. *Journal of Dynamic Behavior of Materials*, pages 1–18, 2022.
- [61] Min Ji, Haoyang Li, Jie Zheng, Shuo Yang, Zahra Zaiemyekeh, and James D Hogan. An experimental study on the strain-rate-dependent compressive and tensile response of an alumina ceramic. *Ceramics International*, 48(19):28121–28134, 2022.
- [62] Jeffrey J Swab. Recommendations for determining the hardness of armor ceramics. *International Journal of Applied Ceramic Technology*, 1(3):219–225, 2004.
- [63] Luke A Hanner, John J Pittari III, and Jeffrey J Swab. Dynamic hardness of cemented tungsten carbides. *International Journal of Refractory Metals and Hard Materials*, 75:294–298, 2018.
- [64] Shoulei Yang, Sirui Yang, Yinxiao Zhu, Lei Fan, and Mengwen Zhang. Flash sintering of dense alumina ceramic discs with high hardness. *Journal of the European Ceramic Society*, 42(1):202–206, 2022.
- [65] Nicolas Moës, Anthony Gravouil, and Ted Belytschko. Non-planar 3d crack growth by the extended finite element and level sets—part i: Mechanical model. *International journal for numerical methods in engineering*, 53(11):2549–2568, 2002.
- [66] Michael L Falk, Alan Needleman, and James R Rice. A critical evaluation of cohesive zone models of dynamic fractur. *Le Journal de Physique IV*, 11(PR5):Pr5–43, 2001.
- [67] Cyril Williams and Bryan Love. Dynamic failure of materials: a review. Technical report, Army Research Lab Aberdeen Proving Ground Md Weapons and Materials Research, 2010.
- [68] C Yu Rena, Gonzalo Ruiz, and Anna Pandolfi. Numerical investigation on the dynamic behavior of advanced ceramics. *Engineering Fracture Mechanics*, 71(4-6):897–911, 2004.

- [69] Fenghua Zhou, Jean-François Molinari, and KT Ramesh. A cohesive model based fragmentation analysis: effects of strain rate and initial defects distribution. *International Journal of Solids and Structures*, 42(18-19):5181–5207, 2005.
- [70] Horacio D Espinosa, Pablo D Zavattieri, and Sunil K Dwivedi. A finite deformation continuum\discrete model for the description of fragmentation and damage in brittle materials. *Journal of the Mechanics and Physics of Solids*, 46(10):1909–1942, 1998.
- [71] Irene Arias, Jaroslaw Knap, Vijaya B Chalivendra, Soonsung Hong, Michael Ortiz, and Ares J Rosakis. Numerical modelling and experimental validation of dynamic fracture events along weak planes. *Computer Methods in Applied Mechanics and Engineering*, 196(37-40):3833–3840, 2007.
- [72] Wei Zhou, Wei Yuan, and Xiaolin Chang. Combined finite-discrete element method modeling of rock failure problems. In *International Conference on Discrete Element Methods*, pages 301–309. Springer, 2016.
- [73] OK Mahabadi, A Lisjak, A Munjiza, and G Grasselli. Y-geo: new combined finite-discrete element numerical code for geomechanical applications. *International Journal of Geomechanics*, 12(6):676–688, 2012.
- [74] HY Liu, YM Kang, and P Lin. Hybrid finite–discrete element modeling of geomaterials fracture and fragment muck-piling. *International Journal of Geotechnical Engineering*, 9(2):115–131, 2015.
- [75] Paola Costanza Miglietta. *Application of the Hybrid Finite/Discrete Element Method to the Numerical Simulation of Masonry Structures*. PhD thesis, University of Toronto (Canada), 2017.
- [76] A Lisjak, Q Liu, Q Zhao, OK Mahabadi, and G Grasselli. Numerical simulation of acoustic emission in brittle rocks by two-dimensional finite-discrete element analysis. *Geophysical Journal International*, 195(1):423–443, 2013.
- [77] B Paliwal and KT Ramesh. An interacting micro-crack damage model for failure of brittle materials under compression. *Journal of the Mechanics and Physics of Solids*, 56(3):896–923, 2008.
- [78] F Gálvez, J Rodríguez, and V Sánchez. Tensile strength measurements of ceramic materials at high rates of strain. *Le Journal de Physique IV*, 7(C3):C3–151, 1997.
- [79] F Gálvez, J Rodríguez, and V Sánchez Gálvez. A wave propagation technique to measure the dynamic tensile strength of brittle materials. *Le Journal de Physique IV*, 10(PR9):Pr9–203, 2000.

- [80] F Gálvez, J Rodríguez, and V Sánchez Gálvez. Influence of the strain rate on the tensile strength in aluminas of different purity. *Le Journal de Physique IV*, 10 (PR9):Pr9–323, 2000.
- [81] F Galvez Diaz-Rubio, J Rodriguez Perez, and V Sánchez Gálvez. The spalling of long bars as a reliable method of measuring the dynamic tensile strength of ceramics. *International Journal of Impact Engineering*, 27(2):161–177, 2002.
- [82] JJ Chen, BQ Guo, HB Liu, H Liu, and PW Chen. Dynamic brazilian test of brittle materials using the split hopkinson pressure bar and digital image correlation. *Strain*, 50(6):563–570, 2014.
- [83] Eugene Medvedovski. Ballistic performance of armour ceramics: Influence of design and structure. part 1. *Ceramics International*, 36(7):2103–2115, 2010.
- [84] Jeffrey J Swab, John J Pittari III, and William Robert Gamble. Uniaxial tensile strength and fracture analysis of a hot-pressed boron carbide. *Journal of the European Ceramic Society*, 39(6):1965–1973, 2019.
- [85] Zhiyong Wang, Ruitao Li, and Weidong Song. Dynamic failure and inelastic deformation behavior of sic ceramic under uniaxial compression. *Ceramics International*, 46(1):612–617, 2020.
- [86] JJ Swab, Wayne Chen, James Hogan, Hangjie Liao, Calvin Lo, Steven Mates, Christopher Meredith, JJ Pittari, Richard Rhorer, and GD Quinn. Dynamic compression strength of ceramics: What was learned from an interlaboratory round robin exercise? *Journal of Dynamic Behavior of Materials*, 7(1):34–47, 2021.
- [87] Yuan Xu and Feng Dai. Dynamic response and failure mechanism of brittle rocks under combined compression-shear loading experiments. *Rock Mechanics and Rock Engineering*, 51(3):747–764, 2018.
- [88] Muhammad Shafiq and Ghatu Subhash. An extended mohr–coulomb model for fracture strength of intact brittle materials under ultrahigh pressures. *Journal of the American Ceramic Society*, 99(2):627–630, 2016.
- [89] J Lankford, CE Anderson Jr, GR Johnson, and TJ Holmquist. Dynamic compressive failure of ceramics under confinement. In *Proceedings of the 1991 Combat Vehicle Survivability Conference*, volume 2, pages 15–17, 1991.
- [90] Charles E Anderson, Padraic E O’Donoghue, James Lankford, and James D Walker. Numerical simulations of shpb experiments for the dynamic compressive strength and failure of ceramics. *International journal of fracture*, 55(3):193–208, 1992.

- [91] Zdeněk P Bažant and Ferhun C Caner. Comminution of solids caused by kinetic energy of high shear strain rate, with implications for impact, shock, and shale fracturing. *Proceedings of the National Academy of Sciences*, 110(48):19291–19294, 2013.
- [92] Ferhun C Caner and Zdeněk P Bažant. Impact comminution of solids due to local kinetic energy of high shear strain rate: Ii–microplane model and verification. *Journal of the Mechanics and Physics of Solids*, 64:236–248, 2014.
- [93] RJ Clifton. An analysis of combined longitudinal and torsional plastic waves in a thin-walled tube. Technical report, Brown Univ Providence Ri Div of Engineering, 1966.
- [94] William Ernest Baker and CH Yew. Strain-rate effects in the propagation of torsional plastic waves. 1966.
- [95] J Duffy, JD Campbell, and RH Hawley. On the use of a torsional split hopkinson bar to study rate effects in 1100-0 aluminum. 1971.
- [96] W Zheng, SL Xu, C Cai, and S Hu. A study of dynamic combined compression-shear loading technique based on hopkinson pressure bar. *Chin J Theor Appl Mech*, 44(1):124–31, 2012.
- [97] Songlin Xu, Junyu Huang, Pengfei Wang, Chao Zhang, Lijiang Zhou, and Shisheng Hu. Investigation of rock material under combined compression and shear dynamic loading: an experimental technique. *International Journal of Impact Engineering*, 86:206–222, 2015.
- [98] Lijiang Zhou, Songlin Xu, Junfang Shan, Yonggui Liu, and Pengfei Wang. Heterogeneity in deformation of granite under dynamic combined compression/shear loading. *Mechanics of Materials*, 123:1–18, 2018.
- [99] D Rittel, S Lee, and G Ravichandran. A shear-compression specimen for large strain testing. *Experimental Mechanics*, 42(1):58–64, 2002.
- [100] J Zhao, WG Knauss, and G Ravichandran. A new shear-compression-specimen for determining quasistatic and dynamic polymer properties. *Experimental mechanics*, 49(3):427, 2009.
- [101] Stephen P Timoshenko and James N Goodier. Theory of elasticity. 1951.
- [102] Weinong W Chen and Bo Song. *Split Hopkinson (Kolsky) bar: design, testing and applications*. Springer Science & Business Media, 2010.

- [103] Hongbo Du, Feng Dai, Mingdong Wei, Ang Li, and Zelin Yan. Dynamic compression–shear response and failure criterion of rocks with hydrostatic confining pressure: an experimental investigation. *Rock Mechanics and Rock Engineering*, 54(2):955–971, 2021.
- [104] Brendan ML Koch, Phillip Jannotti, Debjoy Mallick, Brian Schuster, Tomoko Sano, and James David Hogan. Influence of microstructure on the impact failure of alumina. *Materials Science and Engineering: A*, 770:138549, 2020.
- [105] T Jiao, Yulong Li, KT Ramesh, and AA Wereszczat. High rate response and dynamic failure of structural ceramics. *International Journal of applied ceramic technology*, 1(3):243–253, 2004.
- [106] James Lankford, WW Predebon, JM Staehler, G Subhash, BJ Pletka, and CE Anderson. The role of plasticity as a limiting factor in the compressive failure of high strength ceramics. *Mechanics of Materials*, 29(3-4):205–218, 1998.
- [107] Zhiyong Wang and Peifeng Li. Dynamic failure and fracture mechanism in alumina ceramics: Experimental observations and finite element modelling. *Ceramics International*, 41(10):12763–12772, 2015.
- [108] J Lankford. Mechanisms responsible for strain-rate-dependent compressive strength in ceramic materials. *Journal of the American Ceramic Society*, 64(2): C–33, 1981.
- [109] JM Staehler, WW Predebon, BJ Pletka, and G Subhash. Micromechanisms of deformation in high-purity hot-pressed alumina. *Materials Science and Engineering: A*, 291(1-2):37–45, 2000.
- [110] Matthew DeVries, Ghatu Subhash, Alexander Mcghee, Peter Ifju, Tyrone Jones, James Zheng, and Virginia Halls. Quasi-static and dynamic response of 3d-printed alumina. *Journal of the European Ceramic Society*, 38(9):3305–3316, 2018.
- [111] Guruswami Ravichandran and Ghatuparthi Subhash. Critical appraisal of limiting strain rates for compression testing of ceramics in a split hopkinson pressure bar. *Journal of the American Ceramic Society*, 77(1):263–267, 1994.
- [112] HY Li, P Motamedi, and JD Hogan. Characterization and mechanical testing on novel $(\gamma + \alpha_2)$ -tial/ti3al/al2o3 cermet. *Materials Science and Engineering: A*, 750: 152–163, 2019.
- [113] Brendan ML Koch, Calvin Lo, Haoyang Li, Tomoko Sano, Jonathan Ligda, and James David Hogan. Dynamic mechanical response of damaged alumina ad995. *Journal of the European Ceramic Society*, 41(3):2034–2048, 2021.

- [114] Calvin Lo, Tomoko Sano, and James D Hogan. Deformation mechanisms and evolution of mechanical properties in damaged advanced ceramics. *Journal of the European Ceramic Society*, 40(8):3129–3139, 2020.
- [115] KT Ramesh and G Ravichandran. Dynamic behavior of a boron carbide aluminum cermet: experiments and observations. *Mechanics of Materials*, 10(1-2):19–29, 1990.
- [116] Weinong Chen and G Ravichandran. Dynamic compressive failure of a glass ceramic under lateral confinement. *Journal of the Mechanics and Physics of Solids*, 45(8):1303–1328, 1997.
- [117] Danny J Frew, Michael J Forrestal, and W Chen. Pulse shaping techniques for testing brittle materials with a split hopkinson pressure bar. *Experimental mechanics*, 42(1):93–106, 2002.
- [118] Brendan ML Koch, Calvin Lo, Haoyang Li, Tomoko Sano, Jonathan Ligda, and James David Hogan. Two-dimensional dynamic damage accumulation in engineered brittle materials. *Engineering Fracture Mechanics*, 244:107539, 2021.
- [119] Jung Ho Yoo, Jong Chul Nam, and Sunggi Baik. Quantitative evaluation of glass-forming impurities in alumina: Equivalent silica concentration (esc). *Journal of the American Ceramic Society*, 82(8):2233–2238, 1999.
- [120] SR Stock. Recent advances in x-ray microtomography applied to materials. *International materials reviews*, 53(3):129–181, 2008.
- [121] So Ik Bae and Sunggi Baik. Determination of critical concentrations of silica and/or calcia for abnormal grain growth in alumina. *Journal of the American ceramic society*, 76(4):1065–1067, 1993.
- [122] RL Landingham and AW Casey. Final report of the light armor materials program. Technical report, California Univ., 1972.
- [123] FP Knudsen. Dependence of mechanical strength of brittle polycrystalline specimens on porosity and grain size. *Journal of the American Ceramic Society*, 42(8):376–387, 1959.
- [124] Dennis E Grady and Marlin E Kipp. Continuum modelling of explosive fracture in oil shale. In *International Journal of Rock Mechanics and Mining Sciences & Geomechanics Abstracts*, volume 17, pages 147–157. Elsevier, 1980.
- [125] E Eberhardt, D Stead, and B Stimpson. Quantifying progressive pre-peak brittle fracture damage in rock during uniaxial compression. *International Journal of Rock Mechanics and Mining Sciences*, 36(3):361–380, 1999.

- [126] DH Warner and JF Molinari. Micromechanical finite element modeling of compressive fracture in confined alumina ceramic. *Acta Materialia*, 54(19):5135–5145, 2006.
- [127] Jian Fu Shao and John W Rudnicki. A microcrack-based continuous damage model for brittle geomaterials. *Mechanics of Materials*, 32(10):607–619, 2000.
- [128] Tomoko Sano, Lionel Vargas-Gonzalez, Jerry LaSalvia, and James David Hogan. Dynamic failure and fragmentation of a hot-pressed boron carbide. *Journal of Dynamic Behavior of Materials*, 3(4):548–556, 2017.
- [129] Amartya Bhattacharjee, Anindya Bhaduri, Ryan C Hurley, and Lori Graham-Brady. Failure modeling and sensitivity analysis of ceramics under impact. *Journal of Applied Mechanics*, 88(5):051007, 2021.
- [130] MB Cil, Q Zeng, RC Hurley, and L Graham-Brady. An integrative model for the dynamic behavior of brittle materials based on microcracking and breakage mechanics. *Journal of Dynamic Behavior of Materials*, 6(4):472–488, 2020.
- [131] Martina Scapin, Lorenzo Peroni, and Massimiliano Avale. Dynamic brazilian test for mechanical characterization of ceramic ballistic protection. *Shock and Vibration*, 2017, 2017.
- [132] A Brückner-Foit, T Fett, D Munz, and K Schirmer. Discrimination of multiaxiality criteria with the brazilian disc test. *Journal of the European Ceramic Society*, 17(5):689–696, 1997.
- [133] ASTM C496-11. Standard test method for splitting tensile strength of cylindrical concrete specimens, 2011.
- [134] Y Belrhiti, JC Dupre, O Pop, A Germaneau, P Doumalin, M Huger, and T Chotard. Combination of brazilian test and digital image correlation for mechanical characterization of refractory materials. *Journal of the European Ceramic Society*, 37(5):2285–2293, 2017.
- [135] J Li, J Zhao, HC Wang, K Liu, and QB Zhang. Fracturing behaviours and ae signatures of anisotropic coal in dynamic brazilian tests. *Engineering Fracture Mechanics*, 252:107817, 2021.
- [136] Qi-Zhi Wang and Lei Xing. Determination of fracture toughness k_{ic} by using the flattened brazilian disk specimen for rocks. *Engineering fracture mechanics*, 64(2):193–201, 1999.

- [137] Qi-Zhi Wang and LZ Wu. The flattened brazilian disc specimen used for determining elastic modulus, tensile strength and fracture toughness of brittle rocks: experimental results. *International Journal of Rock Mechanics and Mining Sciences*, 41:26–30, 2004.
- [138] Qi-Zhi Wang, XM Jia, SQ Kou, ZX Zhang, and P-A Lindqvist. The flattened brazilian disc specimen used for testing elastic modulus, tensile strength and fracture toughness of brittle rocks: analytical and numerical results. *International Journal of Rock Mechanics and Mining Sciences*, 41(2):245–253, 2004.
- [139] Qi-Zhi Wang, W Li, and HP Xie. Dynamic split tensile test of flattened brazilian disc of rock with SHPB setup. *Mechanics of Materials*, 41(3):252–260, 2009.
- [140] JR Antonn and AM Rajendran. Effect of strain rate and size on tensile strength of concrete. In *Proceedings of the topical conference on shock compression of condensed matter. Elsevier, Amsterdam*, volume 501, 1992.
- [141] R John, T Antoun, and AM Rajendran. Effect of strain rate and size on tensile strength of concrete. In *Shock Compression of Condensed Matter–1991*, pages 501–504. Elsevier, 1992.
- [142] Shiming Dong, Kaiwen Xia, Sheng Huang, and Tubing Yin. Rate dependence of the tensile and flexural strengths of glass–ceramic macor. *Journal of Materials Science*, 46(2):394–399, 2011.
- [143] YX Zhou, Kai-wen Xia, XB Li, Hong-Bo Li, GW Ma, Jian Zhao, ZL Zhou, and Feng Dai. Suggested methods for determining the dynamic strength parameters and mode-i fracture toughness of rock materials. In *The ISRM Suggested Methods for Rock Characterization, Testing and Monitoring: 2007-2014*, pages 35–44. Springer, 2011.
- [144] James David Hogan, Jamie Kimberley, Kavan Hazeli, Jeffrey Plescia, and KT Ramesh. Dynamic behavior of an ordinary chondrite: The effects of microstructure on strength, failure and fragmentation. *Icarus*, 260:308–319, 2015.
- [145] Mohammad Reza Khosravani and Kerstin Weinberg. A review on split Hopkinson bar experiments on the dynamic characterisation of concrete. *Construction and Building Materials*, 190:1264–1283, 2018.
- [146] Shuai Cao, Erol Yilmaz, and Weidong Song. Dynamic response of cement-tailings matrix composites under shpb compression load. *Construction and Building Materials*, 186:892–903, 2018.

- [147] Xudong Chen, Shengxing Wu, and Jikai Zhou. Quantification of dynamic tensile behavior of cement-based materials. *Construction and Building Materials*, 51: 15–23, 2014.
- [148] Achouak Elghazel, Rym Taktak, and Jamel Bouaziz. Investigation of mechanical behaviour of a bioceramic. *Fracture Mechanics: Properties, Patterns and Behaviours*, page 277, 2016.
- [149] Mohammad Reza Khosravani, Mohammad Silani, and Kerstin Weinberg. Fracture studies of ultra-high performance concrete using dynamic brazilian tests. *Theoretical and Applied Fracture Mechanics*, 93:302–310, 2018.
- [150] Pengwan Chen, Baoqiao Guo, and Jingjing Chen. Comparative study of the dynamic fracture toughness determination of brittle materials using the kolsky-hopkinson bar machine. In *The Kolsky-Hopkinson Bar Machine*, pages 143–156. Springer, 2018.
- [151] Zelin Yan, Feng Dai, Yi Liu, Mingdong Wei, and Wei You. New insights into the fracture mechanism of flattened brazilian disc specimen using digital image correlation. *Engineering Fracture Mechanics*, 252:107810, 2021.
- [152] Malcolm Mellor and Ivor Hawkes. Measurement of tensile strength by diametral compression of discs and annuli. *Engineering Geology*, 5(3):173–225, 1971.
- [153] Harald Schuler, Christoph Mayrhofer, and Klaus Thoma. Spall experiments for the measurement of the tensile strength and fracture energy of concrete at high strain rates. *International Journal of Impact Engineering*, 32(10):1635–1650, 2006.
- [154] PSB Colback. An analysis of brittle fracture initiation and propagation in the brazilian test. In *1st ISRM Congress*. OnePetro, 1966.
- [155] Diyuan Li and Louis Ngai Yuen Wong. The brazilian disc test for rock mechanics applications: review and new insights. *Rock mechanics and rock engineering*, 46(2):269–287, 2013.
- [156] Ch F Markides, DN Pazis, and SK Kourkoulis. Closed full-field solutions for stresses and displacements in the brazilian disk under distributed radial load. *International Journal of Rock Mechanics and Mining Sciences*, 47(2):227–237, 2010.
- [157] Nazife Erarslan, Zheng Zhao Liang, and David John Williams. Experimental and numerical studies on determination of indirect tensile strength of rocks. *Rock Mechanics and Rock Engineering*, 45(5):739–751, 2012.

- [158] G Hondros. The evaluation of poisson's ratio and the modulus of materials of low tensile resistance by the brazilian (indirect tensile) test with particular reference to concrete. *Australian J. Appl. Sci.*, 10(3):243–268, 1959.
- [159] B Amadei. Importance of anisotropy when estimating and measuring in situ stresses in rock. In *International journal of rock mechanics and mining sciences & geomechanics abstracts*, volume 33, pages 293–325. Elsevier, 1996.
- [160] Chao-Shi Chen, Ernian Pan, and Bernard Amadei. Determination of deformability and tensile strength of anisotropic rock using brazilian tests. *International Journal of Rock Mechanics and Mining Sciences*, 35(1):43–61, 1998.
- [161] P Pandey and DP Singh. Deformation of a rock in different tensile tests. *Engineering geology*, 22(3):281–292, 1986.
- [162] R Nova and A Zaninetti. An investigation into the tensile behaviour of a schistose rock. In *International Journal of rock mechanics and mining sciences & geomechanics abstracts*, volume 27, pages 231–242. Elsevier, 1990.
- [163] Ch F Markides, DN Pазis, and SK Kourkoulis. The brazilian disc under non-uniform distribution of radial pressure and friction. *International Journal of Rock Mechanics and Mining Sciences*, 50:47–55, 2012.
- [164] Ch F Markides and SK Kourkoulis. The stress field in a standardized brazilian disc: the influence of the loading type acting on the actual contact length. *Rock Mechanics and Rock Engineering*, 45(2):145–158, 2012.
- [165] S Okubo and K Fukui. Complete stress-strain curves for various rock types in uniaxial tension. In *International journal of rock mechanics and mining sciences & geomechanics abstracts*, volume 33, pages 549–556. Elsevier, 1996.
- [166] TR Stacey. A simple extension strain criterion for fracture of brittle rock. In *International Journal of Rock Mechanics and Mining Sciences & Geomechanics Abstracts*, volume 18, pages 469–474. Elsevier, 1981.
- [167] Xibing Li, Ming Tao, Chengqing Wu, Kun Du, and Qihong Wu. Spalling strength of rock under different static pre-confining pressures. *International Journal of Impact Engineering*, 99:69–74, 2017.
- [168] Huatao Zhao, Ming Tao, Xibing Li, Wenzhuo Cao, and Chengqing Wu. Estimation of spalling strength of sandstone under different pre-confining pressure by experiment and numerical simulation. *International Journal of Impact Engineering*, 133:103359, 2019.
- [169] KMW KMW. Ceramic materials for light-weight ceramic polymer armor systems.

- [170] Feng Dai, Sheng Huang, Kaiwen Xia, and Zhuoying Tan. Some fundamental issues in dynamic compression and tension tests of rocks using split hopkinson pressure bar. *Rock mechanics and rock engineering*, 43(6):657–666, 2010.
- [171] DW Hobbs. The tensile strength of rocks. In *International Journal of Rock Mechanics and Mining Sciences & Geomechanics Abstracts*, volume 1, pages 385–396. Elsevier, 1964.
- [172] JT Gomez, A Shukla, and A Sharma. Static and dynamic behavior of concrete and granite in tension with damage. *Theoretical and Applied Fracture Mechanics*, 36(1):37–49, 2001.
- [173] Herbert Kolsky. An investigation of the mechanical properties of materials at very high rates of loading. *Proceedings of the physical society. Section B*, 62(11):676, 1949.
- [174] H Kolsky. Stress waves in solids. dover books on physics, new york (1963).
- [175] Longhui Zhang, Antonio Pellegrino, David Townsend, and Nik Petrinic. Strain rate and temperature dependent strain localization of a near α titanium alloy. *International Journal of Impact Engineering*, 145:103676, 2020.
- [176] Q B Zhang and Jian Zhao. A review of dynamic experimental techniques and mechanical behaviour of rock materials. *Rock mechanics and rock engineering*, 47(4):1411–1478, 2014.
- [177] Haoyang Li, Chenwei Shao, David Funes Rojas, Mauricio Ponga, and James D Hogan. Micro-hardness and strain-rate-dependent compressive response of an ultra-light-weight Mg-Li-Al alloy. *Journal of Alloys and Compounds*, 890:161703, 2022.
- [178] Nazife Erarslan and David John Williams. Experimental, numerical and analytical studies on tensile strength of rocks. *International Journal of Rock Mechanics and Mining Sciences*, 49:21–30, 2012.
- [179] Jason T Gomez, Arun Shukla, and Atul Sharma. Photoelastic evaluation of stress fields and fracture during dynamic splitting experiments. *Journal of testing and evaluation*, 30(3):186–196, 2002.
- [180] Helmuth Späth. *Mathematical algorithms for linear regression*. Academic Press, 2014.
- [181] Maria Jesus Pérez-Martín, B Erice, DA Cendón, and F Gálvez. Spalling uniaxial strength of Al_2O_3 at high strain rates. *The European Physical Journal Special Topics*, 206(1):117–128, 2012.

- [182] Jeffrey J Swab, Christopher S Meredith, Daniel T Casem, and William Robert Gamble. Static and dynamic compression strength of hot-pressed boron carbide using a dumbbell-shaped specimen. *Journal of Materials Science*, 52(17):10073–10084, 2017.
- [183] William D Neal, Gareth J Appleby-Thomas, and Gareth S Collins. Meso-scopic deformation in brittle granular materials. In *Journal of Physics: Conference Series*, volume 500, page 112047. IOP Publishing, 2014.
- [184] Yong Yu, Jianxun Zhang, and Jichun Zhang. A modified brazilian disk tension test. *International journal of rock mechanics and mining sciences*, 46(2):421–425, 2009.
- [185] Jeffrey J Swab, Jian Yu, Robert Gamble, and Steve Kilczewski. Analysis of the diametral compression method for determining the tensile strength of transparent magnesium aluminate spinel. *International journal of fracture*, 172(2):187–192, 2011.
- [186] James D Hogan, Robert J Rogers, John G Spray, and Suporn Boonsue. Dynamic fragmentation of granite for impact energies of 6–28 j. *Engineering Fracture Mechanics*, 79:103–125, 2012.
- [187] MA Aswad and TJ Marrow. Intergranular crack nuclei in polycrystalline alumina. *Engineering Fracture Mechanics*, 95:29–36, 2012.
- [188] François Hild, Christophe Denoual, Pascal Forquin, and Xavier Brajer. On the probabilistic–deterministic transition involved in a fragmentation process of brittle materials. *Computers & Structures*, 81(12):1241–1253, 2003.
- [189] G Subhash and Guruswami Ravichandran. Split-Hopkinson pressure bar testing of ceramics. *Materials Park, OH: ASM International, 2000.*, pages 497–504, 2000.
- [190] Zhiyong Wang and Peifeng Li. Characterisation of dynamic behaviour of alumina ceramics: evaluation of stress uniformity. *AIP Advances*, 5(10):107224, 2015.
- [191] J Kimberley, KT Ramesh, and NP Daphalapurkar. A scaling law for the dynamic strength of brittle solids. *Acta Materialia*, 61(9):3509–3521, 2013.
- [192] Cristian Dascalu. Dynamic damage law with fragmentation length: strain-rate sensitivity of the tensile response. *Journal of Dynamic Behavior of Materials*, 7(1):156–160, 2021.
- [193] Teresa Gómez del Río and Jesús Rodríguez Pérez. Elastic wave propagation in cylindrical bars after brittle failures: Application to spalling tests. *International journal of impact engineering*, 34(2):377–393, 2007.

- [194] Jeffrey J Swab, Jerry C Lasalvia, Gary A Gilde, Parimal J Patel, and Matthew J Motyka. Transparent armor ceramics: Alon and spinel. In *23rd Annual Conference on Composites, Advanced Ceramics, Materials, and Structures: B: Ceramic Engineering and Science Proceedings*, pages 79–84. Wiley Online Library, 1999.
- [195] Gerd Willmann. Ceramic femoral head retrieval data. *Clinical Orthopaedics and Related Research*, 379:22–28, 2000.
- [196] Ghatu Subhash, Spandan Maiti, Philippe H Geubelle, and Dipankar Ghosh. Recent advances in dynamic indentation fracture, impact damage and fragmentation of ceramics. *Journal of the American Ceramic Society*, 91(9):2777–2791, 2008.
- [197] Eugene Medvedovski. Ballistic performance of armour ceramics: Influence of design and structure. part 2. *Ceramics International*, 36(7):2117–2127, 2010.
- [198] Christian Kaufmann, Duane Cronin, Michael Worswick, Gilles Pageau, and Andre Beth. Influence of material properties on the ballistic performance of ceramics for personal body armour. *Shock and Vibration*, 10(1):51–58, 2003.
- [199] G. Toussaint, Y. Martinez-Rubi, S. Noormohammed, and C. Li. Novel alternative multi-hit ballistic testing method developed to evaluate bonding technologies performance. Technical report, DRDC-RDDC-2020-R045, 2020.
- [200] Jeffrey J Swab, Andrew A Wereszczak, Kevin T Strong Jr, Dominic Danna, Jerry C LaSalvia, Meredith E Ragan, and Patrick J Ritt. Knoop hardness–apparent yield stress relationship in ceramics. *International Journal of Applied Ceramic Technology*, 9(3):650–655, 2012.
- [201] Matthew DeVries and Ghatu Subhash. Influence of carbon nanotubes as secondary phase addition on the mechanical properties and amorphization of boron carbide. *Journal of the European Ceramic Society*, 39(6):1974–1983, 2019.
- [202] Munro MUNRO. Evaluated material properties for a sintered alpha-alumina. *Journal of the American Ceramic Society*, 80(8):1919–1928, 1997.
- [203] Serkan Nohut. Influence of sample size on strength distribution of advanced ceramics. *Ceramics International*, 40(3):4285–4295, 2014.
- [204] JC Langford and Matthew A Perras. Obtaining reliable estimates of intact tensile strength. In *48th US Rock Mechanics/Geomechanics Symposium*. OnePetro, 2014.
- [205] Jeffrey J Swab, Jason Tice, Andrew A Wereszczak, and Reuben H Kraft. Fracture toughness of advanced structural ceramics: applying astm c1421. *Journal of the American Ceramic Society*, 98(2):607–615, 2015.

- [206] Ghatu Subhash, Amnaya Awasthi, and Dipankar Ghosh. *Dynamic response of advanced ceramics*. John Wiley & Sons, 2021.
- [207] Salil Bavdekar and Ghatu Subhash. Failure mechanisms of ceramics under quasi-static and dynamic loads: overview. *Handbook of Damage Mechanics: Nano to Macro Scale for Materials and Structures*, pages 579–607, 2022.
- [208] Jie Zheng, Haoyang Li, and James D. Hogan. Strain-rate-dependent tensile response of an alumina ceramic: Experiments and modelling. *International Journal of Impact Engineering*, 173:104487, 2022. ISSN 0734-743X.
- [209] Gareth James Appleby-Thomas, Kevin Jaansalu, Amer Hameed, Jonathan Painter, James Shackel, and Julie Rowley. A comparison of the ballistic behaviour of conventionally sintered and additively manufactured alumina. *Defence Technology*, 16(2):275–282, 2020.
- [210] Andy Nieto, Lin Huang, Young-Hwan Han, and Julie M Schoenung. Sintering behavior of spark plasma sintered alumina with graphene nanoplatelet reinforcement. *Ceramics International*, 41(4):5926–5936, 2015.
- [211] Martin Schwentenwein and Johannes Homa. Additive manufacturing of dense alumina ceramics. *International Journal of Applied Ceramic Technology*, 12(1): 1–7, 2015.
- [212] Mattia Biesuz and Vincenzo M Sglavo. Flash sintering of alumina: Effect of different operating conditions on densification. *Journal of the European Ceramic Society*, 36(10):2535–2542, 2016.
- [213] GE Andreev. A review of the brazilian test for rock tensile strength determination. part i: calculation formula. *Mining Science and Technology*, 13(3):445–456, 1991.
- [214] Lori Graham-Brady. Statistical characterization of meso-scale uniaxial compressive strength in brittle materials with randomly occurring flaws. *International Journal of Solids and Structures*, 47(18-19):2398–2413, 2010.
- [215] Liang Sun, Dejun Ma, Lizhi Wang, Xinzheng Shi, Jialiang Wang, and Wei Chen. Determining indentation fracture toughness of ceramics by finite element method using virtual crack closure technique. *Engineering Fracture Mechanics*, 197:151–159, 2018.
- [216] Han Wang, Han Dong, Zhenwei Cai, Yuhang Li, Weizhe Wang, and Yingzheng Liu. Peridynamic-based investigation of the cracking behavior of multilayer thermal barrier coatings. *Ceramics International*, 48(16):23543–23553, 2022.

- [217] Peng Cao, Changbing Tang, Zai Liu, Feiting Shi, Ziyu Wang, Xuhao Wang, and Changjun Zhou. Study on fracture behaviour of basalt fibre reinforced asphalt concrete with plastic coupled cohesive model and enhanced virtual crack closure technique model. *International Journal of Pavement Engineering*, pages 1–21, 2022.
- [218] Godofredo T Camacho and M Ortiz. Computational modelling of impact damage in brittle materials. *International Journal of solids and structures*, 33(20-22): 2899–2938, 1996.
- [219] ME Walter, DM Owen, and G Ravichandran. Static and dynamic tension testing of ceramics and ceramic composites. *ASME APPLIED MECHANICS DIVISION-PUBLICATIONS-AMD*, 197:13–13, 1994.
- [220] Zhiyong Wang and Peifeng Li. Voronoi cell finite element modelling of the intergranular fracture mechanism in polycrystalline alumina. *Ceramics International*, 43(9):6967–6975, 2017.
- [221] Fenghua Zhou and Jean-Francois Molinari. Stochastic fracture of ceramics under dynamic tensile loading. *International journal of solids and structures*, 41(22-23): 6573–6596, 2004.
- [222] Nitin P Daphalapurkar, KT Ramesh, Lori Graham-Brady, and Jean-Francois Molinari. Predicting variability in the dynamic failure strength of brittle materials considering pre-existing flaws. *Journal of the Mechanics and Physics of Solids*, 59(2):297–319, 2011.
- [223] Z Zou, SR Reid, and S Li. A continuum damage model for delaminations in laminated composites. *Journal of the Mechanics and Physics of Solids*, 51(2): 333–356, 2003.
- [224] Veena Tikare and Sung R Choi. Combined mode i and mode ii fracture of monolithic ceramics. *Journal of the American Ceramic Society*, 76(9):2265–2272, 1993.
- [225] DK Shetty, AR Rosenfield, and WH Duckworth. Mixed-mode fracture of ceramics in diametral compression. *Journal of the American Ceramic Society*, 69(6):437–443, 1986.
- [226] Zdenek P Bazant and Jaime Planas. *Fracture and size effect in concrete and other quasibrittle materials*, volume 16. CRC press, 1997.
- [227] Jean-François Molinari, G Gazonas, R Raghupathy, A Rusinek, and F Zhou. The cohesive element approach to dynamic fragmentation: the question of energy

- convergence. *International Journal for Numerical Methods in Engineering*, 69(3): 484–503, 2007.
- [228] Fenghua Zhou and Jean-Francois Molinari. Dynamic crack propagation with cohesive elements: a methodology to address mesh dependency. *International Journal for Numerical Methods in Engineering*, 59(1):1–24, 2004.
- [229] Shay I Heizler, David A Kessler, and Herbert Levine. Propagating mode-i fracture in amorphous materials using the continuous random network model. *Physical Review E*, 84(2):026102, 2011.
- [230] Xiaodan Ren and Jie Li. Dynamic fracture in irregularly structured systems. *Physical Review E*, 85(5):055102, 2012.
- [231] Stephen W Freiman and John J Mecholsky Jr. *The fracture of brittle materials: testing and analysis*. John Wiley & Sons, 2019.
- [232] Waloddi Weibull. A statistical theory of strength of materials. *IVB-Handl.*, 1939.
- [233] Nickolai Savchenko, Irina Sevostyanova, Tatiana Sablina, László Gömze, and Sergei Kulkov. The influence of porosity on the elasticity and strength of alumina and zirconia ceramics. In *AIP Conference Proceedings*, volume 1623, pages 547–550. American Institute of Physics, 2014.
- [234] SB Sapozhnikov, OA Kudryavtsev, and N Yu Dolganina. Experimental and numerical estimation of strength and fragmentation of different porosity alumina ceramics. *Materials & Design*, 88:1042–1048, 2015.
- [235] Dionissios T Hristopoulos and Melina Demertzi. A semi-analytical equation for the young’s modulus of isotropic ceramic materials. *Journal of the European Ceramic Society*, 28(6):1111–1120, 2008.
- [236] S Falco, N Fogell, S Kasinos, and L Iannucci. Homogenisation of micromechanical modelling results for the evaluation of macroscopic material properties of brittle ceramics. *International Journal of Mechanical Sciences*, 220:107071, 2022.
- [237] OA Kudryavtsev and SB Sapozhnikov. Numerical simulations of ceramic target subjected to ballistic impact using combined dem/fem approach. *International Journal of Mechanical Sciences*, 114:60–70, 2016.
- [238] Anand Pai, R Divakaran, S Anand, and Satish B Shenoy. Advances in the whipple shield design and development: A brief review. *Journal of Dynamic Behavior of Materials*, pages 1–19, 2022.

- [239] Yao Huang, Navid Zolfaghari, Osgar John Ohanian III, and Andrew P Bungler. An inversion algorithm to estimate maximum and minimum horizontal stress based on field test data for sleeve fracturing. *Computers and Geotechnics*, 137:104274, 2021.
- [240] Haiyan Liu, Lihong Liang, Yingbiao Wang, and Yueguang Wei. Fracture characteristics and damage evolution of coating systems under four-point bending. *International Journal of Applied Ceramic Technology*, 13(6):1043–1052, 2016.
- [241] LH Liang, XN Li, HY Liu, YB Wang, and YG Wei. Power-law characteristics of damage and failure of ceramic coating systems under three-point bending. *Surface and Coatings Technology*, 285:113–119, 2016.
- [242] Xinying Liu, Yi Liu, Feng Dai, and Zelin Yan. Tensile mechanical behavior and fracture characteristics of sandstone exposed to freeze-thaw treatment and dynamic loading. *International Journal of Mechanical Sciences*, 226:107405, 2022.
- [243] Chien-Ching Ma and Kuang-Ming Hung. Exact full-field analysis of strain and displacement for circular disks subjected to partially distributed compressions. *International Journal of Mechanical Sciences*, 50(2):275–292, 2008.
- [244] J Rodriguez, C Navarro, and V Sanchez-Galvez. Splitting tests: an alternative to determine the dynamic tensile strength of ceramic materials. *Le Journal de Physique IV*, 4(C8):C8–101, 1994.
- [245] Zhen Wang, Dayou Ma, Tao Suo, Yulong Li, and Andrea Manes. Investigation into different numerical methods in predicting the response of aluminosilicate glass under quasi-static and impact loading conditions. *International Journal of Mechanical Sciences*, 196:106286, 2021.
- [246] A Coviello, Rocco Lagioia, and Roberto Nova. On the measurement of the tensile strength of soft rocks. *Rock Mechanics and Rock Engineering*, 38(4):251–273, 2005.
- [247] Hadi Haeri, Kouros Shahriar, Mohammad Fatehi Marji, and P Moarefvand. Simulating the bluntness of tbn disc cutters in rocks using displacement discontinuity method. In *Proc. of 13th Int. Conf. on Fracture, China*, 2013.
- [248] M Lak, M Fatehi Marji, AR Yarahamdi Bafghi, and A Abdollahipour. Discrete element modeling of explosion-induced fracture extension in jointed rock masses. *Journal of Mining and Environment*, 10(1):125–138, 2019.
- [249] Meysam Lak, Mohammad Fatehi Marji, Alireza Yarahmadi Bafghi, and Abolfazl Abdollahipour. Analytical and numerical modeling of rock blasting operations using a two-dimensional elasto-dynamic green’s function. *International Journal of Rock Mechanics and Mining Sciences*, 114:208–217, 2019.

- [250] Michał Kucewicz, Paweł Baranowski, Roman Gieleta, and Jerzy Małachowski. Investigation of dolomite'rock brittle fracture using fully calibrated karagozian case concrete model. *International Journal of Mechanical Sciences*, 221:107197, 2022.
- [251] Zahra Zaiemyekheh, Haoyang Li, Saman Sayahlatifi, Min Ji, Jie Zheng, Dan L Romanyk, and James D Hogan. Computational finite element modeling of stress-state-and strain-rate-dependent failure behavior of ceramics with experimental validation. *Ceramics International*, 49(9):13878–13895, 2023.
- [252] R Abedi. A comparative and parametric study of dynamic cohesive and linear elastic fracture mechanics models. *International Journal of Solids and Structures*, 102:163–175, 2016.
- [253] Jie Zheng, Haoyang Li, and James D Hogan. Hybrid finite-discrete element modeling of the mode i tensile response of an alumina ceramic. *Modelling*, 4(1): 87–101, 2023.
- [254] AV Ignatova, SB Sapozhnikov, and N Yu Dolganina. Development of microstructural and voxel based models of deformation and failure of the porous ceramics for assessment of ballistic performance. *International Journal of Mechanical Sciences*, 131:672–682, 2017.
- [255] Giulio Alfano and Elio Sacco. Combining interface damage and friction in a cohesive-zone model. *International Journal for Numerical Methods in Engineering*, 68(5):542–582, 2006.
- [256] Renaud Gutkin and Silvestre T Pinho. Combining damage and friction to model compressive damage growth in fibre-reinforced composites. *Journal of composite materials*, 49(20):2483–2495, 2015.
- [257] Bahador Bahmani, Reza Abedi, and Philip L Clarke. A stochastic bulk damage model based on mohr-coulomb failure criterion for dynamic rock fracture. *Applied Sciences*, 9(5):830, 2019.
- [258] Guangli Hu, KT Ramesh, Buyang Cao, and JW McCauley. The compressive failure of aluminum nitride considered as a model advanced ceramic. *Journal of the Mechanics and Physics of Solids*, 59(5):1076–1093, 2011.
- [259] Ala Tabiei and Wenlong Zhang. Cohesive element approach for dynamic crack propagation: Artificial compliance and mesh dependency. *Engineering Fracture Mechanics*, 180:23–42, 2017.
- [260] Shen Wang, Dongyin Li, Zhenhua Li, Jinzhao Liu, Shuang Gong, and Guoyan Li. A rate-dependent model and its user subroutine for cohesive element method

- to investigate propagation and branching behavior of dynamic brittle crack. *Computers and Geotechnics*, 136:104233, 2021.
- [261] ZT Bieniawski and I Hawkes. Suggested methods for determining tensile strength of rock materials. *Int J Rock Mech Min Sci Geomech Abstr*, 15(3):99–103, 1978.
- [262] Yi-Lin Gui, Ha H Bui, Jayantha Kodikara, Qian-Bing Zhang, Jian Zhao, and Timon Rabczuk. Modelling the dynamic failure of brittle rocks using a hybrid continuum-discrete element method with a mixed-mode cohesive fracture model. *International Journal of Impact Engineering*, 87:146–155, 2016.
- [263] Andreas Krell and Elmar Strassburger. Discrimination of basic influences on the ballistic strength of opaque and transparent ceramics. In *Ceram Eng Sci Proc*, volume 33, pages 161–176, 2012.
- [264] Adam Healey, John Cotton, Stuart Maclachlan, Paul Smith, and Julie Yeomans. Understanding the ballistic event: methodology and initial observations. *Journal of Materials Science*, 52(6):3074–3085, 2017.
- [265] Piotr Nicewicz, Peter Peciar, Oliver Macho, Tomoko Sano, and James D Hogan. Quasi-static confined uniaxial compaction of granular alumina and boron carbide observing the particle size effects. *Journal of the American Ceramic Society*, 103(3):2193–2209, 2020.
- [266] J Silvestre, N Silvestre, and J De Brito. An overview on the improvement of mechanical properties of ceramics nanocomposites. *Journal of Nanomaterials*, 2015, 2015.
- [267] Zahra Zaiemyekheh, Haoyang Li, Dan L Romanyk, and James D Hogan. Strain-rate-dependent behavior of additively manufactured alumina ceramics: Characterization and mechanical testing. *Journal of Materials Research and Technology*, 2024.
- [268] Hong, Wang, , , K.T, and Ramesh. Dynamic strength and fragmentation of hot-pressed silicon carbide under uniaxial compression. *Acta Materialia*, 2004.
- [269] B Paliwal, KT Ramesh, and JW McCauley. Direct observation of the dynamic compressive failure of a transparent polycrystalline ceramic (alon). *Journal of the American Ceramic Society*, 89(7):2128–2133, 2006.
- [270] Sheng-Wang Hao, Feng Rong, Lu Ming-Fu, Hai-Ying Wang, Meng-Fen Xia, Ke Fu-Jiu, and Yi-Long Bai. Power-law singularity as a possible catastrophe warning observed in rock experiments. *International Journal of Rock Mechanics and Mining Sciences*, 60:253–262, 2013.

- [271] Seong Hyeok Song. *Fracture of asphalt concrete: a cohesive zone modeling approach considering viscoelastic effects*. PhD thesis, University of Illinois at Urbana-Champaign, 2006.
- [272] Jie Zheng, Haoyang Li, and James D Hogan. Advanced tensile fracture analysis of alumina ceramics: Integrating hybrid finite-discrete element modeling with experimental insights. *Engineering Fracture Mechanics*, 302:110075, 2024.
- [273] M F&ashby and SD Hallam. The failure of brittle solids containing small cracks under compressive stress states. *Acta metallurgica*, 34(3):497–510, 1986.
- [274] K Sairam, JK Sonber, TSR Ch Murthy, C Subramanian, RK Fotedar, P Nanekar, and RC Hubli. Influence of spark plasma sintering parameters on densification and mechanical properties of boron carbide. *International Journal of Refractory Metals and Hard Materials*, 42:185–192, 2014.
- [275] Namtae Cho, Zhihao Bao, and Robert F Speyer. Density-and hardness-optimized pressureless sintered and post-hot isostatic pressed B₄C. *Journal of materials research*, 20(8):2110–2116, 2005.
- [276] Stephen L Dole, Svante Prochazka, and Robert H Doremus. Microstructural coarsening during sintering of boron carbide. *Journal of the American Ceramic Society*, 72(6):958–966, 1989.
- [277] AK Suri, C Subramanian, JK Sonber, and TSR Ch Murthy. Synthesis and consolidation of boron carbide: a review. *International Materials Reviews*, 55(1):4–40, 2010.
- [278] Muhammet Fatih Toksoy and Richard A Haber. Modification of commercial boron carbide powder using rapid carbothermal reduction. *International Journal of Applied Ceramic Technology*, 16(3):1120–1125, 2019.
- [279] Vladislav Domnich, Sara Reynaud, Richard A Haber, and Manish Chhowalla. Boron carbide: structure, properties, and stability under stress. *Journal of the American Ceramic Society*, 94(11):3605–3628, 2011.
- [280] Sisi Xiang, Luoning Ma, Bruce Yang, Yvonne Dieudonne, George M Pharr, Jing Lu, Digvijay Yadav, Chawon Hwang, Jerry C LaSalvia, Richard A Haber, et al. Tuning the deformation mechanisms of boron carbide via silicon doping. *Science advances*, 5(10):eaay0352, 2019.
- [281] Sisi Xiang, Qirong Yang, Hsu-Ming Lien, Keya Shial, Eric Gronske, Richard Haber, and Kelvin Y Xie. The effect of boron and aluminum additions on the

- microstructure of arc-melted boron carbide. *Journal of the American Ceramic Society*, 103(6):3453–3457, 2020.
- [282] David M Stump. Toughening and strengthening of ceramics reinforced by dilatant transformations and ductile particles. *International journal of solids and structures*, 28(6):669–689, 1991.
- [283] AM Rajendran and DJ Grove. Modeling the shock response of silicon carbide, boron carbide and titanium diboride. *International Journal of Impact Engineering*, 18(6):611–631, 1996.
- [284] T Sadowski and S Samborski. Prediction of the mechanical behaviour of porous ceramics using mesomechanical modelling. *Computational materials science*, 28(3-4):512–517, 2003.
- [285] Timothy Holmquist, Sidney Chocron, and Art Nicholls. The effect of the third invariant on the strength and failure of boron carbide and silicon carbide. *Journal of the American Ceramic Society*, 104(5):2348–2357, 2021.
- [286] A Chakraborti, N Vast, and Y Le Godec. Synthesis of boron carbide from its elements at high pressures and high temperatures. *Solid State Sciences*, 104:106265, 2020.
- [287] Russlan Jaafreh, Yoo Seong Kang, Jung-Gu Kim, and Kotiba Hamad. Machine learning guided discovery of super-hard high entropy ceramics. *Materials Letters*, 306:130899, 2022.
- [288] Mohammad Rezasefat, Haoyang Li, and James D Hogan. Prediction of microstructural-dependent mechanical properties, progressive damage, and stress distribution from x-ray computed tomography scans using a deep learning workflow. *Computer Methods in Applied Mechanics and Engineering*, 424:116878, 2024.
- [289] Qiaolei Li, Weiqiang Hou, Jingjing Liang, Chaowei Zhang, Jinguo Li, Yizhou Zhou, and Xiaofeng Sun. Controlling the anisotropy behaviour of 3d printed ceramic cores: From intralayer particle distribution to interlayer pore evolution. *Additive Manufacturing*, 58:103055, 2022.